



**HAL**  
open science

# Nanometre-thick alumina coatings deposited by ALD on metals: a comparative electrochemical and surface analysis study of corrosion properties

Shadi Mirhashemihaghighi

► **To cite this version:**

Shadi Mirhashemihaghighi. Nanometre-thick alumina coatings deposited by ALD on metals: a comparative electrochemical and surface analysis study of corrosion properties. Chemical Physics [physics.chem-ph]. Université Pierre et Marie Curie - Paris VI, 2015. English. NNT : 2015PA066349 . tel-01265540

**HAL Id: tel-01265540**

**<https://theses.hal.science/tel-01265540>**

Submitted on 1 Feb 2016

**HAL** is a multi-disciplinary open access archive for the deposit and dissemination of scientific research documents, whether they are published or not. The documents may come from teaching and research institutions in France or abroad, or from public or private research centers.

L'archive ouverte pluridisciplinaire **HAL**, est destinée au dépôt et à la diffusion de documents scientifiques de niveau recherche, publiés ou non, émanant des établissements d'enseignement et de recherche français ou étrangers, des laboratoires publics ou privés.



**THESE DE DOCTORAT DE  
L'UNIVERSITE PIERRE ET MARIE CURIE**

Spécialité

Chimie Physique et Chimie Analytique (Paris Centre, ED388)

Présentée par

**Shadi Mirhashemihaghighi**

Pour obtenir le grade de

**DOCTEUR de L'UNIVERSITE PIERRE ET MARIE CURIE**

Sujet de la thèse :

**Nanometre-thick alumina coatings deposited by ALD on metals: a comparative electrochemical and surface analysis study of corrosion properties**

Soutenance le 17 juillet 2015

devant le jury composé de :

M. Hans-Henning Strehlow	Professeur, Heinrich-Heine-Universität Düsseldorf	Rapporteur
M. Bernard Normand	Professeur, MATEIS- INSA	Rapporteur
M. Lorenzo Fedrizzi	Professeur, Università degli Studi di Udine	Examineur
Mme. Isabelle Frateur	Chargée de recherche, CNRS	Examineur
M. Vincent Maurice	Directeur de recherche, CNRS	Directeur de thèse
M. Philippe Marcus	Directeur de recherche, CNRS	Co-directeur de thèse
Mme. Jolanta Światowska	Chargée de recherche, CNRS	Co-encadrante (Membre invité)



# Acknowledgement

The present thesis work was done in the Physico-Chimie des Surfaces group in Chimie ParisTech with the fellowship provided by UPMC.

The First and foremost, I would like to express my deepest sense of gratitude to my thesis advisor, Vincent Maurice, for his strong scientific supervision and guidance on my thesis work during all these three years and especially during these last months, for his precise and valuable comments on the thesis manuscript. I would also like to express my sincere thanks to Philippe Marcus, the leader of the PCS group and the co-director of my thesis, for his surveillance on my work and for providing me the opportunity to benefit all the possibilities in PCS group to accomplish my thesis work. I am thankful to Jolanta Światowska, the supervisor of my thesis for all her scientific help, her kindness and especially for her support for the startup of my work in the group.

Moreover, I would like to express my sincere regards to the jury members, Hans-Henning Strehblow, Bernard Normand, Isabelle Frateur and Lorenzo Fedrizzi for devoting their precious time to the review of my thesis manuscript and for their scientific evaluation.

I must acknowledge Mikko Ritala and especially Emma Härkönen from University of Helsinki for their important collaboration in this thesis work for the deposition of ALD coatings, and their valuable scientific advice.

Furthermore, I would like to thank Antoine Seyeux for all the ToF-SIMS measurements in addition to all the worthwhile scientific discussions I have had with him. Thanks to Lorena H. Klein for all her initial instructions for the preparation of copper samples, and her instructions on AFM measurements. Finally, thanks to Sandrine Zanna for the last urgent XPS measurements. I would also like to thank Sylvie Gandziarski and Frédéric Wiame.

My special thanks to my friend and colleague Blanca, for all the fruitful scientific discussions that we had, which helped me through my thesis. I should express my regards to the organizers of the impedance formation at LISE, including Isabelle Frateur, who helped me to improve my knowledge about the impedance.

My sincere thanks to my colleagues, who spiced up my professional life in the lab. Thanks to them in the alphabetic order: Bingbing, Elise, Emna, Hao, Hu, Jun Tao, Marion, Matthieu, Oumaima, Rémi, Slava, Svetlana and Zuzana for all our tasteful lunch times, strategic coffee breaks, glorious tea times and joyful after works.

Many thanks to all my friends out of the lab, who were with me all these three years. My deepest thanks to Candela, for being there as a strong source of happiness, like before. Thanks to Nikita for all the nice time that we spent together. Thanks to my friend and old colleague Isabel, especially for providing me with the urgent missing references. Many thanks to my friends with who I spent many joyful Friday nights after the hard work during the week: Samy, Rafa, Shahin, Romain, Benoît, Ioana, Kuba, Tristan, Lourdes, Nico, Charlotte, Benjamin, Seb, Claribet, Jean-Philippe and Guillaume.

I should express my deepest appreciation to my aunt, uncle and cousin, who were there for me all the time and served me as a second family.

And of course, my most unique thanks to Luis, for his endless support, with whom it was easy to go through the difficult moments.

And finally all my love to my parents and brothers; without whom, none of this would be possible.



## Table of contents

General introduction.....	1
Chapter I. State of the art on ALD and its application to corrosion protection.....	5
I.1. Atomic Layer Deposition.....	5
I.1.1. Introduction.....	5
I.1.2. Terminology .....	6
I.1.3. The mechanism and main features of ALD .....	7
I.1.4. Main advantages of ALD.....	9
I.1.5. Non-ideal ALD behaviour .....	10
I.1.6. Limitations of ALD .....	11
I.1.7. Precursors and their requirements in ALD .....	12
I.1.8. Nucleation and growth in ALD .....	13
I.1.9. Film morphology .....	16
I.1.10. ALD of alumina ( $\text{Al}_2\text{O}_3$ ).....	17
I.2. ALD for corrosion protection .....	19
Chapter II. Experimental .....	23
II.1. Substrate preparation.....	23
II.1.1. Copper substrate .....	23
II.1.1.1. Mechanical polishing.....	23
II.1.1.2. Electropolishing.....	24
II.1.1.3. Annealing .....	25
II.1.1.4. Oxide removal pre-treatment.....	27
II.1.2. Aluminium substrate .....	27
II.1.2.1. Mechanical polishing.....	28
II.2. ALD coating deposition .....	28
II.3. Surface analysis.....	30
II.3.1. Time-of-Flight Secondary Ion Mass Spectrometry .....	30

II.3.1.1. Principles.....	30
II.3.1.2. Instrumentation and analytical conditions .....	33
II.3.2. Atomic Force Microscopy .....	35
II.3.2.1. Principles and instrumentation.....	35
II.3.3. Scanning Electron Microscopy .....	38
II.4. Electrochemical analysis.....	39
II.4.1. Experimental conditions .....	39
II.4.1.1. Instrumentation .....	39
II.4.1.1.1. Electrochemical cell.....	39
II.4.1.1.2. Potentiostat.....	40
II.4.2. Techniques .....	41
II.4.2.1. Open Circuit Potential vs time .....	41
II.4.2.2. Electrochemical Impedance Spectroscopy.....	42
II.4.2.3. Linear Sweep Voltammetry .....	44
Chapter III. Analysis of the corrosion protection of copper by ALD alumina coatings and effect of deposited layer thickness .....	47
III.1. Introduction .....	47
III.2. Electrochemical behaviour of bare Cu substrate .....	48
III.2.1. Linear sweep voltammetry .....	48
III.2.2. Electrochemical Impedance Spectroscopy .....	55
III.3. Surface and electrochemical analysis of Cu coated with ALD Al <sub>2</sub> O <sub>3</sub> .....	58
III.3.1. Time-of-Flight Secondary Ion Mass Spectrometry .....	58
III.3.2. Atomic Force Microscopy .....	64
III.3.3. Linear Sweep Voltammetry .....	67
III.3.4. Electrochemical Impedance Spectroscopy .....	70
III.4. Conclusions .....	80
Chapter IV. Effect of the interfacial native oxide layer on the corrosion of ALD alumina coated copper.....	83

IV.1. Introduction.....	83
IV.2. Electrochemical analysis of bare substrates.....	85
IV.2.1. Electrochemical Impedance Spectroscopy.....	85
IV.2.2. Linear Sweep Voltammetry.....	86
IV.3. Surface and electrochemical analysis of coated substrates.....	90
IV.3.1. Time-of-Flight Secondary Ion Mass Spectrometry on pristine coated samples.....	90
IV.3.2. Electrochemical Impedance Spectroscopy.....	94
IV.3.3. Linear Sweep Voltammetry.....	97
IV.3.4. Time-of-Flight Secondary Ion Mass Spectrometry of polarized coated samples.....	100
IV.4. Conclusions.....	104
Chapter V. Effect of copper substrate annealing on the corrosion protection of ALD alumina coatings.....	107
V.1. Introduction.....	107
V.2. Time-of-Flight Secondary Ion Mass Spectrometry of pristine coated samples.....	108
V.3. Atomic Force Microscopy.....	112
V.4. Linear Sweep Voltammetry.....	114
V.5. Electrochemical Impedance Spectroscopy.....	117
V.6. Scanning Electron Microscopy.....	122
V.7. ToF-SIMS surface images.....	124
V.8. Conclusions.....	127
Chapter VI. Durability of the corrosion protection of copper by ALD alumina coating.....	129
VI.1. Introduction.....	129
VI.2. Electrochemical Impedance Spectroscopy.....	130
VI.3. Time-of-Flight Secondary Ion Mass Spectrometry.....	135
VI.4. Atomic Force Microscopy.....	138
VI.5. Conclusions.....	139
Chapter VII. Investigation of corrosion protection of aluminium by ALD alumina coatings and effect of deposited layer thickness.....	141

VII.1. Introduction.....	141
VII.2. Electrochemical behaviour of bare Al substrate .....	142
VII.2.1. Corrosion mechanisms .....	142
VII.2.2. Linear Sweep Voltammetry .....	144
VII.2.3. Electrochemical Impedance Spectroscopy.....	147
VII.3. Surface analysis and electrochemical study of coated samples .....	153
VII.3.1. Time-of-Flight Secondary Ion Mass Spectrometry of pristine samples.....	153
VII.3.2. Linear Sweep Voltammetry of coated aluminium .....	158
VII.3.3. Electrochemical Impedance Spectroscopy of ALD coated aluminium.....	162
VII.4. Conclusions.....	165
General conclusions .....	167
References.....	173
List of Figures .....	181
List of Tables .....	187

# General introduction

Corrosion dates back to the start of the metal age in human civilization. As long as the metals and alloys are used, their corrosion and the aftermaths need to be considered also. Corrosion damage costs are estimated to be considerably high in different countries all around the world, and therefore corrosion science, including corrosion protection studies, has evolved as an important field.

In this work, pure copper and aluminium metals have been studied. The results will also be a basis for future work on the corrosion protection of Cu-containing aluminium alloys.

Copper is an important engineering metal and finds widespread application in heat exchangers, electrical power lines, water utilities, oil refineries, marine environments and microelectronics owing to its high electrical and thermal conductivity and mechanical workability [1–3]. Many studies have been dedicated to the copper corrosion mechanisms, especially in presence of aggressive ions like chloride [4–8], and various corrosion protection methods have been explored including coating techniques such as Chemical Vapour Deposition (CVD) [9,10], plasma deposition [11] or electrochemical polymerization [12], and the use of inhibitors [13–16] or self-assembled monolayers [17,18].

Aluminium is an attractive engineering metal mainly due to its high electrical and thermal conductivity, low density, high ductility and high reflectivity. Aluminium finds application in many domains including aircraft structures, automobile and electronic devices. Several studies have been dedicated to the aluminium corrosion mechanisms in presence of aggressive chloride ions [19–27]. Corrosion protection of aluminium has

## General Introduction

---

likewise been studied *via* methods such as application of inhibitors [28–32], anodization [33], polymer coatings [34], chemical passivation [35], electrolytic plasma [36] and electrodeposited films [37].

Among different methods investigated and developed for corrosion prevention, coating is one of the most popular ones. Application of coating is a strategy to separate the metallic substrate from the corrosive environment. By covering the substrate, the coating serves as a barrier between the substrate and its surrounding. Regarding such definition, for a coating to be efficient in corrosion protection of its underlying substrate, the proper sealing of the substrate and blocking any connection between the substrate and the environment is crucial. In addition to good sealing and barrier properties, coatings should have other characteristics including high chemical and mechanical stability, good adhesion to the substrate and high durability.

In order to manufacture coatings of high quality fulfilling the requirements mentioned above, different coating deposition methods have been developed and applied to different domains, depending on the major concerns for each domain. Along with the development of nanotechnology and device miniaturization, corrosion protection of high precision components becomes increasingly challenging and corrosion science is among the leading fields for integration and protection of small functional parts in complex micro and nano systems. For protection of high precision devices against corrosion by the use of coatings, ultrathin film deposition methods have been studied and continue to be developed. The major challenge for manufacturing ultrathin films for corrosion protection is to overcome problems such as the presence of defects extending through the whole coating, morphological surface heterogeneities and poor conformality, cracking of the coating and impurities. Significantly better corrosion resistance being obtained with layers of micrometric thickness, the challenge would be to obtain similar protection with coatings of nanometric thickness which would reduce dimensional modifications, costs and weight. To achieve high protection efficiency while keeping the coating thickness small at the same time, the improvement of the existing methods and the evolution of modern techniques for coating deposition are crucial.

## General Introduction

---

Atomic Layer Deposition (ALD) is a powerful technique for deposition of ultrathin films. ALD, as a CVD (Chemical Vapour Deposition) derived method, is a very appropriate technique for growing high quality nanometre-thick films. It takes advantage of sequential precursor pulsing on the substrate with self-limiting saturative steps to produce conformal films with accurate thickness control. As a result of excellent stepwise coverage on even difficult substrate surfaces with high aspect ratios, the grown films tend to be continuous and pinhole-free [38–41]. Being already commercialized in microelectronics, ALD is a high potential candidate for deposition of ultrathin coatings for corrosion protection. Application of ALD for corrosion protection was initially considered by Matero *et al.* [42]. Coatings with hundreds of nanometre thickness showed promising results for corrosion protection of stainless steel and the results implied suitability of ALD for corrosion protection. After that, several studies have been performed for investigation of ALD coatings for corrosion protection with lower thickness (tens of nanometres) and on different substrates (see section 1.2).

In the present work, ultrathin (10, 20 and 50 nm) ALD alumina films were deposited on copper and aluminium substrates at 250°C. Corrosion protection was investigated in 0.5 M NaCl aqueous solution by combining surface analysis by Time-of-Flight Secondary Ion Mass Spectrometry (ToF-SIMS) with electrochemical analysis by Linear Sweep Voltammetry (LSV) and Electrochemical Impedance Spectroscopy (EIS). Microscopic methods including Atomic Force Microscopy (AFM) and Scanning Electron Microscopy (SEM) were applied additionally.

After providing an introduction to ALD and its application to corrosion protection in Chapter I, and presenting the applied experimental techniques and conditions in Chapter II, the study of the corrosion properties of copper and aluminium coated with ALD Al<sub>2</sub>O<sub>3</sub> is covered in Chapter III to Chapter VII. This thesis work was mainly devoted to the study of ALD Al<sub>2</sub>O<sub>3</sub> on a copper substrate investigating the effect of the coating thickness (Chapter III), the effect of an interfacial oxide (Chapter IV), the effect of surface preparation (Chapter V) and the durability of the coating (Chapter VI). For ALD Al<sub>2</sub>O<sub>3</sub> on aluminium substrate, the work focused on the examination of the effect of the deposited coating thickness (Chapter VII).



# Chapter I

## State of the art on ALD and its application to corrosion protection

This chapter is first devoted to an introduction on ALD technique and its principles. Although the main objective of the present thesis is the electrochemical and surface analysis of the ALD coated metal substrates, it is believed that a basic knowledge of the ALD technique is necessary for the interpretation of the results. Next, a brief state of the art of ALD for corrosion protection is given.

### I.1. Atomic Layer Deposition

#### I.1.1. Introduction

Atomic Layer Deposition (ALD) is a developing technology for deposition of films with thicknesses down to submonolayer scale [43]. As a Chemical Vapour Deposition (CVD) derived method, ALD is an ideal technique for growing high quality ultrathin films.

The first use of ALD, also known as ALE (Atomic Layer Epitaxy), was in the 1970s in Finland [44]. However, there are evidences of ALD origins also in the Soviet Union in

the 1960s [43]. Considering only the first case, ALD originally emerged for manufacturing of polycrystalline luminescent ZnS:Mn and amorphous Al<sub>2</sub>O<sub>3</sub> insulator films for thin film electroluminescent flat panel displays (TFEL). This application is still in industrial use today. Since the first demonstration of ALD, a large interest has developed around the technique, leading to appearance of notable number of meetings and publications on the subject. In the mid-1990s, silicon-based microelectronics turned out as an appealing field for the application of ALD [38,40,45]. The demand for smaller device dimensions and higher aspect ratios in microelectronic devices were the driving forces for a shift to new materials and techniques for the deposition of thin films with better quality and conformality [38]. Miniaturization in semiconductor industry has led to the construction of very high aspect ratio structures, which necessity to be coated conformally has given rise to the challenge for atomic level control of thin film deposition [39]. Due to its best potential, among the existing techniques for deposition of thin films with the requirements mentioned above, ALD is considered as a very good candidate for production of ultrathin films with atomic level control.

### I.1.2. Terminology

ALD in its first appearances was introduced as ALE (Atomic Layer Epitaxy), a term that was inspired by the sequential controlled surface reactions upon a previously deposited layer, transferring the meaning of epitaxy (on-arrangement) to the mind [45]. In its real meaning, epitaxy describes the growth of a single crystal film on a single crystal substrate [45,46]. Considering later developments in ALE and deposition of amorphous or polycrystalline films, the further use of ALE was confusing and different synonyms were suggested and used for the same method. A list of such different terms can be found in Table I.1. Although the words “atomic” and “layer” have also put the term ALD to question, it is still used due to the strong motivation to keep the terminology persistent [45].

**Table I.1:** Alternative names for ALD, from reference [45]

Name	Acronym	Comments
Atomic Layer Deposition	ALD	General, taking into account all types of films. In a close connection with the original name
Atomic Layer Epitaxy	ALE	The original name, but should be reserved for epitaxial films only
Atomic Layer Growth	ALG	Same as ALD, but less used
Atomic Layer Chemical Vapour Deposition	ALCVD	Emphasizes the relationship with CVD
Molecular Layer Epitaxy	MLE	Emphasizes the digital thickness control
Digital Layer Epitaxy	DLE	
Molecular Layering	ML	Used in old Russian literature
Successive layerwise chemisorption		
Sequential surface chemical reaction growth		
Pulsed beam chemical vapour deposition		

---

### I.1.3. The mechanism and main features of ALD

ALD film growth happens cyclically and each cycle for deposition of a binary compound can be simplified and modelled into four steps (Figure I.1) [40,45]:

1. Exposure of the substrate to the first precursor
2. Purging (with an inert gas) or evacuation of the chamber
3. Exposure of the substrate to the second precursor
4. Purging (with an inert gas) or evacuation of the chamber

The cycle (steps 1 to 4) is repeated as many times as needed to obtain a specific film thickness. The cyclic character of ALD is the main feature that makes it distinct from CVD [40]. Another distinction between ALD and CVD is that in ALD, contrary to CVD, reactions with values of  $\Delta G$  as negative as possible are preferred [45]. This means that precursors should react aggressively with each other [46]. It is worthy to mention that the reactions in ALD occur spontaneously at various temperatures and are referred as thermal, because they can be performed without the use of plasma or radical assistance [39]. The majority of ALD processes are thermally activated under isothermal

conditions; however additional activation methods (for example, plasma or radical-enhanced ALD) have been studied also [45].

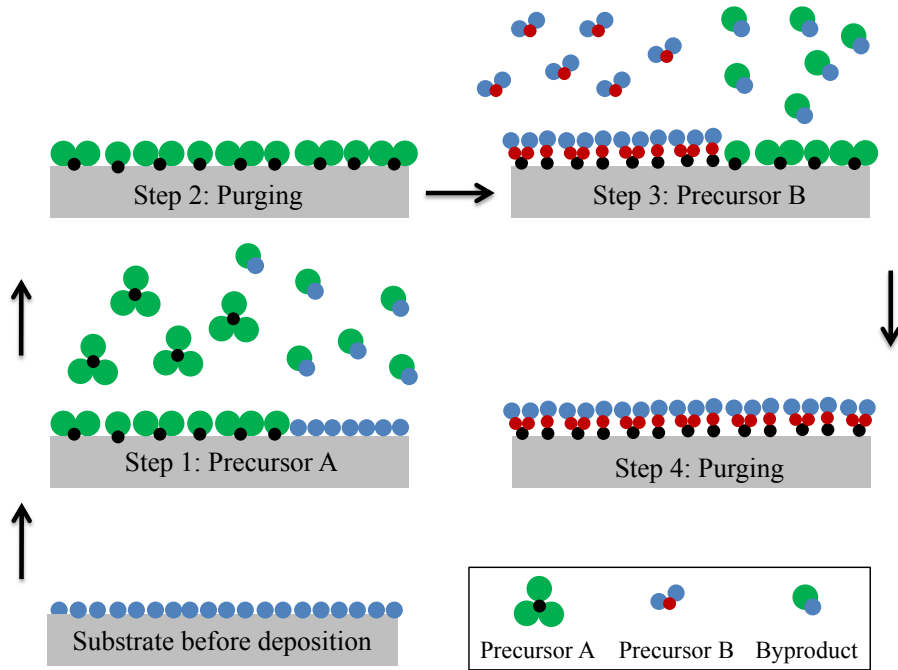


**Figure I.1:** Schematic representation of an ALD cycle, from references [43,47]

Before commencing an ALD process, the surface is stabilized to a specific controlled condition, for instance by a heat treatment [43]. As mentioned above, the substrate is exposed to each precursor separately and alternately. ALD is based on the sequential use of gas-solid reactions [43]. The precursor molecules, when pulsed onto the substrate, can react or chemisorb on the surface [40,45]. The first one happens in the presence of reactive functional groups on the surface. Otherwise, the precursor molecules can only chemisorb (intact or dissociatively) on the surface [45]. In both cases, due to limited number of reaction or chemisorption sites on the surface, only one monolayer (at the most) can be strongly bound to the surface. In the next step (purging or evacuation), the excess precursor molecules and volatile byproducts are removed from the chamber. When the second precursor is dosed to the surface, it reacts with the layer formed in the previous step, liberating the ligands and producing the desired composition [45]. The cycle is finished after the second purging/evacuation, and it can be repeated until achievement of the desired thickness.

As mentioned above, the reaction sites on the surface are limited. Therefore, the reaction for each precursor when pulsed onto the surface is saturative. The saturative nature of the reactions makes them self-limiting. This self-limiting aspect of the growth mechanism in ALD brings many advantages to it, which will be discussed hereafter.

It is worthy to mention that the model described above for a binary reaction sequence chemistry in ALD is the simple widespread accepted model; however, the actual mechanism can be much more complex [48].

### **I.1.4. Main advantages of ALD**

The self-limiting aspect of the growth mechanism implies that the amount of material deposited in each reaction cycle is constant [40]. This means that the rate of the film growth is proportional to the number of reaction cycles, and not to the reactants fluxes or the growth time [49]. The fact that the film growth is proportional to the number of reaction cycles makes the thickness control simple and accurate (at Ångström or (sub)monolayer level) [39,40]. It should be mentioned that although the same amount of material is deposited in each cycle, during the very first cycles when the surface is converted from the substrate to the film material, the surface density of the chemisorption or reactive sites and therefore the growth rate may change [45].

Another benefit from the growth rate dependence on the number of reaction cycles and not on the reactant flux is that the inhomogeneity of the reactant flux or its nonuniformity over the substrate is less problematic which allows for large area capability (large batch), excellent conformality (high trench-filling capability) and reproducibility and simplifies the use of solid precursors [40]. Even if due to variations in gas fluxes, some surface areas react before the others, the precursor desorption step allows the deposition to stop on the surface areas where the reaction has reached completion and to complete the other unreacted surface areas, thus guarantying excellent step coverage [39].

As mentioned before, the growth rate is of a monolayer at maximum in each cycle. The ability to deposit films with submonolayer thicknesses enables the thickness control down to nanometre scale and in some ideal cases even to an atomic level. Such ability in

thickness control finds application in creation of superlattices [50], nanolaminate insulators and optical multilayers for soft X-ray [51] or visible light [52].

The separation of precursors and the alternate dosing to the substrate limits the possible gas phase reactions (between the precursors), which can form particles that could deposit on the surface to produce granular films [39]. On the other hand, separate pulsing of the precursors to the surface allows for the use of highly reactive precursors and gives enough time for each reaction step to reach completion. This feature gains importance for deposition at low temperature [40]. The insensitivity of ALD to small changes in temperature and precursor flows makes the processing window wide and gives it more applicability. Wide temperature range is important in deposition of multilayer structures in a continuous manner [45].

Another important advantage resulting from the self-limiting aspect of ALD growth is avoiding the randomness of the precursor flux as a detrimental factor. This by itself makes ALD a nonstatistical deposition method. Consequently, layers formed by ALD are very smooth and conformal to the initial substrate. It should be mentioned that the growth of smooth films is mostly the case of amorphous ALD films [45]. Furthermore, as no surface sites are left behind during the film growth, the ALD films are likely continuous and pinhole-free [39], which is of huge importance for deposition of dielectric films, passivation layers and protective coatings of high quality. A “no pinholes” growth on non-perfect substrate is feasible thanks to the conformal deposition in ALD [49]. ALD encapsulates the microcontamination, constructing a conformal packaging around it [49]. Conformal coverage of microcontaminations prevents formation of weak points in the film [49], unless the contamination particles are poorly adherent and detach from the substrate with the covering ALD coating.

### **I.1.5. Non-ideal ALD behaviour**

As mentioned above, alternate pulsing and self-limiting aspects of ALD are the origins of main advantages of this method. However, it should be mentioned that deviations from absolutely self-limiting growth conditions can happen and be acceptable with certain

precautions [45]. If each reaction and purge cycle is complete (ideal case), the self-limiting aspect is achieved, but this is not always the case [40,45]. The reactions can be not completely saturative or there may be some precursor decomposition in the gas phase in addition to chemisorption on the surface. As long as the reactions at the origin of these non-ideal behaviour are under surface control and not mass control, the coverage and therefore the deposition remains constant everywhere and therefore the main beneficial character of ALD is preserved. The mentioned non-ideal growth condition can be overcome by increasing the exposure time (to complete the reactions), although the increase of process time can be considered as a negative effect. The decrease of the deposition temperature (to prevent gas phase decomposition) is also an alternative; however, it can decrease the film quality [45]. Therefore, there is a compromise between these factors.

### **I.1.6. Limitations of ALD**

Obviously, the main drawback of ALD is that it is a slow process due to the fact that in the best case only one monolayer can be deposited in each cycle [45,53]. Typical deposition rates are 100-300 nm.h<sup>-1</sup> [40,53]. This shortcoming is partly circumvented by large batch processing capability and deposition on many substrates at the same time [45,53]. Furthermore, miniaturization (decrease of film thickness) in application domains of ALD makes slowness less problematic [53].

Another obstacle for ALD application and use in a large scale is the lack of cost-effective processes for deposition of some important materials [40,45].

Considering that ALD is a chemical technique, there is a higher risk of presence of precursor residuals in ALD films than with other techniques like PVD (Physical Vapour Deposition) where a much cleaner environment is possible due to application of high vacuum [40]. Furthermore, ALD grown materials may not be totally comparable in their properties with the equivalent PVD ones, because of the unique impurity background of ALD films (impurity content depends on the conditions of a specific deposition batch) [40].

### I.1.7. Precursors and their requirements in ALD

The precursors used for ALD should meet some requirements, which explanation helps to understand better the ALD process. Therefore, these requirements are listed shortly below:

- Volatility:

The reactants used in ALD should be volatile at the temperature of deposition [43]. Even though solid precursors can be used in ALD, since the self-limiting growth mechanism makes the problem of variable precursor flux less important than in CVD, liquid and gas precursors are still preferred [45]. This is because of the risk of transportation of solid precursor particles with small size in the carrier gas to the substrate and causing detrimental effects [45].

- Stability:

Obviously, in order to achieve self-limiting growth, the precursors should not decompose [38,43,45] and they should be thermally stable at the growth temperature [40]. Due to the fact that the decomposition is a thermally activated reaction, the increase in the temperature enhances the risk of decomposition of precursors [45]. Decomposition of reactants can also be a major source of impurity in the grown films [49]. In some applications (for example protective coatings), slightly thermally unstable reactants are acceptable if their decomposition is slow in comparison with the pulsing sequence times. In this case, their decomposition makes only a small contribution to the global growth [40].

- Aggressiveness of reactions:

As mentioned above, as a result of alternate pulsing of the precursors on the substrate, there is no risk of gas phase reactions and therefore, contrary to CVD, reactions with very negative  $\Delta G$  can be used. Indeed, reactions with  $\Delta G$  as negative as possible are preferred, because aggressiveness of the reactants

promotes surface reaction completion and decreases the cycle times, which in overall means more efficient utilization of the reactants [45,46].

- No etching:

There is always the possibility of etching of the substrate or the film material itself by one of the precursors. This is where the negative effect of separate precursor dosing appears. Alternate pulsing of the precursors eliminates the competing reaction pathways with the possible etching reactions [45]. Hence, less etching precursors are preferred.

There are also other important requirements for the precursors used in ALD. The precursors should react with the surface or chemisorb on it, but they should not dissolve on the substrate or on the deposited film [45]. The byproducts of ALD reactions should be unreactive compounds which can be purged out easily. Reactive byproducts can cause many problems such as corrosion in the reactor or in the exhaust, adsorbing on the surface and blocking the adsorption sites and therefore decreasing the growth rate [45]. Precursors should meet specific purity specifications. Purity gains more importance for applications such as semiconductors, while for protective coatings is of less importance [45]. Like all other deposition methods, low cost, environmental friendliness and easy synthesis and handling are required for ALD precursors also [45].

Typical metal precursors used in ALD are halides, alkyl compounds and alkyoxides. Nonmetal precursors for oxygen are mostly water, hydrogen peroxide and ozone [40].

### **I.1.8. Nucleation and growth in ALD**

One of the factors behind the different growth rates reported in ALD deposition is surface chemistry and reactions [54]. Proper nucleation of the ALD precursors is of huge importance. For deposition of continuous ultrathin films without pinholes, the precursors should react effectively with the substrate and nucleate on it. In case of nonhomogeneous nucleation, islands may grow and even if the growth of islands leads to a continuous film

in the end, the roughness and nonconformality to the original substrate may be at risk in the ultrathin film regime [39]. For an effective nucleation in ALD, the precursors need to react with the surface species from the very first ALD cycle [39]. That is why the surface chemistry and presence of reactive functional groups on the surface is decisive. For instance, the presence or absence of hydroxyl groups on the surface is essential for the interpretation of growth mechanism of oxides [46]. Smart chemistry is a paramount issue in ALD for development of new processes and deposition of new materials [40].

As mentioned before, slowness is a drawback in ALD. Therefore, inspection of different factors influencing the growth rate in ALD can be useful in improving the growth rate and overcoming the slowness. Some important factors controlling the growth rate are discussed in the following.

- Pulse time and precursor flux:

By increasing the pulse time, more species chemisorb on the surface. The chemisorption rate depends also on the precursor flux and the rate of other reactions on the surface that reopen the temporarily blocked sites for chemisorption [45]. For instance, the steric hindrance caused by big precursor molecules leads to the decrease of the growth rate. Their reordering or desorption increases the chemisorption [45,46].

Although both pulsing time and precursor flux contribute to the precursor dose, they do not have exactly the same effect in the growth rate [45]. In some examples the growth rate can be augmented only by increase of pulsing time, due to the slowness of the surface reactions [55]. On the other hand, there are examples in which the growth rate can only be enhanced by increasing the precursor flux [53]. For the latter case, in the specific example of water precursor, increasing hydroxyl groups as reactive functional groups leads to the increase of saturation level and therefore the growth rate [53].

- Purge time:

If the applied purging times are not long enough, the precursors from two separate pulses overlap, leading to a CVD growth, and therefore eliminating all benefits resulting from the ALD growth mechanism. On the other hand, purge

times should not be very high, as longer purging can promote desorption of chemisorbed precursor molecules or dehydroxylation as a result of combination of hydroxyl groups on the surface with each other (mostly in case water is used as precursor) [45].

- Temperature:

The temperature dependence of the growth rate in ALD reflects in different ways, as illustrated in Figure 1.2 [39,45]. The so-called “ALD window” is the region in the middle where the growth proceeds in a self-limiting manner [39,46]. In this region, if the surface density of chemisorbed species is temperature dependant, the growth is also temperature dependant (S2) and *vice versa* (S1) [45]. In the case of temperature dependency (S2), the growth rate usually decreases with increase of temperature because of decreased density of the reactive species [45]. Anyhow, if temperature dependence is the case, it is very weak [45] and this is a key feature in ALD process [47].

At lower temperatures (left side of Figure 1.2), the growth rate often declines with decrease of temperature (L1). This is because the growth reactions become so slow that they cannot reach completion during the given pulse time [45]. The enhancement of growth rate with decrease of temperature can also happen (L2) as a result of multilayer adsorption and condensation of low vapour pressure precursors [39,45]. At higher temperatures (right side of Figure 1.2), the reduction of the growth rate with increase of temperature (H1) is due to desorption of precursors, while decomposition of surface species results in expansion of growth rate with increase in temperature (H2) [39,45].

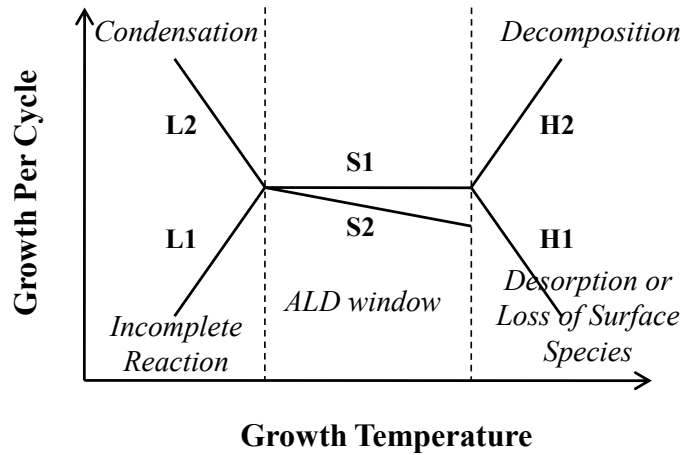


**Figure 1.2:** Schematic description of ALD growth rate per growth temperature, from references [39,45]

### 1.1.9. Film morphology

One of the determining factors in the properties of ALD layers is whether they are amorphous or crystalline. While crystalline films with a particular phase can be desired for their specific chemical or electrical properties, amorphous films are preferred in applications such as diffusion barriers and protective coatings [47]. In diffusion barrier application, crystallinity is not recommended, as the grain boundaries are preferential pathways for the leakage of ions leading to device failure [47]. Likewise, in protective coatings for corrosion protection, grain boundaries serve as weak points, favouring localized corrosion, and therefore should be avoided [42].

In the case of polycrystalline films, the surface roughness increases with the film thickness and agglomeration starts since the beginning of film growth [46]. On the contrary, amorphous films have very smooth surfaces. For instance, the surface roughness of a 800 nm ALD  $\text{Al}_2\text{O}_3$  is  $\sim 2$  nm [46]. Certainly deposition of smooth surfaces is preferred in ultrathin film regimes.

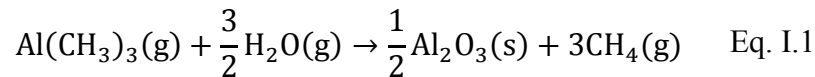
The crystalline output of the deposited film depends on several factors including the substrate material, the film material, the deposition temperature, the precursors used and the thickness of the film [46].

### I.1.10. ALD of alumina (Al<sub>2</sub>O<sub>3</sub>)

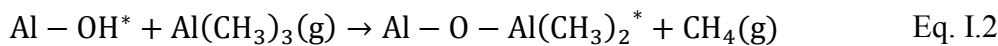
Protective and passivating films are one of the categories deposited by ALD. The interest in the deposition of these films by ALD is the pinhole-free and dense structure of ALD deposited films [45]. Al<sub>2</sub>O<sub>3</sub> was the first oxide deposited by ALD as both a dielectric oxide and an ion barrier layer for application in TFEL devices [45,46]. Deposition of Al<sub>2</sub>O<sub>3</sub> as a high-k oxide has been one of the most widely explored areas of ALD [40].

ALD Al<sub>2</sub>O<sub>3</sub> has been established as a model ALD system [39], as it can be considered as an ideal ALD process [43]. The precursors for ALD Al<sub>2</sub>O<sub>3</sub> are usually trimethyl aluminium (TMA) and water (H<sub>2</sub>O) [39]. TMA/H<sub>2</sub>O benefits from being a thermal ALD process, instead of an “energy-enhanced” one. Thermal ALD processes accomplish best the requirements of self-limiting reactions on 3D substrates [43]. Water is the most frequently used precursor as oxygen source in ALD for deposition of oxide films [43]. TMA as a metal precursor is often used in ALD of oxides [46].

The TMA/H<sub>2</sub>O process is one of the most studied processes [43]. The overall stoichiometric reaction can be presented according to Eq. I.1 [39,43,48,54]:



This reaction (Eq. I.1) has an extremely high enthalpy, one of the highest to be found for ALD reactions [39]. The chemistry during TMA/H<sub>2</sub>O ALD process is usually described by the following two successive “half reactions” [39,43,48,54]:



where asterisks stand for surface species. As it can be seen in Eq. I.2 and Eq. I.3, the surface functionality switches from hydroxyl-terminated to methyl-terminated and *vice versa*. This is well known and illustrated by, for example, FTIR studies [48,56]. However, the TMA/H<sub>2</sub>O process is more complex than what is represented *via* Eq. I.2

and Eq. I.3 [43]. A schematic representation of the possible surface chemistry of ALD  $\text{Al}_2\text{O}_3$  is provided in Figure I.3 [48].

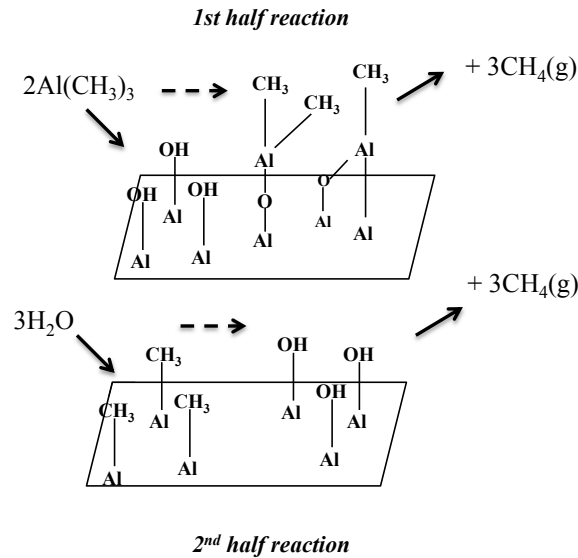


**Figure I.3:** Schematic illustration of possible mechanism for the surface chemistry of ALD  $\text{Al}_2\text{O}_3$  using TMA and water, from reference [48]

The growth of ALD  $\text{Al}_2\text{O}_3$  is self-limiting with respect to time [43]. The self-limiting aspect of the surface reactions has been confirmed by FTIR [56]. The growth is linear with the number of deposition cycles [54,57], and growth rates are around 0.1 nm per cycle [48,54,57], which correspond to less than one  $\text{Al}_2\text{O}_3$  monolayer thickness [39,54]. The films are smooth and extremely conformal to the underlying substrate [39].

Generally, the increase of temperature leads to a decline of growth rate, which is mostly attributed to a decrease of the surface OH groups at higher temperatures [43], or correlated to the stability of  $\text{AlOH}^*$  and  $\text{AlCH}_3^*$  surface species [56]. Promotion of dehydroxylation of  $\text{Al}_2\text{O}_3$  surface at higher temperatures has been documented [56]. However, at lower temperatures (less than 450 K) [54] the growth rate enhances slightly with the increase of temperature, which is due to the fact that the TMA reaction is thermally activated and does not go to completion at lower temperatures [56].

Water dosing has been shown to be an influencing factor in the growth rate of ALD  $\text{Al}_2\text{O}_3$  [53]. It was shown that the growth rate was saturated with both small and large

water doses, but the saturated level was considerably higher for the large water dose [53]. Higher water dosed was confirmed to not affect markedly the properties of ALD  $\text{Al}_2\text{O}_3$  [53].

Taking advantage of the combination of the ALD unique mechanism and valuable material properties of  $\text{Al}_2\text{O}_3$ , ALD  $\text{Al}_2\text{O}_3$  is an attractive candidate for corrosion protection. The most distinctive characteristics of ALD alumina as a potential candidate for deposition of protective films for corrosion protection are the good uniformity over large areas, the large batch processing capability, the exceptional conformality to the underlying substrate, the pinhole-free structure and high density of the films [42]. Furthermore, the good adhesion expected from ALD due to saturative chemical reactions, is an important aspect for protective films against corrosion [42]. Considering the low deposition rate in ALD, it can be considered as not important for deposition of ultrathin coatings. However, as mentioned before, the low deposition rate can be compensated by large batch processing capability [42].  $\text{Al}_2\text{O}_3$  has exceptional material properties.  $\text{Al}_2\text{O}_3$  films are refractory ceramic materials, which can provide high temperature corrosion resistance [54]. Being amorphous at deposition temperatures below  $600^\circ\text{C}$  [47], its high dielectric properties [58], high resistivity and high breakdown voltage [58], good adhesion to many surfaces and thermal and chemical stability (at neutral conditions) make  $\text{Al}_2\text{O}_3$  a good candidate for corrosion protection coating material.

### I.2. ALD for corrosion protection

In the present study, Atomic Layer Deposition (ALD) of ultrathin ( $\leq 50$  nm) alumina coatings has been investigated for the corrosion protection of pure copper and aluminium. Alumina ( $\text{Al}_2\text{O}_3$ ) was chosen by virtue of its several advantages as a ceramic coating material and more notably as a well-behaved studied ALD material. ALD alumina has high dielectric properties, uniform good adhesion to many surfaces, amorphous structure at chosen deposition temperature, good thermal stability and mechanical properties [40,42,58,59].

ALD alumina for corrosion protection has already been studied, and mostly on steel substrate. On stainless steel, Matero *et al.* [42] showed that ALD Al<sub>2</sub>O<sub>3</sub>-TiO<sub>2</sub> multilayers of 400 nm total thickness deposited at 250°C provided corrosion protection for 12 weeks in 0.3 wt.% NaCl. Al<sub>2</sub>O<sub>3</sub>-TiO<sub>2</sub> multilayers showed better results than Al<sub>2</sub>O<sub>3</sub> or TiO<sub>2</sub> alone, due to combination of grain boundary-free dense structure of alumina with good chemical stability of TiO<sub>2</sub>. In the study done by Díaz *et al.* [60] on stainless steel 316L substrate in 0.8 M NaCl, a decrease of current density up to four orders of magnitude was achieved with increasing ALD alumina coating thickness from 5 to 50 nm deposited at 250°C, and up to 3 orders of magnitude for the deposition temperature of 160°C, denoting the effect of deposition temperature on coating quality. In the same study, Al<sub>2</sub>O<sub>3</sub> coatings showed better results than their equivalent Ta<sub>2</sub>O<sub>5</sub> coatings. In another work, Díaz *et al.* [61] reported the corrosion protection provided to low alloy steel (AISI 52100) substrate by ALD alumina deposited at 160°C. A decrease in coating porosity up to four orders of magnitude was reported with 100 nm coating. Härkönen *et al.* [62] deposited nanolaminates of Al<sub>2</sub>O<sub>3</sub>-Ta<sub>2</sub>O<sub>5</sub> on the same steel substrate and reported corrosion properties of nanolaminates to be superior to Ta<sub>2</sub>O<sub>5</sub> and lower than Al<sub>2</sub>O<sub>3</sub>. The best protection for 40 and 80 nm laminates was achieved with 10 and 20 nm layers respectively.

In another study, Härkönen *et al.* [63] improved the corrosion properties of the ALD coatings on steel substrate by using 50 nm Al<sub>x</sub>Ta<sub>y</sub>O<sub>z</sub> mixture coatings. The sealing properties of these coatings were improved by increasing aluminium oxide content, while their durability was improved with increasing tantalum oxide content. The mixtures had better corrosion properties than both single layer and nanolaminate Al<sub>2</sub>O<sub>3</sub> and Ta<sub>2</sub>O<sub>5</sub> coatings. Härkönen *et al.* [64] studied also the sealing of micrometric hard CrN and diamond-like carbon (DLC) coatings on low alloy steel substrate by 50 nm thick nanolaminates and mixtures of Al<sub>2</sub>O<sub>3</sub> and Ta<sub>2</sub>O<sub>5</sub>. A further decrease of current density of CrN coated steel by over two orders of magnitude was reported. Marin *et al.* [65] observed the decrease of the passive current from 10<sup>-7</sup> to less than 10<sup>-9</sup> A.cm<sup>-2</sup> in 0.2 M NaCl for the stainless steel coated with ALD Al<sub>2</sub>O<sub>3</sub>/TiO<sub>2</sub> nanometric coatings. In another study by Marin *et al.* [66] on ALD Al<sub>2</sub>O<sub>3</sub>/TiO<sub>2</sub> multilayers deposited on stainless steel, all the coatings proved to be effective in corrosion protection of stainless steel. Adhesion

tests showed results dependant on coating thickness. While 10 nm coating showed no sign of delamination, and 30 nm coating showed little delamination, 100 nm coating showed higher delamination. Multilayer configurations showed better corrosion protection and delamination resistance.

On Mg/Al alloy substrates, Marin *et al.* [67] achieved corrosion current decrease of two orders of magnitudes for the single layers of 100 nm ALD alumina in 0.05 M NaCl, increasing to four orders of magnitude for equivalent Al<sub>2</sub>O<sub>3</sub>/TiO<sub>2</sub> multilayers.

In the study done by Paussa *et al.* [68] on silver substrates, ALD alumina/titania bilayers of 90 nm thickness showed to have an initial porosity of 0.003% defined from EIS in 3 g/l Na<sub>2</sub>SO<sub>4</sub>. These coatings showed a corrosion protection at least ten times superior to conventional organic varnishes. In another study on silver by Fedel *et al.* [69], the corrosion current was decreased up to two orders of magnitude in presence of 80 nm ALD alumina.

On copper, apart from recent investigation of ALD alumina films for corrosion protection in hot water [70] and for thermal oxidation protection of copper moulds for patterned optical components [71], corrosion protection at room temperature in aggressive chloride-containing electrolyte (0.1 M NaCl) was very recently reported for ALD alumina films grown at 150°C [72]. Abdulagatov *et al.* [70] reported corrosion protection of copper in hot water at 90°C for ~80 days with Al<sub>2</sub>O<sub>3</sub> films with a TiO<sub>2</sub> capping layer deposited at 120°C. This corrosion protection could not be achieved with Al<sub>2</sub>O<sub>3</sub> or TiO<sub>2</sub> alone. Chang *et al.* [71] observed that 20 nm alumina coatings grown at 100°C were sufficient to retard the oxidation reaction of copper at 200°C in air for 336 h. Finally in the very recent study done by Chai *et al.* [72] it was reported that the alumina coatings deposited at 150°C and with the thicknesses more than 7.8 nm could protect the copper substrate from corrosion in 0.1 M NaCl.

On aluminium, apart from the study done by Potts *et al.* [73] on Al2024-T3 alloys, no other work has been published to our knowledge. Potts *et al.* reported poor corrosion protection of Al-2024-T3 by ALD alumina as a result of poor adhesion of coating on the substrate.

## **Chapter I. State of the art on ALD and its application to corrosion protection**

---

The background on the corrosion mechanisms of copper and aluminium is provided with the experimental results in Chapter III and Chapter VII.

# Chapter II

## Experimental

### II.1. Substrate preparation

#### II.1.1. Copper substrate

The copper samples used as substrate material in this study were disks of 10 mm diameter, 2 mm thickness and 99.99% purity. The samples were provided by Goodfellow. The chemical composition of the copper disks can be found in Table II.1.

**Table II.1:** Chemical composition of copper disks (wt%)

	<b>Cu</b>	<b>Sb</b>	<b>Ag</b>	<b>As</b>	<b>Bi</b>	<b>Sn</b>	<b>Fe</b>	<b>Mg</b>	<b>Ni</b>	<b>Pb</b>	<b>Si</b>	<b>Se</b>	<b>Ta</b>
<b>ppm</b>	Matrix	0.18	10	0.89	0.22	0.10	1.7	1.5	0.76	0.22	0.13	0.77	<1

#### II.1.1.1. Mechanical polishing

The copper disks were mechanically polished starting with 1200 abrasive SiC paper and then with water based diamond polishing suspensions of 6  $\mu\text{m}$ , 3  $\mu\text{m}$ , 1  $\mu\text{m}$  and 0.25  $\mu\text{m}$  respectively (Figure II.1). After mechanical polishing and just before electropolishing, the samples were rinsed with acetone, ethanol and ultrapure water successively.

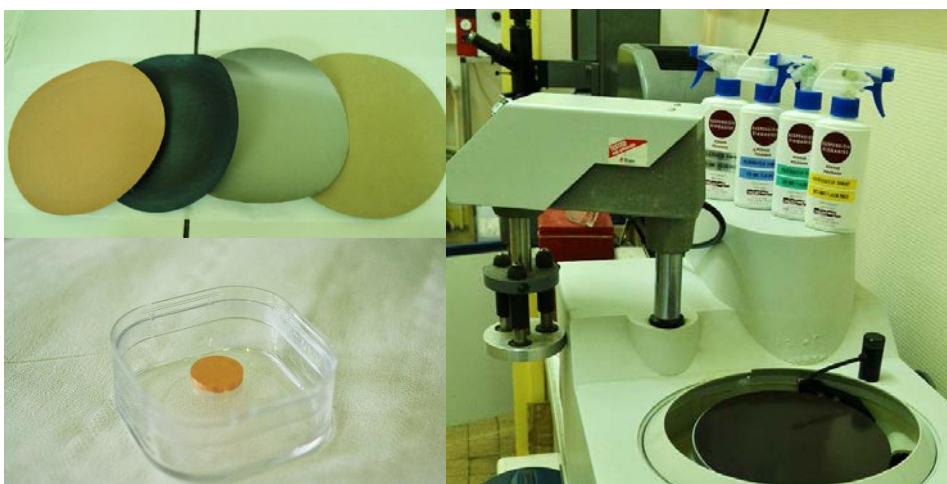


**Figure II.1:** Mechanical polishing disks, suspensions and machine for copper disk

### II.1.1.2. Electropolishing

Immediately after mechanical polishing, the copper samples were electropolished in orthophosphoric acid to further reduce the surface roughness. The electropolishing of copper in orthophosphoric acid was first introduced by Jacquet [74].

In this study, the electropolishing was done in  $\text{H}_3\text{PO}_4$  (60 wt. %) for 5 min at 1.4 V versus a copper counter electrode (Figure II.2). The potential difference applied between the copper sample and the copper counter electrode leads to the change in chemical potential at the surface of both, promoting redox reactions and leading to modification of surface topography of copper. Connecting the copper sample to the positive terminal of the direct current power supply, it will serve as the anode. Preferential anodic dissolution of surface asperities will lead to surface smoothening. Such smoothening is achieved due to the different values of electrical potential for the protruded (peaks) and recessed (valleys) areas. Higher positive charge accumulation on protruded areas leads to more current density on these parts and therefore their faster dissolution. After electropolishing, the samples were rinsed with  $\text{H}_3\text{PO}_4$  (10 wt. %) and ultrapure water successively, and blow-dried with nitrogen.

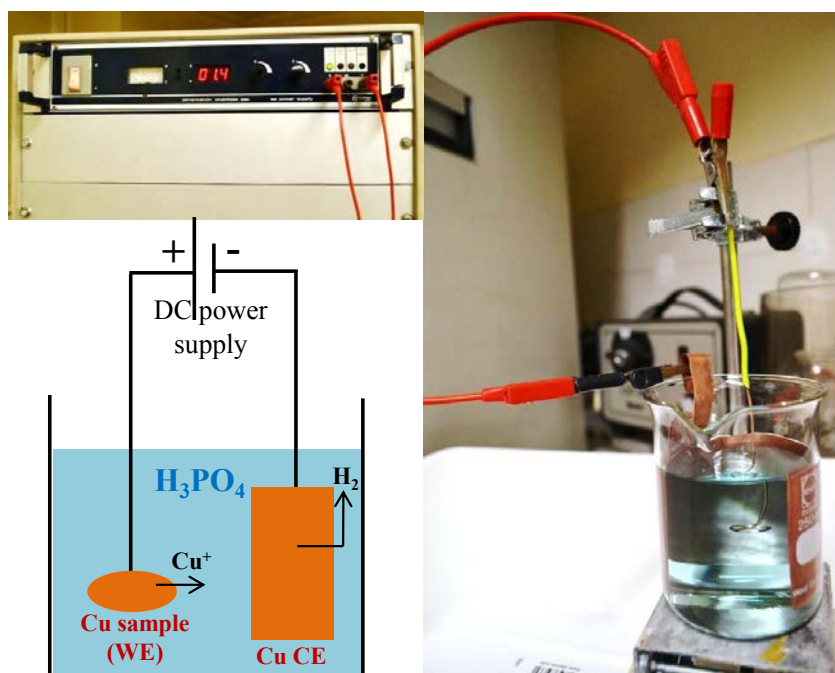


**Figure II.2:** Electropolishing of copper in  $\text{H}_3\text{PO}_4$

### II.1.1.3. Annealing

The effect of annealing as surface finishing was studied on copper. The samples were annealed immediately after being electropolished. For these samples, annealing was done in order to further improve the smoothness of the surface.

Annealing was done at  $725^\circ\text{C}$  for several hours under the flow of ultrapure hydrogen (99.9999%) and at atmospheric pressure. A pictorial representation of the annealing system can be found in Figure II.3.

After introduction of the sample in the quartz tube in the annealing system, the system is closed and the vacuum is made using the primary and secondary pumps. In order to pump the system, valves  $A_1$ ,  $A_2$ ,  $A_3$  and  $V_1$  are opened one after another. Water vapour is reduced using a liquid nitrogen trap (refilled from time to time). When the pressure is low enough ( $1.5 \times 10^{-4}$  mbar), hydrogen is introduced in the system.  $V_1$  should be closed and hydrogen should be turned on. Then,  $A_3$  is closed. Closing  $V_1$  and  $A_3$  disconnects the first part of the system (in green colour) from the pumping. Then  $V_1$  is opened and after

## Chapter II. Experimental

reading the pressure of 1000 mbar from the manometer,  $A_4$  is opened to let the hydrogen out of the system *via* a bubbler filled with glycerine. Before introducing hydrogen in the second part of the system (in blue colour), the pressure should go down to  $4 \times 10^{-5}$  mbar. Reaching this pressure may need several hours. When the pressure is low enough, the second part is disconnected from pumping by closing  $A_1$ . Hydrogen is then introduced in this part.  $A_4$  is first closed to close the way out of hydrogen. Then,  $A_3$  is opened to let the hydrogen circulate in the second part of the system. Here again after the pressure reaches 1000 mbar, the hydrogen is let out by opening  $A_5$ . As no more pumping is needed, the pumps are switched off.

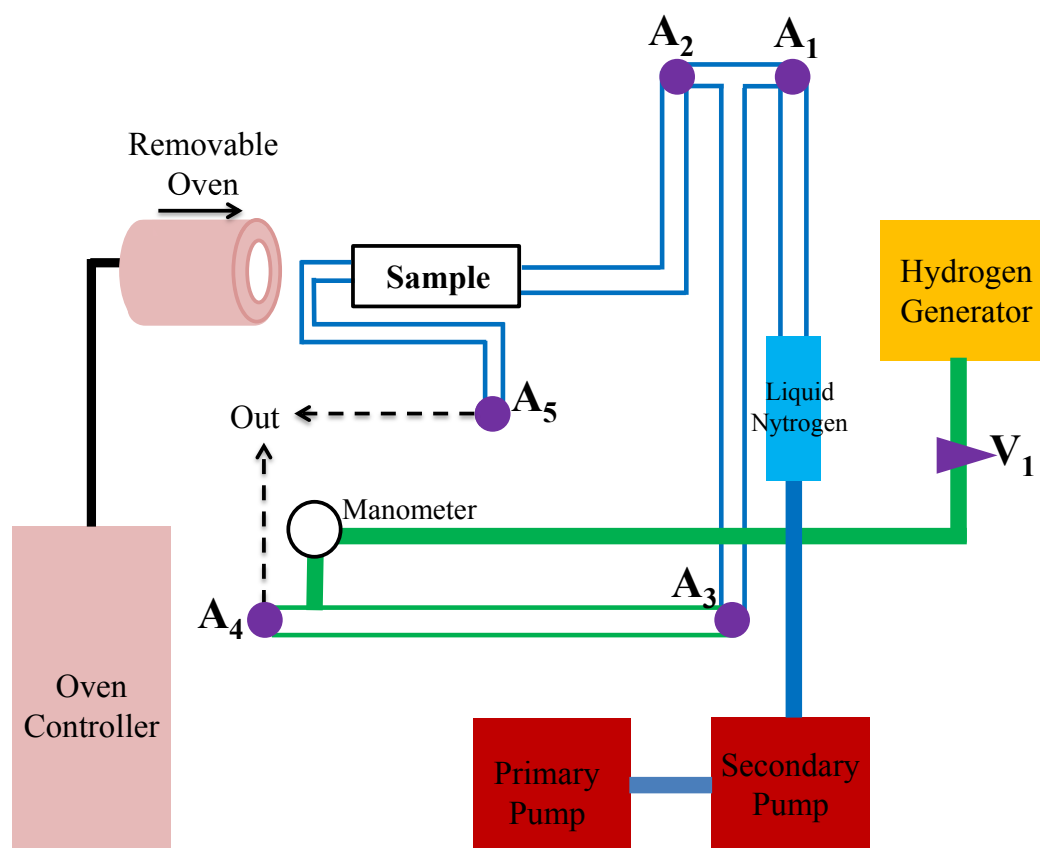


**Figure II.3:** Schematic and simplified representation of annealing system

After introduction of hydrogen in all the system, the annealing is started by sliding the oven, pre-set at the temperature of  $725^\circ\text{C}$ , over the quartz tube containing the sample. The sample is annealed for around 12 hours. To stop annealing, the oven is moved away

(to the left) from the sample, switched off and isolated with a shield. The sample is let to cool down under the hydrogen flow. This step takes few hours. Before taking the sample out, the hydrogen flow is stopped. The procedure is reversed to that for introducing hydrogen in the system.

### II.1.1.4. Oxide removal pre-treatment

For the samples on which the native oxide layer was removed before coating deposition, the procedure was as following. The samples were etched with 10 wt.%  $H_3PO_4$  for 5 seconds, rinsed with ethanol, dried with compressed air and introduced in the ALD reactor (or electrochemical cell) in less than 5 min. This pre-treatment was taken from Shimizu *et al.* [75]. In order to study the electrochemical properties of these pre-treated samples, the reference bare sample was pre-treated in the same way just before introduction in the electrochemical cell. Samples, pre-treated or not, to be coated were placed in membrane boxes for shipping to the University of Helsinki.

### II.1.2. Aluminium substrate

The aluminium samples used as substrate material in this study were disks of 10 mm diameter, 2 mm thickness and 99.999% purity. The samples were provided by Goodfellow. The chemical composition of the aluminium disks can be found in Table II.2.

**Table II.2:** Chemical composition of aluminium disks (wt%)

	Al	Cu	Ce	Fe	La	Mg	Mn	Hg	Si
<b>ppm</b>	Matrix	0.6	0.5	0.6	0.3	1.3	0.1	< 0.3	1.3

### II.1.2.1. Mechanical polishing

The aluminium disks were mechanically polished starting with 1200 and 2400 abrasive SiC papers and following with alumina polishing slurries of 2-3  $\mu\text{m}$ , 1  $\mu\text{m}$  and 0.3  $\mu\text{m}$  successively. After mechanical polishing, the samples were rinsed with ultrapure water, and put in ultrasonic bath of isopropanol and ethanol successively for 3 min each. Then the samples were blow dried with compressed air. Samples, to be coated were placed in membrane boxes for shipping to the University of Helsinki.

### II.2. ALD coating deposition

After substrate preparation, the samples were sent to Laboratory of Inorganic Chemistry of the University of Helsinki (E. Härkönen, M. Ritala) to be coated with ALD alumina. The coatings were prepared with a Picosun SUNALE R-150 ALD reactor. The nominal deposited thicknesses were 10, 20 and 50 nm. The precursors employed for the deposition procedure were trimethyl aluminium ( $\text{Al}(\text{CH}_3)_3$ ) manufactured by Chemtura (AXION<sup>®</sup> PA 1300, purity 99.9%) and  $\text{H}_2\text{O}$  (ultra-pure with resistivity  $> 18 \text{ M}\Omega \text{ cm}$ ). Both TMA and water were vaporized at room temperature (around  $25^\circ\text{C}$ ). The pulse and purge times were 0.1 and 5 s respectively, for both precursors. The temperature in the deposition chamber was  $250^\circ\text{C}$ . Nitrogen ( $> 99.999\%$ ) was used as the carrier and purge gas with an overall flow rate of 300 sccm (standard cubic centimetre per minute) into the reaction space and a flow rate of 600 sccm in the intermediate space, while the reactor was constantly pumped with a vacuum pump. The pressure in the precursor lines was approximately 5 mbars at  $250^\circ\text{C}$  and under 5 mbars at RT, 10 mbars in the intermediate space and 0.1 mbar in the pump line. Direct pressure in the reaction space was between the pump line pressure (0.1 mbar) and precursor line pressure (5 mbar), closer to the pressure of the pump line. The heating to  $250^\circ\text{C}$  took 1 hour. The stay time in the reactor at  $250^\circ\text{C}$ , before the deposition to start was 10 min. Cooling to  $100^\circ\text{C}$  (taking approximately 4 hours) was always done after the deposition before the samples were exposed to laboratory air. The deposition time for each sample depends on the coating

## Chapter II. Experimental

---

thickness (the number of cycles used). For instance, for the 50 nm coating, if 500 cycles were used, the deposition time was 85 min.

The deposited thickness values were measured with X-ray Reflectivity (XRR) using XRR Bruker AXS D8 Advance and Panalytical X'Pert Pro MPD diffractometers. The thickness was measured from a silicon wafer coated simultaneously with the substrates. The modelling was done with Leptos 7.05 and X'Pert Reflectivity.

The number of cycles used for deposition, the deposition rate and the measured thickness for the samples used in this study are gathered in Table II.3. The surface finishing of the samples are mentioned in their name. In the case of the samples for which the oxide removal pre-treatment ( $H_3PO_4$  pre-treatment) was done before coating deposition, PT is added at the end of the name.

**Table II.3:** ALD Deposition conditions for the samples used in this study

Sample	Number of Cycles	Measured Thickness	Deposition Rate
Cu-electropolished-PT	105	10 nm	0.095 nm/cycle
Cu-electropolished-PT	210	19.9 nm	0.095 nm/cycle
Cu-electropolished-PT	525	49.5 nm	0.094 nm/cycle
Cu-annealed-PT	120	9.81 nm	0.082 nm/cycle
Cu-annealed-PT	240	20.3 nm	0.085 nm/cycle
Cu-annealed-PT	600	51.4 nm	0.086 nm/cycle
Cu-electropolished-PT	214	20 nm	0.093 nm/cycle
Cu-electropolished	214	20 nm	0.093 nm/cycle
Al-polished	100	12 nm	0.120 nm/cycle
Al-polished	200	20 nm	0.100 nm/cycle
Al-polished	500	52 nm	0.104 nm/cycle

### II.3. Surface analysis

After receiving the coated samples back from the University of Helsinki, the surface analysis was done with Time-of-Flight Secondary Ion Mass Spectrometry (ToF-SIMS) and Atomic Force Microscopy (AFM).

#### II.3.1. Time-of-Flight Secondary Ion Mass Spectrometry

##### II.3.1.1. Principles

ToF-SIMS is a SIMS (Secondary Ion Mass Spectrometry) technique with the specific use of a Time-of-Flight (ToF) mass analyser. In SIMS, primary ions are used to bombard the surface of the sample to emit secondary particles. Among the different secondary particles emitted (electrons, neutral species, atoms, molecules, atomic or cluster ions), only ions (the secondary ions) are detected and filtered in mass by the spectrometer. The mass spectrum provided by this process permits a detailed chemical analysis of the surface [76].

When the energetic primary ion beam bombards the surface, the particle energy is transferred to the solid by a collision process. In the solid, a “cascade of collisions” (Figure II.4) takes place between the atoms. Some of these collisions return to the surface and result in the emission of atoms (or clusters), among which some are ionized. Over 95% of the secondary particles result from the top two layers of the solid [76].

The yield of secondary ions depends on many factors which complicate the quantitative SIMS analysis. The basic SIMS equation is [76]:

$$I_s^m = I_p y_m \alpha^\pm \theta_m \eta \quad \text{Eq. II.1}$$

where  $I_s^m$  is the secondary ion current of species  $m$ ,  $I_p$  is the primary particle flux,  $y_m$  is the sputter yield,  $\alpha^\pm$  is the ionization probability to positive or negative ions,  $\theta_m$  is the fractional concentration of  $m$  in the surface layer and  $\eta$  is the transmission of the analysis system.

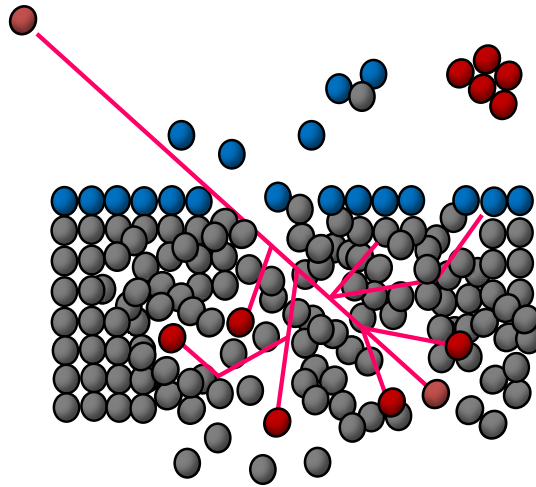


**Figure II.4:** SIMS process and “collision cascade”

As mentioned above, the quantitative analysis using SIMS is complicated. For instance, the sputtering yield ( $y_m$ ) cannot be known precisely. This parameter depends on many factors including the mass, energy and the incident angle of the primary beam and the angular distribution of the secondary particles. Furthermore, the chemical nature and the structure of the analysed material have a strong influence on the secondary ion yield, known as “matrix effect”. More clearly the same element shows different secondary ion yields in different chemical environments (for example in an oxide or in a metal). Another parameter that prevents SIMS from being quantitative is the difference in ionization probability for different elements. As mentioned above, among the secondary particles, only the ionized ones are detected and analysed. Therefore, the neutral particles do not participate to the final spectrum. In this case, obviously more electropositive/electronegative elements show higher intensity in the final spectrum, even if they are present only as traces. Another major issue is the electronic state of the material being analysed. As ionization occurs close to emission of the particles from the surface, the matrix participates in the process involved. Therefore, its electronic state influences strongly the ionization of the emitted particle [76].

SIMS can be “static” or “dynamic”, depending on the primary particle flux density. The SIMS technique is basically destructive. The sample surface is modified as a result of primary ion bombardment, not only by the loss of secondary particles, but also by further radiation effects such as mixing of atoms, primary ion implantation and fragmentation of

## Chapter II. Experimental

---

surface molecular structures. However, using a very low primary particle flux density ( $< 1\text{ nA}\cdot\text{cm}^{-2}$ ) can lead to generation of mass spectral data in a time scale that is very short in comparison with the lifetime of the surface layer [76]. Therefore, the derived information would be characteristic of the chemistry of the surface layer, since statistically no point on the surface would be impacted more than once by the primary particle during an analysis. In this case, the surface can be considered “static”. The use of very low primary flux density leads to very low yield of secondary particles, and therefore imposes the requirement of high sensitivity on the detection equipment [76]. In order to keep in the “static” limit, primary ion density of  $\leq 10^{13}$  ions. $\text{cm}^{-2}$  should be used. On the other hand, “dynamic” SIMS uses high dose of primary particles ( $\geq 10^{15}$  ions. $\text{cm}^{-2}$ ) to provide analysis of elemental composition of the material as a function of depth.

For the static SIMS applications, a ToF-mass analyser is used. In ToF-SIMS, the secondary ions are accelerated before entering a flight tube by an applied potential and therefore have common kinetic energy, so that their flight time to the detector varies as the square root of mass. The time to arrive the detector, *i.e.* the flight time, is measured and used for calculation of the mass, which in turn is used for detection of the element. The fact that the ions with different masses flight with different velocities leads to their different arrival times to the detector. The mass is calculated from flight time, using Eq. II.2:

$$m = \frac{t^2 \times 2qU}{L^2} \quad \text{Eq. II.2}$$

where  $m$  is the mass of the secondary particle,  $q$  is the charge of the secondary particle,  $t$  is the time of the flight,  $U$  is the applied potential and  $L$  is the length of the flight. This equation is obtained from the extraction of mass from the relationship between kinetic energy (KE) and velocity ( $v$ ) according to Eq. II.3:

$$\text{KE} = \frac{1}{2}mv^2 = \frac{1}{2}m \frac{L^2}{t^2} = qU \quad \text{Eq. II.3}$$

The mass resolution (Eq. II.4) is proportional to the time resolution:

$$R = \frac{m}{\Delta m} = \frac{t}{2\Delta t} \quad \text{Eq. II.4}$$

The mass resolution in a ToF mass analyser is at least  $10^4$ . To compensate for the possible dispersion of the kinetic energy of secondary ions with same  $m/q$  ratio and therefore improving the mass resolution, a reflectron can be used on the top of the time flight analyser, among other correcting elements. With ToF-SIMS, spatial resolution of 100 nm, depth resolution of 1 nm (or less) and detection limit in the range of ppm are possible.

### II.3.1.2. Instrumentation and analytical conditions

In this work, ToF-SIMS was performed using a ToF-SIMS<sup>5</sup> spectrometer provided by ION-TOF GmbH. The spectrometer was run at an operating pressure of  $10^{-9}$  mbar. A picture of the ToF-SIMS spectrometer used in the present study can be found in Figure II.5.

The analysis modes used in the present study were “depth profiling” and “chemical imaging”. For depth profile elemental analysis, two ion beams are operated in a “Dual Beam Mode”. While a sputtering ion beam is used to sputter a crater, an analysis ion beam is used to measure progressively the centre bottom of the crater (Figure II.6). A lower energy of the sputtering beam permits higher sensitivity and higher depth resolution. Short pulses and small spot size (focus) of the  $\text{Bi}^+$  analysing beam permit higher mass and lateral resolution. The mass spectrum provided at each level in the sputtered depth yields a depth profile, *i.e.* a plot of the intensity of the selected ions vs the sputtering time. The sputtering time can be transformed to depth (nm) by using a profilometer and measurement of the sputtered depth. In the present study, a pulsed 25 keV  $\text{Bi}^+$  primary ion source was employed for analysis, delivering 1.1 pA of current over a  $100 \times 100 \mu\text{m}^2$  sputtered area. Analysis was performed in the centre of the sputtered crater using a 2 keV  $\text{Cs}^+$  sputter beam giving a 100 nA target current over a  $500 \times 500 \mu\text{m}^2$  area. Negative ion profiles were recorded because of their higher sensitivity to fragments coming from oxide matrices.

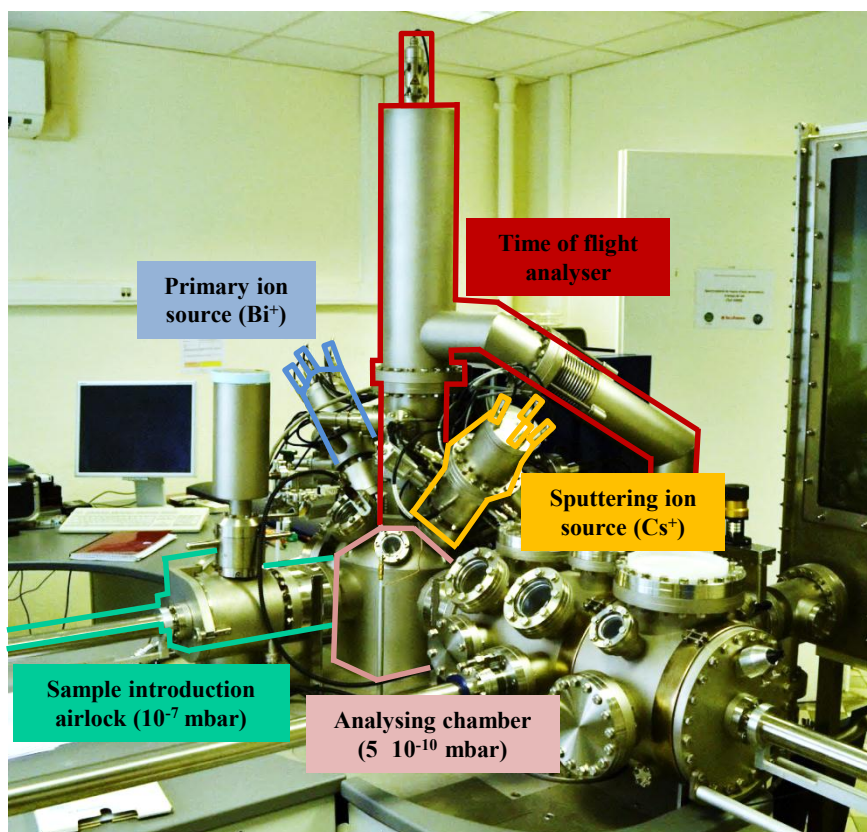


Figure II.5: Picture of the ToF-SIMS<sup>5</sup> spectrometer used in the present study

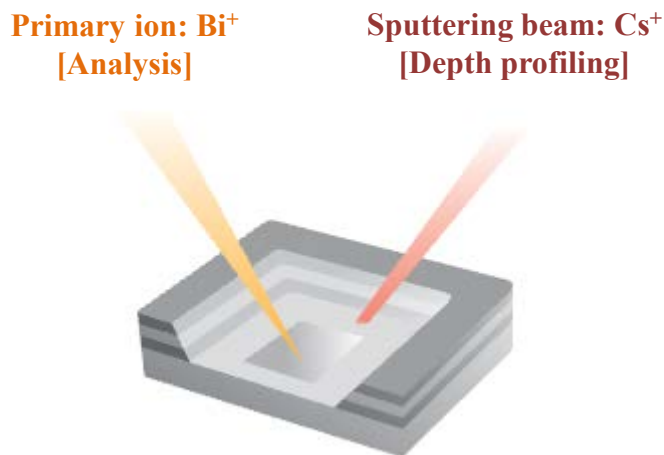


Figure II.6: Dual beam mode depth profiling, from ToF-SIMS<sup>5</sup> brochure

The “chemical imaging” provides an elemental 2D map of the surface. These maps are obtained by rastering a fine-focussed ion beam over the surface. The lateral resolution is controlled by the intensity of the primary ion beam. Lower current of the primary beam leads to higher lateral resolution (lower lateral perturbation). For the present study, a

pulsed 25 keV Bi<sup>+</sup> primary ion source was employed, delivering 0.1 pA of current over a  $100 \times 100 \mu\text{m}^2$  area with a resolution of 150 nm.

### II.3.2. Atomic Force Microscopy

#### II.3.2.1. Principles and instrumentation

Atomic Force Microscopy (AFM) like all other Scanning Probe Microscopy (SPM) methods, measures a local physical quantity related to the interaction of a tip with the surface to construct a surface image. AFM involves the measurement of the forces acting between a fine tip interacting with the sample. The force sensing tip is attached to a cantilever as shown in Figure II.7. Deflections are produced in the cantilever as a result of the interaction of the tip with the sample and consequent attractive/repulsive forces. These deflections are measured and used to compile a topographic image of the surface. Since AFM is based upon force measurements, there is no need for the sample to be electrically conductive, the most important distinction of AFM from STM (Scanning Tunnelling Microscope), making AFM very attractive and applicable to any sample.

The deflection of the cantilever is detected by the use of the laser beam reflected from the backside of the cantilever and collected in a position-sensitive photodiode. The vertical and horizontal displacements of the laser indicate the bending of the cantilever due to the topography and the friction (lateral forces).

The interaction between the tip and the sample depends on the distance between them. The probe should interact with the force field associated to the surface of the sample. The dependence of van der Waals forces on the distance between the tip and the sample is shown in Figure II.8.

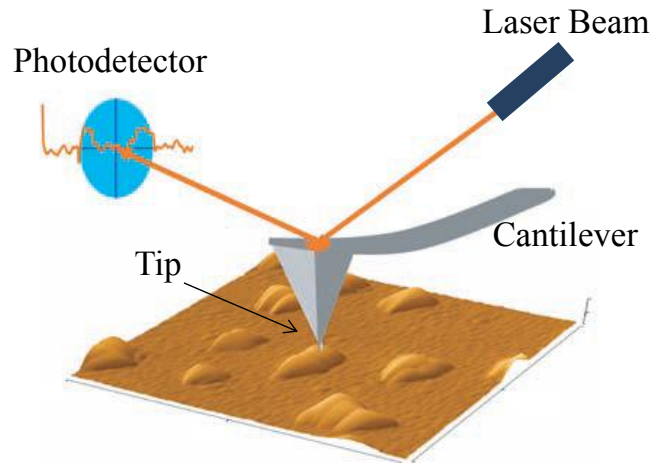


**Figure II.7:** Schematic illustration of AFM tip-sample interaction, from reference [76]

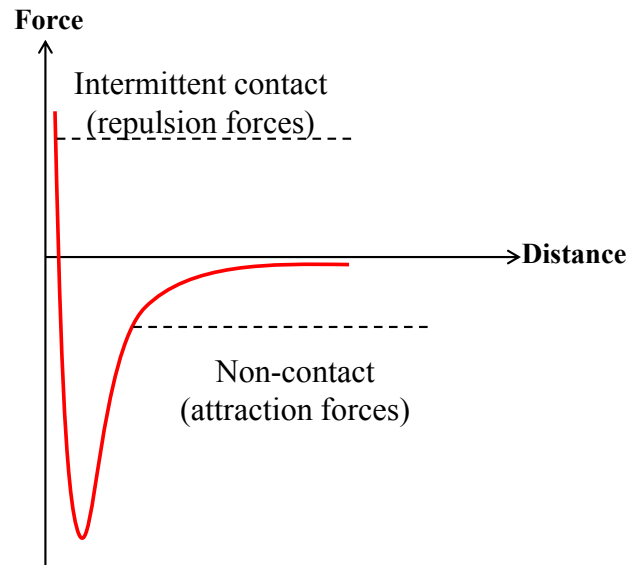


**Figure II.8:** Sample-tip interaction modes in AFM

The “non-contact” regime (on the right) is where the tip is held at tens to hundreds of angstrom from the sample surface. Forces between the tip and the sample are attractive in this regime. When the tip gets closer to the sample’s surface, the repulsive van der Waals forces dominate. This is the “intermittent-contact” regime. When the tip is held at less than a few angstroms from the sample surface, the forces balance and the net force drops to zero. When the total forces are positive (repulsive), the atoms are in the “contact” regime.

## Chapter II. Experimental

---

Apart from van der Waals forces, additional forces such as capillary and adhesive forces complicate the interaction between the tip and the sample.

As implied from the explanation above, there are different modes of operation in AFM: “non-contact” mode, “contact” mode and “intermittent contact” mode. The last two are explained in the following:

- Contact Mode:

The tip makes a soft physical contact with the surface of the sample. In this case the cantilever is treated as a Hookean spring and therefore the Hook’s law is applied, which means that the deflection of the cantilever ( $x$ ) is proportional to the force acting on the tip ( $F$ ), with the force constant of the cantilever ( $k$ ):

$$F = -k \cdot x \qquad \text{Eq. II.5}$$

The contact mode by itself can be performed at a “constant height” or a “constant force” mode. In the first one the height of the tip is fixed, while in the second one the deflection of the cantilever is fixed. Although atomic resolution in principle is achievable with the “constant height” mode, the “constant force” mode is preferred, due to the possibility to image the surfaces with greater height variability.

- Intermittent Contact (“Tapping Mode”):

In this mode, the cantilever oscillates close to its resonance frequency, in a sinusoidal motion. The tip-sample interaction causes changes in the amplitude, phase and resonance frequency of the cantilever.

An electronic feedback loop ensures that the oscillation amplitude remains constant at a set point value, such that a constant tip-sample interaction is maintained during the scanning. The topographic image is the multiplication product of the voltage applied to the piezo required to keep the oscillation amplitude constant and the sensitivity of the piezo ( $\text{nm} \cdot \text{V}^{-1}$ ). The difference between the amplitude and the set point (error signal) is used as the input of the

feedback system. The map of the output signal provides the “amplitude image”, which is plotted simultaneously as the topographic image.

The phase changes are used to provide phase images. The phase and amplitude images may point out the physical properties that cannot be recognized from topographic images.

The main advantage of the intermittent (tapping) mode is the considerable reduction of shearing forces, leading to less damage to the sample surface and higher lateral resolution.

AFM imaging in the present study was performed with an Agilent 5500 microscope used in intermittent contact (tapping<sup>®</sup>) mode in air. A silicon cantilever with a force constant of 25-75 N.m<sup>-1</sup> at a resonance frequency of 200-400 kHz was employed. The silicon tip nominal radius was < 10 nm.

### II.3.3. Scanning Electron Microscopy

Scanning Electron Microscopy (SEM) was used as an additional technique to visualize the surface of some of the coated samples. Having a much larger field of depth and magnification than an optical microscope, SEM is a technique for high-resolution imaging of the surfaces which uses electrons for imaging.

Focused electrons impinge on the surface of the sample, which leads to emission of electrons from the surface of the sample due to elastic and inelastic scattering events. The emitted low-energy electrons resulting from inelastic scattering are called secondary electrons and are used to produce secondary electron images.

Secondary electron images were taken at LISE (Laboratoire Interfaces et Systèmes Electrochimiques) with a digital scanning electron microscope S440 LEICA with a tungsten filament (FEG-SEM).

### II.4. Electrochemical analysis

#### II.4.1. Experimental conditions

All electrochemical experiments were carried out at room temperature in a 0.5 M NaCl solution as electrolyte, prepared with ultrapure Millipore<sup>®</sup> water (resistivity > 18 MΩ.cm), and reagent grade chemicals (NaCl Analar Normapur analytical reagent, VWR<sup>®</sup> BDH Prolabo<sup>®</sup>). The electrolyte was bubbled by argon for 30 min prior to the measurements and during analysis. For the bare copper samples on which the native oxide layer was removed before the electrochemical tests (as explained in section II.1.1.4), the pre-treatment was done just before introducing the sample in the electrochemical cell and starting the measurements. Coated samples were rinsed in ultrasonic bath of ethanol for 5 min and dried with compressed air before the electrochemical measurements.

##### II.4.1.1. Instrumentation

###### II.4.1.1.1. Electrochemical cell

All electrochemical tests were performed in a conventional three-electrode cell. The three-electrode cell consisted of a working electrode (WE), a counter (CE) or auxiliary electrode and a reference electrode (RE). An electrode is a (semi-) conductive solid that interacts with the electrolyte. The WE is the electrode being studied, where the electrochemical reactions take place. In corrosion experiments, the WE is the material that is corroded. The CE is the electrode with which the current path is completed. All the current needed to balance the current produced at the WE passes through the CE. The RE is used to measure the voltage between the WE and the electrolyte. It has a constant potential and serves as an experimental reference point. Therefore, no current should pass through the reference electrode.

All electrochemical tests were performed in a conventional three-electrode cell designed and manufactured at Chimie ParisTech, with a platinum wire as the counter electrode and

a saturated calomel reference electrode (SCE) as shown in Figure II.9. A Luggin capillary (filled with the electrolyte) was used to hold the reference electrode and make the connection between the reference electrode and the cell. The distance between each two electrodes was about 2 cm and the diameter of the cross section of the cell was about 6 cm. The volume of the electrolyte used was about 100 mL. The working electrode area was delimited to 0.29 cm<sup>2</sup> by a Viton O-ring.

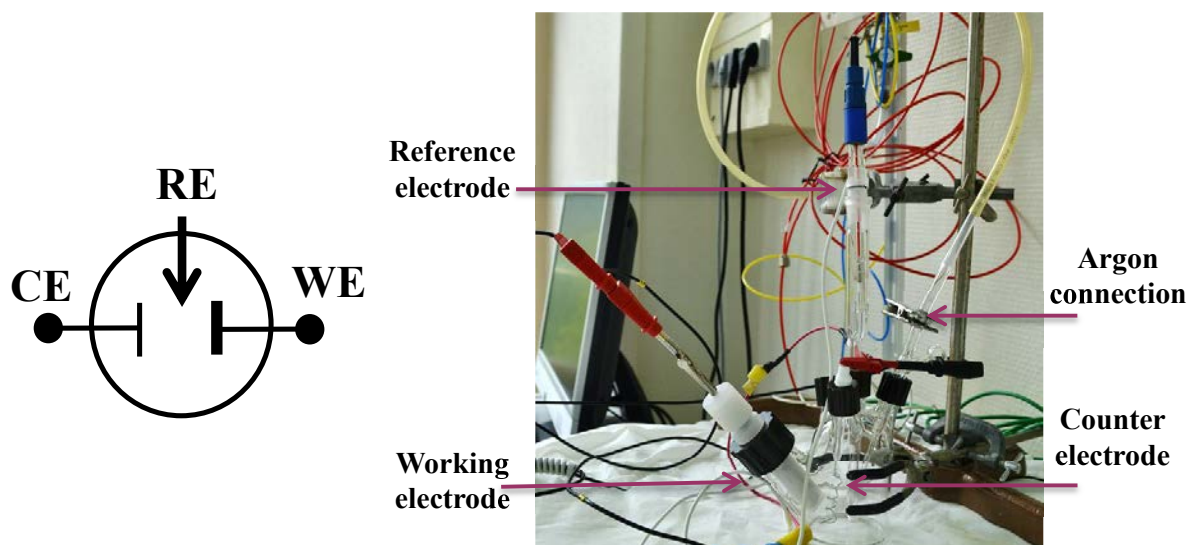


**Figure II.9:** Three-electrode set up and the electrochemical cell used in the present study

### II.4.1.1.2. Potentiostat

To control the experiments done in the three-electrode cell a potentiostat is used. In potentiostatic mode, the potentiostat controls the potential of the CE against WE precisely in order to keep the potential difference between the WE and RE well defined, corresponding to the value determined by the user. In a three-electrode setup, the current flows between the CE and WE. The potential is measured between the RE and WE, and controlled between them by controlling the polarization of the CE.

The potentiostats used in the present study were an Autolab PGSTAT30 potentiostat/galvanostat and an EC-Lab SP-200 system from Bio-Logic. The Autolab was

used for the copper substrates with the possibility of measuring the currents from 1 A down to 100 pA with the ECD module for extremely low currents. For aluminium substrates, the Bio-Logic was used with the ability of measuring the currents down to 1 pA with the ULC (Ultra Low Current) option.

The softwares used with Autolab were GPES and FRA for the voltammetry and impedance measurements, respectively. EC-Lab<sup>®</sup> was the software used with Bio-Logic for both the voltammetry and impedance measurements.

### **II.4.2. Techniques**

Application of accelerated precise methods for measuring the rate of the corrosion is of huge importance. While direct analytical methods, such as weight loss measurements or solution analysis can be used, the application of AC and DC electrochemical methods can save time and lead to more detailed information about the corrosion mechanism of the system under study.

#### **II.4.2.1. Open Circuit Potential vs time**

The Open Circuit Potential (OCP) is the equilibrium potential of the metal in the absence of any electrical connections to the metal. The OCP vs time measurement involves the measurement of the evolution of the potential difference between the WE and RE electrodes, immersed in the electrolyte at zero net current, as a function of time. This is usually the first step in corrosion measurements and is used in order to allow sufficient time for the OCP to stabilize and reach the steady state, which is especially important for the impedance measurements. The OCP depends on many factors including the WE material, the temperature, the electrolyte composition and pH and the hydrodynamics.

In the present study, before starting the DC and AC electrochemical experiments, the open circuit potential (OCP) was measured for 30 minutes in order to reach a stable potential.

### II.4.2.2. Electrochemical Impedance Spectroscopy

Electrochemical Impedance Spectroscopy (EIS) is a powerful technique applied in corrosion research. In this technique the system is perturbed with an AC signal (potential or current) of small amplitude, resulting in an output signal (current or potential). While resistance is a parameter describing the opposition to the flow of electrons in an ideal resistor, impedance is used for more complicated systems containing other elements than only a resistor.

If an excitation potential signal (Eq. II.6) is used, the response is a current signal with a phase shift (Eq. II.7), only if the system has a linear behaviour:

$$E_t = E_0 \sin \omega t = E_0 \exp(j\omega t) \quad \text{Eq. II.6}$$

$$I_t = I_0 \sin(\omega t + \phi) = I_0 \exp(j\omega t - \phi) \quad \text{Eq. II.7}$$

$E_0$  is the input potential amplitude,  $I_0$  is the output current amplitude,  $t$  is time and  $\phi$  is the phase shift.

Therefore, the impedance will be:

$$Z = \frac{E_t}{I_t} = Z_0 \exp(j\phi) = Z_0 (\cos \phi + j \sin \phi) \quad \text{Eq. II.8}$$

where  $j$  is the imaginary number ( $j = \sqrt{-1}$ ) and  $Z_0$  (in Ohm) is the modulus of the impedance and is obtained from the real ( $Z_r$ ) and imaginary ( $Z_i$ ) parts of impedance according to Eq. II.9:

$$Z_0 = |Z| = \sqrt{Z_r^2 + Z_i^2} \quad \text{Eq. II.9}$$

The phase shift is related to the real and imaginary parts of  $Z$  according to Eq. II.10:

$$\phi = \tan^{-1} \frac{Z_i}{Z_r} \quad \text{Eq. II.10}$$

As mentioned above, the excitation signal should have small amplitude in order to keep the system linear. Linearity means that the response to an input signal consisting of the weighted sum of several signals should be the weighted sum (superposition) of the responses to each individual signal. Electrochemical systems are not linear. Therefore only by keeping the excitation signal amplitude low enough, it is possible to stay in the linear domain.

The most popular plots for representation of the EIS data are the Nyquist (Figure II.10, left) and Bode (Figure II.10, right) plots. In Nyquist plot, the opposite of the imaginary part ( $-Z_i$ ) is plotted against the real part ( $Z_r$ ). The results are presented as a group of points, each one corresponding to a measured frequency. The disadvantage of this kind of representation is that the frequency dependence is not clear, as the frequency cannot be read on the axes. The high frequency (HF) limit (on the left) corresponds to the resistance of the electrolyte ( $R_e$ ), while the low frequency (LF) limit (on the right) corresponds to the polarization resistance ( $R_p$ ). The Bode plot, including two y-axes, represents the logarithm of the modulus and the phase angle vs the logarithm of the frequency. This representation has the advantage of showing the frequency explicitly. Other types of representations are developed also for better analysis of the EIS data, making the visualization of the data easier [77].

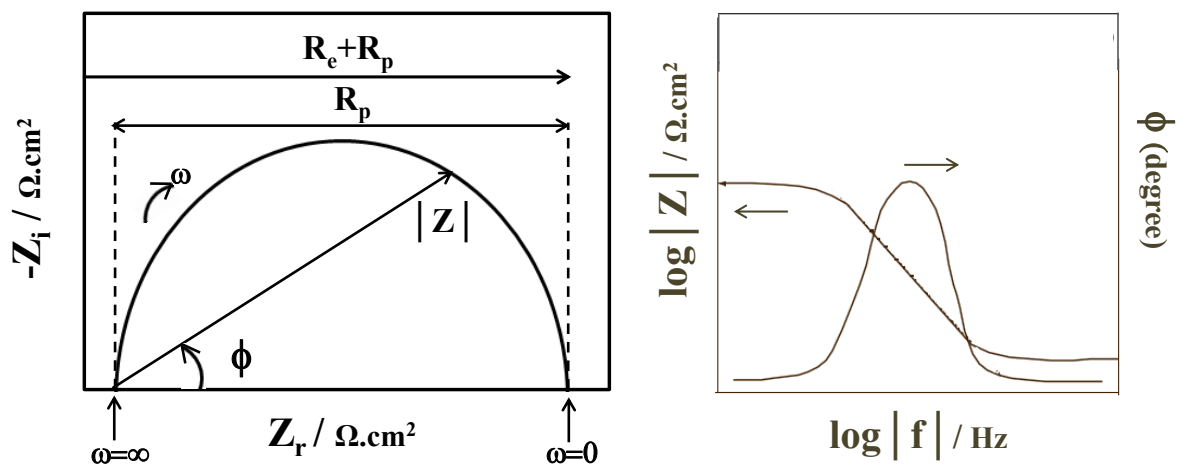


Figure II.10: Nyquist (left) and Bode (right) representations used for visualisation of EIS data

The analysis of EIS data needs application and use of equivalent circuits, which should be able to describe the mechanism happening in the system under study. The simple fact that an equivalent circuit fits a system is not enough for choosing that model, as more than one circuit could fit a system. Therefore, the chosen model should be based on the physics of the system.

In the present study, the EIS measurements were performed after 30 min of OCP measurement and stabilization. The EIS measurements were done at  $E_{OCP}$  in a frequency range of  $10^{-2}$  to  $10^5$  Hz with a peak-to-peak excitation signal set at 10 mV. Fitting of EIS data was done using Simad® software developed at Laboratoire Interfaces et Systèmes Electrochimiques, UPMC, Paris.

### II.4.2.3. Linear Sweep Voltammetry

DC techniques have been used widely for corrosion measurements. Linear Sweep Voltammetry (LSV) as a potentiodynamic scan is a useful tool in corrosion studies to monitor the change of the current as a result of the change in the potential applied to the system under study. In LSV, the potential is swept linearly at specific steps (scan rate /  $\text{mV}\cdot\text{s}^{-1}$ ) and the produced current as a result of polarization of the WE is measured and monitored. Obviously LSV leads to perturbation of the system and irreversible changes in it, as a result of the externally imposed polarization. Therefore, it is considered as a destructive method. The potentiodynamic polarization plots provide useful information including the corrosion current and potential of the system under study, the polarization resistance, the passivity and the pitting susceptibility.

The evolution of current *vs* potential, *i.e.* the polarization curve can be reported in a linear or logarithmic scale. While the slope of linear E-i curve in the vicinity of the corrosion potential can be used to determine the polarization resistance ( $R_p$ ), the logarithmic polarization curve ( $\log |I|$  *vs* E) can be used to obtain the corrosion current ( $I_{corr}$ ) from the intersection of the linear portions of the logi-E curve extrapolated to the corrosion potential ( $E_{corr}$ ) in the case of cathodic and anodic Tafel behaviours. These procedures are illustrated in Figure II.11.

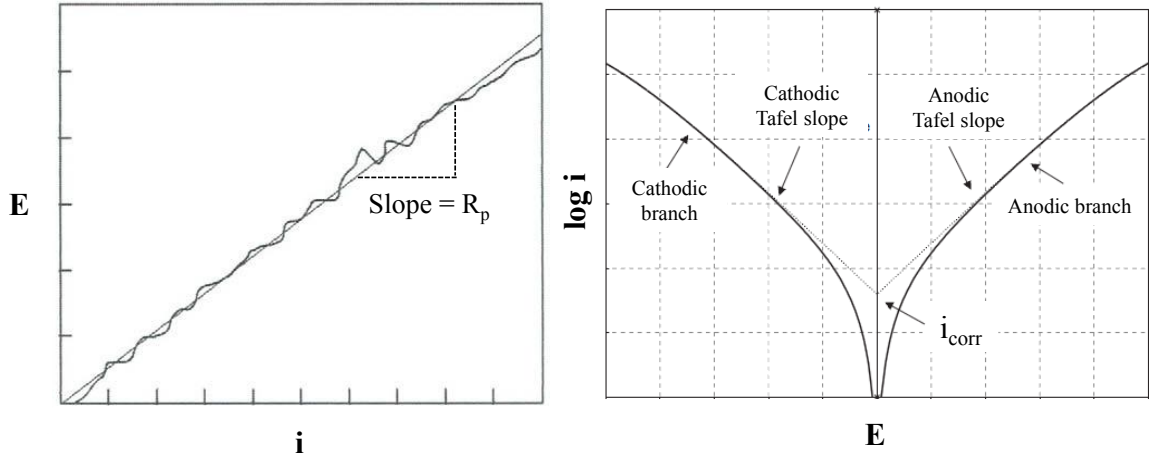


**Figure II.11:** Linear polarization technique: calculation of  $R_p$  (left). Tafel polarization technique: calculation of  $i_{corr}$  (right)

As mentioned above, the polarization resistance at  $E_{corr}$  can be obtained from the following equation and in agreement with Ohm's law:

$$R_p = \left( \frac{dE}{di} \right)_{E=E_{corr}} \quad \text{Eq. II.11}$$

$R_p$  can be related to  $i_{corr}$  using the Stern-Geary equation [78]:

$$i_{corr} = \frac{b_a \cdot b_c}{2.303(b_a + b_c)} \times \frac{1}{R_p} \quad \text{Eq. II.12}$$

where  $b_a$  and  $b_c$  are the anodic and cathodic Tafel slopes. They are obtained from the inverse of the slope of the tangent lines to the linear portions of anodic and cathodic parts in log*i*-*E* curves as shown in Figure II.11 (right). Eq. II.12 can be used only for the simple case where both anodic and cathodic reactions are charge transfer controlled reactions. However, this is not always the case. For instance the cathodic part may be diffusion controlled, due to diffusion of oxygen. In this case, Eq. II.12 can be reduced to [79]:

$$i_{corr} = \frac{b_a}{2.303} \times \frac{1}{R_{ct}} \quad \text{Eq. II.13}$$

## Chapter II. Experimental

---

where  $R_{ct}$  is the charge transfer resistance.

The LSV tests in the present study were performed after the EIS measurements with a scan rate of  $1 \text{ mV}\cdot\text{s}^{-1}$  in one direct positive-going sweep started from a cathodic potential and extended to an anodic potential.

# **Chapter III**

## **Analysis of the corrosion protection of copper by ALD alumina coatings and effect of deposited layer thickness**

### **III.1. Introduction**

The corrosion of copper in chloride media has been extensively studied due to the strong influence of chloride ions on the corrosion mechanisms [4,5,7,80–83]. Although copper is a relatively noble metal, its corrosion takes place at a significant rate in sea water and in chloride environments. In neutral conditions protective layers of copper oxide and hydroxide can form on the metal surface [16,84,85]; however, their formation gets complicated in presence of chloride ions and gives more complexity to the corrosion mechanism [4].

The corrosion protection of copper using ALD alumina coating was studied in this chapter, as well as the effect of varying the coating thickness. Corrosion performance of an inert coating as a barrier layer depends on many factors including the coating thickness. Increasing the coating thickness is favourable for the barrier properties.

## Chapter III. Analysis of the corrosion protection of copper by ALD alumina coatings and effect of deposited layer thickness

---

However, there is high interest in decreasing the coating thickness for several reasons including better adhesion to the substrate with reduction of coating's weight and subsequent coating peel off and the ability to coat substrates of small dimensions. However, the ability to reduce the coating thickness without losing its performance is limited, as the possibility of having leakage current increases with the reduction of coating thickness.

Electropolished copper was used as the substrate. Electropolishing of copper is done immediately after its mechanical polishing, as mentioned in Chapter II. Such preparation leads to smoothing of the surface and decrease of the roughness, as discussed in Chapter V. The coating thickness was varied between 10 and 50 nm.

### III.2. Electrochemical behaviour of bare Cu substrate

#### III.2.1. Linear sweep voltammetry

Polarization curve obtained by LSV for Cu substrate is presented in Figure III.1.A. The sample was polished, electropolished and pre-treated ( $H_3PO_4$  pre-treatment) as explained in Chapter II. The polarization curve was well reproducible. Parameters extracted from the LSV polarization curve (Figure III.1.A) are presented in Table III.1. The polarization resistance (Figure III.2.A) was obtained from the reciprocal of the slope of the linear  $i$ - $E$  curve close to the corrosion potential ( $E_{corr} \pm 20$  mV).

**Table III.1:** Parameters related to LSV curve presented in Figure III.1

	$E_{corr} /$ V(SCE)	$i_{corr} / A.cm^{-2}$	$R_p /$ Ohm.cm <sup>2</sup>	$b_a / V.dec^{-1}$	$b_c / V.dec^{-1}$
<b>Cu bare substrate</b>	-0.395	$2.8 \times 10^{-8}$	$5.22 \times 10^5$	0.065	-0.190

### Chapter III. Analysis of the corrosion protection of copper by ALD alumina coatings and effect of deposited layer thickness

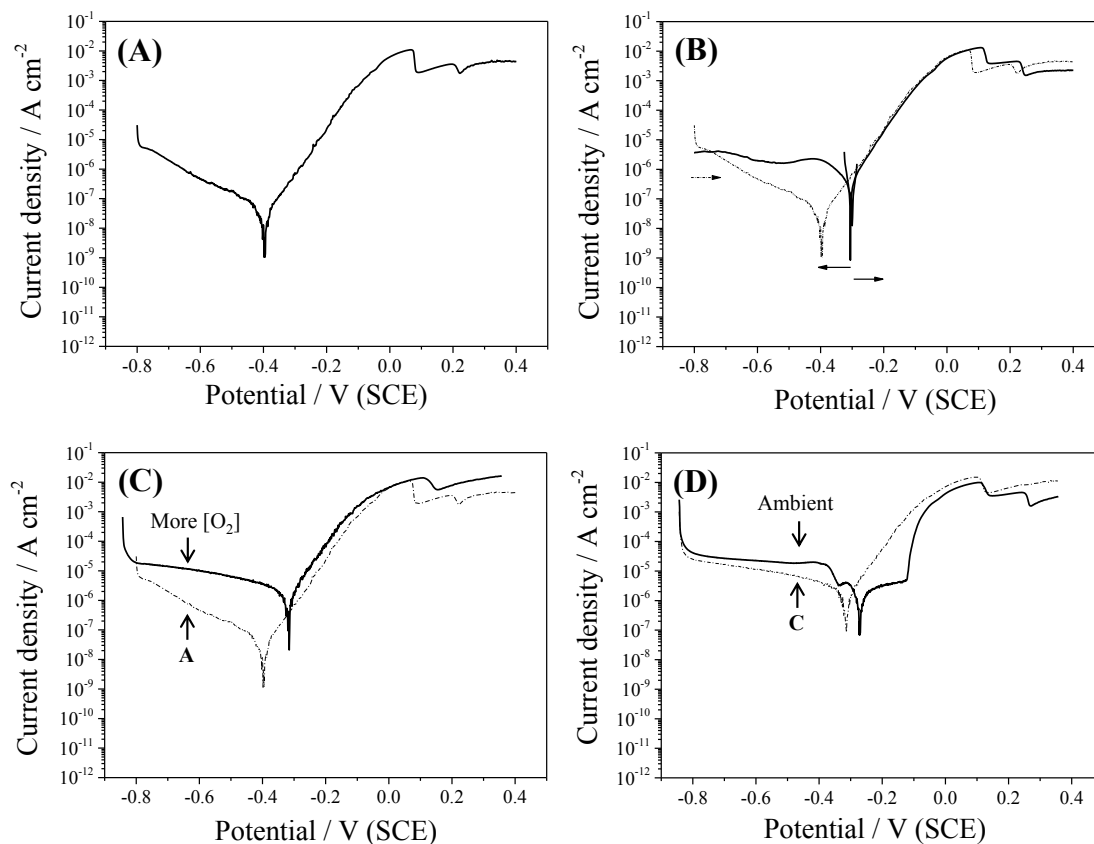


**Figure III.1:** LSV polarization curves (after 45 min OCP) for bare electropolished Cu substrates in 0.5 M NaCl, (scan rate: 1 mV.s<sup>-1</sup>): Pre-treated, under argon bubbling and swept from -0.8 V/SCE (A). Pre-treated, under argon bubbling and swept separately, positive and negative-going from OCP (B). Pre-treated, under lower rate of argon bubbling and swept from -0.8 V/SCE (C). Freshly polished, under ambient conditions and swept from -0.8 V/SCE (D)

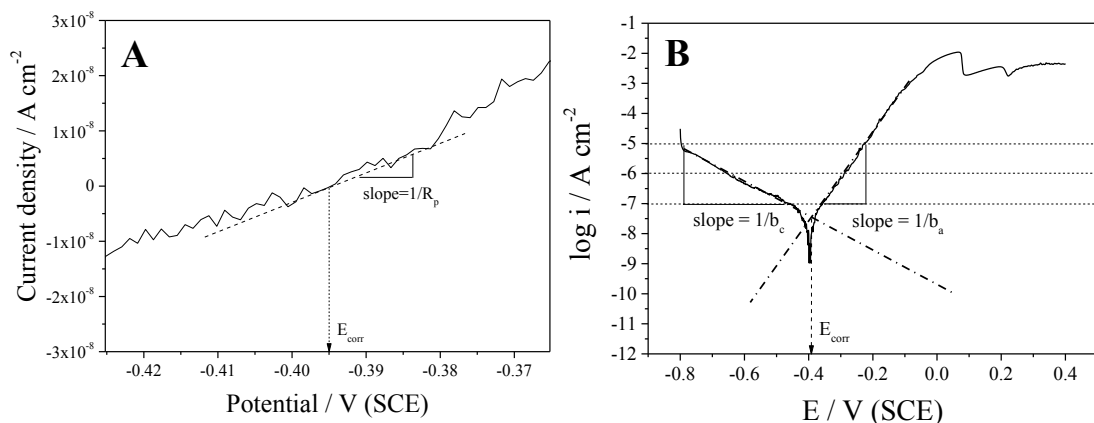
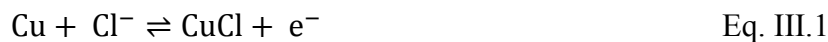


**Figure III.2:** Representation of measurement of polarization resistance (A) and Tafel slopes (B) on polarization curve presented in Figure III.1.A

### Chapter III. Analysis of the corrosion protection of copper by ALD alumina coatings and effect of deposited layer thickness

---

Copper anodic dissolution takes place through oxidation of Cu to Cu<sup>+</sup> and its reaction with Cl<sup>-</sup> ions to produce CuCl (Eq. III.1) which is not stable and reacts with Cl<sup>-</sup> ions to dissolve into soluble cuprous chloride complexes (Eq. III.2) [4,5,16,82,86–90]:



CuCl<sub>2</sub><sup>-</sup> is the main cuprous chloride complex for chloride concentrations lower than 0.55 M [6,82,83,87,91,92]. For higher chloride concentrations, CuCl<sub>3</sub><sup>2-</sup> and CuCl<sub>4</sub><sup>3-</sup> are produced sequentially. The anodic reactions are reversible, mainly due to the fast and thermodynamically favourable complexation of cuprous ion by chloride ion [4].

Oxidative formation of CuCl and dissolution to form CuCl<sub>2</sub><sup>-</sup> give rise to an anodic peak in the polarization curves observed here at 0.07 V (Figure III.1.A). This peak appears when the CuCl surface coverage reaches a maximum, as a result of diffusion limitation of CuCl<sub>2</sub><sup>-</sup> to the bulk of the solution. Following this anodic peak, any increase in anodic current density is due to the oxidative formation of Cu<sup>2+</sup> species (Eq. III.3).



However, in some cases, a disproportionation reaction can happen between Cu and Cu<sup>2+</sup> to form CuCl (Eq. III.4),

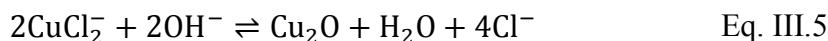


making the corrosion process to go back to Eq. III.2 and reinitiating the process, which can lead to a second peak, as seen at 0.19 V in Figure III.1.A [93,94]. The second anodic peak has also been attributed to completion of a CuCl<sub>ads</sub> monolayer, while the first one is due to its formation [95].

CuCl and Cu<sub>2</sub>O are the two main corrosion products formed at corrosion potential [96]. While CuCl is formed rapidly, Cu<sub>2</sub>O is the main component of surface layer at longer immersion times [96]. Cuprous oxide is produced in presence of hydroxide ions as a precipitation reaction according to Eq. III.5 [4,83]:

### Chapter III. Analysis of the corrosion protection of copper by ALD alumina coatings and effect of deposited layer thickness

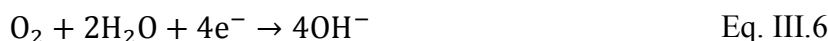
---



The equilibrium in Eq. III.5 is shifted to the right if  $\text{OH}^-$  increases. Besides, the stability of  $\text{Cu}_2\text{O}$  is inversely dependant on the concentration of chloride ions [4]. Therefore, in presence of chloride ions,  $\text{Cu}_2\text{O}$  is not stable and can dissolve with a rate depending on the pH and the concentration of chloride ions in the electrolyte. The rate of re-dissolution of cuprous in chloride-containing solutions has been reported to be much higher than that observed in chloride free, neutral/alkaline solutions [4,97,98].  $\text{Cu}_2\text{O}$  can also form electrochemically at higher potentials (anodic oxide) [99–101] which thickness, electrical and protective properties depend on pH, applied potential and anodization time [102–104,104–106]. While in alkaline  $\text{Cl}^-$ -free solutions passive anodic oxides are formed, in presence of  $\text{Cl}^-$  ions the anodic oxides are thinner and locally dissolved, due to the competition between the chloride and  $\text{OH}^-$  adsorption and blocking effect of copper chloride compound for adsorption of  $\text{OH}^-$  [107].

The cathodic reaction is usually oxygen reduction (Eq. III.6) [8] and its kinetics is known to be very specific to the system under study and the surface condition of the electrode [4]. The presence, composition, thickness and surface coverage of thermal and air formed oxides and corrosion products can have considerable influence on the mechanisms [4,97,108–110]. The copper oxide formed on the surface of a freshly polished sample at room temperature and stable in contact with air is usually accepted to be cuprous oxide [98,111], while when the surface is heated in air, oxygen or water, a duplex film is formed which is mostly cuprous oxide with a lower concentration of cupric oxide and/or cupric hydroxide [112,113].

Cathodic reaction is usually dominated by oxygen reduction (Eq. III.6) (hydrogen evolution finds importance only at potentials more negative than -1 V/SCE) and, contrary to anodic reaction, is assumed to be relatively irreversible [4].



In contrast with the general agreement on the anodic dissolution of copper and its mechanism, interpretation of the cathodic behaviour varies in different studies, which is

### Chapter III. Analysis of the corrosion protection of copper by ALD alumina coatings and effect of deposited layer thickness

---

mostly due to the variations in the surface conditions [4], amount of dissolved oxygen in the electrolyte [8,108] and pH [109]. The reaction shown in Eq. III.6 is a simplified oxygen reduction involving a single step of exchange of four electrons, resulting in production of OH<sup>-</sup> ions (or water molecules in acidic electrolytes) [4]. However, the mechanism can be more complicated, involving cumulative two-electron steps and the production of intermediate peroxide species [4]. The variation of the kinetics of the intermediate electrochemical and chemical steps and the rate of adsorption/desorption processes make the kinetics of the oxygen reduction very specific to the system under study [4]. The cathodic reaction (oxygen reduction) at mixed potential is reported to be under full charge transfer control [80,83], under mixed control [8,114], and under mass transport control [92] by different authors. Mass transfer limitation in cathodic part at corrosion potential has been reported to gain importance with decrease of concentration of dissolved oxygen ([O<sub>2</sub>]) [8] and low flow rate [83].

To verify the behaviour of the substrate at OCP, the potential was swept negative and positive-going from OCP, separately as shown in Figure III.1.B. The hysteresis in the cathodic branch points out the change in the kinetics of oxygen reduction on two different surfaces formed at different potentials. While the cathodic plateau in Figure III.1.B can be extrapolated to the corrosion potential and the oxygen reduction can be assumed to be under diffusion control at  $E_{\text{corr}}$ , the absence of plateau on the cathodic branch in Figure III.1.A indicates more kinetic control of oxygen reduction on the copper surface when the potential is switched to -0.8 V and scanned positive-going. The origin of the difference in oxygen reduction mechanism on the copper surface in Figure III.1.A and B is the change in copper oxide species at -0.8 V and at OCP. This change may be in terms of composition, thickness, coverage and reactivity of surface species.

The cathodic behaviour of the copper electrode in the present study will be further discussed in Chapter IV. However, it is worthy to point out that the higher corrosion potential and current in Figure III.1.B in comparison with Figure III.1.A is consistent with the presence of more copper oxide species on the surface at OCP in comparison with when the potential is switched to -0.8 V and scanned positive-going. The partial reduction of copper oxide species when the potential is switched to -0.8 V is the reason for lower corrosion current and potential. The shift of corrosion current and potential to

### Chapter III. Analysis of the corrosion protection of copper by ALD alumina coatings and effect of deposited layer thickness

---

lower values in the conditions of LSV test (starting from -0.8 V and positive-going) is less pronounced with more dissolved oxygen in the electrolyte. This is evidenced in Figure III.1.C for a copper substrate (pre-treated) in an electrolyte with a lower rate of argon bubbling (more oxygen present in the electrolyte). Therefore, it is suggested that promoting oxide formation by the presence of more dissolved oxygen in the electrolyte at OCP leads to less reduction of Cu<sub>2</sub>O when the potential is switched to -0.8 V.

Apart from the oxygen reduction, for the polarization curve presented in Figure III.1.A, water reduction (Eq. III.7) [115] can be the reaction at lower potentials:



Anodic dissolution of copper in NaCl is usually believed to be under mixed charge transfer and mass transport control [4,88]. While the active dissolution of Cu to Cu<sup>+</sup> leads to an apparent Tafel region near the corrosion potential, the mass transport controlled component of the anodic dissolution is diffusion of Cl<sup>-</sup> to the surface [6] and CuCl<sub>2</sub><sup>-</sup> away from the electrode [7,82,87,89]. The anodic Tafel slope for the copper in the present study (Figure III.2.B, Table III.1) is in agreement with the values in the literature for a mixed charge transfer and mass transport control of the kinetics of anodic dissolution of copper in 0.5 M NaCl [5–7,82,83,86,87,98,114]. Mass transport limitation in anodic part can sometimes be identified as an anodic plateau [81,116] attributed to diffusion of CuCl<sub>2</sub><sup>-</sup> through both a Cu<sub>2</sub>O layer and the electrolyte [81,96]. Such anodic plateau was observed here for a freshly electropolished copper electrode immersed in an electrolyte without argon bubbling (ambient conditions) as can be seen in Figure III.1.D. The small peak observed in the cathodic part near OCP may be due to reduction of CuCl, compared with a similar irreproducible peak observed by Deslouis *et al.* [5] for short time of immersion of copper in aerated 0.5 M NaCl. As the main difference between the samples in Figure III.1.A and D is the [O<sub>2</sub>] level in the electrolyte, the absence of this plateau for the polarization curve in Figure III.1.A is therefore linked to the lower amount of Cu<sub>2</sub>O at E<sub>corr</sub> on this sample. As discussed above (Eq. III.5), one of the factors promoting the formation of Cu<sub>2</sub>O in chloride-containing solutions is alkalinity (OH<sup>-</sup> ions). Lower level of oxygen for the sample in Figure III.1.A leads to less production of OH<sup>-</sup> and thus less formation of cuprous oxide. Apart from the anodic plateau, the sample in Figure III.1.D

### Chapter III. Analysis of the corrosion protection of copper by ALD alumina coatings and effect of deposited layer thickness

---

shows higher corrosion current and potential, and a cathodic plateau in comparison with Figure III.1.A. Increase of corrosion current and shift of corrosion potential to more noble values in presence of more dissolved oxygen is expected for corrosion processes where oxygen reduction is the cathodic reaction [78], and is observed for other studies done on copper in NaCl [8]. The cathodic plateau observed in Figure III.1.D and its absence in Figure III.1.A is linked to more reduction of oxygen and its diffusion limitation in Figure III.1.D.

Comparing the position of the anodic peak in the polarization curves in Figure III.1, it can be noticed that wherever the corrosion potential is shifted to higher values due to the presence of more dissolved oxygen in the electrolyte (Figure III.1.D) or due to more copper oxide present at corrosion potential (Figure III.1.B), the anodic peak is shifted positively, but less than the corrosion potential. For instance, comparing Figure III.1.D with Figure III.1.A, the corrosion potential is shifted by 130 mV to positive values in Figure III.1.D, while the anodic peak is shifted by only 40 mV. This is in agreement with presence of more Cu<sub>2</sub>O in Figure III.1.D. According to Deslouis *et al*, [5] the hydrolytic formation of Cu<sub>2</sub>O from Cu(I) species is competitive with complexation of CuCl with Cl<sup>-</sup> and the removal of the produced CuCl<sub>2</sub><sup>-</sup> by mass transport. Therefore, earlier appearance of anodic peak in Figure III.1.D and B in comparison with Figure III.1.A is in agreement with less removal of CuCl<sub>2</sub><sup>-</sup> in presence of more Cu<sub>2</sub>O. More clearly, diffusion of CuCl<sub>2</sub><sup>-</sup> away from the electrolyte is slower in presence of more Cu<sub>2</sub>O. Competition between formations of Cu<sub>2</sub>O and nucleation of CuCl has been reported by others also [107,117].

In summary, the copper substrate used in the present study (Figure III.1) shows an apparent Tafel behaviour in anodic part, before reaching the anodic peak, and mass transport limitation in cathodic part near OCP (due to oxygen diffusion limitation as judged by the plateau observed in Figure III.1.B). The absence of a plateau in the cathodic branch in Figure III.1.A and the lower corrosion potential and corrosion current in comparison with Figure III.1.B are attributed to reducibility of the fresh oxide formed on the substrate after H<sub>3</sub>PO<sub>4</sub> pre-treatment, and its reduction in an electrolyte with low amount of dissolved oxygen when the potential is switched to -0.8 V/SCE to start the LSV test.

### Chapter III. Analysis of the corrosion protection of copper by ALD alumina coatings and effect of deposited layer thickness

---

This discussion of the electrochemical behaviour of the bare substrate used in our study was necessary. Although the applied conditions for the LSV test made the interpretation of the electrochemical behaviour of the copper substrate difficult, the choice of these conditions was necessary. Argon bubbling was used in the electrolyte to make the present study comparable with former studies done in the group on ALD coatings on other substrates [60–62,118–121]. Removing the native oxide was done firstly in order to have a bare substrate comparable to that under the coatings, and secondly to avoid the possible detrimental effect of an interfacial native oxide layer under the coatings, as shown in previous studies [120,121]. Finally single anodic sweep from a low potential was preferred to separate positive and negative-going sweeps from OCP, in order to have an optimum use of coated samples in different analytical tests, regarding the limited number of available coated samples. Furthermore, it is believed that to study the corrosion protection performance of the coatings, such way of analysis is properly applicable.

#### III.2.2. Electrochemical Impedance Spectroscopy

Figure III.3 shows the EIS Bode plot for the bare copper at OCP.

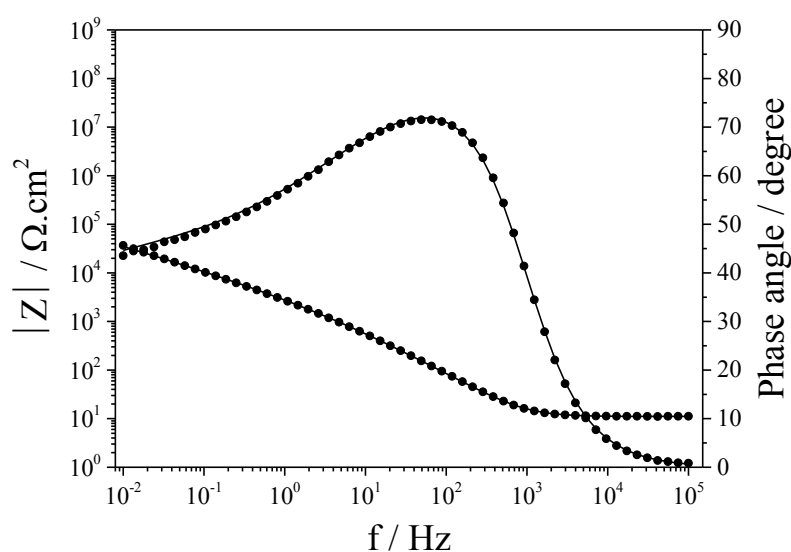


**Figure III.3:** EIS Bode plot for bare copper substrate (after 30 min immersion) in 0.5 M NaCl under argon bubbling (pH = 6) at OCP. Points and lines correspond to measured and fitted data, respectively.

### Chapter III. Analysis of the corrosion protection of copper by ALD alumina coatings and effect of deposited layer thickness

An equivalent electrical circuit corresponding to a corroding electrode at OCP can be considered as shown in Figure III.4 [122].

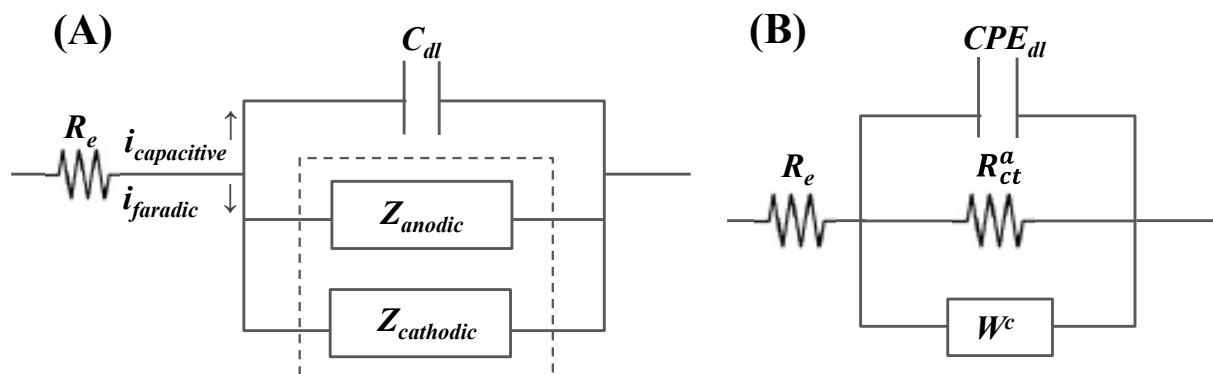


**Figure III.4:** A: Equivalent electrical circuit of the interfacial impedance of a corroding electrode at open circuit potential. B: Equivalent circuit model adopted for the bare Cu substrate for the present study at open circuit potential (E.C.1).

The electrolyte resistance ( $R_e$ ) is in series with an interfacial impedance consisting of Faradic ( $Z$ ) and capacitive ( $C_{dl}$ ) responses in parallel with each other. As the sum of anodic and cathodic currents at corrosion potential is zero, the Faradic impedance is the parallel combination of anodic ( $Z_a$ ) and cathodic impedances ( $Z_c$ ). For the Cu substrate of the present study,  $Z_a$  and  $Z_c$  are modelled as  $R_{ct}^a$  (anodic charge transfer resistance) and  $W^c$  (cathodic Warburg impedance), respectively (Figure III.4.B), in agreement with the model used by Torres *et al.* [123] for the study of Cu-Ni alloys in sea water. In that study, the HF loop was modelled with  $CPE_{dl}/R_{ct}^a/W^c$  and the LF loop corresponded to anodic mass transport, which is mass transport of  $CuCl_2^-$  and  $Cu^+$  and partial blocking effect by absorbed species such as  $CuCl$ , although finally it was not taken into account as it was not well resolved (few points at LF). In the present case of Cu in an electrolyte with lower amount of oxygen, two time constants can be noticed in the phase plot in Figure III.3. It is suggested that the time constant at higher frequencies is a double layer capacitance and the time constant at lower frequencies is a cathodic Warburg impedance ( $W^c$ ) in parallel with an anodic charge transfer resistance ( $R_{ct}^a$ ).  $W^c$  was used for the cathodic part, in agreement with residual  $O_2$  diffusion limitation at OCP (cathodic plateau in Figure III.1.B) which becomes restrictive with reduction of dissolved oxygen level in the electrolyte [8]. Cathodic charge transfer resistance is neglected, as the cathodic

### Chapter III. Analysis of the corrosion protection of copper by ALD alumina coatings and effect of deposited layer thickness

---

plateau in Figure III.1.B is assumed to be extrapolated to  $E_{\text{corr}}$ . Anodic mass transport is not considered here, as the studied frequencies were not low enough to reach a time constant related to anodic mass transport.

It should be mentioned that no separate time constant was assigned to the capacitance of a copper oxide layer in the equivalent circuit in Figure III.4.B. Nevertheless, depending on the value that will be obtained for the CPE in Figure III.4.B, the contribution of the oxide to the total capacitance can be neglected or taken into account. It should be reminded that the oxide layer contributes to anodic mass transport impedance at LF, due to  $\text{Cu}^+$  mass transport through such layer.

A Constant Phase Element ( $\text{CPE}_{\text{dl}}$ ) related to the double layer is used instead of the double layer capacitance ( $C_{\text{dl}}$ ) to account for non-ideal capacitive behaviour of the system. The CPE is representative of the distribution of time constants along or perpendicular to the surface of the electrode in electrochemical systems. Such distribution may be associated with surface heterogeneities, uneven distribution of current or potential due to the electrode geometry, porosity and non-uniform conductivity of the layers on the surface, which lead to distribution of reactivity [124]. The impedance of a CPE is defined as [125]:

$$Z_{\text{CPE}} = \frac{1}{Q(j\omega)^n} \quad \text{Eq. III.8}$$

where  $Q$  and  $n$  are independent of frequency.  $Q$  has units of  $\text{F.cm}^{-2}.\text{s}^{(n-1)}$ , which is equal to the unit of capacity when  $n=1$ . The factor  $n$  is the CPE power and its deviation from unity is an indication of deviation of  $Q$  from ideal capacitance. Whenever  $n = 0.5$ , CPE should be substituted with a Warburg impedance [126,127].

**Table III.2:** Results of fitting EIS data of Figure III.3 with E.C.1 (Figure III.4.B)

	$R_e / \Omega.\text{cm}^2$	$R_{\text{ct}}^2 / \Omega.\text{cm}^2$	$Q / \text{F.cm}^{-2}.\text{s}^{(n-1)}$	$n$	$C_{\text{eff}} / \text{F. cm}^{-2}$	$S / \Omega.\text{s}^{-0.5}.\text{cm}^2$ ( $Z_{\text{wc}} = \frac{S}{\sqrt{\frac{j\omega}{2}}}$ )
<b>Bare substrate</b>	11.09	$6.28 \times 10^5$	$2.03 \times 10^{-5}$	0.96	$1.48 \times 10^{-5}$	$6.69 \times 10^3$

## Chapter III. Analysis of the corrosion protection of copper by ALD alumina coatings and effect of deposited layer thickness

---

The fitting results are compiled in Table III.2. Effective capacitance ( $C_{\text{eff}}$ ) is presented in addition to  $Q$  (obtained directly from the fitting), assuming a surface contribution of time constants and using Brug formula [128]:

$$C = Q^{\frac{1}{n}} \left( \frac{R_e \times R_{ct}}{R_e + R_{ct}} \right)^{\frac{1-n}{n}} \quad \text{Eq. III.9}$$

which can be simplified to Eq. III.10 when  $R_e \ll R_{ct}$ :

$$C = Q^{\frac{1}{n}} (R_e)^{\frac{1-n}{n}} \quad \text{Eq. III.10}$$

The effective capacity obtained for the bare substrate ( $15 \mu\text{F}\cdot\text{cm}^{-2}$ ) is in the range of typical values for a double layer capacitance ( $10\text{-}100 \mu\text{F}\cdot\text{cm}^{-2}$ ), which means that the contribution of any possible oxide layer to the total capacitance can be neglected and the CPE in Figure III.4.B is related to the double layer capacitance.

$R_e$  is the ohmic or uncompensated resistance of the electrolyte between the working and the reference electrode [129]. The value obtained for  $R_e$  (Table III.2) is almost constant in different polarization tests (with the same electrolyte and cell geometry) in our study, which is expected. The relatively high value obtained for  $R_{ct}^a$  (charge transfer resistance at electrode/solution interface) is due to the low amount of oxygen in the electrolyte, which leads to lower corrosion of copper.

### III.3. Surface and electrochemical analysis of Cu coated with ALD $\text{Al}_2\text{O}_3$

#### III.3.1. Time-of-Flight Secondary Ion Mass Spectrometry

Figure III.5 shows the ToF-SIMS negative ion depth profiles of the 10, 20 and 50 nm ALD alumina coated copper substrates. The selected ions were  $^{12}\text{C}^-$ ,  $^{17}\text{OH}^-$ ,  $^{18}\text{O}^-$ ,  $^{31}\text{P}^-$ ,  $^{32}\text{S}^-$ ,  $^{35}\text{Cl}^-$ ,  $^{59}\text{AlO}_2^-$ ,  $^{95}\text{CuO}_2^-$  and  $^{126}\text{Cu}_2^-$ .  $^{18}\text{O}^-$  is the naturally occurring oxygen isotope recorded since the  $^{16}\text{O}^-$  signal was close to saturation. The ion intensities are presented in

### Chapter III. Analysis of the corrosion protection of copper by ALD alumina coatings and effect of deposited layer thickness

---

logarithmic scale in order to emphasize the low intensity signals, and plotted versus  $\text{Cs}^+$  sputtering time.

Three regions (marked) can be easily distinguished: the coating region, the substrate region and the coating/substrate interfacial region. The coating region is characterized by an intensity plateau of the  $^{18}\text{O}^-$  and  $\text{AlO}_2^-$  ions characteristic of the deposited material. The identical plateau intensities of these ions for the different coatings confirm the growth of films with similar and homogenous bulk stoichiometry and with no in-depth variation, as already observed for ALD alumina on copper at lower deposition temperatures (100-200°C) [71,72] and on other substrates [60,61,118].

The  $\text{Cu}_2^-$  ion is the most representative of the metallic substrate. Its identical intensity in the bulk substrate region for all samples is indicative of the excellent reproducibility of the selected ToF-SIMS analytical conditions. The entry in the substrate bulk region is where the  $\text{Cu}_2^-$  ion starts to have a constant intensity, at ~105, ~225 and ~610 s of sputtering time for the 10, 20 and 50 nm specimens, respectively. The increase of the coating sputtering time is expected from the increase of the film thickness. Calculated sputtering rate yields values of 0.095, 0.088 and 0.081  $\text{nm}\cdot\text{s}^{-1}$  using the measured film thicknesses of 10, 19.9 and 49.5 nm, respectively. Possibly, the lower sputtering rate obtained on thicker films results from the densification of the deposited material that would increase with increasing deposition (*i.e.* annealing) time [61]. However, one cannot exclude charging effects increasing with the thickness of the deposited alumina insulator and decreasing the sputtering yield.

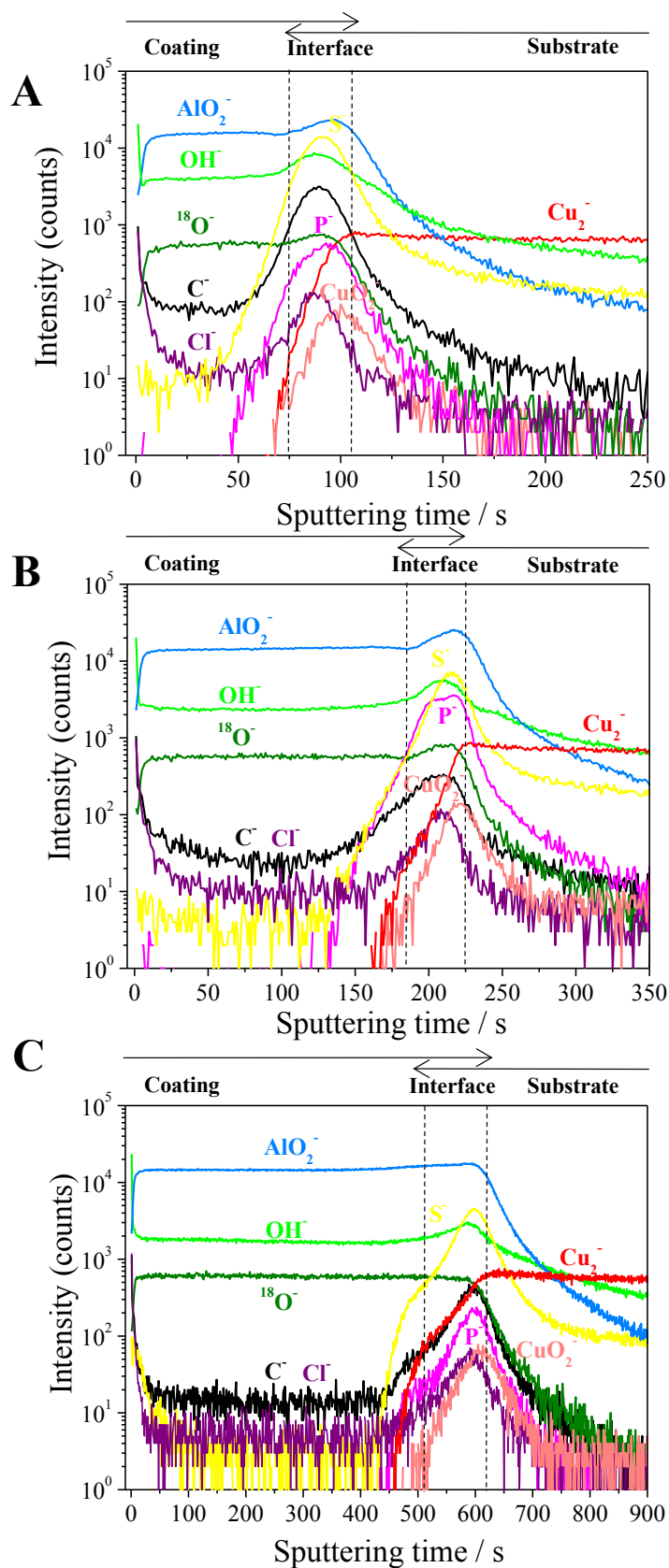


Figure III.5: ToF-SIMS negative ion depth profiles for 10 nm (A), 20 nm (B) and 50 nm (C) ALD alumina coatings prepared at 250°C on copper substrate

### Chapter III. Analysis of the corrosion protection of copper by ALD alumina coatings and effect of deposited layer thickness

---

The measured width of the coating/substrate interfacial region also increases with increasing film thickness. Indeed, the beginning of this region was taken where the coating ions deviate from plateau, *i.e.* at  $\sim 75$ ,  $\sim 185$  and  $\sim 510$  s of sputtering time which leads to measured width values of  $\sim 30$ ,  $\sim 40$  and  $\sim 100$  s of sputtering time for the 10, 20 and 50 nm films, respectively. Substrate roughness is known to cause shadowing effect in ToF-SIMS depth profiling due to ion beam geometry, which leads to apparent enlargement of the measured interfacial region compared to the actual width. The measured increasing width of the interfacial region is unexpected since the substrate preparation and initial deposition conditions were identical for all specimens. It is most likely only apparent and possibly results from the variation of the sputtering rate with increasing deposition time discussed above. The formation of a coating/substrate inter-diffusion layer of increasing width with increasing deposition time was not observed in TEM cross-sections for 100 nm ALD alumina deposited on copper at 100-200°C [71]. In the present case, it cannot be excluded for the films deposited at 250°C since segregation of sulphur is observed (see below) which denotes mass transport.

The  $\text{CuO}_2^-$  peak, the related  $\text{Cu}^-$  peak (not shown) and the absence of  $\text{Cu}_2^-$  peak in the interfacial region evidence the presence of copper oxide at the ALD alumina/copper substrate interface. The origin of this interfacial substrate oxide can be the presence of an air-formed native oxide and/or the spurious growth of a thermal oxide on the copper substrate. The native oxide would form on the substrate during the few minutes after the  $\text{H}_3\text{PO}_4$  pre-treatment and before introduction in the ALD reactor. The spurious thermal oxide would grow on the substrate surface exposed to the water vapour until full coverage by the alumina film and/or during thermal stabilization of the reactor at 250°C before deposition begins. This finding of a substrate oxide at the interface between ALD coating and the substrate is in agreement with previous data for alumina and other oxides on stainless steel and low alloy steel substrates [60–63,73,118,120,130]. On copper, interfacial copper oxide was not reported from AES depth profile and low resolution TEM cross-section measurements of 100 nm ALD alumina deposited at 100-200°C [71,72]. However, AES poorly discriminates Cu(I) oxide from Cu metal and TEM may require high resolution if copper oxide forms a possibly discontinuous layer only a few nanometres thick. Our ToF-SIMS data show a much lower, by more than 2 orders of

### Chapter III. Analysis of the corrosion protection of copper by ALD alumina coatings and effect of deposited layer thickness

---

magnitude, intensity of the  $\text{CuO}_2^-$  peak compared to the  $\text{AlO}_2^-$  peak, which suggests that copper oxide, observed here for the first time at the ALD alumina/copper metal interface, must be present in quite low concentration (less than 1 equivalent monolayer) and likely forms a discontinuous layer.

All  $\text{OH}^-$  ion profiles (highlighted in Figure III.6.A) show a maximum at the extreme surface of the coatings, which is related to hydroxylation of alumina in ambient conditions [131]. In the bulk coating regions, the lower  $\text{OH}^-$  signal is indicative of the residual hydroxyl contamination originating from the water precursor due to incomplete surface reactions. The existence of a plateau in the  $\text{OH}^-$  ion intensity in the bulk of the coating indicates homogeneous in-depth residual hydroxyl contamination before reaching the interface. Figure III.6.A clearly shows that the intensity of the plateau decreases with increasing thickness of the coating. The incomplete surface reactions responsible for the hydroxyl contamination may be partly completed during the subsequent ALD cycles. Therefore, for the thicker coatings that require a longer deposition time, there would be more time to complete the reactions. The lower hydroxyl contamination level seems to lead to a denser coating structure, as suggested by the increase of its sputtering time discussed above. At the interface, all  $\text{OH}^-$  ion profiles show a peak, which is consistent with hydroxylation of the surface native oxide on the substrate, if present, prior to deposition or in the beginning of the ALD process. Like already discussed [118], this peak may also be indicative of less effective hydroxyl removal during the initial cycles of the ALD growth, in which case the decreasing intensity of the peaks with increasing deposition time is also consistent with completion of the surface reactions for the first deposited alumina layers and related densification during the further growth of the coating. Another explanation for the variation of the OH contamination both in the bulk of the alumina coating and at the interface with the substrate is that hydroxyl groups may arise from water uptake during sample storage in air after the film growth. If so, the higher intensities measured for thinner films would indicate higher porosity, as confirmed by the electrochemical results presented hereafter. These two explanations, reaction completion during growth and subsequent water uptake, do not contradict each other and may both take place and lead to the observed variation of the OH residual contamination level. Correlation between the OH residual level and porosity of the

### Chapter III. Analysis of the corrosion protection of copper by ALD alumina coatings and effect of deposited layer thickness

coating has been proposed in previous studies on other substrates [60,121]. The present data also point out a correlation between OH residual level and densification of the coating as revealed by the variation of sputtering rate.

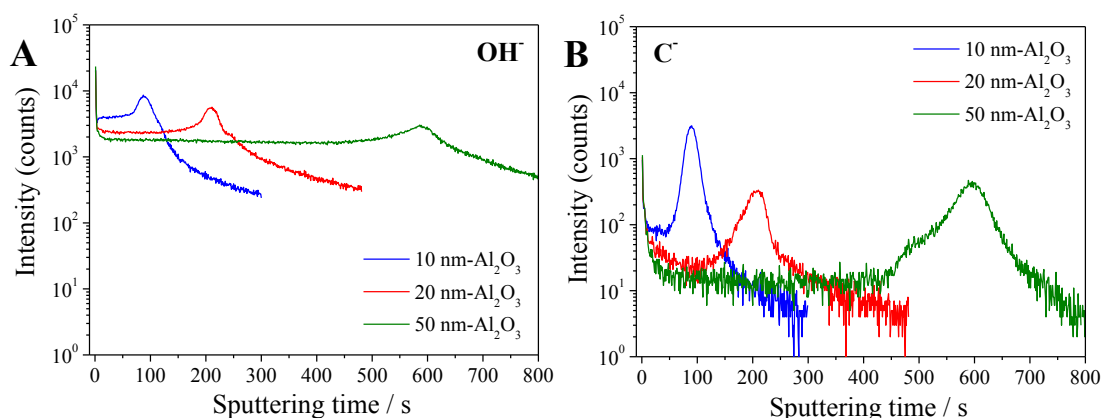


**Figure III.6:** ToF-SIMS OH<sup>-</sup> (A) and C<sup>-</sup> (B) ion depth profiles for 10 nm, 20 nm and 50 nm ALD alumina coatings

Likewise, the presence of a peak in C<sup>-</sup> ion profiles (highlighted in Figure III.6.B) at the extreme coating surface is assigned to hydrocarbon contamination from the ambient, as verified by the intensity decrease within a few seconds of sputtering. Carbon contamination at the extreme surface of ALD alumina coatings was previously observed by XPS [61] and AES [71,72]. In the bulk coating regions, the lower intensities of these ions are indicative of the presence of unreacted fragments of the TMA precursor trapped inside the films, as observed previously [60,61,71,72,118]. One notices that this carbon contamination from the precursor also decreases in the bulk coatings with increasing coating thickness, *i.e.* with increasing deposition time. As for the OH contamination, this can be an effect of more effective reaction completion during the longer deposition time on the removal of the precursor fragments, or of the decreasing porosity of the coating. At the interfaces, the amount of carbon contamination is larger than in the bulk coatings, which is assigned to organic contamination present on the substrate before deposition and/or, less effective removal of the organic fragments of TMA in the initial stages of deposition.

## Chapter III. Analysis of the corrosion protection of copper by ALD alumina coatings and effect of deposited layer thickness

One notices also the presence of other contaminants (Figure III.7). The detection of Cl<sup>-</sup> ions in the bulk coatings may be due to trace chlorine contamination of the TMA precursor, as already discussed for alumina coatings [63,118] and shown to be below the detection limit of XPS [61]. On the extreme surface and at the interface, the Cl<sup>-</sup> ions may come from exposure to the ambient before and after the deposition of the coating. The Cl<sup>-</sup> peak at the interface decreases slightly with increasing coating thickness. As a result of the sensitivity of copper to sulphur, this contamination is observed in the bulk substrate regions. The sulphur peak observed at the substrate surface below the coating is assigned to sulphur segregation from the bulk substrate during the thermal ALD process, not excluding possible trace contamination after surface preparation. Like Cl<sup>-</sup>, S<sup>-</sup> ion peak on the interface decreases with coating thickness increase (Figure III.7). Electropolishing of the substrate in H<sub>3</sub>PO<sub>4</sub> and the H<sub>3</sub>PO<sub>4</sub> pre-treatment before ALD deposition are most likely the origin of the presence of phosphorus at the coating/substrate interface (Figure III.5).

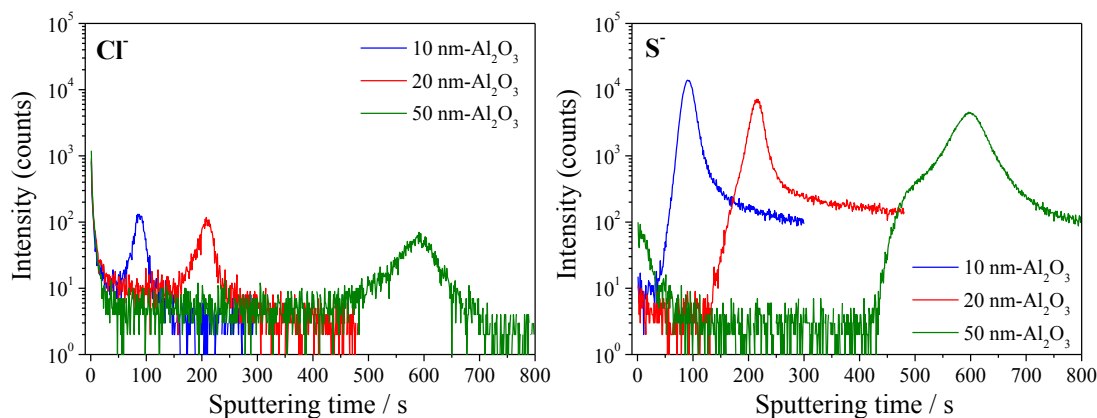


**Figure III.7:** ToF-SIMS Cl<sup>-</sup> and S<sup>-</sup> ion depth profiles for 10 nm, 20 nm and 50 nm ALD alumina coatings

### III.3.2. Atomic Force Microscopy

Figure III.8 (A-C) shows AFM topographic images of the 10, 20 and 50 nm coated substrates. The rms roughness values (ranging between 2 and 8 nm over  $1 \times 1 \mu\text{m}^2$ ) for

### Chapter III. Analysis of the corrosion protection of copper by ALD alumina coatings and effect of deposited layer thickness

---

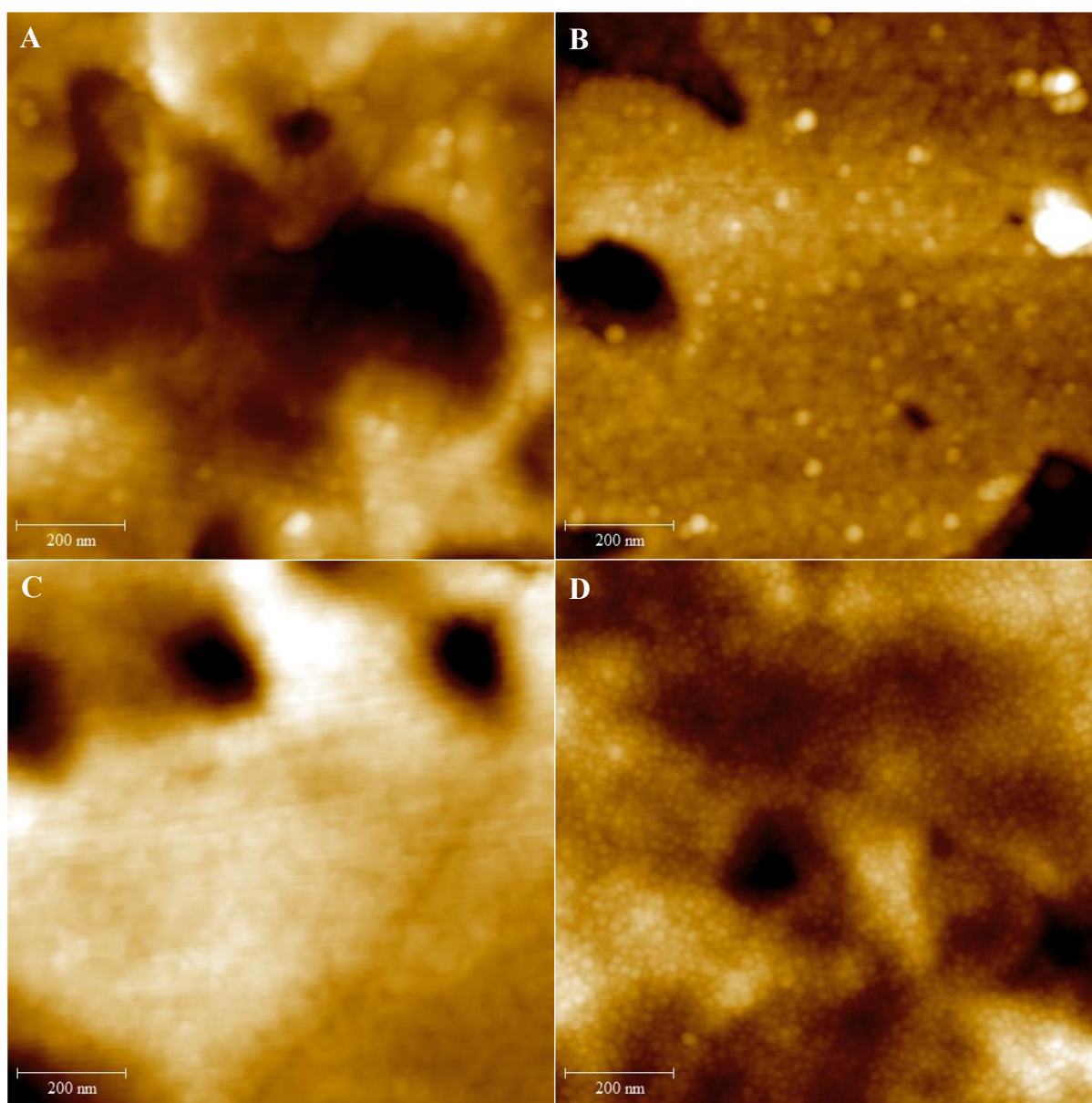
the coated samples are close to the value ( $\sim 6$  nm) for the bare substrate, which is consistent with homogeneous nucleation of the alumina coatings and homogeneous coverage of the Cu substrate and confirms the expected conformality of the ALD in agreement with previous findings [70]. Some of the observed depressions exceed in depth the coating thickness, implying that they originate from the substrate topography and not from a discontinuity of the coatings. In other words, the observed surface morphology of the coated samples is mostly governed by the Cu substrate. A granular-like morphology is seen in the images in the flatter substrate areas, which can be assigned to the morphology of the alumina film possibly replicating that of the substrate. The grains, or more strictly speaking the nodules since ALD alumina grown at  $250^\circ\text{C}$  has an amorphous structure [42], have lateral dimensions measured by AFM of about  $40 \pm 8$  nm in average. The depth measured between adjacent nodules, *i.e.* at internodular sites, is of the order of  $0.7 \pm 0.3$  nm, which is markedly lower than the coating thickness for all specimens. This is consistent with full substrate coverage by the coating, however with the presence of internodular sites where two adjacent nodules have grown into contact with each other. These sites may be potential locations for channel defects connecting the substrate to the environment.

Figure III.8.D shows the surface morphology of the 50 nm coated substrate after the electrochemical EIS and LSV measurements reported below. The rms roughness value ( $\sim 6$  nm over  $1 \times 1 \mu\text{m}^2$ ) remains similar to that prior to the electrochemical measurements. The surface morphology observed at higher magnification on the flat areas of the substrate is essentially similar to that observed before electrochemical analysis, however with slightly different dimensions. The nodules have a lateral size of  $20 \pm 5$  nm and the depth at intergranular sites is  $1.3 \pm 0.7$  nm. The smaller nodules suggest that corrosion products of copper may possibly accumulate at the interface between the coating and the substrate or redeposit at the coating extreme surface. However, ToF-SIMS depth profiling allows excluding these possibilities. Another possible explanation for the observed changes is the dissolution of ALD alumina coating, like previously observed upon immersion at OCP in neutral NaCl solution of coated low alloy steel samples [118] and in hot water on copper [70]. In the present case, an inhomogeneous dissolution of the coating at the nanometre scale of the nodules would

### Chapter III. Analysis of the corrosion protection of copper by ALD alumina coatings and effect of deposited layer thickness

---

lead to the decrease of their lateral dimension and to the increase of the depth measured at the jointing sites, if the internodular corrosion proceeds faster. From ToF-SIMS depth profiling, dissolution (*i.e* thickness decrease) is confirmed after immersion at OCP for timespans of several hours (see Chapter VI) but not after the LSV and EIS measurements reported below, possibly owing to their shorter immersion timespan. However, the AFM data indicate significant variation only of the lateral dimensions of the grains which is not detectable by ToF-SIMS.



**Figure III.8:** Topographical AFM images ( $1 \times 1 \mu\text{m}^2$ ) of ALD alumina coated Cu substrates: (A) pristine 10 nm sample, z range = 50 nm, (B) pristine 20 nm sample, z range = 20 nm, (C) pristine 50 nm sample, z range = 20 nm and (D) 50 nm sample after LSV test, z range = 35 nm

### III.3.3. Linear Sweep Voltammetry

LSV polarization curves for coated (and bare) substrates are presented in Figure III.9. For the coated specimens, a corrosion mechanism similar to that of the bare substrate is suggested as no marked change is evident in the shape of polarization curve. This is in agreement with the fact that the coatings are electrochemically inactive and the electrochemical reactions of the coated specimens take place only at the bottom of channel defects of the coating that connect the electrolyte to the substrate, as previously concluded for other substrates [60,61]. Considerably lower current observed for the coated samples in both cathodic and anodic parts, indicates good sealing of the substrate.

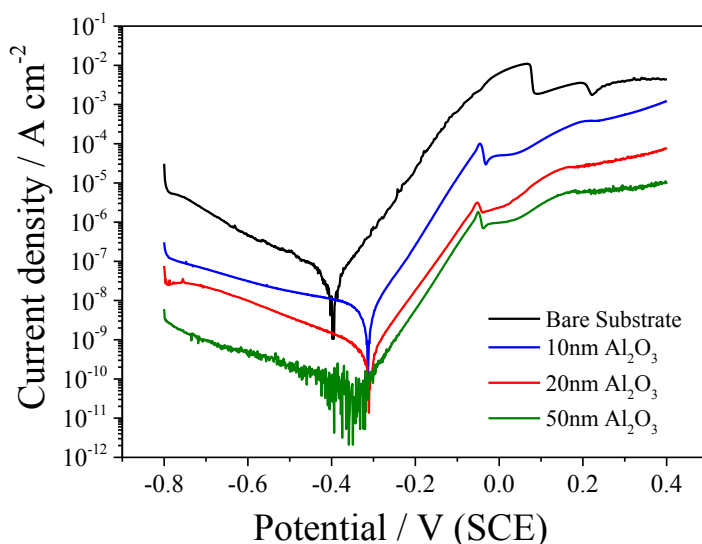


**Figure III.9:** LSV polarization curves for the bare and ALD alumina coated Cu substrates in 0.5 M NaCl under argon bubbling (pH = 6), swept from -0.8 V/SCE (scan rate: 1 mV.s<sup>-1</sup>)

**Table III.3:** LSV parameters related to Figure III.9

	$E_{corr} / V$ (SCE)	$i_a$ (at $E = -0.2$ V/SCE) / $A.cm^{-2}$	$R_p /$ $\Omega.cm^2$	$b_a /$ $V.dec^{-1}$	$b_c /$ $V.dec^{-1}$
<b>Bare substrate</b>	-0.395	$2.04 \times 10^{-5}$	$5.22 \times 10^5$	0.065	-0.190
<b>Al<sub>2</sub>O<sub>3</sub> 10nm</b>	-0.313	$2.49 \times 10^{-7}$	$3.54 \times 10^6$	0.064	-0.380
<b>Al<sub>2</sub>O<sub>3</sub> 20nm</b>	-0.311	$1.69 \times 10^{-8}$	$3.77 \times 10^7$	0.065	-0.235
<b>Al<sub>2</sub>O<sub>3</sub> 50nm</b>	-0.320	$5.40 \times 10^{-9}$	$8.7 \times 10^8$	0.064	-0.330

### Chapter III. Analysis of the corrosion protection of copper by ALD alumina coatings and effect of deposited layer thickness

---

The corrosion potential for all coated samples is shifted anodically in comparison with the bare substrate (Table III.3), leading to the enlargement of the cathodic polarization range. Modification of the reactive uncoated substrate for the coated specimens is one possible reason for this ennoblement, like reported in previous studies [61,62]. In the present case, aging of the native oxide film freshly formed prior to deposition and/or by spurious thermal growth in the initial stages of deposition (as discussed in section III.3.1) could increase its resistance to cathodic reduction in the conditions of the LSV test (starting LSV from a cathodic potential) and it is proposed to be the cause for this anodic shift. The higher Tafel slopes (in absolute value) of the cathodic branches for the coated samples can be similarly explained by the copper oxide remaining at the bottom of the channel defects (Table III.3), promoting oxygen reduction as will be discussed in Chapter IV.

The shift to lower potential (-0.05 V instead of 0.07 V) of the anodic peak related to the formation and dissolution of CuCl for the coated samples could be an effect of hindered mass transport in the channel defects from the substrate to the electrolyte, leading to earlier establishment of maximum surface coverage of CuCl at the bottom of the defects. However, the remaining copper oxide could also contribute to faster surface saturation, as discussed in section III.2.1.

Coating porosity was used as a parameter for evaluation of the coating performance [132,133]. As a consequence of electrochemical activity of the substrate only, porosity values were defined as the surface fraction of the uncoated substrate exposed to the electrolyte *via* permeable channel defects in the coating. Here, evaluation of porosity was based on both LSV and EIS data. Porosity values were quantified using the ratio of the polarization resistance of the bare substrate  $R_p^0$  to that of the coated substrate  $R_p$  and taking into account the difference in corrosion potential for the bare and coated substrates, using Eq. III.11, which was developed for thin films and ceramic films [132,134–136]:

$$P_{R_p} = \left( \frac{R_p^0}{R_p} \right) \times 10^{-\left( \frac{\Delta E_{corr}}{b_a} \right)} \times 100 \quad \text{Eq. III.11}$$

### Chapter III. Analysis of the corrosion protection of copper by ALD alumina coatings and effect of deposited layer thickness

In this expression,  $\Delta E_{\text{corr}}$  is the difference between the corrosion potential of the bare and coated substrates and  $b_a$  is the anodic Tafel slope of the bare substrate. The polarization resistance was obtained from the reciprocal of the slope of linear  $i$ - $E$  curve in the vicinity of the corrosion potential ( $E_{\text{corr}} \pm 20\text{mV}$ ) (Table III.3).

Similarly, the porosity was also obtained from the ratio of the anodic current of the coated substrate  $I_a$  to that of the bare substrate  $I_a^0$ , both measured at a fixed anodic potential ( $-0.2\text{V/SCE}$ ) (Table III.3), using Eq. III.12 [137]:

$$P_{i_a} = \frac{i_a}{i_a^0} \times 100 \quad \text{Eq. III.12}$$

This method takes advantage of ruling out the cathodic branch [84,85], thus avoiding the difficulties related to kinetics of the cathodic part and its high dependence on surface preparation and dissolved oxygen level in the electrolyte. In fact, as it will be discussed in more details in Chapter IV, the cathodic parts for the bare and coated substrates are not totally comparable, due to presence of more interfacial copper oxide on the substrate for coated samples. This difference in anodic part leads to different corrosion potential for bare and coated substrates, which effect is ruled out, using Eq. III.11 instead of direct comparison of  $R$  values.

The parameters related to polarization curves (Figure III.9) and resulting porosity values of bare and coated substrates are compiled in Table III.3 and Table III.4.

**Table III.4:** Average porosity values obtained from LSV and EIS for 2 series of coated samples

	$P_{i_a}$ %	$P_{R_p}$ %	$P_{R_{ct}}$ (E.C.2) %	$P_{R_{ct}}$ (E.C.3) %	$P_{C_{dl}}$ (E.C.3)%
<b>Bare substrate</b>	100	100	100	100	100
<b>Al<sub>2</sub>O<sub>3</sub> 10nm</b>	0.9 ± 0.3	0.64 ± 0.17	0.6 ± 0.01	0.64	0.36 ± 0.23
<b>Al<sub>2</sub>O<sub>3</sub> 20nm</b>	0.34 ± 0.26	0.18 ± 0.29	0.24 ± 0.2	0.13 ± 0.09	0.1
<b>Al<sub>2</sub>O<sub>3</sub> 50nm</b>	0.02 ± 0.005	0.03 ± 0.02	0.01 ± 0.005	0.02	0.02

Good agreement was obtained between  $P_{i_a}$  and  $P_{R_p}$  values, which confirms the reliability of both methods. According to the results in Table III.3, a reduction of anodic current densities (and an increase of polarization resistances) reaching four orders of magnitude is achieved for the coated substrate. The coating sealing performance (porosity decrease) increases with increasing coating thickness to 50 nm (Table III.4).

### III.3.4. Electrochemical Impedance Spectroscopy

Figure III.10 shows the EIS Bode plots for the coated (and bare) substrates at OCP. Coated samples show considerably higher global impedance in comparison with the bare substrate. The much wider capacitive frequency region with phase angles equal to  $90^\circ$  observed for the coated substrates is characteristic of high performance and good quality of the coatings [42].

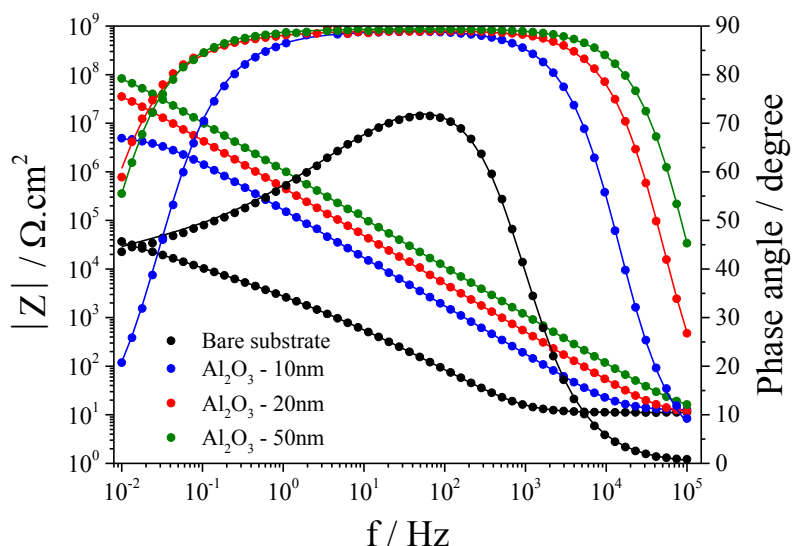


**Figure III.10:** EIS Bode plots for the bare and ALD alumina coated copper substrates in 0.5 M NaCl under argon bubbling (pH = 6) at OCP. Points and lines correspond to measured and fitted data, respectively

The equivalent circuit shown in Figure III.11.A is a typical model used for coated samples in the literature [122,129,138,139].  $\text{CPE}_{\text{coating}}$  is the constant phase element

### Chapter III. Analysis of the corrosion protection of copper by ALD alumina coatings and effect of deposited layer thickness

related to the coating and  $R_{pore}$  is the resistance of the electrolyte within the pores of the coating. The impedance at the interface localized at the end of the pores is a parallel combination of  $Z_f$  and  $CPE_{dl}$  as discussed before. Therefore, for the Cu substrate in the present study, replacing the equivalent circuit related to the bare substrate (E.C.1), shown in Figure III.4.B, at the end of the pores in Figure III.11.A would lead to the circuit model shown in Figure III.11.B. However, for the present coatings, only one time constant can be identified in the Bode plot. More clearly, only one tangent line is identified in a wide frequency range, with a slope of -0.99 indicating a strong capacitive response in a plot of logarithm of the imaginary part of the impedance versus the logarithm of the frequency (Figure III.12).

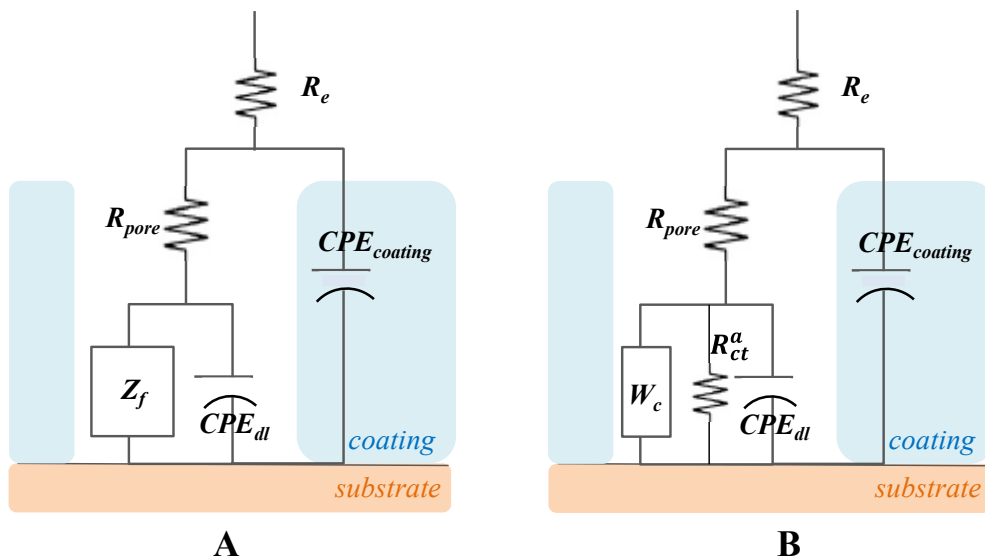


**Figure III.11:** A: Typical equivalent circuit used for coated electrodes. B: Equivalent circuit model adopted for coated Cu substrate for the present study (E.C.3)

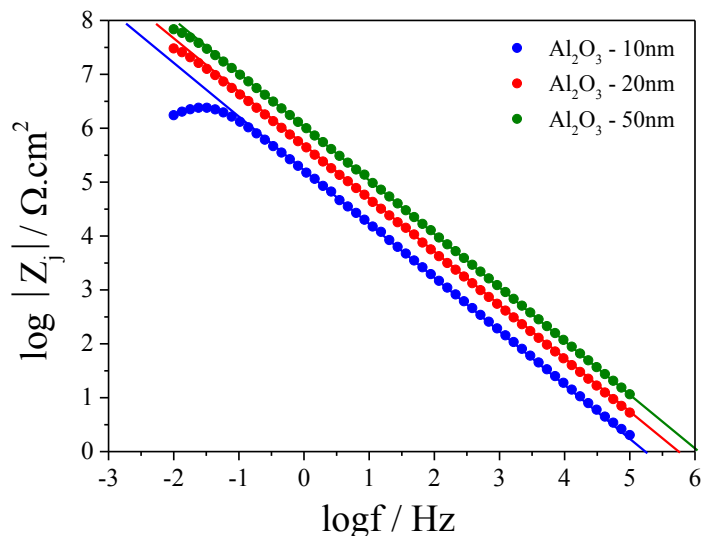


**Figure III.12:** Logarithm of the imaginary part of the impedance as a function of logarithm of frequency for coated substrates

The representation shown in Figure III.12 permits excluding the influence of the electrolyte resistance at high frequency (HF) and obtaining the exponent of the constant phase element (n) directly when the impedance behaviour deviates from purely capacitive. Doing so, n can be obtained graphically from the slope of  $\log |Z_j|$  vs  $\log f$  at high frequency [77].

The absence of two distinct time constants related to the capacitances of the bare substrate and the coating could be due to different reasons including: dominance of one time constant over the other one, exclusion of the frequency needed to observe one time constant from the measured frequency range and finally overlap (merging) of time constants. According to Walter [138] and Dyer [140], the RC relaxation times should differ by at least  $25\times$  to be easily separable by electrochemical measurements; otherwise their interaction with each other makes their differentiation difficult. Thus, it is supposed that the reason for not seeing two time constants in the present study is their overlap.

Regarding the absence of two distinguishable time constants for the coated substrates, in a first approach the EIS results were fitted with the same equivalent circuit used for the bare substrate. In this case,  $R_{ct}^a$  includes  $R_{\text{pore}}$  also [61] and CPE is a parallel combination

### Chapter III. Analysis of the corrosion protection of copper by ALD alumina coatings and effect of deposited layer thickness

---

of the double layer and the coating capacitances as shown in Figure III.13 (E.C.2). The fitting results with E.C.2 are compiled in Table III.5.

For theoretically perfect coatings without pores or channel defects, the capacitance values are obtained using Eq. III.13, valid for a flat parallel capacitor:

$$C = \frac{\epsilon\epsilon_0 A}{d} \quad \text{Eq. III.13}$$

where  $d$  is the coating thickness,  $A$  the coated surface area,  $\epsilon$  the ALD alumina dielectric constant ( $\epsilon = 7.6-8.4$  [58,141]), and  $\epsilon_0$  represents the vacuum permittivity ( $\epsilon_0 = 8.85 \times 10^{-14} \text{ F.cm}^{-1}$ ). Effective capacitance values obtained for the coated samples using Eq. III.9 [60–62,118,120,130,142] and fitting results (Table III.5) are very close to the theoretical  $C$  values for perfect coatings. This means that the CPE values obtained from fitting the EIS results with the chosen equivalent circuit are meaningful and correspond to coating capacitance due to its dominance in a parallel combination with  $C_{dl}$ , in agreement with the low porosity values obtained from LSV analysis (Table III.4). It should be mentioned that the calculated theoretical capacitance values are estimated values due to the uncertainty in the value of the dielectric constant for each coating. It is also worthy to mention that due to the fact that  $n \approx 1$  (Table III.5) for the coated samples, the effective capacitance can be assumed equal to the constant phase element ( $C_{\text{eff}} \approx Q$ ), and that is why  $C_{\text{th}}$  and  $Q$  show very close values in Table III.5.

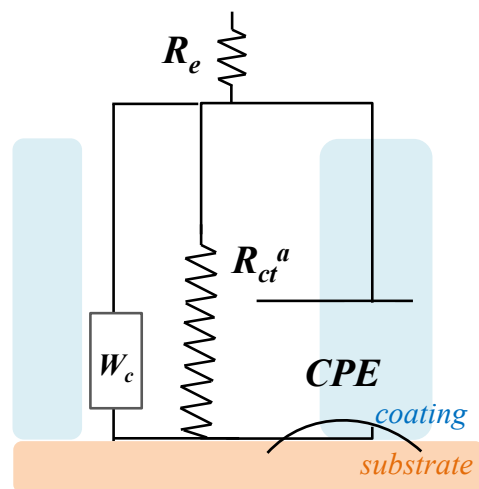


Figure III.13: Adaptation of E.C.1 for coated substrate (E.C.2)

Table III.5: EIS data and results related to Figure III.10 fitted to E.C.2 (Figure III.13)

	$R_e / \Omega \cdot \text{cm}^2$	$R_{ct}^a / \Omega \cdot \text{cm}^2$	$Q / \text{F} \cdot \text{cm}^{-2} \cdot \text{s}^{(\alpha-1)}$	$n$	$C_{\text{eff}} / \text{F} \cdot \text{cm}^{-2}$	$C_{\text{th}} / \text{F} \cdot \text{cm}^{-2}$	$S / \Omega \cdot \text{s}^{-0.5} \cdot \text{cm}^2$ ( $Z_W = \frac{S}{\sqrt{j\omega}}$ )
<b>Bare substrate</b>	11.09	$6.28 \times 10^5$	$2.03 \times 10^{-5}$	0.96	$1.48 \times 10^{-5}$		$6.69 \times 10^3$
<b>Al<sub>2</sub>O<sub>3</sub> 10nm</b>	12.50	$5.51 \times 10^6$	$9.61 \times 10^{-7}$	0.99	$8.75 \times 10^{-7}$	$7.08 \times 10^{-7}$	$1.01 \times 10^7$
<b>Al<sub>2</sub>O<sub>3</sub> 20nm</b>	10.36	$9.47 \times 10^7$	$3.38 \times 10^{-7}$	0.99	$3.02 \times 10^{-7}$	$3.54 \times 10^{-7}$	$4.04 \times 10^7$
<b>Al<sub>2</sub>O<sub>3</sub> 50nm</b>	11.33	$1.60 \times 10^8$	$1.47 \times 10^{-7}$	0.99	$1.39 \times 10^{-7}$	$1.42 \times 10^{-7}$	$7.68 \times 10^7$

### Chapter III. Analysis of the corrosion protection of copper by ALD alumina coatings and effect of deposited layer thickness

---

Table III.5 shows that resistance values are considerably higher for the coated substrates and increase with increasing coating thickness, in agreement with polarization results. Assuming a pure kinetic control in the anodic part, the anodic charge transfer resistance can be also obtained from Eq. III.14 [79] and using LSV results:

$$R_{ct}^a = \frac{b_a}{2.303 \times i_{corr}} \quad \text{Eq. III.14}$$

$i_{corr}$  was graphically deduced at the intersection of the tangent line to the anodic branch of logarithmic  $i$ - $E$  curve with the vertical line corresponding to  $E_{corr}$ . The values are compiled in Table III.6. Good agreement is observed between the  $R_{ct}^a$  values obtained from EIS (Table III.5) and from LSV and using Eq. III.14 (Table III.6). Slight deviation between these values should be related to the uncertainty in measurement of corrosion current, in addition to not being in static conditions ( $1 \text{ mV.s}^{-1}$  scan rate) in the LSV tests.

**Table III.6:** Anodic charge transfer (calculated from Eq. III.14), corrosion current and anodic Tafel slopes for coated samples

	$i_{corr} / \text{A.cm}^{-2}$	$R_{ct}^a / \Omega.\text{cm}^2$	$b_a / \text{V.dec}^{-1}$
<b>Bare substrate</b>	$2.80 \times 10^{-8}$	$1.02 \times 10^6$	0.065
<b>Al<sub>2</sub>O<sub>3</sub> 10nm</b>	$3.50 \times 10^{-9}$	$7.94 \times 10^6$	0.064
<b>Al<sub>2</sub>O<sub>3</sub> 20nm</b>	$3.65 \times 10^{-10}$	$7.73 \times 10^7$	0.065
<b>Al<sub>2</sub>O<sub>3</sub> 50nm</b>	$8.00 \times 10^{-11}$	$3.47 \times 10^8$	0.064

The Warburg coefficient ( $S$ ) is higher for coated substrates in comparison with the bare one (Table III.5). This is consistent with higher diffusion length in presence of coatings [143] and lower substrate area accessible for oxygen reduction.

The coating porosity values could be similarly calculated from the ratio of the charge transfer resistance of the bare ( $R_{ct}^0$ ) to that of the coated ( $R_{ct}$ ) substrates instead of  $R_p$  values in Eq. III.11, as given by Eq. III.15:

$$P_{R_{ct}} = \left( \frac{R_{ct}^0}{R_{ct}} \right) \times 10^{-\left( \frac{\Delta E_{corr}}{b_a} \right)} \times 100 \quad \text{Eq. III.15}$$

### Chapter III. Analysis of the corrosion protection of copper by ALD alumina coatings and effect of deposited layer thickness

---

The  $P_{R_{ct}}$  values are gathered in Table III.4.

Although the simple E.C.2 model used in Figure III.13 is properly enough to analyse the performance of the coatings, it would be still interesting to try to analyse the coating behaviour in more details. Therefore, in a second approach, EIS data for coated samples were fitted with E.C.3 (Figure III.11.B). The validity of the results was verified with comparison with results obtained using E.C.2. Fitting results for E.C.3 are compiled in Table III.7.

Using E.C.3,  $C_{dl}$  can be obtained and can be used similarly to obtain porosity by comparing its value to the value of  $C_{dl}$  for the bare substrate:

$$P_{C_{dl}} = \frac{C_{dl}}{C_{dl}^0} \times 100 \quad \text{Eq. III.16}$$

The  $P_{R_{ct}}$  and  $P_{C_{dl}}$  values obtained using E.C.3, are gathered in Table III.4.  $P_{R_{ct}}$  is calculated using Eq. III.15 as explained above, with the difference that here the resistance value used in Eq. III.15 ( $R_{total}$ ) is the sum of  $R_{pore}$  (electrolyte resistance in the pores of the coating) and  $R_{ct}^a$  (anodic charge transfer resistance of the substrate) [136]. As it can be noticed in Table III.4, P values obtained using E.C.2 and E.C.3 are very close to each other, implying that both models are valid.

Table III.7: EIS data and results related to Figure III.10 fitted to E.C.3 (Figure III.11.B)

	$R_e / \Omega.cm^2$	$R_{pore} / \Omega.cm^2$	$R_{ct}^a / \Omega.cm^2$	$R_{total} / \Omega.cm^2$	$Q_c / F.cm^{-2}.s^{(\alpha-1)}$	$n_c$	$C_{eff-c} / F.cm^{-2}$	$Q_{dl} / F.cm^{-2}.s^{(\alpha-1)}$	$n_{dl}$	$C_{eff-dl} / F.cm^{-2}$	$S / \Omega.s^{-0.5}.cm^2$ ( $Z_W = \frac{S}{\sqrt{\frac{j\omega}{2}}}$ )
Al <sub>2</sub> O <sub>3</sub> 10nm	12.50	2.04 × 10 <sup>6</sup>	3.29 × 10 <sup>6</sup>	5.33 × 10 <sup>6</sup>	9.64 × 10 <sup>-7</sup>	0.99	8.76 × 10 <sup>-7</sup>	5.00 × 10 <sup>-8</sup>	0.69	8.77 × 10 <sup>-8</sup>	1.87 × 10 <sup>7</sup>
Al <sub>2</sub> O <sub>3</sub> 20nm	10.39	4.98 × 10 <sup>6</sup>	7.67 × 10 <sup>7</sup>	8.15 × 10 <sup>7</sup>	3.34 × 10 <sup>-7</sup>	0.99	3.04 × 10 <sup>-7</sup>	9.17 × 10 <sup>-8</sup>	0.87	1.38 × 10 <sup>-8</sup>	7.41 × 10 <sup>7</sup>
Al <sub>2</sub> O <sub>3</sub> 50nm	11.33	1.36 × 10 <sup>7</sup>	1.35 × 10 <sup>8</sup>	1.49 × 10 <sup>8</sup>	1.47 × 10 <sup>-7</sup>	0.99	1.39 × 10 <sup>-7</sup>	6.82 × 10 <sup>-9</sup>	0.79	3.52 × 10 <sup>-9</sup>	2.64 × 10 <sup>9</sup>

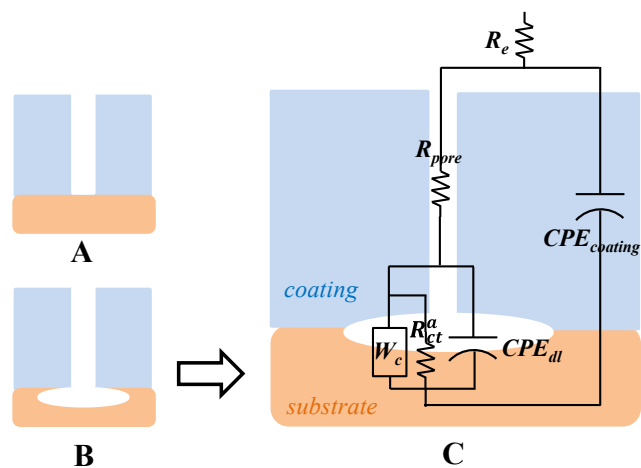


Figure III.14: Channel defects in a coating where: A: channel defect cross section area is equal to the wetted area on the substrate. B: where the wetted area is larger than the channel defect cross section area. C: adaptation of opening at the end of the channel defects in the present study

### Chapter III. Analysis of the corrosion protection of copper by ALD alumina coatings and effect of deposited layer thickness

---

$R_{\text{pore}}$  in E.C.3 is the resistance of the electrolyte in the pores/channel defects through the coating. In fact,  $C_c/R_{\text{pore}}$  in E.C.3 corresponds to the dielectric nature of the coating ( $C_c$ ) and its electric leakage by ionic conduction. Therefore,  $R_{\text{pore}}$  is a bulk property of the coating due to its defects. Assuming the same conductivity of the electrolyte in the bulk solution and in channel defects (pores) in the coating, the resistance of the electrolyte in the pores will be:

$$R_{\text{e-in pores}} = \frac{l}{A_p \times \kappa} = R_{\text{pore}} \quad \text{Eq. III.17}$$

in which  $l$  is the thickness of the coating,  $A_p$  is the total cross sectional (area) of the pathways and  $\kappa$  is the conductivity of the electrolyte. Calculating electrolyte resistance ( $R_{\text{et}}$ ) for a layer of the electrolyte that would occupy the same space (thickness of the coating and total area of the electrode) and dividing by the value obtained in Eq. III.17, leads to the fraction of the coating consisting of pathways filled by the electrolyte [144–146]. Armstrong *et al.* have used this idea to calculate the porosity of the coating [144]. Porosity values obtained in this way were more than  $10^5$  times lower [145] than the porosity values obtained by comparison of  $R_{\text{ct}}^0/R_{\text{ct}}$ ,  $C_{\text{dl}}/C_{\text{dl}}^0$  and  $I_{\text{corr}}/I_{\text{corr}}^0$  values, which are usually used in the literature for calculation of coating porosity. Therefore, the porosity values obtained by latter ratios were attributed to the wetted surface area of the metal under the coating, which is larger than the cross sectional area of the channels through the coating, as a result of penetration of electrolyte down in the channels and spreading as a thin layer between the coating and the metal as shown in Figure III.14 [144]. To sum up, it was differentiated between the porosity of the coating obtained from high frequency information and wetted area of the metal under the coating, obtained from low frequency information.

Similarly, in the present study, the porosities obtained using the definition of Armstrong are about one part in  $10^{11}$  ( $10^{-9}$  %), which is  $10^7$  times lower than the values obtained in Table III.4. Therefore, it is suggested that when the electrolyte penetrates the channels in the coating and reaches the metal/coating interface, the electrochemical reactions on the metal lead to delamination of the coating and/or trenching of the metal substrate under the coating.

### Chapter III. Analysis of the corrosion protection of copper by ALD alumina coatings and effect of deposited layer thickness

It should be mentioned that using the fitting results of E.C.3 (Table III.7) and calculating  $\tau_{\text{coating}}$  ( $\tau_{\text{coating}} = R_{\text{pore}} \times C_{\text{coating}}$ ) and  $\tau_{\text{substrate}}$  ( $\tau_{\text{substrate}} = R_{\text{ct}}^a \times C_{\text{dl}}$ ), the conditions discussed before for observing two distinct time constants are not met for any of the coating thicknesses, confirming our explanation above.

All porosity values obtained from LSV and EIS are presented together in Figure III.15.

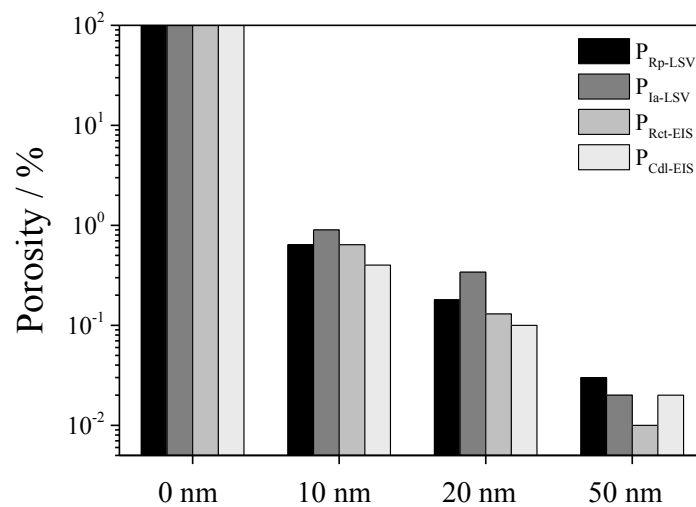


**Figure III.15:** Porosity values calculated from EIS and LSV results for ALD alumina coated Cu substrate

The good agreement between the values obtained from LSV and EIS data evidences proper analysis of LSV results for quantification of porosity in combination with an appropriate choice of the equivalent circuit for EIS data fitting. The porosity values obtained in this study for the 10 and 20 nm coatings are in good agreement with those recently reported for coatings of the same thicknesses deposited on copper at 150°C [72], showing excellent sealing properties of the ALD layer irrespective of the deposition temperature. The present study shows that increasing the deposited thickness to 50 nm decreases the porosity by nearly one order of magnitude. The porosity values for 20 and 50 nm coatings are equal to the values obtained with the same coatings on stainless steel substrate [60], showing that equivalent sealing properties are obtained on different substrates.

### **III.4. Conclusions**

Electrochemical and surface analytical methods were applied to investigate the corrosion protection provided to copper by the deposition of 10, 20 and 50 nm thick ALD alumina coatings at 250°C using trimethyl aluminium and water as precursors.

ToF-SIMS depth profiling allowed characterization of the composition of the bulk coating, as well as the interfacial and substrate regions. The alumina coatings have constant in-depth stoichiometry independent of the film thickness. Their bulk contains residual carbonaceous and hydroxyl fragments from partially unreacted precursors. The coating/substrate interface exhibits traces of copper oxide (formed in air prior to deposition and/or grown thermally in the initial stages of deposition) most likely forming a discontinuous layer. Phosphorus (from electropolishing and pre-treatment) and sulphur (segregating from bulk copper) contaminate the interface in addition to carbon and hydroxyls (from partially unreacted precursor fragments and/or ambient exposure). Increasing deposition time promotes removal of the contaminating precursor fragments by completing the reactions and possibly densifies the deposited alumina.

Electrochemical analysis in 0.5 M NaCl aqueous solution demonstrated considerable improvement of corrosion properties of the coated Cu substrates. The same shape of polarization curves measured by LSV for the bare and coated specimens confirmed corrosion of the substrate *via* residual pinholes and/or channel defects connecting the substrate to the electrolyte through the coating and possibly preferentially located at internodular sites of the coating. The decrease of the anodic current and increase of the polarization resistance reached 4 orders of magnitude for the 50 nm coating, restricting the uncoated surface fraction to ~0.01% and confirming densified ALD alumina as an excellent coating for corrosion protection of copper.

EIS analysis allowed adoption of an equivalent circuit model for the corrosion process at OCP and calculation of charge transfer resistance, total capacitance and Warburg impedance for the coatings. Using an equivalent circuit with separate time constants for the coating and the substrate, it was shown that the channel defect cross section area in the bulk of the coating is much lower than the channel defect opening at the interface

### **Chapter III. Analysis of the corrosion protection of copper by ALD alumina coatings and effect of deposited layer thickness**

---

between the substrate and the coating, where more electrolyte is penetrated. The excellent agreement between the coating porosity values (*i.e.* uncoated surface fraction) calculated from EIS and LSV using four methods validated the choice of the equivalent circuit model and confirmed EIS as a non-destructive *in situ* tool for the study of coating sealing properties.

AFM imaging showed the growth of conformal coatings with a granular-like morphology at the nanometre scale. Non homogenous nanometre scale dissolution of the coating is suggested by AFM after electrochemical analysis, pointing to a possibly limited lifetime of the alumina protection barrier in highly corrosive solution.



# **Chapter IV**

## **Effect of the interfacial native oxide layer on the corrosion of ALD alumina coated copper**

### **IV.1. Introduction**

The presence of an interfacial oxide layer at the substrate/coating interface and its properties may play a key role in the corrosion protection of the substrate coated by ultrathin ALD coatings. Sometimes the interfacial oxide can have a detrimental effect due to its dissolution under the coating at the end of channels, where the substrate is connected to the electrolyte. Díaz *et al.* reported that the presence of an unstable interfacial oxide on low alloy steel in chloride environment leads to its dissolution not only at the bottom of the channels, but also along the coating/substrate interface and causes interfacial voiding [120]. In another study of low alloy steel coated with ALD mixed oxide coatings, promotion of the growth of a less defective coating on a plasma pre-treated brushed substrate as a result of less carbon contamination and formation of an iron-rich duplex oxide layer was reported [130]. Härkönen *et al.* also reported interface-dependent properties of ALD and PEALD alumina coating deposited on steel. The best protective

## Chapter IV. Effect of the interfacial native oxide layer on the corrosion of ALD alumina coated copper

---

properties were achieved with coatings deposited on a clean uniform regrown oxide after plasma pre-treatment before coating deposition [121].

In the present study, as there was a time gap between preparation of the substrates and deposition of the coatings, due to the fact that the coatings were deposited in another laboratory than where the substrates were prepared, the presence of a native oxide layer on the samples was inevitable. In order to remove this native oxide, copper substrates were etched with 10wt.%  $\text{H}_3\text{PO}_4$  for 5 seconds, rinsed with ethanol, dried with compressed air and introduced in the reactor in less than 5 min (after the  $\text{H}_3\text{PO}_4$  pre-treatment), as discussed in Chapter II. This procedure was used by Shimizu *et al.* and was shown to remove the native oxide formed on the copper surface after polishing. Rf-GDOES profiles after this treatment showed an oxygen peak which was attributed to a probable presence of a very thin oxide, probably less than 1 nm [75]. This thin oxide, possibly discontinuous, was formed in the time gap between the pre-treatment and sample analysis by Rf-GDOES.

In this chapter, the effect of the presence of a native oxide at the interface between the coating and the substrate on corrosion protection of the copper by the coatings was studied using electrochemical techniques and ToF-SIMS. What makes this study unique in comparison with other studies [120,121,130] is the comparison of coated samples with two different bare substrates instead of only one bare substrate. To do so, four samples were prepared. Two bare copper samples were polished, electropolished and stored to be aged for 15 days in closed membrane boxes in a desiccator. Before performing the electrochemical tests after 15 days, one sample was pre-treated with  $\text{H}_3\text{PO}_4$  pre-treatment, and introduced in the electrochemical cell immediately, while the other was introduced in the electrochemical cell without any pre-treatment. These samples were labelled B-PT and B-NPT, respectively. Two other samples were prepared in a similar way and stored in membrane boxes, sent to Helsinki and coated 15 days after. The pre-treatment was done on one sample before coating deposition, while the other one was coated without any pre-treatment. The thickness of the deposited coating was 20 nm. These samples were labelled C-PT and C-NPT, respectively. Electrochemical tests were done on the coated samples after receiving them back.

## IV.2. Electrochemical analysis of bare substrates

### IV.2.1. Electrochemical Impedance Spectroscopy

Figure IV.1 shows the Bode plots for the B-PT and B-NPT samples.

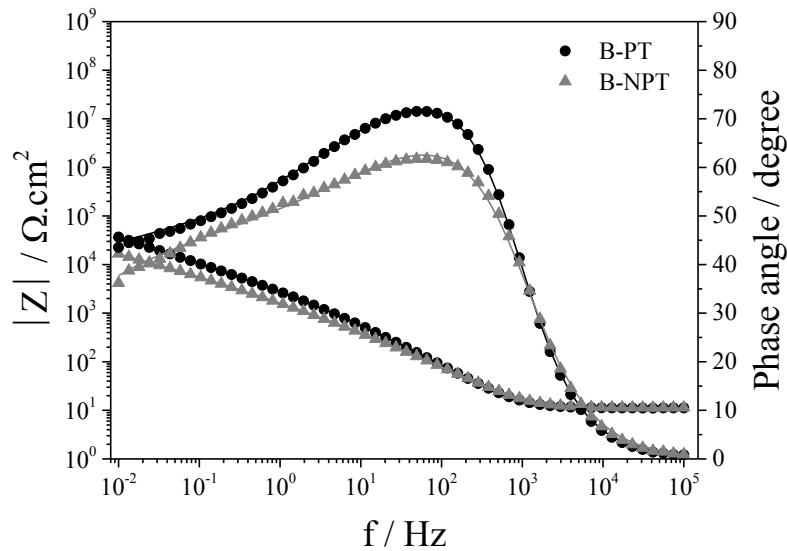


**Figure IV.1:** EIS Bode plots for the bare pre-treated and not pre-treated copper substrates in 0.5 M NaCl under argon bubbling (pH = 6) at OCP. Points and lines correspond to measured and fitted data, respectively

The Bode plots for these samples are very similar and the only difference observed is the phase angle and the resistance at low frequencies. Both samples were fitted with E.C.1 (Figure III.4.B) and the fitting parameters are presented in Table IV.1.

**Table IV.1:** EIS data and results related to B-PT and B-NPT fitted with E.C.1 (Figure III.4.B)

	$R_e / \Omega.cm^2$	$R_{ct}^a / \Omega.cm^2$	$Q / F.cm^{-2}.s^{(a-1)}$	$n$	$C_{eff} / F.cm^{-2}$	$S / \Omega.s^{-0.5}.cm^2$ ( $Z_w = \frac{S}{\sqrt{\frac{j\omega}{2}}}$ )
<b>B-PT</b>	11.09	$6.28 \times 10^5$	$2.03 \times 10^{-5}$	0.96	$1.48 \times 10^{-5}$	$6.69 \times 10^3$
<b>B-NPT</b>	11.18	$7.92 \times 10^4$	$2.48 \times 10^{-5}$	0.92	$1.23 \times 10^{-5}$	$3.52 \times 10^3$

## Chapter IV. Effect of the interfacial native oxide layer on the corrosion of ALD alumina coated copper

---

The most important difference here between B-PT and B-NPT is  $R_{ct}^a$ , which is about 10 times higher for B-PT. The reason for this difference will be discussed further on.

The  $C_{eff}$  values were calculated assuming a surface distribution of time constants and using Eq. III.9. A slight difference is observed for  $C_{eff}$  values between B-PT and B-NPT. As discussed in Chapter III, the capacitance value obtained in order of several tens of  $\mu F.cm^{-2}$  can be taken as the double layer capacitance. However, the contribution of a discontinuous copper oxide layer to the total capacitance cannot be excluded. In case of the oxide layer contributing to the total capacitance, the lower  $C_{eff}$  obtained for B-NPT is assigned to a larger contribution of the aged native oxide layer for B-NPT to the total capacitance or simply to a higher surface coverage by the oxide (reduction of  $C_{dl}$ ) on this sample. Even if the  $C_{eff}$  value would correspond to the capacitance of a thin continuous oxide layer, the lower  $C_{eff}$  value for B-NPT means a higher thickness of the oxide layer on this sample (Eq. III.13) in comparison with that of B-PT.

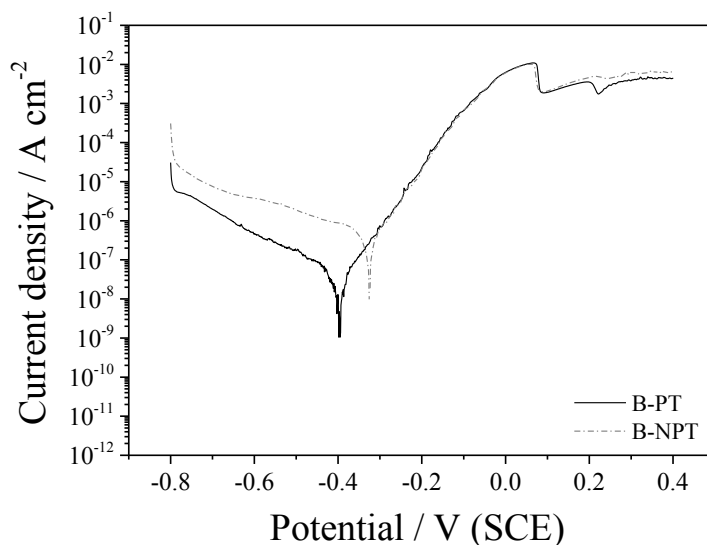
### IV.2.2. Linear Sweep Voltammetry

Figure IV.2 shows the polarization curves for the B-PT and B-NPT samples. Parameters and values related to polarization measurements are gathered in Table IV.2. According to the results presented in Table IV.2, B-PT sample shows a corrosion current and a polarization resistance almost one order of magnitude lower and higher, respectively, than B-NPT, in agreement with the EIS results. This difference in the corrosion behaviour of these two substrates is attributed to the difference in the native oxide layer on them in combination with the effect of low amount of dissolved oxygen in the electrolyte.

**Table IV.2:** LSV data and results related to Figure IV.2

	$E_{ocp} / V(SCE)$	$E_{corr} / V(SCE)$	$i_{corr} / A.cm^{-2}$	$b_a / V.dec^{-1}$	$b_c / V.dec^{-1}$	$R_p / Ohm.cm^{-2}$
<b>B-PT</b>	-0.312	-0.395	$2.80 \times 10^{-8}$	0.065	-0.190	$5.22 \times 10^5$
<b>B-NPT</b>	-0.284	-0.325	$2.13 \times 10^{-7}$	0.065	-0.306	$4.64 \times 10^4$

## Chapter IV. Effect of the interfacial native oxide layer on the corrosion of ALD alumina coated copper



**Figure IV.2:** LSV polarization curves for the bare pre-treated and not pre-treated copper in 0.5 M NaCl under argon bubbling (pH = 6), scan rate: 1 mV.s<sup>-1</sup>

As mentioned in Chapter III, the cathodic reaction is oxygen reduction near OCP and water reduction at lower potentials. Lower cathodic and corrosion currents in combination with lower cathodic Tafel slope for B-PT, as it will be discussed below, suggest lower oxygen reduction occurring on this sample. One also notices the shift of the corrosion potential to negative values for B-PT sample. As it will be discussed below, this is consistent with a surface oxide less resistant to cathodic reduction (more reducible) in the condition of the polarization test (starting from -0.8 V/SCE).

As mentioned in Chapter III, the copper oxide formed on the surface of a freshly polished sample at room temperature is supposed to be cuprous oxide [98,111], which can also be formed in the electrolyte according to Eq. III.5 due to the increase of OH<sup>-</sup> produced by the cathodic oxygen reduction. The semiconductive (p-type) nature of cuprous oxide is expected to inhibit the corrosion process when a fully covering oxide film is present, through which the ionic and electronic transport get limited. In the present study, due to the low amount of oxygen in the electrolyte and short time of immersion, the formation of a fully covering oxide film is likely not reached, preventing corrosion inhibition by a copper oxide film.

## Chapter IV. Effect of the interfacial native oxide layer on the corrosion of ALD alumina coated copper

---

In different studies done on the oxygen reduction on copper, the effect of copper oxide species on the oxygen reduction rate and mechanism was revealed [8,97,108–110]. According to King *et al.* [108], the rate of oxygen reduction is very sensitive to the nature of the electrode during potentiodynamic tests. Oxygen reduction happens on two types of surfaces with different reactivities. It is more catalysed on Cu(0)/Cu(I) sites than on only Cu(0) sites [8,108,109]. A catalytic surface involves Cu(I) species, which can stabilize as  $\text{Cu}(\text{OH})_{\text{ads}}$  and/or a submonolayer of  $\text{Cu}_2\text{O}$ . The formation of catalytic Cu(0)/Cu(I) sites (or  $\text{Cu}_2\text{O}$  submonolayer) is favoured by higher interfacial pH, as a result of oxygen reduction reaction in unbuffered solutions [8,108,109]. At larger cathodic overpotentials and/or with lower  $[\text{O}_2]$  the bare copper surface sites (Cu(0)) dominate. As the extent of surface coverage by catalytic species increases, the cathodic Tafel slope also changes [108]. The increase in Tafel slopes with higher  $[\text{O}_2]$  is due to the potential dependence of electron transfer reaction and the potential dependence of the number of catalytic Cu(I)/Cu(0) sites, whose formation is aided by higher interfacial pH produced at higher  $[\text{O}_2]$  [8]. On the other hand, oxygen reduction was proposed to be inhibited on the complete  $\text{Cu}_2\text{O}$  monolayer which is believed to form at higher anodic potentials [108,109]. The reason for the higher rate of oxygen reduction on Cu(I) surface was proposed to be uncertain [108]. Presence of copper in two oxidation states Cu(0) and Cu(I) was suggested for the possibility of electron relay between neighbouring copper sites of different valence and therefore the electron transfer to oxygen adsorbed on one or other of the sites [108]. Since the oxygen reduction appears to be catalysed up to the potential at which it is covered by a monolayer of  $\text{Cu}_2\text{O}$ , the catalytic sites may consist of adjacent Cu(0) and Cu(I) sites on the surface, rather than on top of the other [109]. Then the complete coverage by a  $\text{Cu}_2\text{O}$  monolayer inhibits oxygen reduction because of the absence of both Cu(0) and Cu(I) species on the surface [109].

In the present case, a possible explanation for higher cathodic currents for B-NPT can be higher surface coverage by catalytic Cu(0)/Cu(I) sites for this sample in comparison with B-PT, when the potential is switched to -0.8 V and shifted positive-going. Although the potential switch to -0.8 V may lead to partial reduction of copper oxide species on both B-PT and B-NPT, the oxide species may have higher coverage or be more resistant to reduction at lower potentials as a result of ageing. Therefore, more remaining Cu(I)/Cu(0)

## Chapter IV. Effect of the interfacial native oxide layer on the corrosion of ALD alumina coated copper

---

sites on B-NPT once the potential is switched to  $-0.8$  V contributes to higher oxygen reduction in cathodic part which leads to higher corrosion current at corrosion potential. Higher measured cathodic Tafel slope (Table IV.2) for B-NPT is in agreement with higher surface coverage of catalytic Cu(I)/Cu(0) sites as observed by King et al. [8,108,109].

Higher oxygen reduction on B-NPT means higher cathodic current, which at corrosion potential, contributes to higher corrosion current. Corrosion current and polarization resistance obtained for B-NPT are almost 10 times higher and lower than the ones obtained for B-PT (Table IV.2). The shift of the corrosion potential to negative values for B-PT sample is in agreement with lower amount of copper oxide species for this sample. As discussed above, the copper oxide freshly formed on B-PT may be less resistant to cathodic reduction when the potential is switched to  $-0.8$  V to be shifted positive-going. An initially lower amount of copper oxide on this sample, could lead to its final lower amount at  $E_{\text{corr}}$  also.

It should be mentioned that the lower cathodic current and the resulting lower corrosion current and higher polarization resistance on a pre-treated substrate can only be observed with low amount of oxygen in the electrolyte. In presence of higher amount of oxygen (lower rate of argon bubbling) in the electrolyte, cathodic current is higher and is the same as for a freshly polished substrate without pre-treatment (Figure IV.3). This reveals the important role of dissolved oxygen, in resulting different cathodic behaviours for B-PT and B-NPT. It is proposed that both B-PT and B-NPT have submonolayers of oxide on their surface (as will be discussed in section IV.3.1 using ToF-SIMS data) which may not increase to a complete monolayer in an electrolyte with the bulk pH of 6 and low amount of dissolved oxygen (Eq. III.5). Figure IV.3 also proves that the only effect of  $\text{H}_3\text{PO}_4$  pre-treatment on electrochemical behaviour of the substrate is linked to the removal of the oxide layer.

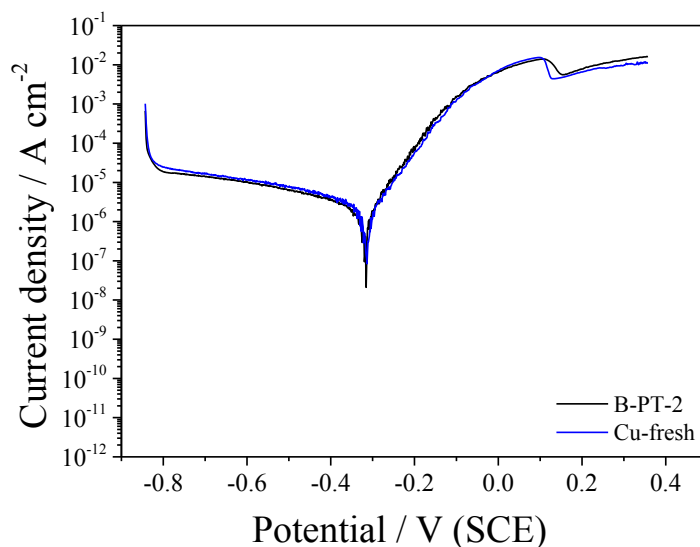


**Figure IV.3:** LSV polarization curves for a freshly polished Cu substrate (Cu-fresh) and B-PT in presence of higher amount of oxygen (argon bubbling done at lower rate) in the electrolyte in 0.5 M NaCl (pH = 6), scan rate: 1 mV.s<sup>-1</sup>

### IV.3. Surface and electrochemical analysis of coated substrates

#### IV.3.1. Time-of-Flight Secondary Ion Mass Spectrometry on pristine coated samples

The ToF-SIMS depth profiles for the coated samples C-PT and C-NPT are presented in Figure IV.4. The sputtering time needed to reach the substrate is slightly higher for C-NPT than for C-PT (~275 s vs 250 s), although both samples have the same sputtering time for the start of the interface (175 s). Therefore, coatings with same thickness were deposited and the longer time needed for C-NPT to arrive to the substrate is related to a broader interface between the coating and the substrate for this sample.

The comparisons between the same ions for C-PT and C-NPT are highlighted in Figure IV.5. In the bulk of the coating, the same level of C<sup>-</sup> contamination is observed (slightly higher for C-NPT). Cl<sup>-</sup> contamination in the bulk of the coating is slightly higher for C-PT, although it still has a very low level in the oxide matrix (log scale). At the

## Chapter IV. Effect of the interfacial native oxide layer on the corrosion of ALD alumina coated copper

interface, both  $C^-$  and  $Cl^-$  show higher intensity for C-NPT, which indicates a cleaner interface for this sample as a result of the pre-treatment.

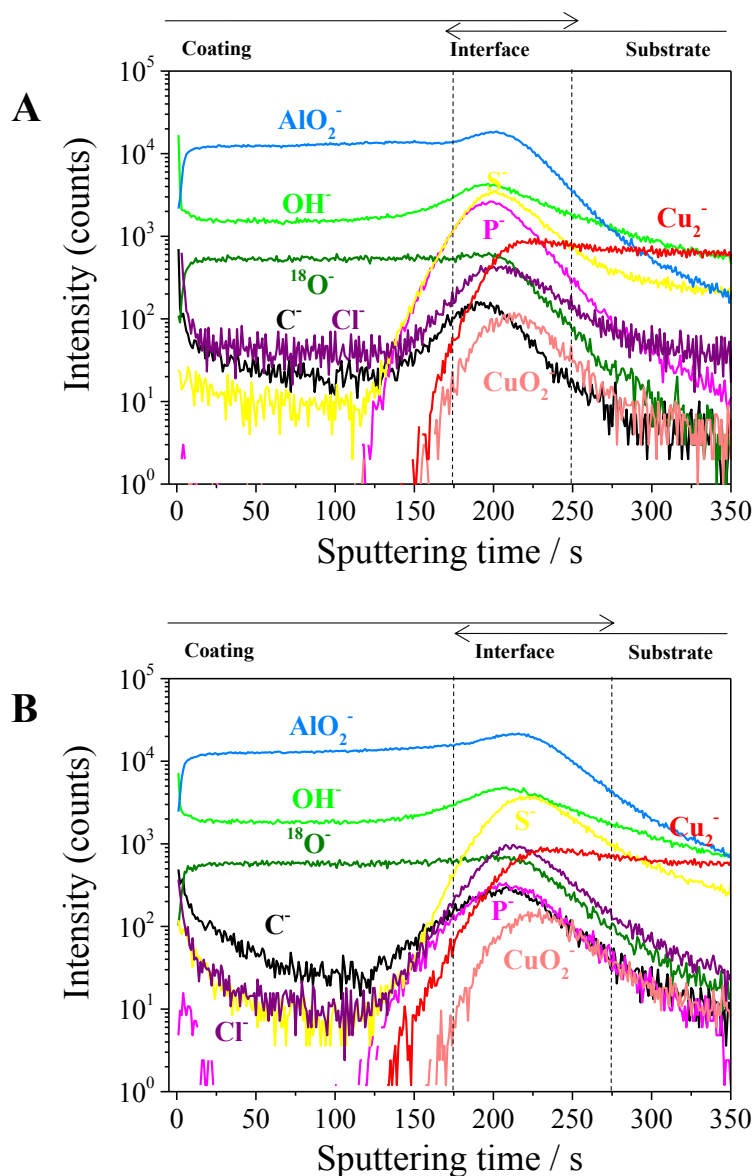


**Figure IV.4:** ToF-SIMS negative ion depth profiles for C-PT (A) and C-NPT (B)

Higher  $OH^-$  intensity for C-NPT in the bulk of the coating may imply a higher porosity or a lower density for this coating (as discussed in Chapter III). Lower  $OH^-$  intensity for C-PT on the interface is in agreement with lower hydroxylation of the native oxide on the surface as a result of the pre-treatment. Therefore, it can also indicate the presence of lower amount of interfacial native oxide for C-NPT.

## Chapter IV. Effect of the interfacial native oxide layer on the corrosion of ALD alumina coated copper

P<sup>-</sup> peak observed at the interface has a higher intensity for C-PT, due to H<sub>3</sub>PO<sub>4</sub> pre-treatment done on this sample. The presence of P<sup>-</sup> on C-NPT is a result of the electropolishing procedure. There is no difference observed for S<sup>-</sup> ion.

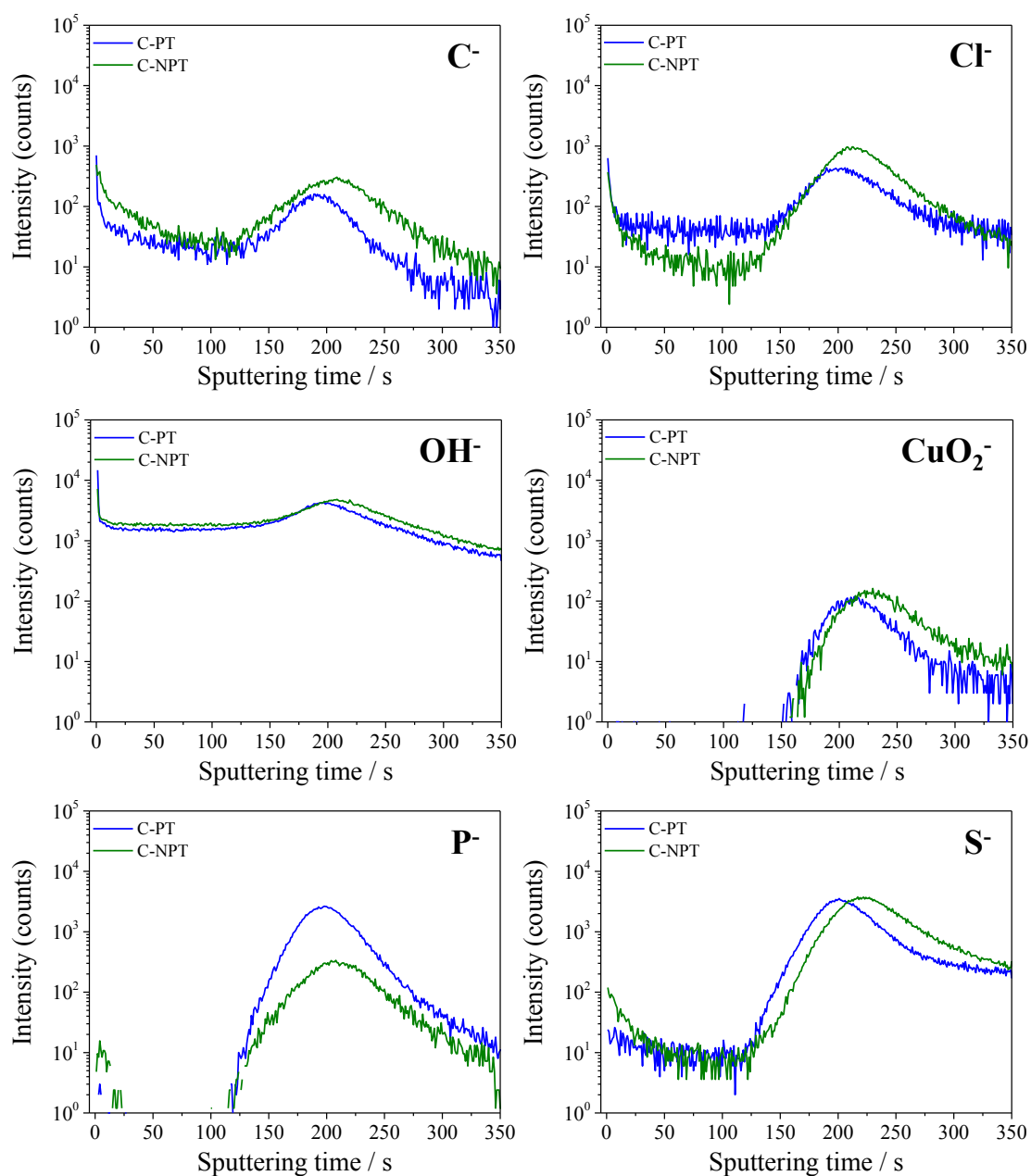


**Figure IV.5:** Comparative representation of ToF-SIMS depth profiles for C-PT and C-NPT for each ion

## Chapter IV. Effect of the interfacial native oxide layer on the corrosion of ALD alumina coated copper

---

The  $\text{CuO}_2^-$  peak observed at the interface between the coating and the substrate indicates the presence of copper oxide, as discussed before (see Chapter III). Its low intensity (for both C-PT and C-NPT), compared to  $\text{AlO}_2^-$  intensity, suggests a submonolayer equivalent thickness and a possibly discontinuous film. This is in agreement with the conclusions of Shimizu *et al.* from Rf-GDOES profiles [75]. As the intensities of the  $\text{CuO}_2^-$  peaks are very low, their comparison for C-PT and C-NPT is highlighted in Figure IV.6 on a linear scale.

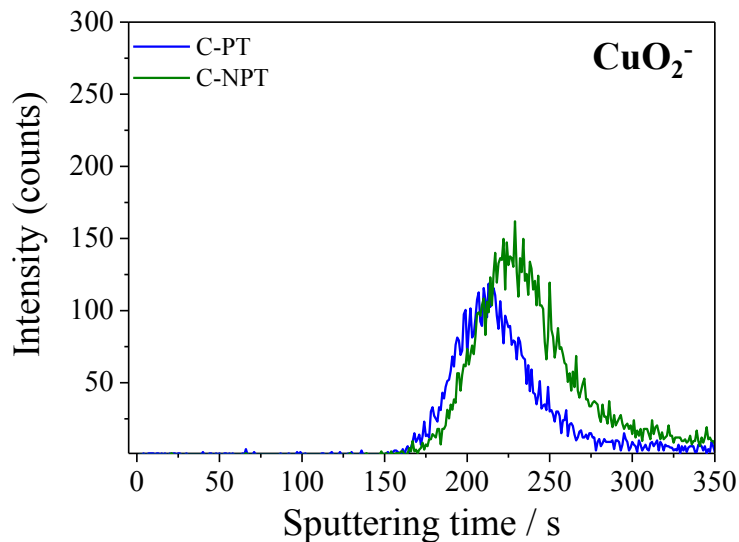


**Figure IV.6:** Comparison of the  $\text{CuO}_2^-$  for C-PT and C-NPT (linear scale)

The slightly higher intensity of  $\text{CuO}_2^-$  for C-NPT indicates higher amount of Cu oxide at the interface for this sample. The  $\text{CuO}_2^-$  peak observed for C-PT at the interface is due to the presence of a native oxide formed on the sample after the pre-treatment and before introducing the sample in the reactor, probably in combination with a spurious thermal oxide grown on the substrate surface exposed to the water precursor until full coverage by the alumina film and/or during thermal stabilization of the reactor at 250°C before deposition begins. The oxide on C-NPT is similarly a combination of a native and a spurious thermal oxide, with differences in the native oxide. The native oxide on the interface on this sample is an oxide aged on the substrate during 15 days before the coating deposition. As it was supposed that the oxides formed on both substrates are most probably

discontinuous, the profiles in Figure IV.6 indicate that the oxide at the interface of C-NPT would have a higher surface coverage and maybe higher thickness than the one on C-PT. The larger interface observed in Figure IV.4 for C-NPT appears consistent with a higher thickness of the interfacial copper oxide. However, it could also be due to a rougher substrate for C-NPT.

### **IV.3.2. Electrochemical impedance spectroscopy**

The Bode plots for C-PT and C-NPT are presented in Figure IV.7, along with the ones for the bare samples. The Bode plots for the coated samples are very similar and the only difference is the phase angle and resistance at low frequency. At high frequencies, the same phase angle denotes the same coating thickness and same quality of the coatings, while at low frequencies, different phase angles indicate difference between the substrates under the coatings. Here again, and as discussed in Chapter III, there is no evidence of two distinct time constants distinguishing the coating from the substrate. Like discussed in Chapter III, both the E.C.3 (Figure III.11.B) and E.C.2 (Figure III.13) equivalent circuits were used for fitting the EIS data. Only the results related to E.C.3 are presented here in Table IV.3 (results from fitting with E.C.2 were used only for verifying validation of the results obtained from E.C.3).

As it can be seen from the fitting results (Table IV.3),  $R_{ct}^a$  (the charge transfer resistance of the substrate under the coating) is about 10 times higher for C-PT. The lower  $R_{pore}$  for C-NPT may be as a result of growth of a coating with more defects at carbon contaminated sites (see section IV.3.1) as observed in previous studies [120]. On the other hand, the lower  $R_{pore}$  for C-NPT appears also consistent with slightly higher OH contamination observed in the bulk of the coating for this sample (Figure IV.5). The  $C_{dl}$  value obtained for C-NPT is slightly higher than for C-PT. For the bare substrates,  $C_{dl}$  for B-NPT was slightly lower (due to more contribution of copper oxide layer to  $C_{dl}$  in E.C.1). The opposite tendency observed here for the coated substrates implies that there is more response from the substrate in case of C-NPT, which means less sealing of the substrate for this sample. For the bare substrates, the slightly lower  $C_{dl}$  for B-NPT appears consistent

## Chapter IV. Effect of the interfacial native oxide layer on the corrosion of ALD alumina coated copper

with a higher copper oxide coverage in comparison with B-PT. For the coated samples, assuming the same porosity, slightly lower  $C_{dl}$  would be expected for C-NPT in comparison with C-PT. Therefore; the higher value of  $C_{dl}$  obtained for C-NPT means a higher porosity (more bare substrate exposed to the electrolyte) in comparison with C-PT.

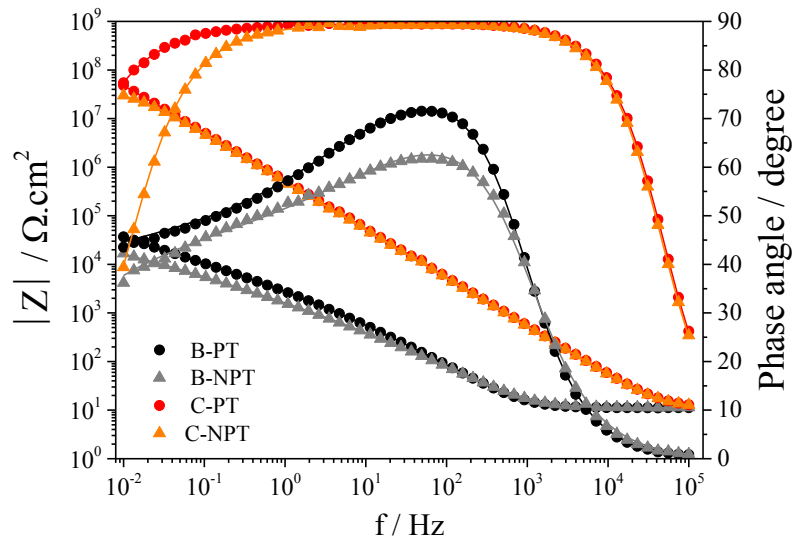


**Figure IV.7:** EIS Bode plots for coated (and bare) pre-treated and not pre-treated copper substrates in 0.5 M NaCl under argon bubbling (pH = 6) at OCP. Points and lines correspond to measured and fitted data, respectively.

The comparison of  $R_{CT}^a$ ,  $R_{pore}$  and  $C_{dl}$  values for C-PT and C-NPT samples suggests higher porosity (wetted surface area under the coating) and more/wider channels in the coating for C-NPT. The latter is deduced from lower  $R_{pore}$  for this sample. However, due to the observation of higher  $OH^-$  contamination for this sample by ToF-SIMS (Figure IV.5), it cannot be decided if the coating was grown with more pores since the beginning, or if more corrosion of substrate under the coating led to more trenching of the substrate and more opening of the channels (as a result of release of corrosion products) in the coating after immersion in the electrolyte.

## Chapter IV. Effect of the interfacial native oxide layer on the corrosion of ALD alumina coated copper

**Table IV.3:** EIS fitting results of EIS data related to coated samples (Figure IV.7) fitted with E.C.3 (Figure III.11.B). Fitting results for bare substrates presented already in Table IV.1 are added for comparison

	$R_c / \Omega.cm^2$	$R_{pore} / \Omega.cm^2$	$R_{ct}^a / \Omega.cm^2$	$R_{total} / \Omega.cm^2$	$\frac{Q_c}{F.cm^{-2}.s^{(\alpha-1)}}$	$n_c$	$\frac{C_{eff-c}}{F.cm^{-2}}$	$\frac{Q_{dl}}{F.cm^{-2}.s^{(\alpha-1)}}$	$n_{dl}$	$\frac{C_{eff-dl}}{F.cm^{-2}}$	$\frac{S}{\Omega.s^{-0.5}.cm^2}$ ( $Z_W = \frac{S}{\sqrt{j\omega}}$ )
<b>C-PT (20nm)</b>	11.57	$9.91 \times 10^6$	$2.88 \times 10^8$	$2.98 \times 10^8$	$2.94 \times 10^{-7}$	0.99	$2.84 \times 10^{-7}$	$9.07 \times 10^{-9}$	0.90	$7.67 \times 10^{-9}$	$1.11 \times 10^8$
<b>C-NPT (20nm)</b>	11.57	$5.57 \times 10^6$	$3.46 \times 10^7$	$4.03 \times 10^7$	$3.12 \times 10^{-7}$	0.99	$2.97 \times 10^{-7}$	$1.00 \times 10^{-8}$	0.99	$1.00 \times 10^{-8}$	$6.49 \times 10^7$
<b>B-PT (bare)</b>	11.09		$6.28 \times 10^5$					$2.03 \times 10^{-5}$	0.96	$1.48 \times 10^{-5}$	$6.69 \times 10^3$
<b>B-NPT (bare)</b>	11.18		$7.92 \times 10^4$					$2.48 \times 10^{-5}$	0.92	$1.23 \times 10^{-5}$	$3.52 \times 10^3$

**Table IV.4:** Porosity values obtained for coated samples from EIS and LSV measurements

	<b>P-R<sub>ct</sub> %</b>	<b>P-C<sub>dl</sub> %</b>	<b>P-R<sub>p</sub> %</b>	<b>P-i<sub>a</sub> %</b>
<b>C-PT</b>	0.03	0.05	0.02	0.03
<b>C-NPT</b>	0.13	0.08	0.08	0.23

## Chapter IV. Effect of the interfacial native oxide layer on the corrosion of ALD alumina coated copper

---

The porosity values obtained from  $R_{ct}^a$  (using Eq. III.15) and  $C_{dl}$  values (using Eq. III.16) are presented in Table IV.4. The values obtained for C-NPT are higher than for C-PT, as expected.  $P-C_{dl}$  is not as high as  $P-R_{ct}^a$ . As discussed above, this is because of the higher surface coverage of the interfacial copper oxide for C-NPT in comparison with C-PT.

### IV.3.3. Linear Sweep Voltammetry

The polarization curves for the coated samples C-PT and C-NPT are presented in Figure IV.8, along with the ones presented in Figure IV.2 for the bare samples. The parameters and values related to the polarization measurements are gathered in Table IV.5. The coated samples have same corrosion potentials, while there is a difference of 70 mV for bare samples. This suggests higher stability (less reducibility) of the oxide layer on the substrate under the coatings. Furthermore, the cathodic Tafel slopes for the coated samples are higher (in absolute value) than for the bare samples and the highest slope is obtained for C-NPT. The higher  $b_c$  values for the coated samples indicate the presence of more copper oxide on the substrate under the coatings for these samples, as discussed in section IV.2.2. More interfacial oxide for these samples (in comparison with B-NPT) would be a result of formation of spurious oxide in the ALD reactor.

For C-NPT, there should be still a higher amount of copper oxide at the interface in comparison with C-PT as indicated by the ToF-SIMS data and as suggested by the larger  $b_c$  value. This is related to presence of a native oxide layer that was aged during 15 days and which was not removed before the coating deposition. More interfacial native oxide on C-NPT in comparison with C-PT leads to  $i_{corr}$  and  $R_p$  values that are 10 times higher and lower, respectively. It also leads to higher anodic current since corrosion potentials are the same. Therefore, the same cause (different amount of interfacial copper oxide) for the variation in electrochemical behaviour between the bare samples can be assigned to the coated samples with the only difference that corrosion potentials were not the same for bare samples. Variation of the corrosion potential for the bare samples, as discussed before, is attributed to more reducibility of the freshly formed oxide layer on B-PT.

## Chapter IV. Effect of the interfacial native oxide layer on the corrosion of ALD alumina coated copper

---

The porosity values, obtained from the polarization resistances (using Eq. III.11) and anodic currents (using Eq. III.12) are presented in Table IV.4. The values obtained from the different measurements and using different parameters are in good accordance and all of them are higher for C-NPT. These porosity values are the ratio of the wetted surface area (opening at the end of the channel defects) on the substrate and under the coatings, as discussed in Chapter III (see section III.3.4). Due to higher corrosion of the substrate for C-NPT, the channels in the coating, through which the electrolyte reaches the substrate, are more opened at the end, and more trenching of the substrate has happened in this case.

The porosity values (Table IV.4) for C-NPT and C-PT were obtained using B-NPT and B-PT respectively as bare substrates. Making comparison to one single bare substrate leads to same results. This is because the formulas used for the porosity calculations take into account the difference in  $E_{\text{corr}}$  between the coated and bare substrates. Besides, using the anodic current values instead of the corrosion current values rules out the effect of the cathodic part. In fact, for the present study, B-PT is not a substrate perfectly comparable with the substrate under the coating for C-PT, due to presence of a more reducible oxide on the substrate of B-PT, as discussed before, which leads to a different  $E_{\text{corr}}$  and cathodic behaviour between C-PT and B-PT. On the contrary, B-NPT can be a better reference for both coated samples, as shown by the nearly identical corrosion potentials obtained as a result of the more stable copper oxide formed by ageing. Still, the comparisons for the coatings with pre-treated substrates were done to B-PT.

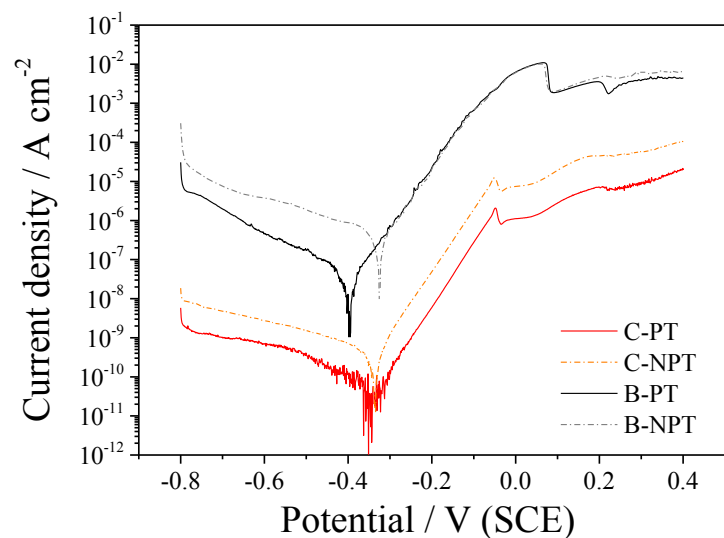


Figure IV.8: LSV polarization curves for bare and coated substrates in 0.5 M NaCl (pH = 6) under argon bubbling, scan rate: 1 mV.s<sup>-1</sup>

Table IV.5: Parameters related to LSV curves in Figure IV.8

	$E_{OCP} / V(SCE)$	$E_{corr} / V(SCE)$	$i_{corr} / A.cm^{-2}$	$b_a / V.dec^{-1}$	$b_c / V.dec^{-1}$	$R_p / Ohm.cm^{-2}$	$i_a (at E = -0.2 V/SCE) / A.cm^{-2}$
<b>B-PT</b>	-0.312	-0.395	$2.80 \times 10^{-8}$	0.065	-0.190	$5.22 \times 10^5$	$2.04 \times 10^{-5}$
<b>B-NPT</b>	-0.284	-0.325	$2.13 \times 10^{-7}$	0.062	-0.300	$4.64 \times 10^4$	$2.04 \times 10^{-5}$
<b>C-PT</b>	-0.322	-0.334	$3.00 \times 10^{-11}$	0.062	-0.315	$3.74 \times 10^8$	$5.62 \times 10^{-9}$
<b>C-NPT</b>	-0.322	-0.334	$2.70 \times 10^{-10}$	0.062	-0.350	$4.64 \times 10^7$	$4.75 \times 10^{-8}$

#### **IV.3.4. Time-of-Flight Secondary Ion Mass Spectrometry of polarized coated samples**

The ToF-SIMS depth profiles measured on the coated samples after the polarization tests are presented in Figure IV.9. No coating dissolution is observed, as indicated by the same sputtering time (~175 s) observed for the coatings before and after polarization. The same intensity is measured for the coating and substrate ions for both samples after polarization, indicating an unchanged coating matrix after polarization. The absence of any Cu-containing ions in the bulk of the coating indicates that no defects have appeared in the coating after immersion with a size detectable with ToF-SIMS.

The direct comparison of the same ions for the two samples is presented in Figure IV.10. The ions related to a third profile (C-NPT-b) measured on the C-NPT sample in an area including a pit is represented along with the ions related to the profiles presented in Figure IV.9. The pit was observable as a dark spot by the ToF-SIMS camera (as shown in the optical micrograph presented in Figure IV.12.A) and was confirmed as a pit according to the discussions provided in the following. Such dark spots were not detected for the C-PT sample.

The same level of C<sup>-</sup> contamination is observed in the bulk of the coating for C-PT and C-NPT. On the interface, the C<sup>-</sup> intensity is slightly higher for C-PT. The OH<sup>-</sup> ions show the same intensity level for both samples. The OH<sup>-</sup> intensity has decreased for both samples after polarization, the decrease being more marked in the case of C-NPT. Such behaviour for OH<sup>-</sup> in a study of alumina coatings on carbon steel substrate (after one hour of immersion in NaCl electrolyte) was attributed to substitution of hydroxyl groups by chlorides in the bulk of the coating [118]. If so, the higher decrease of OH<sup>-</sup> in the case of C-NPT would mean more penetration of chloride in the pores of the coating. For none of the samples an obvious effect is seen for the S<sup>-</sup> ions. The difference for P<sup>-</sup> ions is as discussed in section IV.3.1, and as for S<sup>-</sup> ions, no significant change has happened after polarization.

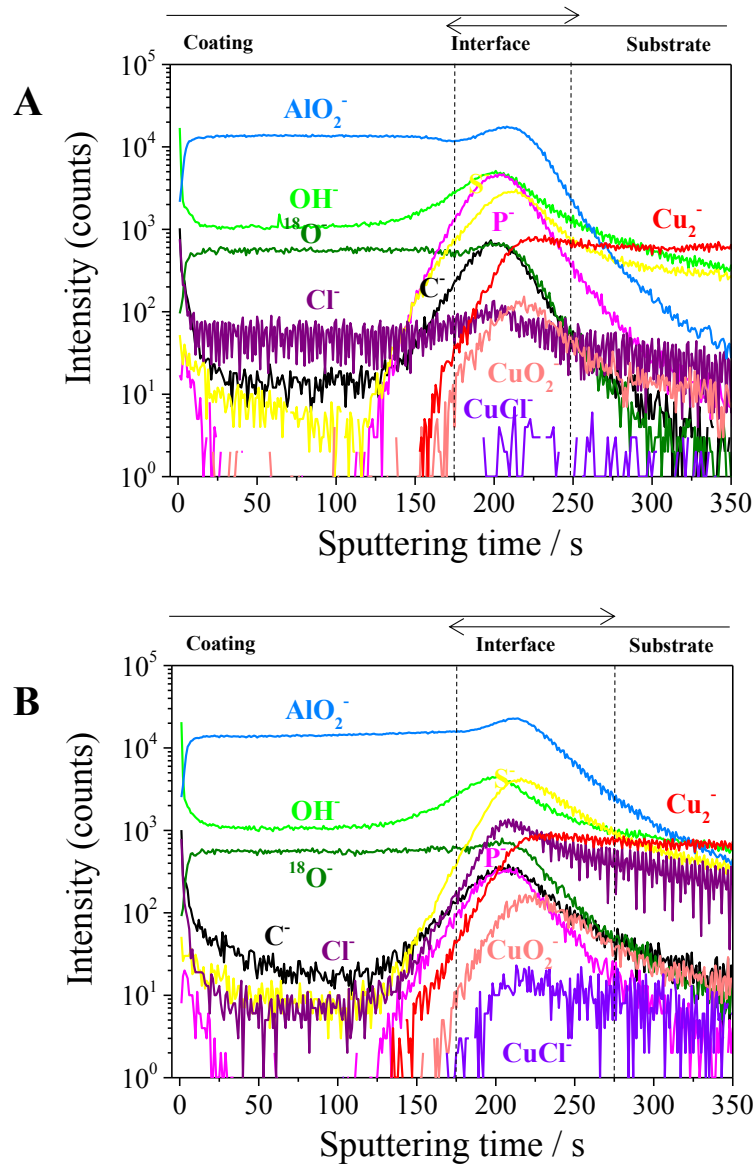


**Figure IV.9:** ToF-SIMS negative ion depth profiles for C-PT (A) and C-NPT (B) after immersion and polarization in 0.5 M NaCl (pH = 6), scan rate:  $1 \text{ mV}\cdot\text{s}^{-1}$

A higher amount of interfacial copper oxide is again observed for C-NPT, as shown mostly by a wider  $\text{CuO}_2^-$  peak in Figure IV.10. The difference in the intensity of the peaks can be better observed using a comparison of  $\text{CuO}^-$  ion profiles as shown in Figure IV.11. The  $\text{CuO}^-$  ion is indicative of metallic copper and copper oxide at the same time. As no difference in the intensity of  $\text{Cu}_2^-$  (the ion representative of metallic copper) can be distinguished for C-PT and C-NPT, the difference in  $\text{CuO}^-$  for these samples is attributed to the difference in the interfacial copper oxide. Therefore, higher amount of interfacial copper oxide for C-NPT can be confirmed from Figure IV.11.

## Chapter IV. Effect of the interfacial native oxide layer on the corrosion of ALD alumina coated copper

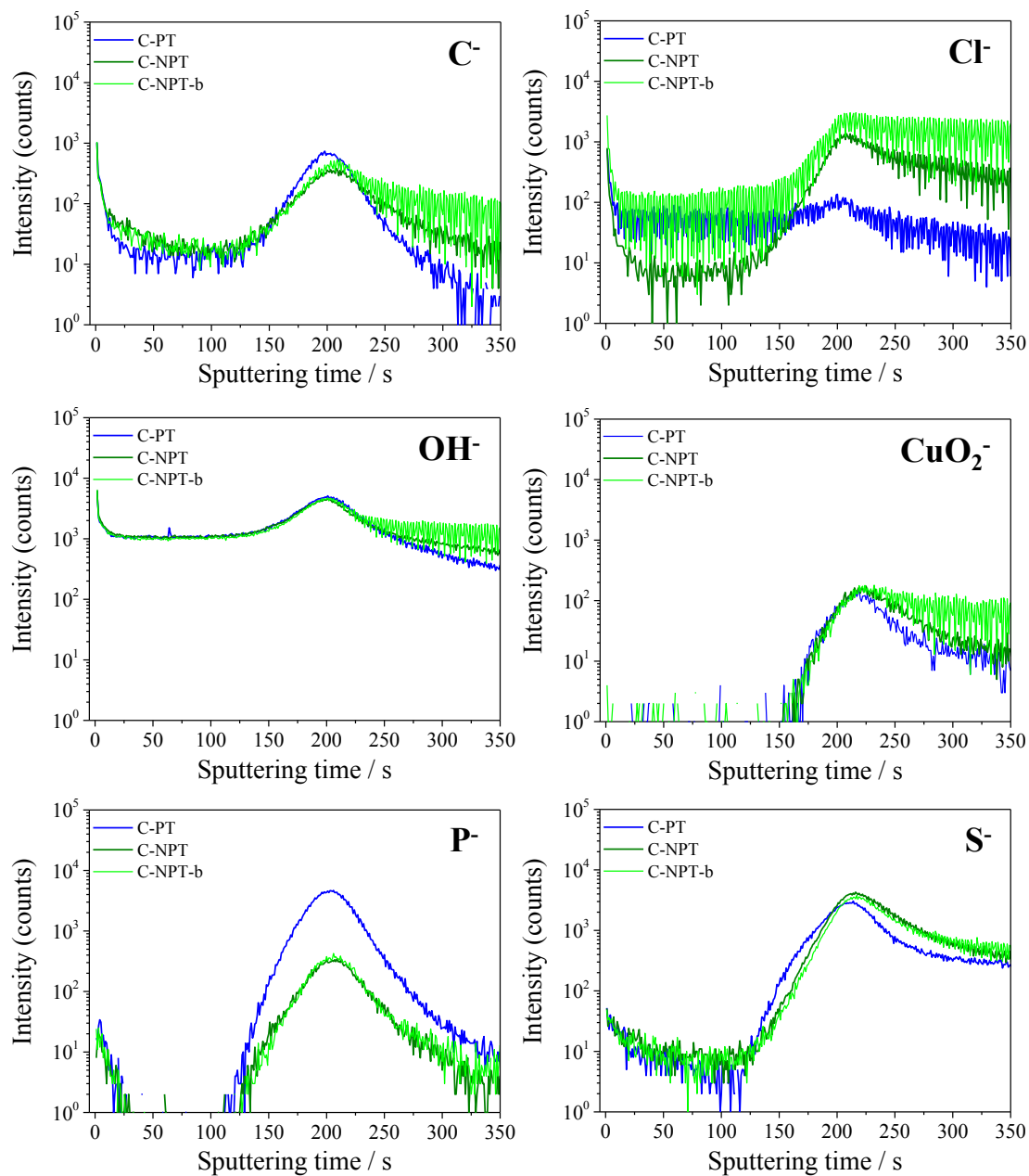


**Figure IV.10:** Comparative representation of ToF-SIMS depth profiles for C-PT and C-NPT for each ion, after immersion and polarization in 0.5 M NaCl (pH = 6), scan rate: 1 mV.s<sup>-1</sup>

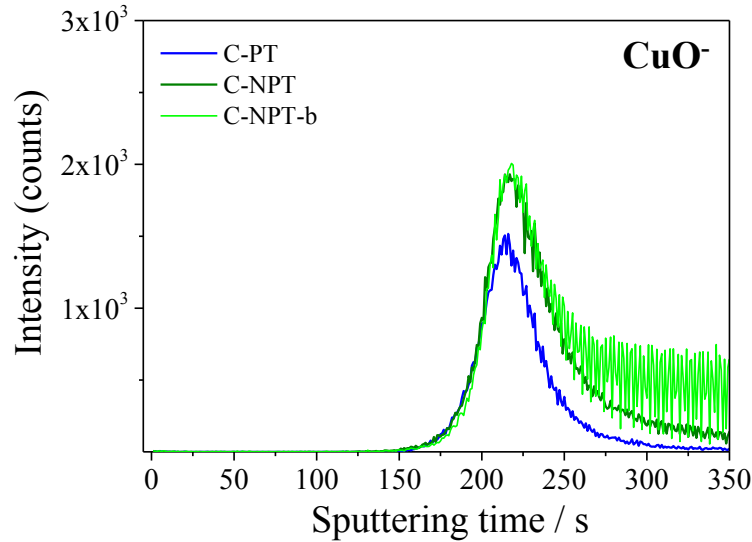


**Figure IV.11:** Comparison of the  $\text{CuO}^-$  profile for C-PT and C-NPT (linear scale), related to Figure IV.9

The  $\text{Cl}^-$  intensity is significantly higher at the interface for C-NPT (and C-NPT-b). In the bulk of the coating, C-PT shows a higher intensity level than C-NPT. The intensity of  $\text{Cl}^-$  for C-PT is not changed after polarization and is the same as in Figure IV.4.A. Therefore,  $\text{Cl}^-$  for C-PT cannot be attributed to the corrosion process or entrance of the electrolyte in the channels through the coating. For C-NPT, the increase of  $\text{Cl}^-$  at the interface after polarization, as well as its increase in the bulk of the coating in the profile taken from the area with a pit (C-NPT-b), indicate entrance of the electrolyte in the channels of the coating and its arrival to the substrate. The non-decreasing tail of  $\text{Cl}^-$  for C-NPT-b in the substrate region confirms formation of pits (entrance of electrolyte in the pit formed in the substrate). This is further confirmed by  $\text{CuCl}^-$  profile for C-NPT shown in Figure IV.12.B. The presence of  $\text{CuCl}^-$  ion at the interface and in the substrate region is a direct indication of formation of corrosion products in the pits. The  $\text{CuCl}^-$  level for C-PT (Figure IV.9.A) is very low in comparison with C-NPT and is observed only as a trace.

The wider interfacial peaks and the higher tails for the ions characteristic of corrosion products evidence more advanced corrosion of the substrate under the coating for C-NPT, than for C-PT. This shows the detrimental effect of the presence of an aged interfacial native oxide on the corrosion resistance of the coated sample.

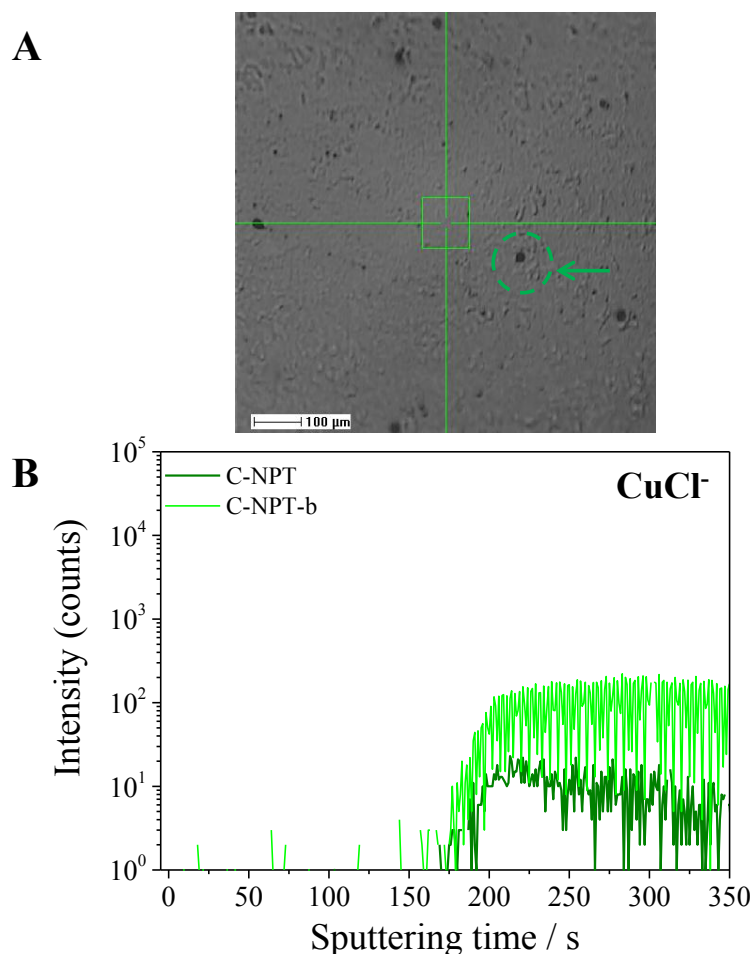


**Figure IV.12:** Optical micrograph after immersion and polarization in 0.5 M NaCl (pH = 6), scan rate: 1 mV.s<sup>-1</sup> (A) and comparison of ToF-SIMS CuCl<sup>-</sup> depth profiles of polarized C-NPT in an area without (dark green) and with (light green) an obvious pit (B)

#### IV.4. Conclusions

The presence of an air-formed native copper oxide on copper metal was shown to affect the electrochemical behaviour in an electrolyte with low amount of dissolved oxygen. The reducibility of such an oxide when freshly formed on a pre-treated substrate led to a lower rate of oxygen reduction on the substrate, and thus a lower corrosion rate at  $E_{\text{cor}}$  in comparison with a substrate not pre-treated and on which this oxide was more stable (less reducible) after ageing.

## Chapter IV. Effect of the interfacial native oxide layer on the corrosion of ALD alumina coated copper

---

On the specimens coated with 20 nm ALD alumina, the difference in corrosion rate is related to the difference of surface coverage and/or thickness of the interfacial oxide, rather than to its reducibility. More Cu(I) sites on the non pre-treated substrate with higher covering interfacial copper oxide, would promote the cathodic oxygen reduction, leading to higher corrosion current. Although the same difference in corrosion rate between the coated and bare substrates suggests that the main origin of different corrosion rates for the coated samples is the electrochemical behaviour of the substrate at the bottom of the channel defects through the coating, the different  $R_{\text{pore}}$  values obtained from EIS in addition to varying  $\text{OH}^-$  and  $\text{C}^-$  ion intensities measured by ToF-SIMS on pristine coated samples point out the role of the coatings grown on the different substrates. Although it cannot be concluded if the lower  $R_{\text{pore}}$  value obtained for C-NPT is due to channels opening after immersion in the electrolyte or if more/wider channels existed after deposition, the higher  $\text{OH}^-$  level in the bulk of the coating and the higher  $\text{C}^-$  level at the coating/substrate interface suggest growth of a more defective coating on the non pre-treated copper sample covered by an aged native oxide.

ToF-SIMS analysis after polarization confirmed localized corrosion at the substrate surface exposed to the bulk electrolyte by channel defects through the coating, with more advanced localized corrosion for the copper substrate covered by an aged native oxide. Thus, it is shown in this chapter that modifying the interfacial oxide by pre-treatment of the copper substrate affects the barrier property of the coatings and that improved corrosion resistance is obtained in the absence of an aged native oxide.



# **Chapter V**

## **Effect of copper substrate annealing on the corrosion protection of ALD alumina coatings**

### **V.1. Introduction**

Surface preparation is a critical issue for ALD ultrathin coatings. Although these coatings are conformal and cover rough aspects of the surface, their function for corrosion protection still depends on the surface state of the substrate. Fragile features and morphological surface heterogeneities (including roughness) on the substrate are more susceptible to corrosion and their exposure to the electrolyte at the bottom of channels in the coating may accelerate the corrosion process.

Excellent corrosion protection performance of the alumina coatings was shown in Chapter III on electropolished copper substrate. Although electropolishing of copper leads to decrease of the roughness, AFM images still showed presence of a rather rough copper surface under the coating. With the ambition to obtain results even better than on the electropolished substrate, annealing of the substrate was performed since it further

## Chapter V. Effect of copper substrate annealing on the corrosion protection of ALD alumina coatings

---

reduces the surface roughness and smooth topographical asperities. In order to study the effect of surface roughness on the corrosion protection provided by the ALD alumina coatings, annealing was done after electropolishing of the substrate according to the procedure detailed in Chapter II. The  $\text{H}_3\text{PO}_4$  pre-treatment was done on the substrate before coating deposition for coherence with the samples studied in Chapter III.

### V.2. Time-of-Flight Secondary Ion Mass Spectrometry of pristine coated samples

The ToF-SIMS depth profiles of the 10, 20 and 50 nm ALD alumina coatings on annealed copper substrates are shown in Figure V.1. In a same way as explained in Chapter III for coatings deposited on electropolished substrates, three regions (coating, interface and substrate) can be defined using the same definitions. To avoid repetition of all the discussions made in Chapter III, only the differences between the present profiles and the former ones (on electropolished substrates) will be pointed out.

The entry in the substrate bulk region (where the  $\text{Cu}_2^+$  ions start to have a constant intensity) is at  $\sim 115$ ,  $\sim 245$  and  $\sim 640$  s of sputtering time for the 10, 20 and 50 nm specimens, respectively. Calculated sputtering rate yields values of 0.085, 0.083 and 0.080  $\text{nm}\cdot\text{s}^{-1}$  using the measured (by XRR) film thicknesses of 9.8, 20.3 and 51.4 nm, respectively. These values are slightly lower than those obtained on the electropolished substrate, with a difference increasing with decreasing deposited thickness.

Comparison of individual ions for the coatings on annealed and electropolished substrates is provided in Figure V.2. The coating ions ( $\text{AlO}_2^+$  and  $^{18}\text{O}^+$ ) show slightly higher intensities on the annealed substrate than on the electropolished one. This may mean higher density for the coatings on the annealed substrate, as supported by the variation of the sputtering rate values.

The profiles on the annealed substrate show narrower/sharper peaks for the interfacial species and faster decreasing tail in the substrate for the ions related to the bulk coating (Figure V.2 and Figure V.3). This is consistent with a smoother copper substrate under

## Chapter V. Effect of copper substrate annealing on the corrosion protection of ALD alumina coatings

---

the coating, as expected from the annealing surface finish and confirmed by the AFM data presented below. The beginning of interfacial region was taken where the coating ions deviate from plateau, i.e. at ~80, ~205 and ~560 s of sputtering time which leads to measured interfacial width values of ~35, ~40 and ~80 s of sputtering time for the 10, 20 and 50 nm films, respectively. These values, very similar to the ~30, ~40 and ~100 s measured values on the electropolished samples, do not allow any reliable quantification of the variation of the width of the interface. Still, the increasing measured width of the interfacial region with increasing deposited thickness is in agreement with what was observed for the coatings on electropolished substrate. As discussed in Chapter III, this increasing width of the interfacial region is most likely apparent and a consequence of variation of the sputtering rate with increasing deposition time. The fact that the variation of interfacial width is apparent is likely the reason to have close interfacial width values for the coatings on both substrates.

The slightly higher intensity of  $\text{CuO}_2^-$  ion peak at the interface of the annealed samples points to the presence of more interfacial copper oxide. This can be also observed from the  $\text{Cu}_2^-$  ion profiles (representative of metallic copper) that show a peak at the interface due to contribution from copper oxide for these samples.

The observed  $\text{Cu}_2^-$  plateau in the bulk region of 20 nm coating suggests the presence of defects on this sample with a lateral size detectable with ToF-SIMS, *i.e.* of at least 20 nm, owing to the incident angle of  $45^\circ$  of Bi ion and the coating thickness of 20 nm.

As discussed in Chapter III, the  $\text{S}^-$  peak observed at the interface is a result of sulphur segregation from the bulk of copper to the surface (Figure V.3). A similar intensity of  $\text{S}^-$  peak is observed at the interface for the annealed and electropolished substrates. Although the  $\text{S}^-$  intensity is markedly decreased in the bulk substrate as a result of annealing at  $725^\circ\text{C}$ , this decrease has not been enough for avoiding formation of a monolayer of sulphur by segregation.

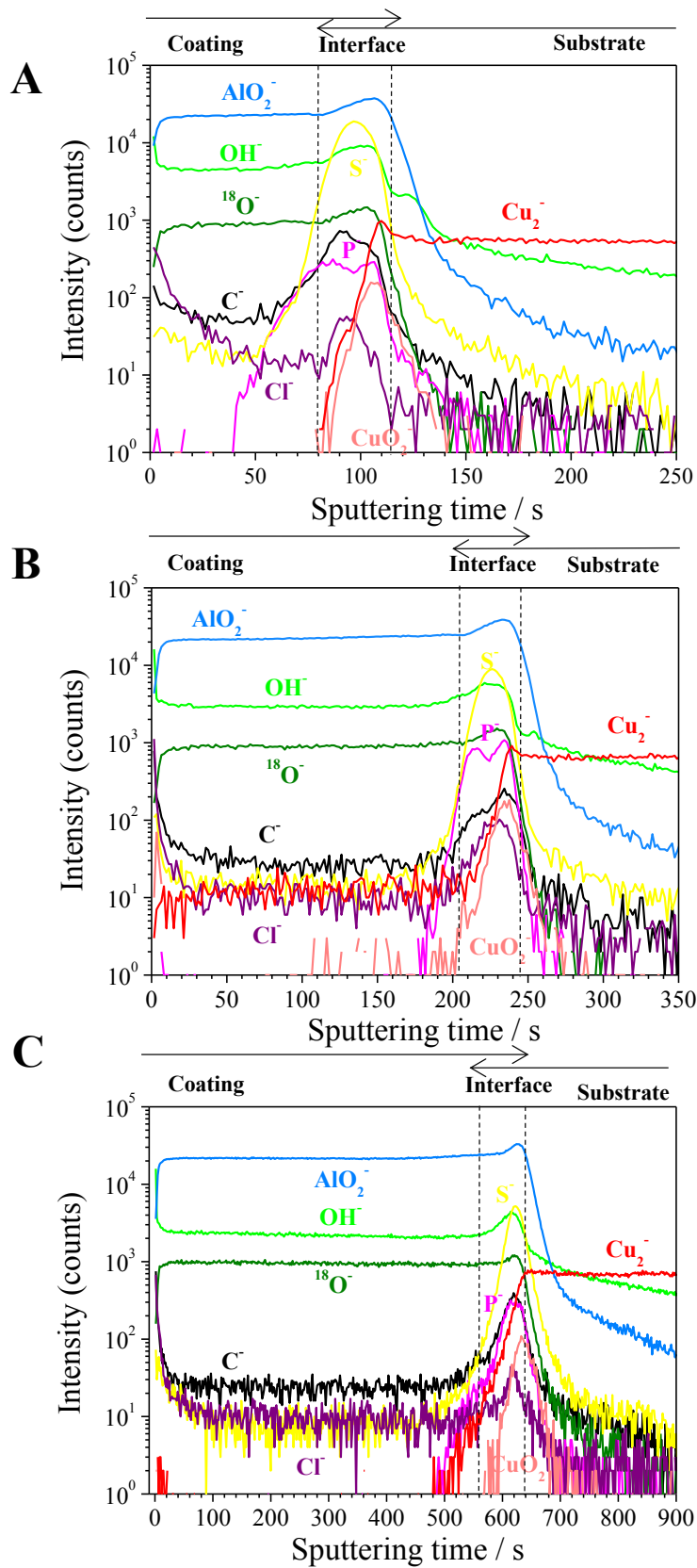
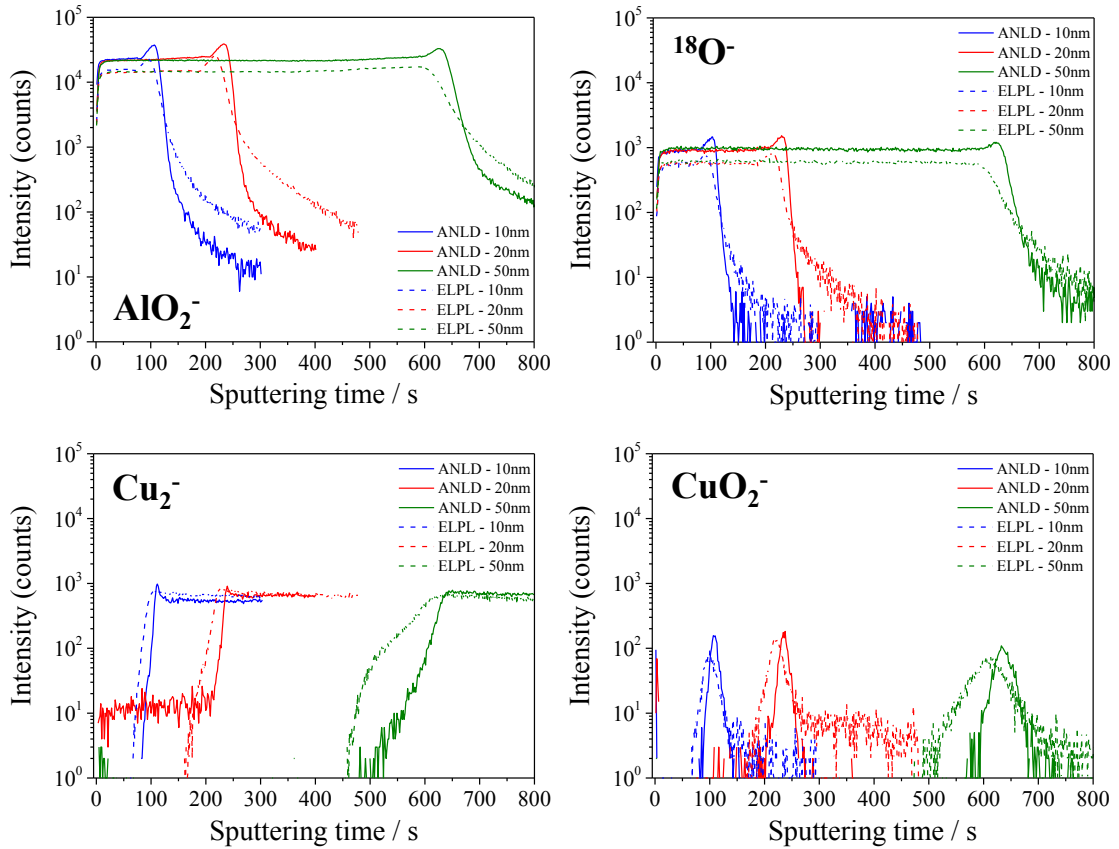


Figure V.1: ToF-SIMS negative ion depth profiles for 10 nm (A), 20 nm (B) and 50 nm (C) ALD alumina coatings prepared at 250°C on annealed copper substrate

## Chapter V. Effect of copper substrate annealing on the corrosion protection of ALD alumina coatings



**Figure V.2:** Comparative representation of ToF-SIMS depth profiles of selected ions for alumina coatings on annealed (ANLD) and electropolished (ELPL) substrates

The slightly lower intensity of  $\text{Cl}^-$  and  $\text{C}^-$  at the interface for annealed substrates (mostly for the 10 nm sample) could be a positive effect of annealing preparation. In the bulk of the coating,  $\text{Cl}^-$  and  $\text{C}^-$  show similarly low intensities for both substrates. The  $\text{OH}^-$  ion intensity decreases at the interface and in the bulk of the coating with increasing coating thickness for both substrates, which is in agreement with the coating densification with thickness increase as a result of the increasing time for completion of the incomplete surface reactions responsible for hydroxyl contamination in the bulk of the coating. However, the  $\text{OH}^-$  signal shows higher level for the coatings on annealed substrates. As discussed for coatings on electropolished substrates, the presence of  $\text{OH}^-$  in the bulk of the coating and at the interface can also be linked to water uptake in the coating after coating deposition and exposure of the sample to the ambient. Considering the higher intensity of coating ions ( $\text{AlO}_2^-$  and  $^{18}\text{O}^-$ ) observed on the annealed samples, the higher  $\text{OH}^-$  intensity cannot be due to higher porosity resulting from a more defective growth of

## Chapter V. Effect of copper substrate annealing on the corrosion protection of ALD alumina coatings

these coatings. But if the coating is not well-attached on the substrate, post-deposition increase of  $\text{OH}^-$  both in the bulk of the coating and on the interface can happen. The detachment of the coatings on annealed substrates will be discussed with more detail in the following parts.

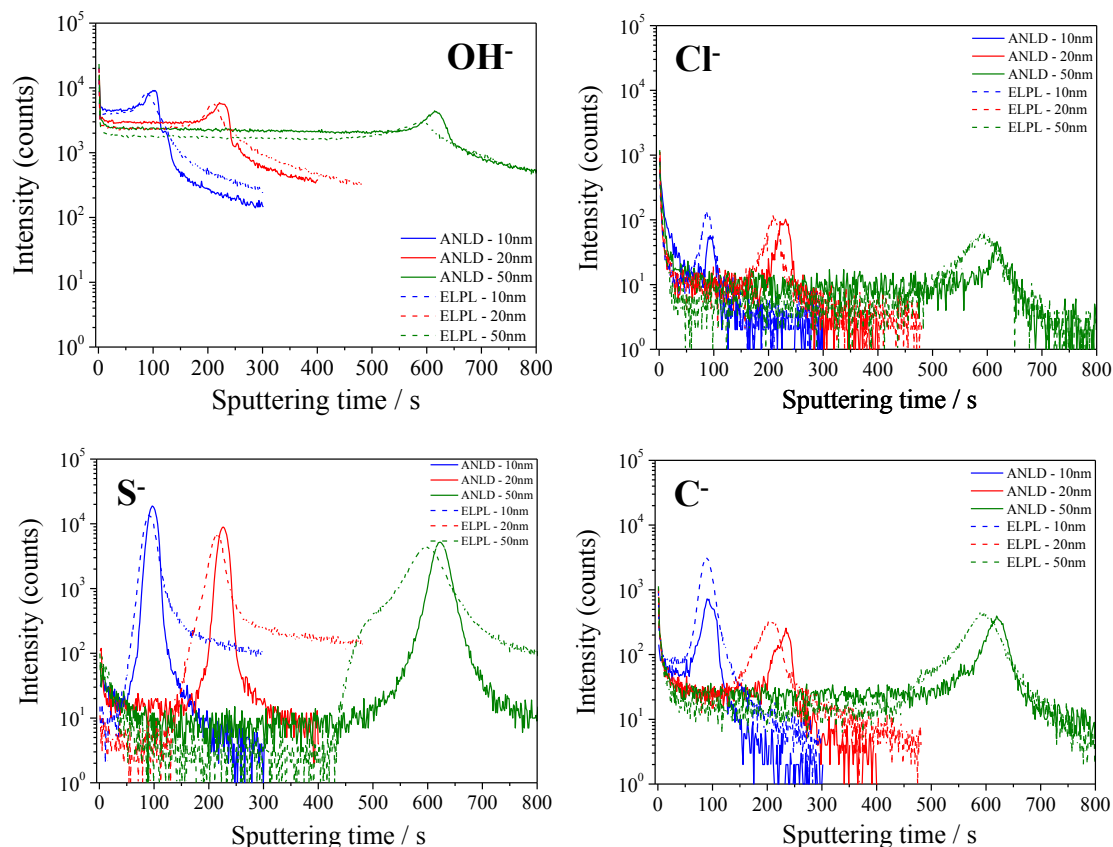


Figure V.3: Comparative representation of ToF-SIMS depth profiles same as Figure V.2

### V.3. Atomic Force Microscopy

Figure V.4 presents the AFM images for the 10, 20 and 50 nm ALD alumina coatings on the electropolished and annealed copper substrates. The surfaces of the annealed samples are obviously smoother than those of the electropolished samples. The rms roughness values calculated for both sample sources are presented in Figure V.5. Given that the same coatings were grown on both substrates, it can be concluded that surface roughness

## Chapter V. Effect of copper substrate annealing on the corrosion protection of ALD alumina coatings

is governed by the substrate. Furthermore, the roughness measured here confirms the smoothing effect of annealing treatment, which could not be evidenced from the comparison of the interface width values from the ToF-SIMS profiles. It is worthy to mention that the small dark spots on the images of the coatings on the annealed substrates are not coating defects or pinholes revealing the bare substrate, as their depths are less than 4 nm which is smaller than the deposited thickness. Most likely, they are defects (holes) in the substrate surface.

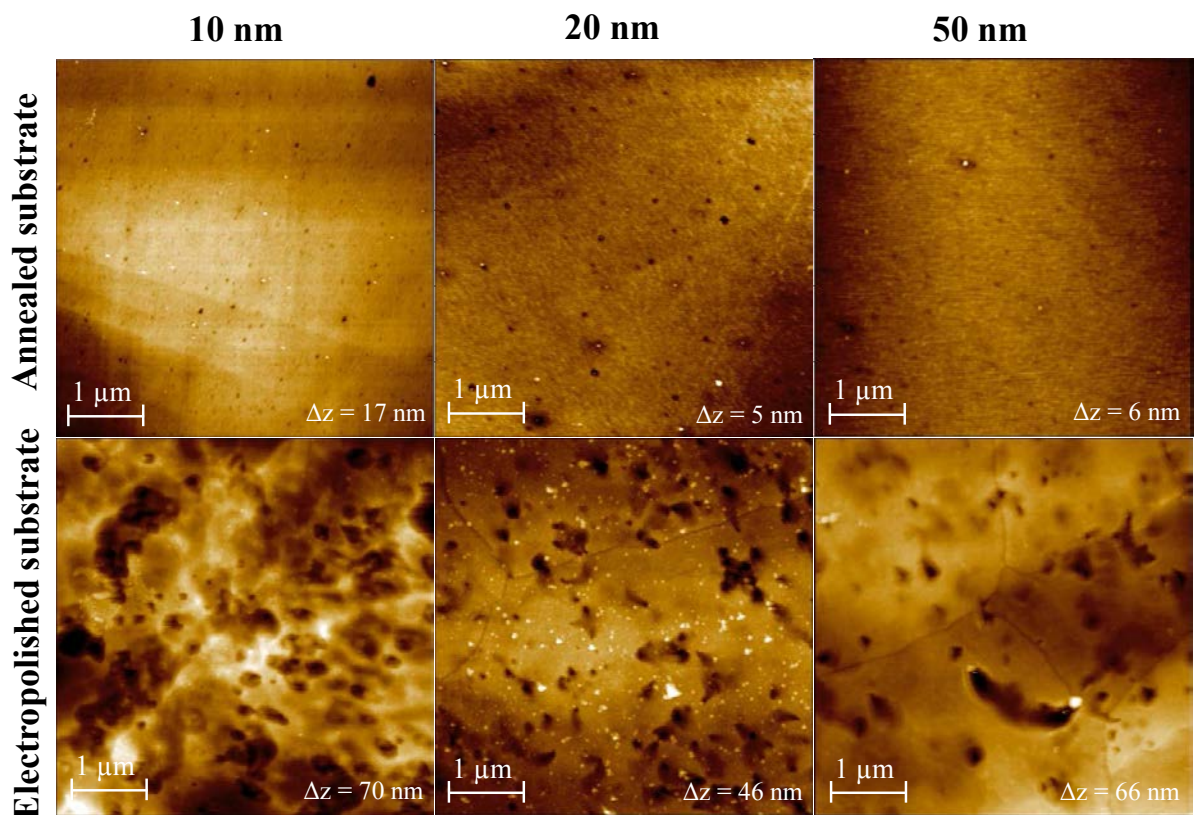


**Figure V.4:** Topographic AFM images ( $5 \times 5 \mu\text{m}$ ) of ALD alumina coated Cu substrates, electropolished and annealed

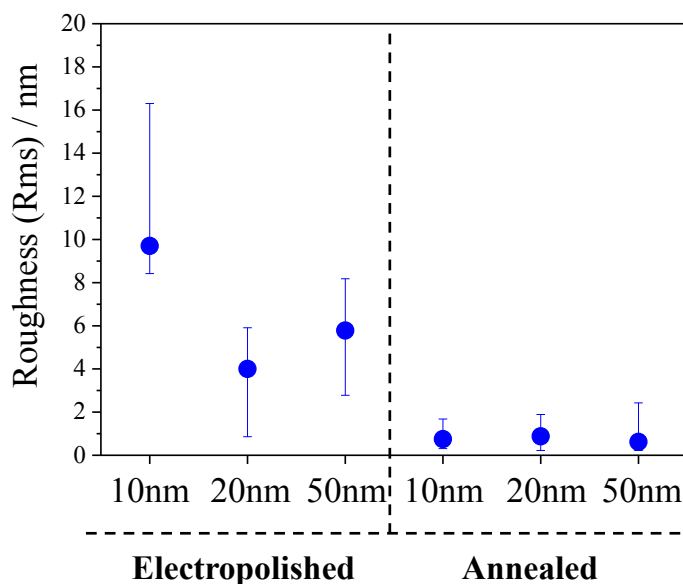


Figure V.5: Roughness values (rms) obtained by AFM for ALD as same as Figure V.4

#### V.4. Linear Sweep Voltammetry

Figure V.6 presents the polarization curves obtained by LSV for the uncoated and coated annealed Cu substrates. The same general shape of the polarization curves as for the electropolished substrates is obtained. Therefore, the same mechanism of copper corrosion is proposed. Extracted parameters are gathered in Table V.1. The corrosion potentials and cathodic Tafel slopes are observed to be higher (in absolute value) for coated substrates in comparison with the bare one, a trend that increases with increasing the deposited thickness. This observation implies the presence of more stable (less reducible in the conditions of the LSV test) copper oxide at the coating/substrate interface than on the bare substrate (as discussed in Chapter IV). However, the increase of this trend (increase of  $b_c$  and  $E_{corr}$ ) with increasing the coating thickness suggests a higher uncoated substrate area exposed to the electrolyte under the thicker coatings. Having a higher amount of copper oxide under a thicker coating than under a thinner one is not supported by the ToF-SIMS  $CuO_2^-$  ion profiles (Figure V.2). The reason for this

## Chapter V. Effect of copper substrate annealing on the corrosion protection of ALD alumina coatings

higher exposure of uncoated substrate areas to the electrolyte for thicker coatings is coating detachment or delamination, as evidenced by the data presented further on.

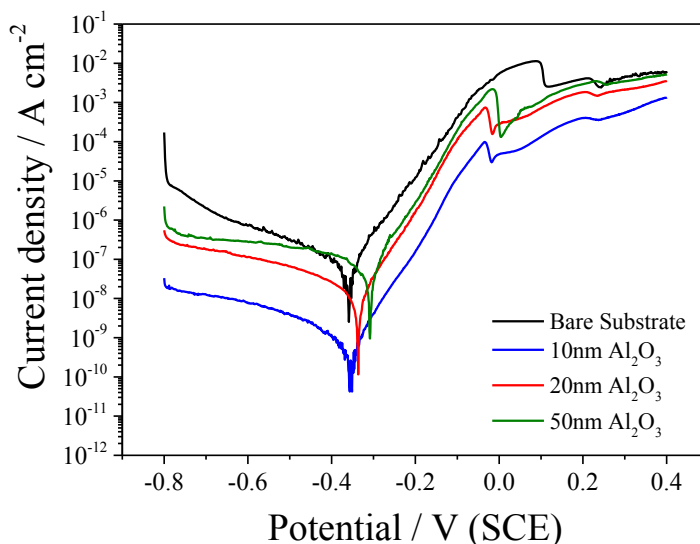


**Figure V.6:** LSV polarization curves for the bare and ALD alumina coated Cu annealed substrates in 0.5 M NaCl under argon bubbling (pH = 6), scan rate: 1 mV.s<sup>-1</sup>

**Table V.1:** LSV data and parameters related to Figure V.6

	$E_{\text{corr}} / \text{V (SCE)}$	$i_a \text{ (at } E = -0.2 \text{ V/SCE) / A.cm}^{-2}$	$R_p / \Omega.\text{cm}^2$	$ba / \text{V.dec}^{-1}$	$bc / \text{V.dec}^{-1}$
<b>Bare substrate</b>	-0.359	$1.19 \times 10^{-5}$	$2.61 \times 10^5$	0.070	-0.215
<b>Al<sub>2</sub>O<sub>3</sub> 10nm</b>	-0.356	$1.50 \times 10^{-7}$	$2.90 \times 10^7$	0.065	-0.360
<b>Al<sub>2</sub>O<sub>3</sub> 20nm</b>	-0.336	$1.52 \times 10^{-6}$	$1.68 \times 10^6$	0.064	-0.350
<b>Al<sub>2</sub>O<sub>3</sub> 50nm</b>	-0.308	$2.71 \times 10^{-6}$	$3.82 \times 10^5$	0.065	-

The anodic peaks for coated samples are shifted to lower potentials in comparison with the bare samples. As discussed in Chapter III, presence of more amount of interfacial copper oxide for the coated specimens than for the uncoated ones can account for this shift.

In order to compare the performance of the coatings in more details, the porosity values (wetted surface area under the coatings) were calculated from the polarization resistance

## Chapter V. Effect of copper substrate annealing on the corrosion protection of ALD alumina coatings

---

and anodic current using Eq. III.11 and Eq. III.12. The data are presented in Table IV.2. The lowest porosity (highest sealing) is obtained with the 10 nm coating, and as expected from the polarization curves, the porosity increases with coating thickness increase. One notices that the porosity values obtained from the anodic currents are higher than the ones obtained from  $R_p$  at OCP, and this difference increases for the higher porosities. The high porosity values obtained here and their increase with the anodic applied potential indicates coating loss and/or detachment, increasing with coating thickness increase. The porosity values obtained here at OCP for 10 nm are close to those obtained on the electropolished substrate, which suggests a higher stability and stronger attachment of the 10 nm coating to the substrate. Considering the ToF-SIMS profiles measured on pristine samples (before immersion in the electrolyte), there is no evidence for growth of a more defective coating on the annealed substrates, or increase of coating porosity with coating thickness. On the contrary, the porosity is suggested to decrease by the decrease of the  $\text{OH}^-$  intensity with coating thickness increase. As discussed in Chapter III, the porosity values obtained with our methods represent the cross section area at the end of the channels through the coating connecting the bulk electrolyte to the substrate. If the coating is not well-adherent to the substrate, delamination in the electrolyte can cause significant increase of this cross section area, leading to large values of the porosity. Therefore, it is suggested that the large porosity values obtained here are mostly due to the coating detachment/delamination affecting more severely the thicker coatings on the annealed samples.

**Table IV.2:** Porosity values obtained from LSV and EIS

	$P_{R_p}$ (LSV) / %	$P_{i_a}$ (LSV) / %	$P_{R_{ct}}$ (EIS) / %
<b>Bare substrate</b>	100	100	100
<b>Al<sub>2</sub>O<sub>3</sub> 10nm</b>	0.83	1.26	0.61
<b>Al<sub>2</sub>O<sub>3</sub> 20nm</b>	7.40	12.77	5.20
<b>Al<sub>2</sub>O<sub>3</sub> 50nm</b>	13.03	22.77	9.68

### **V.5. Electrochemical Impedance Spectroscopy**

The Bode plots at OCP for the bare and coated annealed substrates are presented in Figure V.7. The plot for the 10 nm coating has a similar shape to the one on the electropolished substrate with a wide range of capacitive response and high impedance module. In contrast, the plots for the 20 nm and 50 nm coatings show a considerable decrease in module and phase angle in comparison with the same coatings deposited on the electropolished substrate.

Here again, as discussed for the ALD coated electropolished samples, distinction between the coating and the substrate was not possible. Furthermore, the observation of decrease of frequency at HF for a constant phase angle with the increase of coating thickness means that the time constant at HF is higher for the thicker coatings ( $f = \frac{1}{2\pi RC}$ ). This suggests that the capacitance at HF is not dominated by the coating capacitance anymore. We tried to fit the EIS data with E.C.3 (Figure III.11.B); however, the obtained coating capacitance values were not acceptable for the present coatings. The reason is that the coating capacitance is not dominant at HF. Therefore, E.C.2 (Figure III.13) was used in a simpler approach for fitting, since, and as mentioned in Chapter III, E.C.2 is properly enough to evaluate the performance of the coating as long as no obvious existence of two time constants in the frequency range of study is observed.

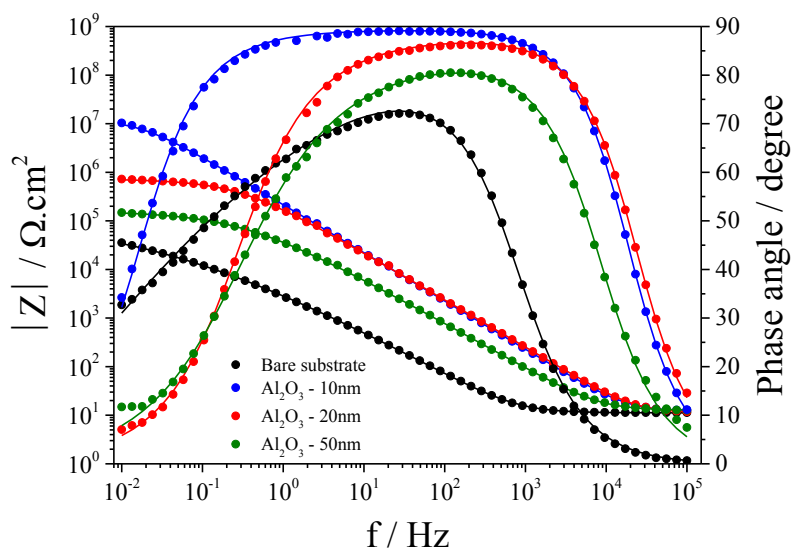


**Figure V.7:** EIS Bode plots for the bare and ALD alumina coated annealed copper substrates in 0.5 M NaCl under argon bubbling at OCP (pH = 6). Points and lines correspond to measured and fitted data, respectively

It should be mentioned that some hint of an extra time constant can be distinguished at the lowest frequencies in the phase angle plots of the 20 and 50 nm samples. This can be observed also in the Nyquist plot (Figure V.8) where a few points seem to start a new loop at LF for the 20 and 50 nm samples. These points correspond to anodic mass transport limitation *via* the copper oxide layer covering the substrate. This is in agreement with higher cathodic Tafel slope for the 20 nm specimen and cathodic plateau for the 50 nm sample observed by LSV. As mentioned in Chapter IV, a higher cathodic Tafel slope for copper samples in the conditions of LSV test in this thesis work is in agreement with higher reduction of oxygen on catalytic Cu(0)/Cu(I) sites, and presence of more Cu(I) species. Anodic mass transport related to the few points at LF was not taken into account in E.C.2 due to the low resolution of this loop (few points) in agreement with what was done by Torres *et al.* [123].

The fitting results are presented in Table V.3. The resistance values obtained from the fitting match well with the diameters of the depressed semicircles extrapolated to the real axis ( $Z_j = 0$ ) in the Nyquist graphs. Such an extrapolation cannot be done (or can be done with less precision) for the 10 nm sample, due to a higher time constant (RC) that leads

## Chapter V. Effect of copper substrate annealing on the corrosion protection of ALD alumina coatings

to reduction of the characteristic frequency ( $f = \frac{1}{2\pi RC}$ ) and makes possible the completion of the loop at frequencies out of the measured frequency range.

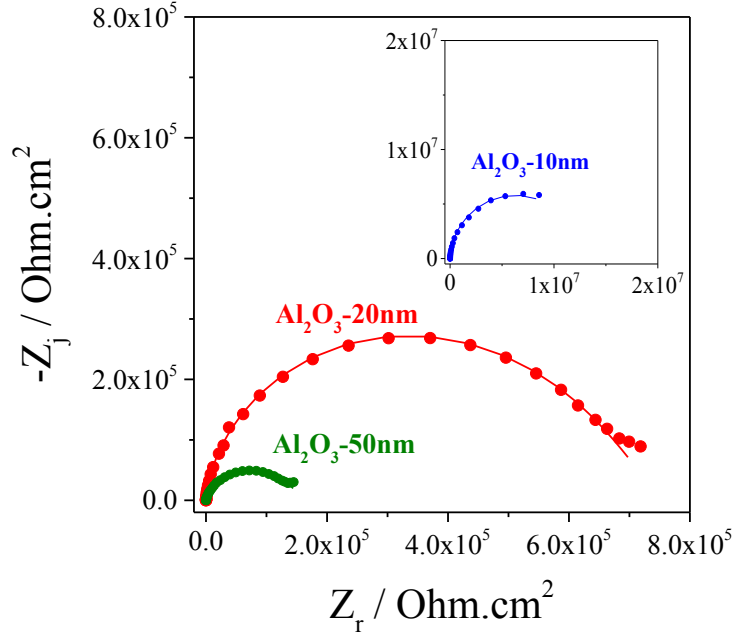


**Figure V.8:** EIS Nyquist plots for ALD alumina coated annealed copper substrates in 0.5 M NaCl under argon bubbling at OCP. Points and lines correspond to measured and fitted data, respectively

**Table V.3:** Results of EIS data (Figure V.7) fitted with E.C.2 (Figure III.13)

	$R_e / \Omega.cm^2$	$R_{ct}^a / \Omega.cm^2$	$Q / F.cm^{-2}.s^{(a-1)}$	$n$	$C_{eff} / F.cm^{-2}$	$S / \Omega.s^{-0.5}.cm^2$ ( $Z_w = \frac{S}{\sqrt{j\omega}}$ )
<b>Bare substrate</b>	11.18	$8.04 \times 10^4$	$3.57 \times 10^{-5}$	0.91	$1.73 \times 10^{-5}$	$1.02 \times 10^4$
<b>Al<sub>2</sub>O<sub>3</sub> 10nm</b>	12.31	$1.26 \times 10^7$	$7.36 \times 10^{-7}$	0.99	$6.85 \times 10^{-7}$	$1.53 \times 10^7$
<b>Al<sub>2</sub>O<sub>3</sub> 20nm</b>	11.43	$7.56 \times 10^5$	$7.55 \times 10^{-7}$	0.98	$5.87 \times 10^{-7}$	$1.33 \times 10^6$
<b>Al<sub>2</sub>O<sub>3</sub> 50nm</b>	12.73	$1.65 \times 10^5$	$2.90 \times 10^{-6}$	0.94	$1.47 \times 10^{-6}$	$1.73 \times 10^5$

Effective capacitance values ( $C_{eff}$ ) presented in Table V.3 are obtained using Eq. III.9. In the equivalent circuit used here (E.C.2, Figure III.13), CPE for coated specimens includes both the double layer capacitance ( $C_{dl}$ ) related to the substrate at the end of the channels through the coating and the coating capacitance ( $C_c$ ). As these two capacitances are in

## Chapter V. Effect of copper substrate annealing on the corrosion protection of ALD alumina coatings

---

parallel, the total capacitance can be estimated taking into account the surface coverage of the coating (porosity or wetted surface at the end of the channels through the coating) using Eq. V.1:

$$C = P \times C_{dl} + (1 - P) \times C_c \quad \text{Eq. V.1}$$

$C_{dl}$  for the bare substrate is of the order of  $10^{-5} \text{ F.cm}^{-2}$  and  $C_c$  (theoretical capacity of coatings) is in order of  $10^{-7} \text{ F.cm}^{-2}$ . Therefore for coatings with higher porosities (more than 1% ( $10^{-2}$ ))  $C_{dl}$  will become dominant while with decreasing the porosity  $C_c$  will be dominant. This is why for the 50 nm coating with the highest porosity ( $P \approx 10\%$  ( $10^{-1}$ ) Table V.2),  $C_{eff}$  obtained by the fitting is one order of magnitude higher than the theoretical capacitance ( $1.42 \times 10^{-7} \text{ F.cm}^{-2}$ ) for this coating. In this case  $C_{dl}$  is important and cannot be neglected in Eq. V.1. Thus, it is confirmed here that the reason for not seeing the increase of the phase angle at HF with increased coating thickness in the Bode plot is that  $C_c$  is not dominant for the 20 nm and 50 nm specimens. We remind that, contrary to here, for the coated electropolished specimens discussed in Chapter III, the first term in Eq. V.1 was negligible as a consequence of the low porosity of the coatings and the capacitance obtained from the fitting corresponded to the coating capacitance.

The Warburg coefficient (S) is higher for the coated substrates in comparison with the bare one due to the increased length of diffusion. However, it is smaller for the coatings with higher porosity as a result of the higher detached area exposed to the electrolyte and the consequent higher oxygen reduction.

The porosity ( $P_{R_{ct}}$ ) values were calculated from the  $R_{ct}$  values obtained from EIS and using Eq. III.15. They are presented in Table V.2. The 10 nm sample has the lowest porosity and the 50 nm sample the highest porosity as expected from the EIS plots and in agreement with the LSV results. The porosity values obtained from LSV at the corrosion potential are higher than those obtained from EIS at OCP. Furthermore,  $P_{i_a}$  values are the highest. This means that coating delamination happens very fast after immersion in the electrolyte and increases rapidly with the time of immersion (higher  $P_{R_p}$  from LSV than  $P_{R_{ct}}$  from EIS) and increases markedly (high  $P_{i_a}$  values) under the effect of anodic dissolution at applied increasing potential.

## Chapter V. Effect of copper substrate annealing on the corrosion protection of ALD alumina coatings

Figure V.9 presents porosity values obtained for different samples from the same deposition batch and for samples from another deposition batch. As it can be seen, the results are only partially reproducible, which is expected if the coating is detached or lost upon immersion.

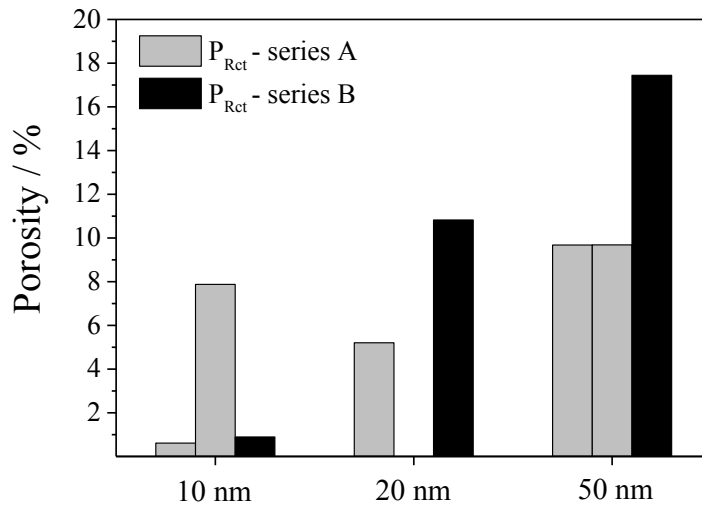


**Figure V.9:** Comparison of porosity values obtained for samples from the same and from different deposition batches on the annealed copper substrate

If ignoring the 10 nm sample of high porosity from series A and comparing the thicknesses in each series, one can say that coating detachment increases with increasing coating thickness, which was already observed for ALD coatings on stainless steel substrate with adhesion tests [66]. As discussed above, detachment of the coating happens mostly during immersion in the electrolyte. However, it is not clear if increased detachment for the thicker coatings is induced by electrochemical reactions, or results simply from a mechanical effect. Adhesion tests performed by Marin *et al.* [66] on pristine coatings revealed a mechanical effect linked to lower adhesion of thicker coatings. Furthermore, in the work of Miller *et al.* [147], it was shown that mechanical robustness of ALD alumina coating increased with decreasing coating thickness from 125 nm to 5 nm. Apart from the mechanical effect, higher delamination for thicker coatings can be linked to the oxygen reduction reaction and related local pH increase.

The cathodic reaction (Eq. III.6) occurring at the coating/substrate interface at the bottom of channel defects leads to a local increase of pH and to the resulting local dissolution of alumina [34] at the interface with the substrate, contributing to local delamination of the coating. It is suggested that local increase of pH at coating/substrate interface could be higher for a thicker coating due to the longer diffusion length of  $\text{OH}^-$  ion to reach the bulk electrolyte. Thus even if the primary reason for local coating detachment is a mechanical effect increasing with the deposited thickness, the detachment can be assisted by a delamination mechanism induced by electrochemical reactions, especially oxygen reduction which is favoured in presence of more copper oxide exposed where the coating is detached.

## **V.6. Scanning Electron Microscopy**

Scanning electron microscopy (SEM) images for the 50 nm specimens are displayed in Figure V.10. As it can be seen in Figure V.10.A (lower magnification) and Figure V.10.B (higher magnification), four types of regions are observed on the sample:

- Regions where the coating seems to be well attached and no defect is observable.
- Regions where the coating is detached and lost (Figure V.10.B). Examples of lost coating pieces are shown in Figure V.10.C and D.
- Regions where the coating remains on the substrate, but it is detached (coating lift-up). Such regions look like swollen bubbles as magnified in Figure V.10.E.
- Grain boundaries regions that appear well coated (Figure V.10.C) as also observed by ToF-SIMS imaging, as discussed in next section (V.7). The fact that the grain boundaries are well coated is a result of conformality of ALD coatings. The small features observable beside the grain boundary lines in Figure V.10.C are detached pieces of coating from other areas (for example from an area like the one in Figure V.10.B).

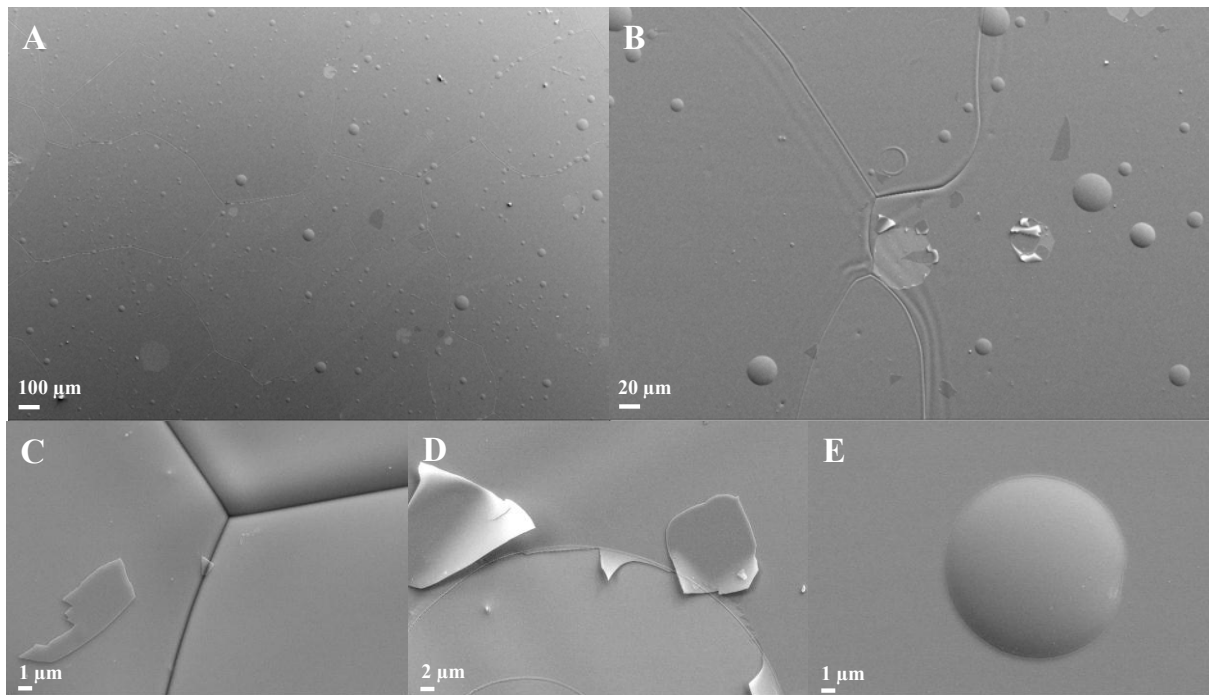


Figure V.10: SEM images of a 50 nm ALD alumina coating on the annealed copper substrate

Figure V.11 shows SEM images taken from a 20 nm sample after the polarization test. As it can be seen in Figure V.11.A and B, corrosion has happened both at the grain boundaries and in the grains, on places where the coating was lost before polarization (Figure V.10.B) and on other places, probably where the coating was detached before polarization (Figure V.10.E). Corrosion has propagated deeply at the grain boundaries although they seemed to be initially well coated (Figure V.10.C). It is proposed that, upon immersion, the electrolyte has reached the copper substrate *via* the channel defects in the coating. Then, corrosion has occurred faster at grain boundaries (*i.e.* preferential intergranular corrosion) and trenched the coating/substrate interface with liberation of corrosion products which has caused the coating to swell (Figure V.11.B) or to fracture in some parts (Figure V.11.D). Thus, although grain boundaries seemed to be initially well coated (Figure V.10.C), the coating adhesion in these sites appeared insufficient to counteract the local substrate corrosion initiated by the penetration of the electrolyte, the latter being possibly preferential at or near the substrate grain boundaries.

Therefore, it appears that relatively poor adhesion of the coating to the smooth (as a result of annealing) surface is one reason for corrosion of the substrate, as local

## Chapter V. Effect of copper substrate annealing on the corrosion protection of ALD alumina coatings

---

detachment of the coating is observed prior to immersion. However, immersion-induced local detachment and fracture of the coating as a result of corrosion-induced delamination occurring preferentially at grain boundaries and following electrolyte penetration to the interface appears as another reason for the increase of the uncoated area observed upon immersion.

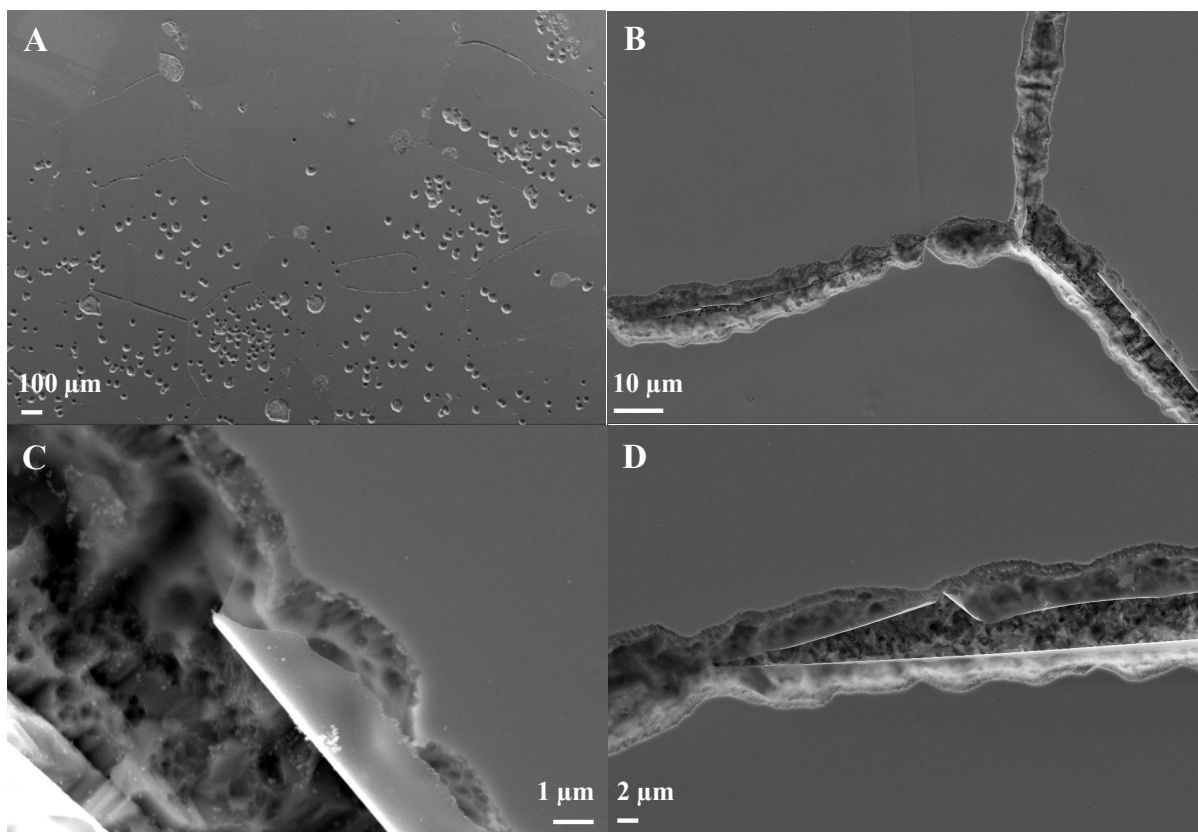


**Figure V.11:** SEM images taken from a 20 nm coating on copper annealed substrate after polarization in 0.5 M NaCl

### V.7. ToF-SIMS surface images

ToF-SIMS chemical maps (negative ions) for the 10 nm coating on annealed copper substrate are shown in Figure V.12. As shown by the images, the substrate is covered uniformly by the coating ( $O^-$  and  $AlO_2^-$  ions) and no defect is revealed by the substrate ions ( $Cu^-$  and  $CuO^-$ ) at the space resolution of the measurements, including at grain boundaries. The lines observed on  $O^-$  map correspond to the grain boundaries, but they

## Chapter V. Effect of copper substrate annealing on the corrosion protection of ALD alumina coatings

---

are coated and their appearance in the map is only due to roughness (*i.e.* shadowing) effect. Good coating coverage observed here for 10 nm coating is in agreement with its good electrochemical behaviour as discussed above.

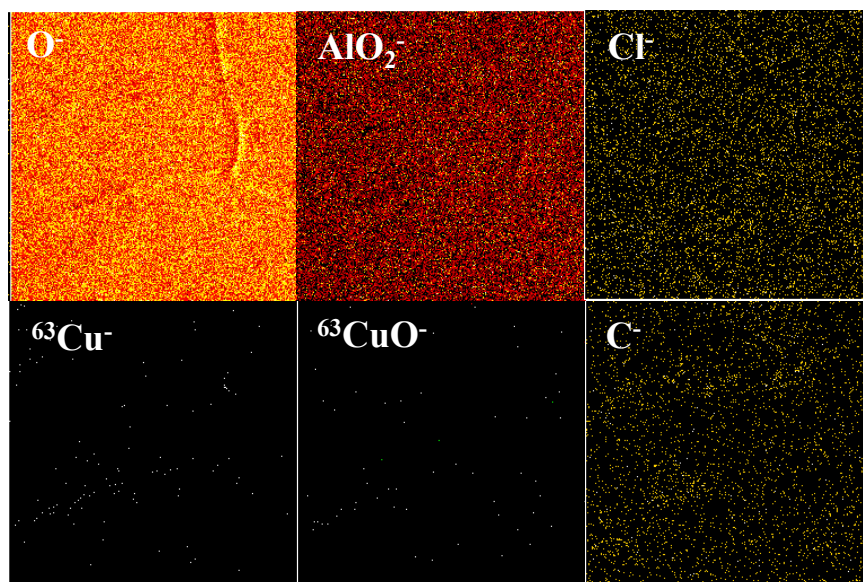


**Figure V.12:** ToF-SIMS surface images ( $100\ \mu\text{m} \times 100\ \mu\text{m}$ ) from the 10 nm coating on copper annealed substrate

For the 50 nm specimen (Figure V.13), a spot of  $20\ \mu\text{m}$  lateral size without coating is evidenced by the chemical map, as observed by SEM (Figure V.10.B). In the O<sup>-</sup> map, a dark ring is observed instead of a dark circle. In fact as the O<sup>-</sup> ions correspond not only to the coating ions, but also to oxygen generally, the intensity inside the ring is a result of oxygen coming from copper oxide on the substrate (as confirmed by the CuO<sup>-</sup> map). The dark colour at the circumference ring is also possibly due to, at least partially, the shadowing effect of the edge of the missing coating disk. Such a defect confirms the loss of the coating before immersion. Here again, there is no evidence of lack of coating on grain boundaries at the resolution of the ToF-SIMS images.

## Chapter V. Effect of copper substrate annealing on the corrosion protection of ALD alumina coatings

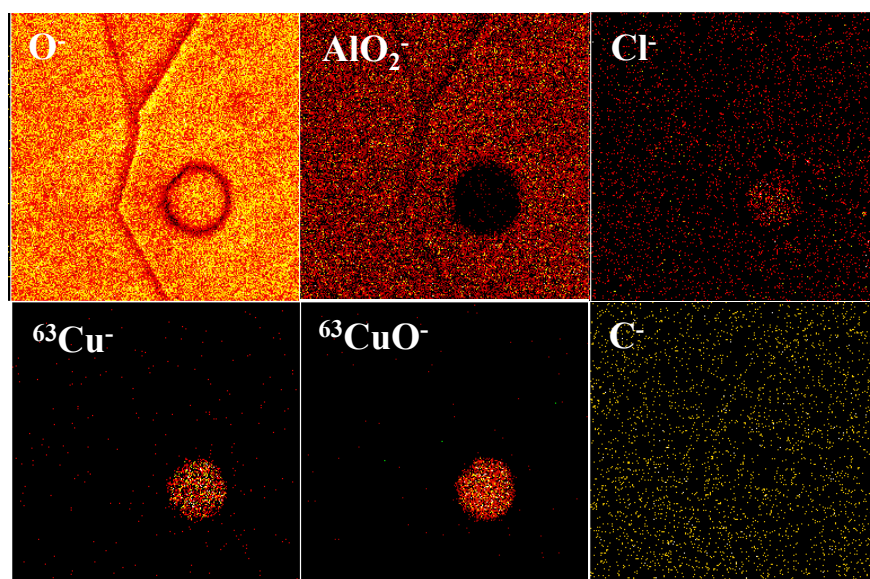


**Figure V.13:** ToF-SIMS chemical images ( $100\ \mu m \times 100\ \mu m$ ) from the 50 nm coating on copper annealed substrate

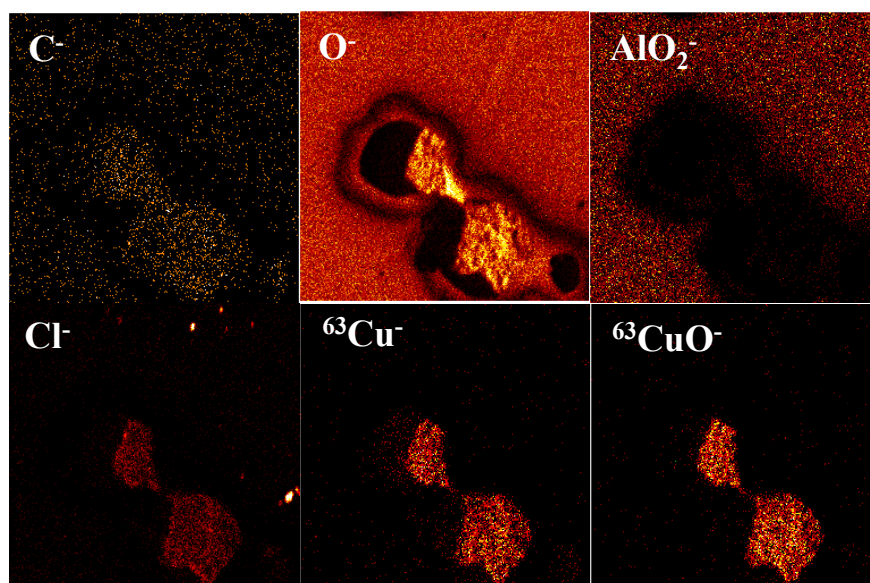


**Figure V.14:** ToF-SIMS surface images ( $100\ \mu m \times 100\ \mu m$ ) from the 20 nm coating on copper annealed substrate after the polarization test in 0.5 M NaCl

Figure V.14 presents chemical maps for the 20 nm sample after the polarization test. The presence of defect areas characterized by the lack of Al-containing ions and presence of Cu-containing ions indicates loss of coating in areas of tens of micrometres in lateral size. The presence of  $Cl^-$  on these areas indicates their corrosion. The similar size of these areas with those without coating observed in Figure V.10.B and Figure V.13, suggests

that localized corrosion of copper has happened on micrometric scale, where coating was initially detached and lost.

## **V.8. Conclusions**

In an effort to improve the corrosion protection properties of ALD alumina coatings on copper substrate, copper surface preparation was modified to include thermal annealing at 725°C. Although a better performance of ALD alumina coating was expected on a smoother substrate, the results evidenced poorer adhesion of the coatings on the smoother annealed copper substrate preventing the improvement of the corrosion protection.

ToF-SIMS depth profiling on the pristine coated samples confirmed the growth of alumina coating with sputtering rates (*i.e.* densities) close to the ones obtained on the electropolished substrate. Apart from decreasing the interfacial C<sup>-</sup> and Cl<sup>-</sup> contamination, annealing led to a surface smoothing under the coatings, as indicated by the profiles of the ions of the coating decreasing sharply in the substrate. The higher intensity of the CuO<sub>2</sub><sup>-</sup> and OH<sup>-</sup> ions on the annealed substrates implied detachment of the coatings, which was confirmed with electrochemical measurements as well as ToF-SIMS and SEM imaging. Although S<sup>-</sup> intensity was markedly decreased in the bulk substrate as a result of annealing, the same intensity of the S<sup>-</sup> peak was measured on the interface as a result of surface segregation. AFM imaging and the measured roughness confirmed surface smoothing of the substrate as a result of annealing.

The LSV measurements showed the increase of the corrosion potential and cathodic Tafel slopes for coated samples in comparison with the bare one. These variations were attributed to the presence of a more stable copper oxide present at the coating/substrate interface in comparison with the bare substrate, as discussed for electropolished samples. The increase of these variations on the annealed copper surfaces implies the detachment of the coating, leading to an increase of the uncoated area covered by copper oxide and exposed to the electrolyte. Detachment of the coatings was confirmed from porosity measurements. The EIS measurements led to calculation of porosity values lower than the values obtained from LSV, which confirmed instability of the coatings and increasing

## **Chapter V. Effect of copper substrate annealing on the corrosion protection of ALD alumina coatings**

---

detachment with increasing immersion time and anodic polarization. Evidence of anodic mass transport control was observed in the Bode and Nyquist plots for 20 and 50 nm specimens, where more copper oxide was exposed to the electrolyte.

SEM imaging of pristine samples (not immersed in the electrolyte) revealed the presence of grain boundaries covered by the coating. The loss of coating in some places indicated poor adhesion of the coating and its loss before polarization. After polarization, intergranular corrosion was observed in addition to corrosion inside the grains where the coating was lost as shown by ToF-SIMS chemical mapping.

The poor adhesion of alumina coating on smooth annealed copper substrate is concluded to be the major cause for local exposure of substrate to the air (or electrolyte, if immersed) in places where the coating is the most weakly bounded to the substrate. Once the substrate is exposed to the electrolyte upon immersion, penetration of the electrolyte through the channel defects of the coating leads to preferential intergranular corrosion of copper. Delamination by dissolution of the coating as a result of local pH increase, in addition to trenching of the substrate as a result of anodic dissolution of copper, promotes then the coating detachment. Combined with the release of corrosion products, this locally increases the mechanical pressure, eventually leading to the coating fracture observed by SEM at the grain boundaries of the copper substrate.

# **Chapter VI**

## **Durability of the corrosion protection of copper by ALD alumina coating**

### **VI.1. Introduction**

The corrosion protection of copper by ALD alumina coatings was studied in previous chapters. On electropolished copper, the alumina coatings showed remarkable properties, mostly due to excellent sealing of the substrate as a result of growth of coatings with low amount of channel defects. Due to the relationship between the coating growth and performance and the substrate surface state, the effects of different substrate preparations were studied. It was shown that the best results are obtained with electropolishing of the substrate and removal of the native copper oxide.

The electrochemical tests were performed in a Cl-containing electrolyte (0.5 M NaCl). Short immersion times were studied. Quantification of the porosity as an indicator to evaluate the exposure of the substrate to the electrolyte was used to judge the coating sealing performance. As explained in Chapter III, the measured porosity values are representative of the surface area of the substrate exposed to the electrolyte at the bottom of the defect channels through the coatings. Therefore, porosity values were electrochemically-determined quantities depending on the immersion conditions rather

## **Chapter VI. Durability of the corrosion protection of copper by ALD alumina coating**

---

than pristine properties of the coatings. However, they can be used to assess the coating performance due to short time of immersion. Apart from the sealing properties of a coating, its durability is of great importance to ensure a long life time of the corrosion protection.

In order to study the durability of alumina coatings on the copper substrate, longer immersion times were investigated. Electropolished copper was chosen as the substrate due to good results presented in Chapter III, and the native copper oxide was removed before coating deposition to avoid the detrimental effect of such an interfacial layer, as discussed in Chapter IV. Immersion tests were performed at OCP for six hours and corrosion was monitored by EIS measurements performed after 30 minutes at OCP and then repeated every one hour up to six hours of immersion. Argon bubbling was done in the electrolyte 30 minutes before immersing the sample, and was maintained during all six hours of immersion.

Although the initial aim of this study was to investigate the alumina coating durability in NaCl electrolyte during 6 hours of immersion, the fact that the coating was used nine months after its production, gave the opportunity to discuss the effect of the ageing in air.

### **VI.2. Electrochemical Impedance Spectroscopy**

The Bode plots obtained during the immersion tests are displayed in Figure VI.1. The spectra show essentially capacitive behaviour. No significant change is observed in the plots during and after the 6 hours immersion time, indicating good stability of the coatings in the electrolyte. Here again taking into account any separate time constant for the copper oxide layer on the substrate under the coating was not justified by the spectra and therefore the E.C.3 equivalent circuit (Figure III.11.B) was used for fitting the EIS. The results are reported in Table VI.1.

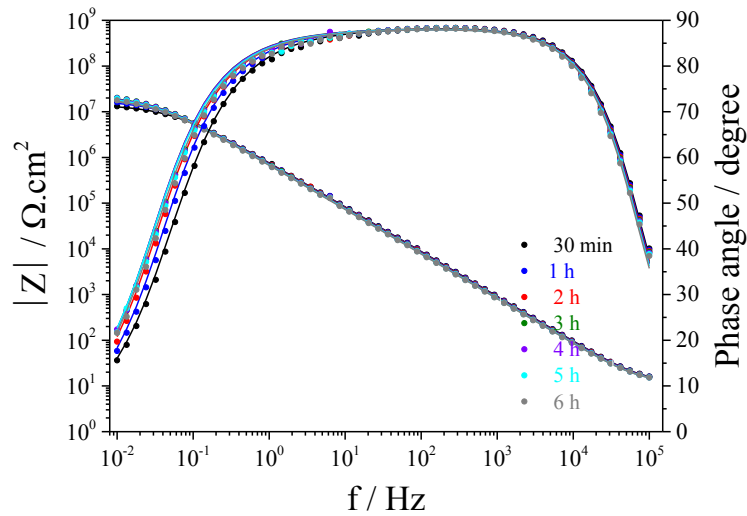


**Figure VI.1:** EIS Bode plots *versus* time for the 50 nm ALD alumina coated electropolished pre-treated copper substrate in 0.5 M NaCl under argon bubbling (pH = 6) at OCP. Points and lines correspond to measured and fitted data, respectively

The coating effective capacitance value (Eq. III.9) is higher than that for the 50 nm coating in Chapter III (see Table III.7). Considering Eq. III.13, an increase of the capacitance can be a result of a decrease of the coating thickness. An increase of the capacitance can also be a result of an increase of the general dielectric constant of the coating. This possibility is excluded since a coating thickness decrease is confirmed by the ToF-SIMS profiles presented in the following section (VI.3). The coating thickness values were calculated applying Eq. III.13 and using the effective capacitance values obtained from the fitting (Table VI.1). The results are presented in Figure VI.2. It should be mentioned that the effect of porosity in surface area in Eq. III.13 is neglected here, due to the very low value of the cross section area of the channels inside the coating (as discussed in Chapter III) [146].

## Chapter VI. Durability of the corrosion protection of copper by ALD alumina coating

**Table VI.1:** EIS results related to Figure VI.1 fitted to E.C.3 (Figure III.11.B)

	$R_e / \Omega.cm^2$	$R_{pore} / \Omega.cm^2$	$R_{ct}^a / \Omega.cm^2$	$R_{total} / \Omega.cm^2$	$Q_c / F.cm^{-2}.s^{(\alpha-1)}$	$n_c$	$C_{eff-c} / F.cm^{-2}$	$Q_{dl} / F.cm^{-2}.s^{(\alpha-1)}$	$n_{dl}$	$C_{eff-dl} / F.cm^{-2}$	$S / \Omega.s^{-0.5}.cm^2$ ( $Z_W = \frac{S}{\sqrt{j\omega}}$ )	$E_{ocp} / V (SCE)$
<b>30 min</b>	12.27	$1.68 \times 10^6$	$1.31 \times 10^7$	$1.48 \times 10^7$	$2.00 \times 10^{-7}$	0.98	$1.63 \times 10^{-7}$	$1.21 \times 10^{-8}$	0.99	$1.19 \times 10^{-8}$	$1.28 \times 10^7$	-0.361
<b>1 hour</b>	12.24	$2.25 \times 10^6$	$1.56 \times 10^7$	$1.78 \times 10^7$	$2.07 \times 10^{-7}$	0.98	$1.66 \times 10^{-7}$	$1.05 \times 10^{-8}$	0.99	$1.01 \times 10^{-8}$	$1.51 \times 10^7$	-0.363
<b>2 hours</b>	12.16	$3.49 \times 10^6$	$1.71 \times 10^7$	$2.06 \times 10^7$	$2.12 \times 10^{-7}$	0.98	$1.70 \times 10^{-7}$	$1.80 \times 10^{-8}$	0.99	$1.75 \times 10^{-8}$	$1.56 \times 10^7$	-0.368
<b>3 hours</b>	12.10	$4.07 \times 10^6$	$1.88 \times 10^7$	$2.29 \times 10^7$	$2.16 \times 10^{-7}$	0.98	$1.73 \times 10^{-7}$	$1.78 \times 10^{-8}$	0.99	$1.73 \times 10^{-8}$	$1.67 \times 10^7$	-0.369
<b>4 hours</b>	11.99	$3.20 \times 10^6$	$1.93 \times 10^7$	$2.25 \times 10^7$	$2.23 \times 10^{-7}$	0.98	$1.76 \times 10^{-7}$	$1.13 \times 10^{-8}$	0.99	$7.72 \times 10^{-9}$	$1.68 \times 10^7$	-0.370
<b>5 hours</b>	11.98	$3.53 \times 10^6$	$1.82 \times 10^7$	$2.17 \times 10^7$	$2.26 \times 10^{-7}$	0.98	$1.79 \times 10^{-7}$	$1.79 \times 10^{-8}$	0.99	$1.74 \times 10^{-8}$	$1.51 \times 10^7$	-0.372
<b>6 hours</b>	11.99	$3.18 \times 10^6$	$1.70 \times 10^7$	$2.02 \times 10^7$	$2.34 \times 10^{-7}$	0.98	$1.82 \times 10^{-7}$	$1.21 \times 10^{-8}$	0.99	$1.17 \times 10^{-8}$	$1.41 \times 10^7$	-0.369

## Chapter VI. Durability of the corrosion protection of copper by ALD alumina coating

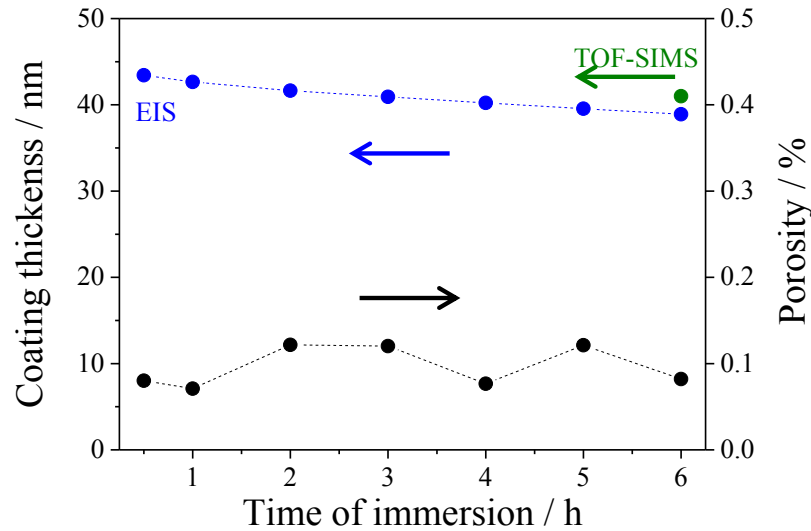


**Figure VI.2:** Coating thickness and porosity *versus* immersion time in 0.5 M NaCl (pH = 6) and under argon bubbling, obtained from EIS and ToF-SIMS

As shown in Figure VI.2, the thickness value after 30 minutes is about 44 nm. A decrease of 6 nm in the coating thickness during the first 30 minutes of immersion does not seem probable, given the speed of dissolution measured in the remaining 5 hours of immersion test. Therefore, it is suggested that this 6 nm decrease of the coating thickness mostly occurred during the nine months exposure to the ambient, possibly as a result of atmospheric corrosion. After 6 hours immersion of the sample in the electrolyte, the coating thickness is calculated to be 39 nm, indicating a 5 nm decrease of coating thickness during the immersion test.

Figure VI.3 illustrates the evolution of  $R_{\text{pore}}$ ,  $R_{\text{ct}}^a$  and  $C_{\text{dl}}$  besides  $C_{\text{coating}}$  values during the immersion test, as obtained from the fitting. The values obtained for  $R_{\text{pore}}$  and  $R_{\text{ct}}^a$  after 30 minutes of immersion are about one order of magnitude lower than the values obtained for 50 nm coating in Chapter III (see Table III.7). It is suggested that atmospheric corrosion of the coating during storage has led to pore opening by dissolution along the walls and at the end of the channel defects leading to one order of magnitude decrease of the  $R_{\text{pore}}$  and  $R_{\text{ct}}^a$  values. The decrease in  $R_{\text{pore}}$  is a direct indication of the degradation of the coating [146]. The same decrease in  $R_{\text{ct}}^a$  indicates that it is a direct consequence of decrease in  $R_{\text{pore}}$ . After 30 minutes, the increase and then decrease

## Chapter VI. Durability of the corrosion protection of copper by ALD alumina coating

of  $R_{\text{pore}}$  and  $R_{\text{ct}}^a$  indicates blocking and unblocking inside or at the end of the channels by corrosion products, in agreement with slight decrease and increase in  $E_{\text{OCP}}$  (Table VI.1). This suggests the formation of less conductive corrosion products at the end of channels and their subsequent dissolution. Similarly, small fluctuations in  $C_{\text{dl}}$  are in agreement with blocking and unblocking at the end of channels. Porosity values obtained from comparison of  $C_{\text{dl}}$  values using Eq. III.16 are presented in Figure VI.2. Slight fluctuations in the porosity values during immersion are in agreement with the build-up and dissolution of the corrosion products in the channels.

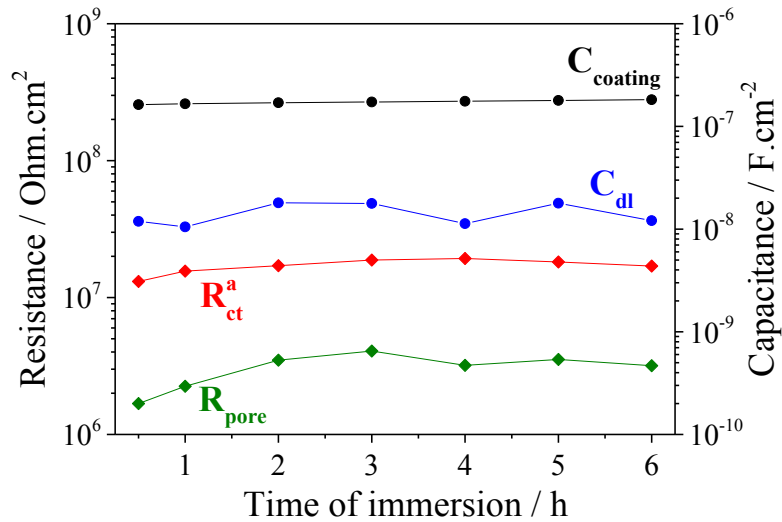


**Figure VI.3:** EIS parameters *versus* immersion time (Table VI.1) obtained from fitting of EIS results of Figure VI.1 with E.C.3 (Figure III.11.B)

Dissolution of ALD alumina coating was already observed on the carbon steel substrates, immersed in 0.2 M NaCl (under argon bubbling) [118], although alumina is supposed to be stable in neutral conditions [148]. Local increase of pH as a result of oxygen reduction on the substrate at the bottom of the channels where the substrate is connected to the electrolyte was proposed to initiate dissolution reaction of alumina [118]. For general dissolution of alumina at the outermost surface of the coating, hydroxide ions produced by oxygen reduction (Eq. III.6) at the bottom of the pores should diffuse in the electrolyte and reach the outermost surface of the coating, where they can trigger an overall dissolution on the surface of the coating [118]. Therefore, for dissolution of the coating to happen, existence of channel defects connecting the substrate to the electrolyte through

## Chapter VI. Durability of the corrosion protection of copper by ALD alumina coating

---

the coating is necessary. The one order of magnitude lower  $R_{\text{pore}}$  and  $R_{\text{ct}}^a$  values obtained initially here in comparison with the fresh coating studied in Chapter III suggests that the same mechanism could operate for the atmospheric corrosion observed after one year of ageing. Oxygen reduction would take place at the end of the channels and hydroxide diffusion to the outermost surface of the coating *via* the condensed layer of humidity as electrolyte would trigger coating surface dissolution, in addition to coating dissolution inside the pores leading to channel opening. Even though a more concentrated electrolyte was used in the present study (0.5 M vs 0.2 M) in comparison with the study done on the carbon steel substrate [118], coating surface dissolution was much less here (0.9 nm.h<sup>-1</sup> vs 7 nm.h<sup>-1</sup>). This is linked to the lower surface area exposed by the open channel defects (lower porosity values) necessary for the oxygen reduction reaction and associated hydroxide production. Therefore, it is supposed that if a fresh coating was used in the immersion test, the dissolution rate would be less than what was observed here for an aged coating.

### VI.3. Time-of-Flight Secondary Ion Mass Spectrometry

Figure VI.4 displays the ToF-SIMS depth profiles taken after the 6 h immersion test. Comparing these profiles and the ones presented in Figure III.5.C for a pristine 50 nm coating and assuming an equal sputtering rate of the coating in both cases, a decrease in coating thickness of about 10 nm is obtained from the decrease of coating region sputtering time (610 s vs 500 s). The 10 nm value obtained by ToF-SIMS is in good agreement with the value obtained from the EIS results (11 nm). Considering the difference in the size of analysis area used in ToF-SIMS and EIS, the close values obtained indicate that the small area used in ToF-SIMS (100 × 100 μm<sup>2</sup>) is well representative of the larger area (0.29 cm<sup>2</sup>) probed by EIS. This also indicates homogeneous dissolution of coating at the micrometric scale. The same interfacial width (100 nm) observed here and for the pristine coating (see Figure III.5.C) indicates absence of major change of interfacial species and roughness. The absence of Cu-containing ions in the bulk of the coating means absence of any defect in the coating with a lateral size detectable by ToF-SIMS (> 50 nm in this case).

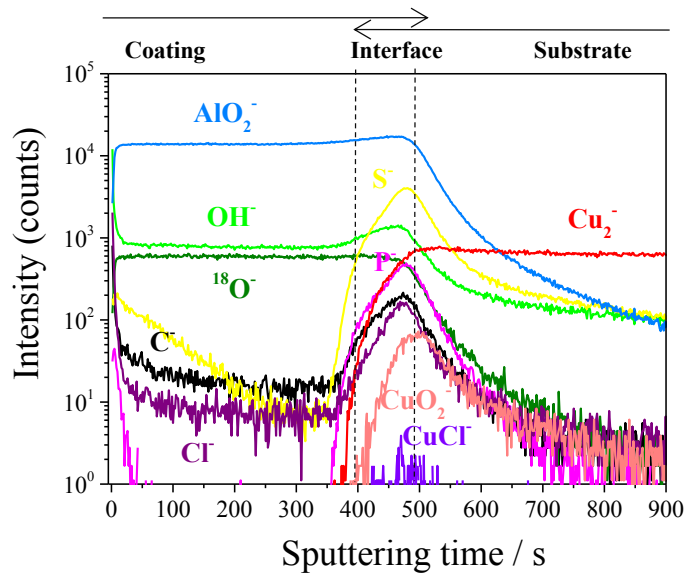


**Figure VI.4:** ToF-SIMS negative ions depth profiles for 50 nm ALD alumina coatings on electropolished copper substrate after immersion test

A comparative representation of each ion for the aged-immersed sample in the present case with the fresh-pristine one in Chapter III is displayed in Figure VI.5. The same time shift observed for all the ions is in agreement with the decrease of coating thickness. The intensity of the coating and substrate ions are unchanged, indicating no marked change in the coating matrix. In the bulk of the coating, except for  $\text{OH}^-$  and  $\text{S}^-$  ions, no difference is observed between the profiles indicating no significant change of the coating induced by the immersion test. As mentioned in Chapter IV, the decrease of  $\text{OH}^-$  after immersion can be attributed to the substitution of hydroxyl groups by chlorides in the channel defects [118]. However, no increase of chloride in the bulk of the coating is detected in the  $\text{Cl}^-$  profile. An initial lower amount of  $\text{OH}^-$  residual contamination for the aged-immersed sample (*i.e.* before immersion) is thus suggested. In any case, the absence of higher level of  $\text{OH}^-$  (and  $\text{Cl}^-$ ) in the bulk of the coating for the aged-immersed sample, excludes the possibility of a water uptake in the coating, and confirms the decrease of the coating thickness as the main origin of increase of the coating capacitance.

## Chapter VI. Durability of the corrosion protection of copper by ALD alumina coating

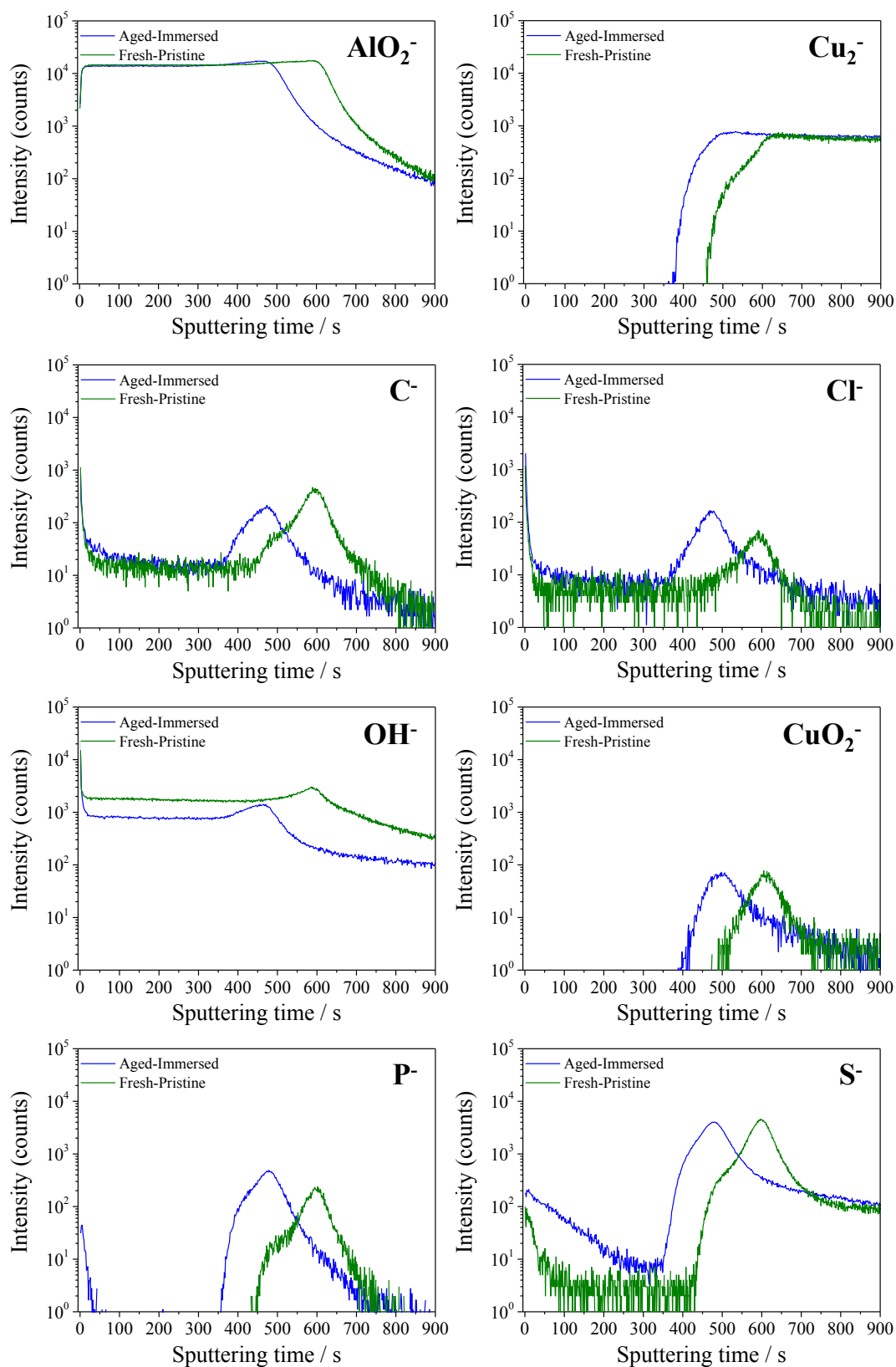


**Figure VI.5:** Comparative representation of ToF-SIMS depth profiles for 50 nm aged-immersed coating with a fresh-pristine one

At the interface, only the  $\text{Cl}^-$  ion profile shows a higher intensity after immersion. If the higher interfacial intensity of the  $\text{Cl}^-$  ion for the aged-immersed sample is a consequence of immersion, the observation of this increase only at the interface (and not in the bulk coating) is in agreement with the penetration and accumulation of electrolyte more at the bottom of the channel defects in the coating in comparison with the bulk coating, due to trenching of the substrate under the coating, as discussed in Chapter III. The same intensity of  $\text{CuO}_2^-$  for both samples suggests no major change of the copper oxide layer, present at the interface between the coating and the substrate. Due to the fact that for long immersion times, formation of  $\text{Cu}_2\text{O}$  by hydrolysis of  $\text{Cu(I)}$  species is expected [5], the absence of significant change in the copper oxide interfacial layer is in agreement with a low corrosion rate of the substrate. The negligible intensity of  $\text{CuCl}^-$  at the interface (Figure VI.4) excludes formation of pits or accumulation of corrosion products on the substrate surface, detectable by ToF-SIMS.

#### **VI.4. Atomic Force Microscopy**

Figure VI.6 shows the surface morphology of the 50 nm coated copper substrate after the 6 h immersion test. Roughness remains almost unchanged ( $\sim 4$  nm over  $1 \times 1 \mu\text{m}^2$ , vs  $\sim 3$ -4 nm and  $\sim 6$  nm for the bare and pristine fresh 50 nm coated samples respectively) in agreement with unchanged interfacial width in ToF-SIMS analysis. The detailed morphology observed on the flatter areas of the substrate is essentially similar to that observed before electrochemical analysis, however with slightly different dimensions. The grains (or nodules) have a lateral size of  $35 \pm 12$  nm and the depth at internodular sites is  $1.9 \pm 1.13$  nm. Comparing these dimensions with the ones ( $40 \pm 8$  nm and  $0.7 \pm 0.3$  nm) obtained for pristine coating discussed in Chapter III, a significant increase of the depth at internodular sites (between next nearest-neighbour nodules) is noticed, like observed after the LSV polarization test. Inhomogeneous dissolution of the coating at the nanometric scale results here from internodular preferential dissolution of the coating while the effect of homogeneous dissolution of the coating is only observed by EIS and ToF-SIMS. It should be mentioned that inhomogeneous dissolution of the coating here is

not in contradiction with unchanged roughness values, but implies that the roughness is ruled by the substrate.

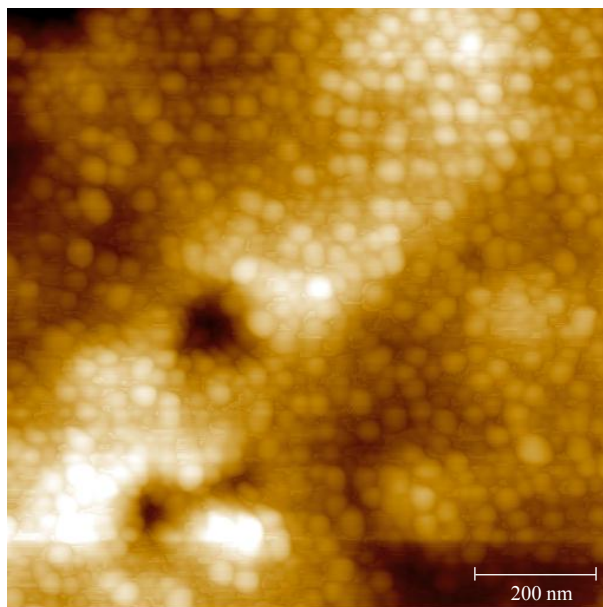


**Figure VI.6:** Topographic AFM image ( $1 \times 1 \mu\text{m}$ ) of 50 nm ALD alumina coated Cu substrate after immersion test,  $z$  range = 35 nm

### VI.5. Conclusions

The coating durability was studied on a 50 nm ALD alumina coating deposited on a copper electropolished substrate. Using a specimen aged for one year provided the opportunity to discuss coating degradation in air.

EIS showed good stability of the coating during the immersion test, however with a capacitance increase indicative of a decrease in the coating thickness. The initially lower resistance and capacitance values obtained for the aged coated specimen in comparison to an equivalent fresh one was assigned to atmospheric corrosion during the nine months storage of the sample. Coating dissolution of  $9.69 \times 10^{-4} \text{ nm}\cdot\text{h}^{-1}$  in ambient air and  $0.9 \text{ nm}\cdot\text{h}^{-1}$  in 0.5 M NaCl were calculated from the EIS data. Even though the coating dissolved during the immersion test, its porosity was unchanged.

## Chapter VI. Durability of the corrosion protection of copper by ALD alumina coating

---

ToF-SIMS depth profiling done on the sample after immersion confirmed that the increase in coating capacitance was related to the coating thickness decrease. The similar values of the coating thickness decrease obtained by ToF-SIMS and EIS indicated homogeneous dissolution at the microscopic scale. Apart from the coating thickness decrease, comparison of the depth profiles for the aged-immersed sample with a fresh-pristine sample indicated the absence of marked change in the coating matrix and absence of marked corrosion of the substrate.

Non homogeneous dissolution of the coating was evidenced at the nanometric scale by AFM images with internodular preferential dissolution. The limited lifetime of the alumina protection barrier in highly corrosive solution, anticipated from AFM images in Chapter III, was confirmed in this chapter for ageing in ambient air and for immersion in corrosive electrolyte.

Given the remarkable sealing property (low porosity) of the ALD alumina coating on electropolished copper substrate, despite its relatively low chemical stability (leading to thickness decrease both in ambient and in corrosive aqueous solution), the combination (mixtures or laminates) of alumina coating with more chemically stable (with a bit lower sealing properties) ALD coatings is proposed as a strategy to produce more durable ultrathin ALD coatings as already studied [63,130].

# **Chapter VII**

## **Investigation of corrosion protection of aluminium by ALD alumina coatings and effect of deposited layer thickness**

### **VII.1. Introduction**

Aluminium is generally passive and corrosion resistant in neutral aqueous solutions due to the passive oxide film that forms rapidly on the surface. However, in the presence of aggressive ions like chlorides, pitting corrosion occurs [19–21,28]. Like all other passive metals, aluminium is sensitive to localized corrosion where the passive oxide film breaks down locally. This breakdown leads to the formation of pits that grow once favourable conditions for their propagation are established [149].

While the corrosion of aluminium is localized at neutral pH conditions and happens mostly by pitting, generalized corrosion takes place at low or high pH by uniform dissolution of the protective oxide layer. In this case the rate of dissolution of the oxide layer is faster than its rate of formation [149].

## **Chapter VII. Investigation of corrosion protection of alumina by ALD coatings and effect of deposited layer thickness**

---

Although the passive oxide on aluminium is rather protective against corrosion, corrosion of aluminium alloys always occurs locally due to the presence of intermetallic second phase particles. In this chapter, the corrosion protection of aluminium by aluminium oxide is studied, but with an ALD alumina layer of controlled nanometric thickness. Controlling the deposition of ALD alumina layer by layer produces high quality films, as explained in Chapter I, and makes it a strong potential candidate for corrosion protection, as confirmed in Chapter III for copper. On aluminium, ALD alumina films can be more protective than the naturally formed passive film on the metal due to their high homogeneity, their stoichiometry and amorphous structure (absence of crystalline defects).

In the present work, apart from the study of the corrosion protection properties of ALD alumina on aluminium, the effect of the deposited layer thickness was also investigated with 10, 20 and 50 nm thick coatings. In contrast to what was done in the case of copper, no effort was done before coating deposition to remove the native oxide layer on the substrate or to markedly reduce the surface roughness of the aluminium substrate by electropolishing.

### **VII.2. Electrochemical behaviour of bare Al substrate**

#### **VII.2.1. Corrosion mechanisms**

As mentioned above, although a passive oxide film forms on aluminium and blocks generalized corrosion, localized corrosion occurs by pitting in chloride-containing neutral solutions. The mechanism of corrosion of aluminium in aggressive neutral solutions is based on the dissolution of aluminium from active sites or defects (flawed regions) in the passivating aluminium oxide [20].

The native oxide film on aluminium has been described as formed of two parts [149,150]. The inner part, attached to the metal, would be a compact amorphous layer with dielectric properties, forming rapidly on the metal surface by a solid state mechanism. The growth of this layer would be promoted at higher temperatures and the

## Chapter VII. Investigation of corrosion protection of alumina by ALD coatings and effect of deposited layer thickness

---

thickness would reach a few nanometres [149]. Above this inner layer, an outer layer would form, and grow by exchange reactions with the environment including hydration. The thickness of this layer would increase, depending on the humidity and temperature, up to tens of nanometres [149].

The passive oxide forms on aluminium by the anodic reaction according to Eq. VII.1:



Dissolution of aluminium takes place according to Eq. VII.2, which will finally lead to the onset of stable pitting and breakdown of the passive film [149]:



The cathodic reaction can be the evolution of hydrogen (Eq. VII.3) and/or the reduction of oxygen (Eq. VII.4, for neutral or alkaline conditions) [149]:



Pitting corrosion happens as a result of the breakdown of the passive oxide film. Chloride ions from the environment are adsorbed (coulombic forces and electrostatic induction of substrate by approaching ions [21]), and would penetrate into the oxide. The mechanism of penetration of chlorides in the oxide have been proposed to be by migration through oxygen vacancies [21,28], water channels [150], cracks or flaws in the oxide [20]. The incorporation of  $\text{Cl}^-$  would happen in localized sites due to the inhomogeneity of flaws in the oxide [20]. In other words, less defective oxide films would be more resistant to pitting initiation [20]. Oxide film breakdown would happen when the cation vacancies, generated to compensate the charge difference related to the incorporation of chloride ions in the oxygen anion vacancies, would agglomerate forming voids at the metal interface [20].

Localized dissolution or thinning of the oxide have also been proposed to cause the breakdown and initiate pitting [151]. Transitory compounds such as  $\text{Al}(\text{OH})_2\text{Cl}$ ,

## Chapter VII. Investigation of corrosion protection of alumina by ALD coatings and effect of deposited layer thickness

---

$\text{Al}(\text{OH})\text{Cl}_2$  and  $\text{AlCl}_3$  would be formed consecutively as a result of the incorporation of  $\text{Cl}^-$  into the oxide film [19,151]. They would finally dissolve as an Al complex ion ( $\text{AlCl}_4^-$ ) and diffuse in the bulk electrolyte [152], thus leading to local breakdown.

Before pitting starts, metastable pits are formed. Metastable pits are very small, grow and repassivate in a few seconds [20]. For metastable pits to not repassivate and to become stable, a critical value of the product of pit depth times pit current density should be reached [21,153]. For pit growth (stable pitting), both acidification and increase of concentration of chloride ions are necessary [20]. The hydrolysis of dissolved aluminium ions produces the acidic environment [21]. It should be mentioned that for chloride-assisted dissolution reactions to happen, water molecules must enter the oxide (usually *via* flaws or weak spots) and be present at the base of the oxide film to provide the electrolyte required for localized dissolution [21].

### VII.2.2. Linear Sweep Voltammetry

The aluminium samples of the present study were polished according to the procedure detailed in Chapter II, and stored for one month in membrane boxes in a desiccator before being immersed in the electrolyte. This one month ageing was done in order to have the same native oxide layer on the bare substrate and under the coating for coated samples. It should be reminded that this time lapse was inevitable as the samples were coated in another laboratory (at the University of Helsinki). The polarization curve obtained by LSV for the Al substrate is presented in Figure VII.1. The potential was switched from OCP to -1.8 V/SCE and stepped positive-going. Polarization conditions are as detailed in Chapter II. Parameters related to the polarization measurements are compiled in Table VII.1.

The corrosion potential is measured here at -1.46 V/SCE. Depending on the native oxide and the polarization conditions, the corrosion potential varies significantly. Anodic and cathodic reactions are as mentioned above (see section VII.2.1). No plateau related to the reduction of oxygen was observed when polarization was conducted from OCP and negative-going. Moreover, no marked difference was observed when the polarization test

## Chapter VII. Investigation of corrosion protection of alumina by ALD coatings and effect of deposited layer thickness

was performed without argon bubbling. As a result, it is assumed that the cathodic reaction is mostly hydrogen evolution, which is expected to be dominant at such low potentials [22].

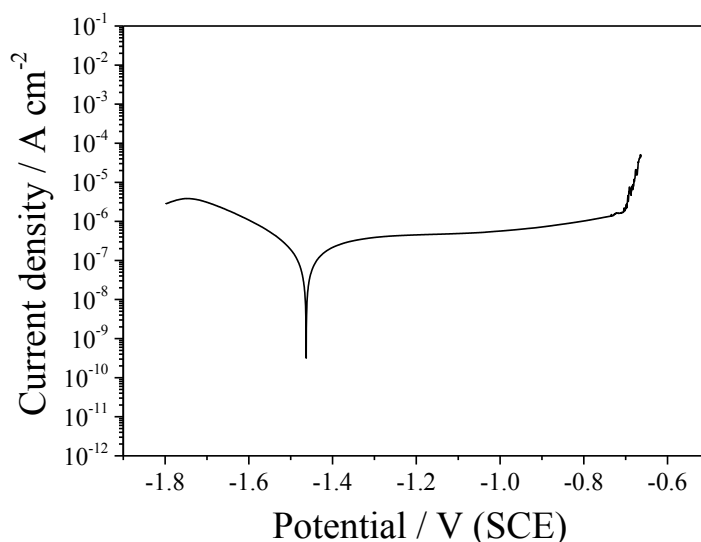


**Figure VII.1:** LSV polarization curve for bare aluminium in 0.5 M NaCl, under argon bubbling (pH = 6), scan rate: 1 mV.s<sup>-1</sup>

**Table VII.1:** Calculated LSV parameters related to Figure VII.1

	$E_{\text{corr}} / \text{V (SCE)}$	$E_{\text{pit}} / \text{V(SCE)}$	$i_{\text{pass}} / \text{A.cm}^{-2}$	$R_p / \text{Ohm.cm}^2$	$R_{\text{pass}} / \text{Ohm.cm}^2$
<b>Bare substrate</b>	-1.463	-0.706	$5.00 \times 10^{-7}$	$2.31 \times 10^5$	$1.23 \times 10^6$

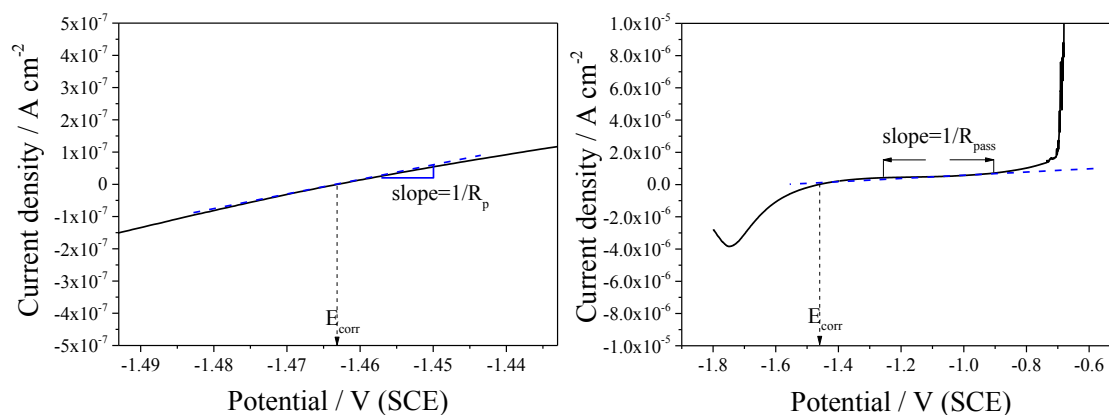


**Figure VII.2:** Illustration of measurement of  $R_p$  and  $R_{\text{pass}}$  from the linear  $i$ - $E$  curves

## Chapter VII. Investigation of corrosion protection of alumina by ALD coatings and effect of deposited layer thickness

---

The polarization curve obtained here is comparable with other studies [23,24,31,154]. The anodic plateau, extending from -1.46 to -0.71 V/SCE, evidences a passive domain due to the presence and possible thickening of aluminium oxide on the aluminium surface. In the passive potential region, the adsorption of chloride ions has been reported to increase with increasing potential up to the pitting potential, where a sharp increase in anodic current marks the onset for stable pit growth [23]. The pitting potential is defined as the potential below which the metal surface remains passive and above which the pitting corrosion starts to propagate [155]. It is observed here at -0.71 V/SCE. Metastable pitting has been observed in the anodic plateau region before the pitting potential [23], at which point the specific conditions for stable pit growth are established [20]. After reaching the pitting potential at -0.7 V/SCE the current increased rapidly and constantly.

Al<sub>2</sub>O<sub>3</sub> has insulating dielectric properties. However, the oxide film grown on Al in aqueous solutions exhibits semiconductive properties as a result of its non stoichiometric composition and its local structural inhomogeneities [20]. In other words, the small current measured during polarization of Al in spite of the low conductivity expected for Al<sub>2</sub>O<sub>3</sub> can be viewed as a result of the presence of defects in the oxide film [20].

The polarization resistance was obtained (Figure VII.2) from the reciprocal of the slope of the linear i-E curve close to corrosion potential ( $E_{\text{corr}} \pm 20\text{mV}$ ). The reciprocal of the slope of the linear i-E polarization curve on the anodic plateau (-1.373 to -0.903 V/SCE) was estimated (Figure VII.2) and used as  $R_{\text{pass}}$  corresponding to the polarization resistance of the passive anodic region [19,22]. The higher resistance obtained in the anodic passive region ( $R_{\text{pass}}$ ) in comparison with the polarization resistance at the corrosion potential ( $R_p$ ) has been related to the increase of the charging resistance and thickening of the oxide film before breakdown [25,26]. The increase of resistance before the pitting potential has been attributed to the incorporation of Cl<sup>-</sup> ions into the aluminium oxide film which would inhibit anodic dissolution rather than enhancing it [24]. It was proposed that the incorporation of chloride into oxygen vacancy sites would decrease their transport and thus lead to a lower conductivity (higher resistivity) of the oxide film [24].

### VII.2.3. Electrochemical Impedance Spectroscopy

The Bode (and Nyquist) plots for the EIS data measured at OCP for the bare Al substrate in 0.5 M NaCl are shown in Figure VII.3.

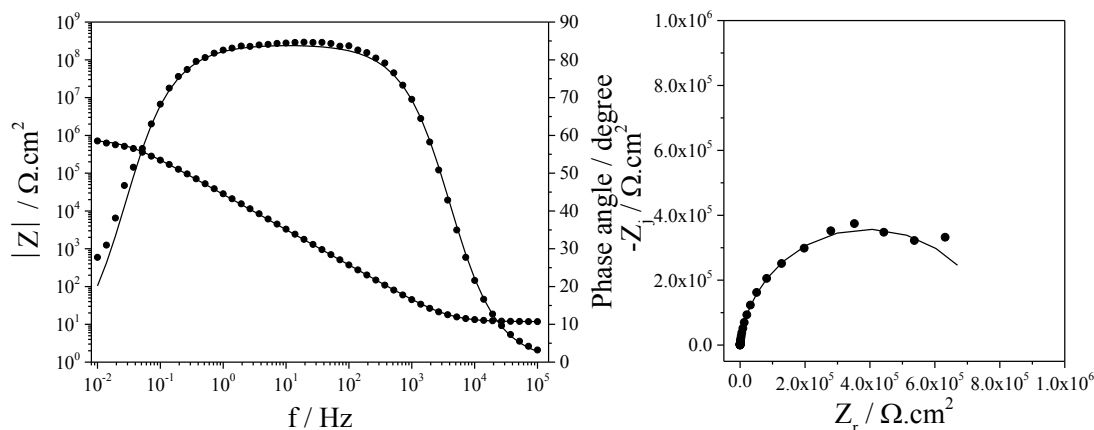


**Figure VII.3:** EIS Bode (left) and Nyquist (right) plots of bare aluminium in 0.5 M NaCl, under argon bubbling (pH = 6) at OCP. Points and lines correspond to measured and fitted data, respectively

The capacitive response observed in Figure VII.3 confirms the presence of a protective aluminium oxide film [26,156]. According to the literature, impedance measurements on aluminium substrate in chloride-containing aqueous solutions can show a response with up to three time constants, or three loops in Nyquist plots [19,22,23,25–27]. The HF (high frequency) capacitive loop usually corresponds to the oxide formation [20,26,33], or oxide layer itself [26]. The MF (medium frequency) inductive loop usually corresponds to surface or bulk relaxation of the oxide species or to absorbed intermediates [25,157,158], or to pitting phenomena observed at short exposure times when  $E_{\text{corr}}$  and  $E_{\text{pit}}$  are close to each other [33], or to the formation of an  $\text{AlCl}_3$  salt film as a result of  $\text{Cl}^-$  incorporation into the oxide [152]. The LF (low frequency) loop is usually associated with dissolution of the oxide layer [26,27]. However, manifestation of all these phenomena may not be possible sometimes, and instead two loops [23,24,27,28,33,34] or only one loop [27,159] can be observed.

## Chapter VII. Investigation of corrosion protection of alumina by ALD coatings and effect of deposited layer thickness

If only one loop (time constant) is observed, different reasons can be invoked: all phenomena are present, but with a strong overlap of their time constants; one process dominates the others in the frequency range of study; the measured frequencies are not low enough to observe all phenomena happening; some phenomena are absent. For the present case, the MF inductive loop is not observed as the impedance is performed at OCP and  $E_{\text{pit}}$  and  $E_{\text{corr}}$  are far away from each other (Figure VII.1), thus excluding pitting. The LF loop is not observed also excluding that dissolution occurs. However, the absence of the LF loop can also be due to the time of immersion (30 min), too short to lead to manifestation of oxide film dissolution.

The EIS data were fitted using the equivalent circuit (E.C.4) shown in Figure VII.4. The fitted results are compiled in Table VII.2.

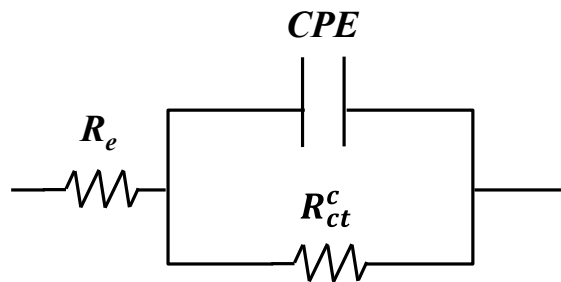


**Figure VII.4:** Equivalent circuit model adopted for the bare Al substrate for the present study at open circuit potential (E.C.4)

**Table VII.2:** Results of EIS data in Figure VII.3 fitted with E.C.4 (Figure VII.4)

	$R_e / \Omega \cdot \text{cm}^2$	$R_{ct}^c / \Omega \cdot \text{cm}^2$	$Q / \text{F} \cdot \text{cm}^{-2} \cdot \text{s}^{(n-1)}$	$n$	$C_{\text{eff}} / \text{F} \cdot \text{cm}^{-2}$
<b>Bare substrate</b>	11.79	$7.93 \times 10^5$	$6.37 \times 10^{-6}$	0.94	$3.39 \times 10^{-6}$

This equivalent circuit is in agreement with the HF part of the equivalent circuits used by other authors [152,156]. The capacitive impedance (CPE) corresponds to the capacitance of the native oxide layer. The faradic response is simply shown as  $R_{ct}^c$ , which corresponds to cathodic charge transfer resistance.  $R_e$  is the resistance of the electrolyte. Diffusion control phenomena through the oxide layer and oxygen diffusion limitation could be present (although no plateau was observed in the LSV cathodic part when polarization was done from OCP and negative-going). Nevertheless, they were not taken

## Chapter VII. Investigation of corrosion protection of alumina by ALD coatings and effect of deposited layer thickness

---

into account in the equivalent circuit as there was no evidence for them in the EIS plots and the fitting could be done without taking them into account. More clearly, in the plot of logarithm of the imaginary part of the impedance vs the logarithm of the frequency (shown in Figure VII.5), the slope is fairly constant with a constant value of  $-n$ . Therefore, the behaviour of bare aluminium in the present study can be modelled as a simple CPE//R circuit, with CPE corresponding to the capacitance of the native oxide layer.

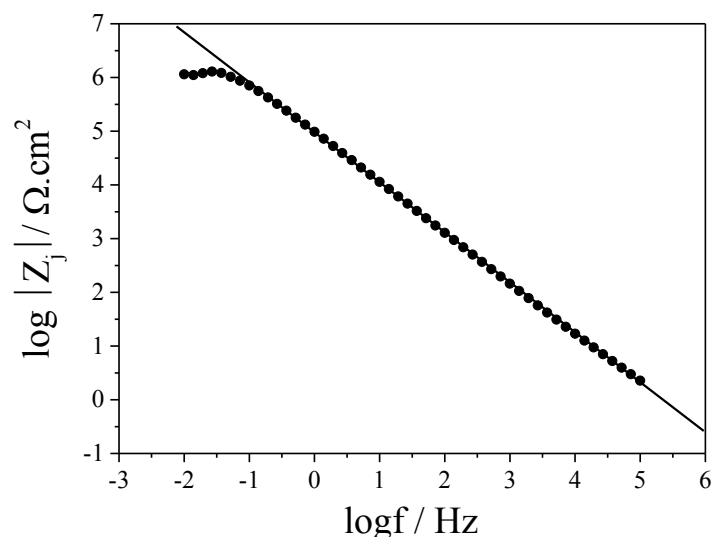


**Figure VII.5:** Logarithm of the imaginary part of the impedance as a function of logarithm of frequency for bare Al substrate

The resistance in Figure VII.4 corresponds to the cathodic charge transfer resistance, as the anodic charge transfer resistance related to the oxide is omitted in a parallel combination with the cathodic resistance due to its high value related to a passive oxide layer.

The value obtained for  $n$  (Table VII.2) corresponds to the negative of the slope of the tangent line of the graph in Figure VII.5. The effective capacitance value obtained here (using Eq. III.9) is the capacitance of the native oxide layer formed on the substrate during one month ageing. The capacitance value obtained for the oxide here, is

## Chapter VII. Investigation of corrosion protection of alumina by ALD coatings and effect of deposited layer thickness

---

comparable with the values obtained for the native aluminium oxide layer by others [26,124,156].

The capacitance of the oxide layer can be used to estimate its thickness. Considering a dielectric constant between 7.5 and 15 for  $\text{Al}_2\text{O}_3$  [160], application of Eq. III.13 yields thickness values of 1.95 nm and 3.91 nm, respectively. If a dielectric constant of 40 [27,161] corresponding to a partially hydrated oxide is assumed, the thickness value of 10.44 nm is obtained. These thickness values obtained by *in situ* analysis can be compared with the thickness values obtained by *ex situ* analysis. In the present case, a value of 8 nm was measured by XPS on the bare sample before polarization. This thickness seems high in comparison with the thickness of 1.4 nm measured by Marcus *et al.* [162] for the oxide layer formed by oxidation at 25°C on pure aluminium. The reason for having a higher thickness of the oxide layer here is the ageing (1 month) of the sample. As mentioned before, the thickness of the oxide layer on aluminium can increase with time, up to tens of nanometres, depending on the humidity and temperature, according to the literature [149].

In other studies trying to estimate the thickness value of the native aluminium oxide layer from EIS data [25–27], it was found that the thickness obtained by EIS was underestimated [26,27] in comparison with the value obtained by XPS. Martin *et al.* [27] mentioned the possibility of sensing of only the space charge layer by impedance, which would be thinner than the oxide layer. In the present study, assuming no change in the thickness of the oxide after 30 min immersion at OCP, and ignoring the thickness value obtained for a hydrated oxide, it seems that the thickness obtained by EIS is underestimated also. This underestimation comes from the fact that assuming only a surface (2D) distribution of time constants for a native oxide film and using Brug formula (Eq. III.9) may not be totally correct. For the native oxide films, a normal (3D) distribution of time constants can be expected [163,164]. A normal distribution can result from the dispersion of the conductivity and possibly the dielectric constant [163] along the axis normal to the electrode surface (*i.e.* within the depth of the oxide), from high porosity, and variation of the in-depth composition of the oxide layer. However, in the absence of additional measurements such as local impedance, a decision about the existence of a surface or normal distribution cannot be taken with certainty [164].

## Chapter VII. Investigation of corrosion protection of alumina by ALD coatings and effect of deposited layer thickness

---

One of the models for the normal distribution of time constants in the literature is the power-law model [163,165] (shown to be consistent with CPE). While the Brug formula (Eq. III.9) is recommended for a 2D distribution of time constants, the power-law model is preferred in case of a 3D distribution [164]. This model takes into account a distribution of resistivity along the oxide thickness (and assumes a uniform dielectric constant along the depth of the oxide) according to Eq. VII.5:

$$\frac{\rho}{\rho_{\delta}} = \left[ \frac{\rho_{\delta}}{\rho_0} + \left( 1 - \frac{\rho_{\delta}}{\rho_0} \right) \xi^{\gamma} \right]^{-1} \quad \text{Eq. VII.5}$$

where  $\rho_0$  and  $\rho_{\delta}$  are the boundary values of the resistivity at the interfaces,  $\delta$  is the thickness of the oxide film,  $\xi$  ( $\xi = x / \delta$ ) is the dimensionless position along the oxide thickness and  $\gamma$  is a constant indicating how sharply the resistivity varies and is related to  $n$  according to Eq. VII.6:

$$\gamma = \frac{1}{1 - n} \quad \text{Eq. VII.6}$$

Under the conditions of  $\rho_0 \gg \rho_{\delta}$  and  $f < (2\pi\rho_{\delta}\epsilon\epsilon_0)^{-1}$ , an analytical expression for the impedance has been given according to Eq. VII.7:

$$Z_f(f) = g \frac{\delta\rho_{\delta}^{1/\gamma}}{(\rho_0^{-1} + j2\pi f\epsilon\epsilon_0)^{(\frac{\gamma-1}{\gamma})}} \quad \text{Eq. VII.7}$$

where  $g = 1 + 2.88\gamma^{-2.375}$  is a numerically evaluated function. The relationship between CPE parameters ( $Q$  and  $n$ ) and dielectric properties of the film ( $\epsilon$  and  $\rho_{\delta}$ ) for  $(2\pi\rho_0\epsilon\epsilon_0)^{-1} < f < (2\pi\rho_{\delta}\epsilon\epsilon_0)^{-1}$  will be:

$$Q = \frac{(\epsilon\epsilon_0)^n}{g\delta\rho_{\delta}^{1-n}} \quad \text{Eq. VII.8}$$

Using the relationship between  $\rho_{\delta}$  and the characteristic frequency  $f_{\delta}$  ( $f_{\delta} = \frac{1}{2\pi\rho_{\delta}\epsilon\epsilon_0}$ ), a maximum value can be obtained for  $\rho_{\delta}$ , if the maximum experimental frequency is used

## Chapter VII. Investigation of corrosion protection of alumina by ALD coatings and effect of deposited layer thickness

---

instead of  $f_{\delta}$  and a minimum value for the thickness ( $\delta$ ) can be obtained using  $\rho_{\delta, \max}$  in Eq. VII.8.  $Q$  and  $n$  can be obtained graphically [77]. The slope of the logarithm of the imaginary part of the impedance vs the logarithm of the frequency (Figure VII.5) is equal to  $-n$ , which can be then applied in Eq. VII.9 to obtain  $Q$ :

$$Q = -\frac{1}{Z_j(f)(2\pi f)^n} \times \sin\left(\frac{n\pi}{2}\right) \quad \text{Eq. VII.9}$$

A maximum value for the thickness of the oxide can be obtained similarly, using a minimum value of  $1 \times 10^{-3} \Omega \cdot \text{cm}$  for  $\rho_{\delta}$  as the typical minimum value for the resistivity of semiconductors and using Eq. VII.8.

Doing so and assuming a power-law distribution of resistivity in the oxide layer for the present study, thickness values from 2.30 up to 16.16 nm are obtained for  $\epsilon$  values between 7.5 and 15. Higher values are obtained here in comparison with the values obtained from  $C_{\text{eff}}$  assuming a surface distribution of time constants. The thickness of 8 nm obtained by XPS suits well in the thickness range achieved by a power-law model. However, the applicability of the power-law model for the present EIS results should be confirmed with a trial to fit the EIS data with an equivalent circuit where power-law model is used for the anodic branch. Nevertheless, the power-law model is mentioned here and the estimated thickness values are provided, as the applicability of this model is already proved for passive aluminium in 0.1 M  $\text{Na}_2\text{SO}_4$  electrolyte [165].

A summary of thickness values obtained using EIS data and different assumptions is presented in Table VII.3. Thickness values from 1.95 up to 16.16 nm are obtained depending on the value of dielectric constant and the method to calculate the thickness from CPE.

**Table VII.3:** Estimation of thickness of aluminium oxide obtained from assumption of 2D and 3D distributions of time constants in the oxide in addition to application of extreme values of dielectric constant of  $\text{Al}_2\text{O}_3$

	$C_{\text{eff}}$ / Brug	$Q$ / power-law
$\epsilon = 7.5$	1.95 nm	2.30 - 8.42 nm
$\epsilon = 15$	3.91 nm	4.61 - 16.16 nm
$\epsilon = 40$	10.44 nm	

### **VII.3. Surface analysis and electrochemical study of coated samples**

#### **VII.3.1. Time-of-Flight Secondary Ion Mass Spectrometry of pristine samples**

Figure VII.6 shows the ToF-SIMS depth profiles of the 10, 20 and 50 nm ALD alumina coated aluminium substrates. The represented ions are  $^{12}\text{C}^-$ ,  $^{17}\text{OH}^-$ ,  $^{18}\text{O}^-$ ,  $^{35}\text{Cl}^-$ ,  $^{62}\text{AlCl}^-$ ,  $^{59}\text{AlO}_2^-$  and  $^{54}\text{Al}_2^-$ . Three regions are distinguished and marked. The first region where the  $^{18}\text{O}^-$ ,  $\text{AlO}_2^-$  and  $\text{Al}_2^-$  ions, characteristic of the coating, show a plateau. The point at which the  $\text{Al}_2^-$  ion starts to deviate from a plateau marks the entry in the interface. This is measured at ~75, ~160 and ~440 s for the 10, 20 and 50 nm samples, respectively. The entry in the bulk substrate is where the  $\text{Al}_2^-$  ions (also representative of the metallic substrate) start a plateau again, at ~390, ~500 and ~860 s for 10, 20 and 50 nm samples, respectively.

The width of the interfacial region is calculated as 315, 340 and 420 s for 10, 20 and 50 nm samples respectively. Having such large values for the width of the interfacial region is assigned to the roughness of the substrate in addition to the presence of a native/spurious aluminium oxide at the coating/substrate interface. The native oxide is formed as a result of one month ageing of the aluminium substrate after preparation and before coating deposition. This oxide is most probably combined with a thermal spurious oxide which is formed on aluminium substrate exposed to water vapour until full coverage by ALD alumina and/or during the thermal stabilization of the reactor at 250°C before deposition begins.

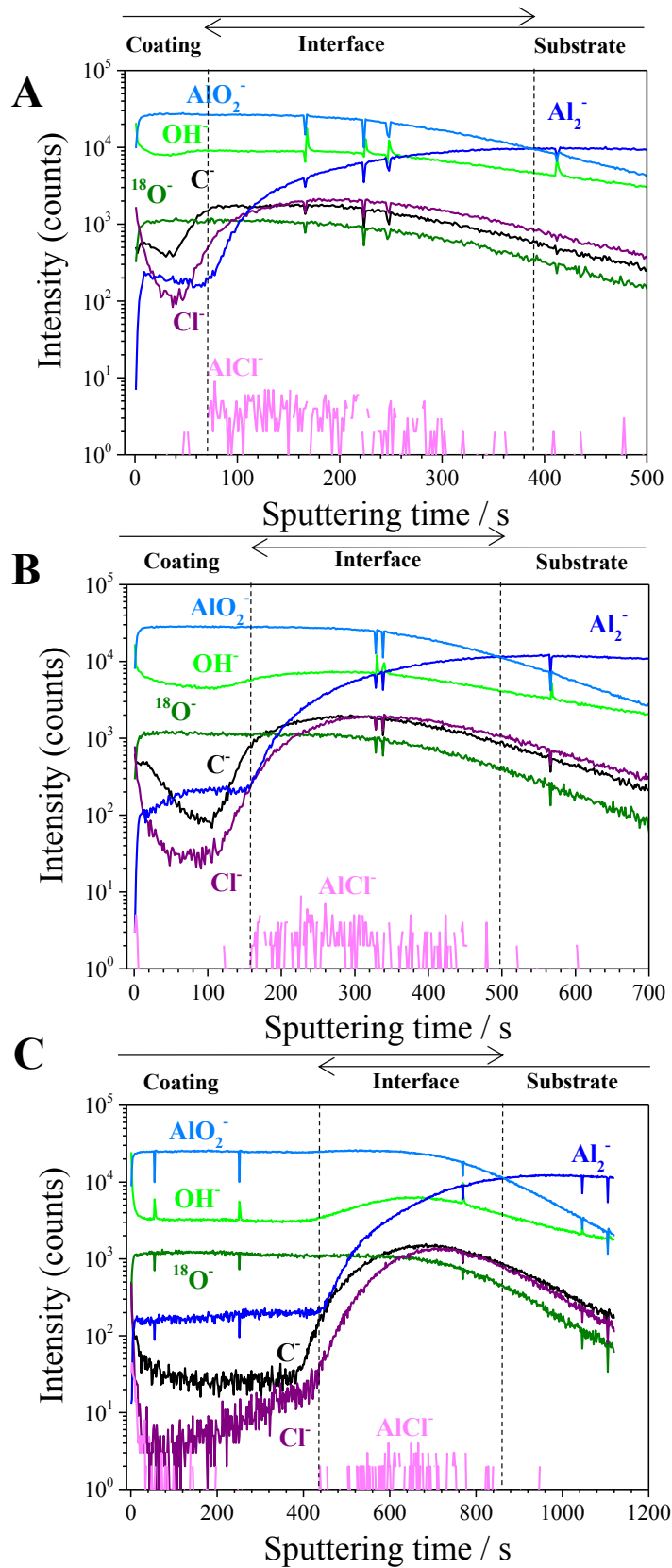


Figure VII.6: ToF-SIMS negative ion depth profiles for 10 nm (A), 20 nm (B) and 50 nm (C) ALD alumina coatings prepared at 250°C on aluminium substrate

## Chapter VII. Investigation of corrosion protection of alumina by ALD coatings and effect of deposited layer thickness

---

The continuation of the intensity plateaus for the  $^{18}\text{O}^-$  and  $\text{AlO}_2^-$  ions in the interface region is related to presence of the interfacial oxide. This is why here, as opposed to the case of the coated copper samples, the end of the plateaus for  $^{18}\text{O}^-$  and  $\text{AlO}_2^-$  ions cannot be used to mark the start of the interface. However, the end of the first plateau of the  $\text{Al}_2^-$  ions corresponds properly to the start of the interface, as confirmed by comparison with the coated copper samples. On copper substrate (Chapter III), sputtering times of  $\sim 75$ ,  $\sim 185$  and  $\sim 510$  s corresponded to the start of the interface region. These sputtering times are comparable with the values for the start of the interface on aluminium ( $\sim 75$ ,  $\sim 160$  and  $\sim 440$  s). Moreover, the intensity of  $\text{Al}_2^-$  ions in the bulk coating region on copper (not shown) was around 140 counts, which is comparable with the intensity of around 160 counts measured on aluminium. This confirms that the  $\text{Al}_2^-$  first plateau is a marker of the bulk coating region and that it can be taken to mark the start of the interface.

As a result of the considerable contribution of native/spurious alumina to the interface region, an estimation of sputtering yield of the coating from ToF-SIMS depth profiles like done in Chapter III cannot be valid. In Chapter III, the sputtering rate values were calculated using the sputtering time at the end of the interface. If done so here, sputtering rate values of  $0.031$ ,  $0.040$  and  $0.060 \text{ nm}\cdot\text{s}^{-1}$  are obtained using the actual deposited thicknesses of  $12$ ,  $20$  and  $52 \text{ nm}$ , respectively. These values are clearly lower than the values obtained for the same coatings on copper substrate ( $0.095$ ,  $0.088$  and  $0.081 \text{ nm}\cdot\text{s}^{-1}$  for  $10$ ,  $19.9$  and  $49.5 \text{ nm}$  respectively). This means that the presence of interfacial native/spurious aluminium oxide cannot be ignored in the calculations of the sputtering rate. Furthermore, the calculated sputtering rates here increase unexpectedly for the thicker coatings. This suggests that the interfacial oxide layers under different coatings may not have the same thickness values. The reason for this discrepancy can also be the high roughness of the substrate, leading to its high contribution to the interfacial region. Moreover, different roughness values would lead to different contributions of the substrate to the interfacial region. Although the substrates are prepared in a similar way, if roughness is high, it may be poorly reproducible. The roughness measurements obtained by profilometry on  $1000 \mu\text{m}^2$  area on different bare samples after the final polishing was estimated as  $36.48 \pm 14.32 \text{ nm}$  ( $R_a$ ), which is quite high.

## Chapter VII. Investigation of corrosion protection of alumina by ALD coatings and effect of deposited layer thickness

---

If only the bulk coating region (before the start of interface) is taken into account, sputtering rates of 0.160, 0.125 and 0.118 nm.s<sup>-1</sup> are obtained for the 12, 20 and 52 nm samples respectively. As observed on copper, the sputtering rate decreases with increase of coating thickness, thus confirming the effect of the deposition time on the densification of the ALD coating. Calculating the sputtering rates for copper coated samples in a same way as done here, values of 0.133, 0.107 and 0.097 nm.s<sup>-1</sup> are obtained for 10, 19.9 and 49.5 nm samples, confirming a densification of the ALD alumina with increasing the deposited thickness. The estimated sputtering rates slightly higher on Al, than on Cu substrate, may indicate a lower density of deposited coatings on Al.

The OH<sup>-</sup>, Cl<sup>-</sup> and C<sup>-</sup> ions have the same origin as discussed in Chapter III. OH<sup>-</sup> ions show a plateau in the bulk coating region and increase in the interface region. In the interfacial region the <sup>18</sup>O<sup>-</sup> and AlO<sub>2</sub><sup>-</sup> ions continue their plateaus before starting to decrease. Observing the increase of OH<sup>-</sup> ions before the decrease of <sup>18</sup>O<sup>-</sup> and AlO<sub>2</sub><sup>-</sup> ions indicates higher hydroxylation of the native/spurious alumina layer than of the ALD alumina layer. Similarly, the C<sup>-</sup> and Cl<sup>-</sup> ions increase sharply when entering the interface region, indicating more carbon and chloride contamination in the native/spurious interfacial alumina layer. The AlCl<sup>-</sup> ion is only observed in the interface region and more at the beginning, indicating that it is mostly due to absorption of chloride in the native alumina oxide from the ambient. Higher contamination of the native alumina layer is expected as it is formed and aged in chloride-containing ambient conditions. This is not the case for the homogeneous alumina layers grown by ALD. ALD layers are only contaminated from the ambient at their extreme surface.

A comparative presentation of each ion for different coatings is shown in Figure VII.7. The observation of the same intensities for <sup>18</sup>O<sup>-</sup>, AlO<sub>2</sub><sup>-</sup> and Al<sub>2</sub><sup>-</sup> ions for the different coatings indicates deposition of coatings with same stoichiometry, in addition to good reproducibility of the selected ToF-SIMS analytical conditions.

## Chapter VII. Investigation of corrosion protection of alumina by ALD coatings and effect of deposited layer thickness

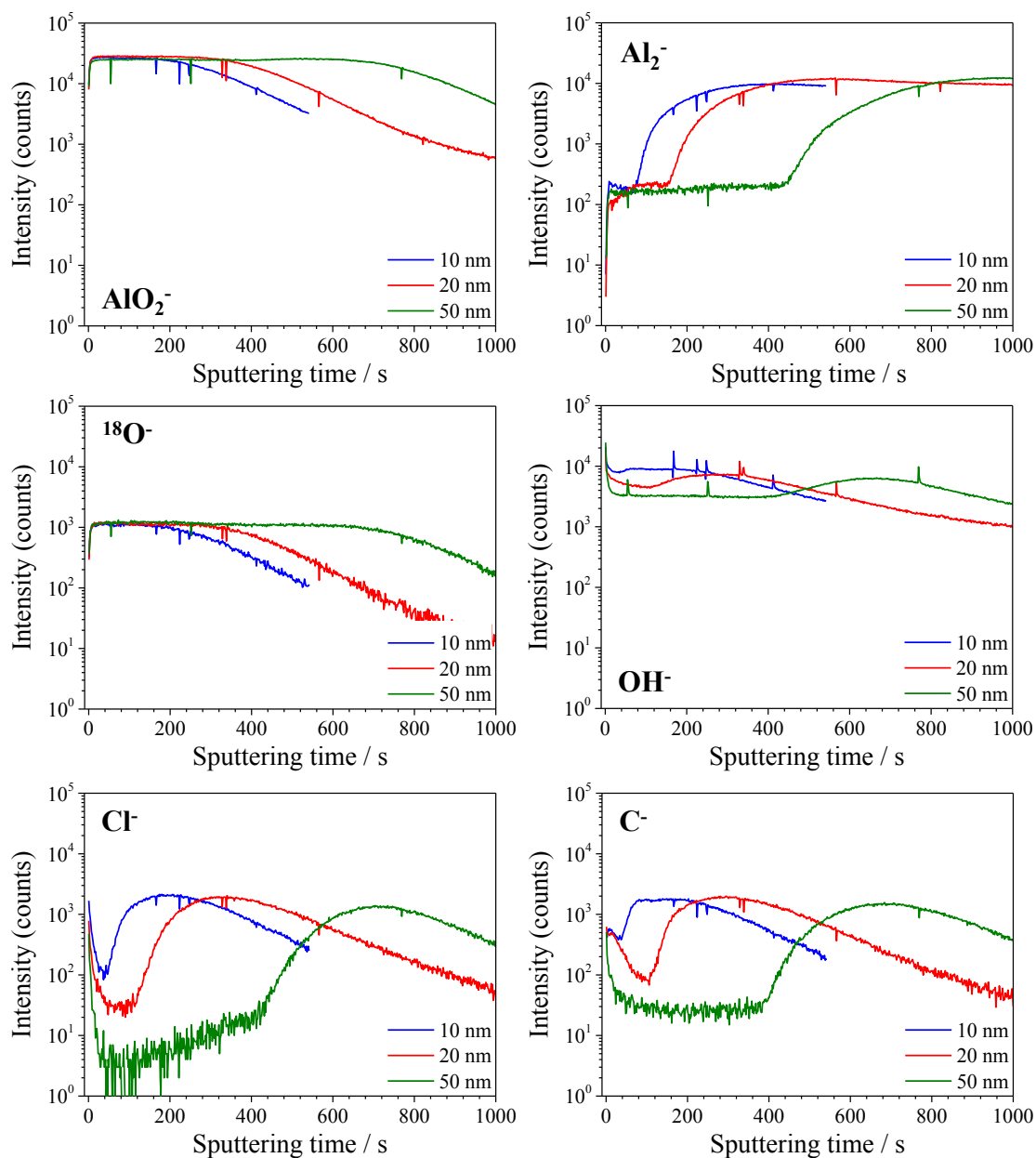


**Figure VII.7:** Comparative representation of selected ToF-SIMS depth profiles for 10, 20 and 50 nm ALD alumina coatings on aluminium substrate

The  $\text{OH}^-$  ion intensity decreases slightly both in the bulk coating and interface region with increasing deposited thickness. As discussed in Chapter III, this is due to the longer deposition time, promoting the completion of the incomplete surface reactions responsible for the hydroxyl contamination. A lower  $\text{OH}^-$  ion intensity in the bulk coating is also consistent with the formation of a denser coating. At the interface, and also as discussed in Chapter III, a lower  $\text{OH}^-$  intensity means more effective hydroxyl removal

## Chapter VII. Investigation of corrosion protection of alumina by ALD coatings and effect of deposited layer thickness

during the initial cycles of the ALD growth, again consistent with completion of the surface reactions for the first deposited alumina layers and related densification during the further growth of the coating. Similarly to  $\text{OH}^-$ , the  $\text{Cl}^-$  and  $\text{C}^-$  ions intensities decrease both in the bulk coating and interface region with coating thickness increase.

### VII.3.2. Linear Sweep Voltammetry of coated aluminium

The LSV polarization curves for the coated aluminium substrates are presented in Figure VII.8. The measured and calculated parameters are presented in Table VII.4.

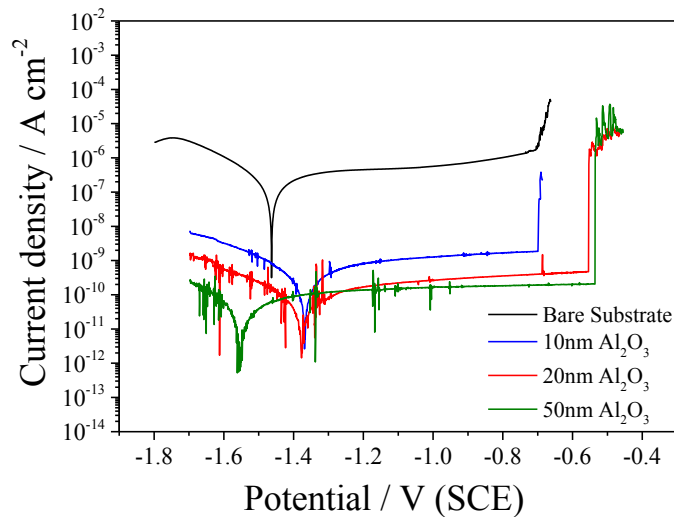


**Figure VII.8:** LSV polarization curves for the bare and ALD alumina coated Al substrates in 0.5 M NaCl, under argon bubbling (pH = 6), scan rate: 1 mV.s<sup>-1</sup>

**Table VII.4:** Parameters related to the polarization curves in Figure VII.8

	$E_{\text{corr}} / \text{V (SCE)}$	$E_{\text{pit}} / \text{V(SCE)}$	$i_{\text{pass}} / \text{A.cm}^{-2}$	$R_p / \text{Ohm.cm}^2$	$R_{\text{pass}} / \text{Ohm.cm}^2$
<b>Bare substrate</b>	-1.463	-0.706	$5.00 \times 10^{-7}$	$2.31 \times 10^5$	$1.23 \times 10^6$
<b>Al<sub>2</sub>O<sub>3</sub> 10nm</b>	-1.368	-0.699	$1.00 \times 10^{-9}$	$1.67 \times 10^8$	$4.60 \times 10^8$
<b>Al<sub>2</sub>O<sub>3</sub> 20nm</b>	-1.377	-0.554	$3.00 \times 10^{-10}$	$6.82 \times 10^8$	$7.40 \times 10^9$
<b>Al<sub>2</sub>O<sub>3</sub> 50nm</b>	-1.558	-0.536	$1.50 \times 10^{-10}$	$1.02 \times 10^9$	$3.00 \times 10^{10}$

## Chapter VII. Investigation of corrosion protection of alumina by ALD coatings and effect of deposited layer thickness

---

The same shape of the polarization curves is observed for the bare and coated samples. This is consistent with the insulating property of ALD alumina coatings and the fact that the electrochemical response is only related to the substrate. Significant decreases of the current in both cathodic and anodic parts shows good barrier properties of the coatings.

A cathodic shift of the corrosion potential has been previously attributed to the adsorption of chloride ions [28]. If so, the higher corrosion potential observed here for 10 and 20 nm coated samples in comparison with the bare substrate would be indicative of lower adsorption of  $\text{Cl}^-$  on the native oxide film at coating/substrate interface than on the bare substrate. This is consistent with the coating sealing most of the substrate surface and leaving very few sites available for  $\text{Cl}^-$  adsorption. The opposite trend of the  $E_{\text{corr}}$  shift observed for 50 nm coated sample indicates that another effect, stronger than the latter one, takes place. The cathodic shift of the corrosion potential for the 50 nm coated sample is proposed to be linked with a local pH increase at the coating/substrate interface at the end of the channel defects in the coating where the substrate is exposed to the electrolyte. The interfacial pH may increase due to cathodic reactions at the coating/substrate interface, producing  $\text{OH}^-$  [166]. A local increase of pH would lead to instability of the native aluminium oxide and its partial dissolution, thus increasing the anodic current [166]. Higher anodic currents would then shift the corrosion potential to lower values. Previous studies confirm this interpretation. According to Lee *et al.* [24], a higher  $\text{OH}^-$  concentration in the electrolyte leads to the decrease of corrosion potential. In a work done by Carbonini *et al.* [23], the polarization test performed on aluminium in deaerated NaCl solution showed a corrosion potential significantly lower than the test in aerated conditions, revealing the effect of promotion of the hydrogen evolution in deaerated condition at the corrosion potential. Other authors have reported that the promotion of hydrogen evolution shifts the corrosion potential cathodically [152]. Therefore, for the 50 nm coated sample in the present study, the longer diffusion length through the thicker coating would retard the diffusion of  $\text{OH}^-$  ions away to the bulk electrolyte and this would promote the local increase of pH at the coating/substrate interface. In other words, a thicker coating could simulate a more deaerated condition (less access to dissolved oxygen in the electrolyte) than a thinner coating at the

## Chapter VII. Investigation of corrosion protection of alumina by ALD coatings and effect of deposited layer thickness

---

coating/substrate interface leading to promotion of hydrogen evolution and therefore decrease of corrosion potential.

As it can be seen in Figure VII.8 (Table VII.4), pitting corrosion is delayed for the 20 and 50 nm coated samples in comparison with the bare substrate. This is due to both barrier and sealing properties of these coatings. As mentioned in section VII.2.1, both acidification of the local environment and increase of chloride ions concentration are necessary for stable pit growth. For chloride-assisted dissolution reactions to take place at the substrate and lead to production of aluminium ions, the entrance of water molecules *via* the flaws and weak spots in the native oxide is necessary. Thanks to their high sealing property, the coatings block most of the surface and reduce considerably the arrival of water molecules to the coating/substrate interface, as shown by the lower passive currents (resulting from the production of aluminium ions in the passive range) for coated samples. In turn, lower dissolution of aluminium would retard acidification by hydrolysis and thus delay the stable pit growth. Another explanation is linked to the effect of the pH reported to increase the adsorption of chloride when decreasing [167]. The barrier property (thickness) of the thicker 20 and 50 nm coatings could lead to lower decrease of pH due to the longer length for OH<sup>-</sup> ions to diffuse into the bulk electrolyte and thus to lower adsorption of chloride ions. In the case of 10 nm coating, the sealing properties (low porosity) also make the passive current decrease substantially, but its barrier properties (thickness) are not high enough to delay the pitting potential.

The passive current ( $i_{\text{pass}}$ ), polarization resistance ( $R_p$ ) and resistance in passive region ( $R_{\text{pass}}$ ) values obtained from the LSV data are presented in Table VII.4. The passive current and resistance are calculated between -1.130 to -0.750 V/SCE for the coated samples. As expected, the resistance values increase and passive current values decrease in the presence of coatings and with an increasing effect for higher coating thickness. The resistance in the passive range is higher than the resistance at the corrosion potential ( $R_p$ ) like observed for the bare sample and due to the same reason as discussed in section VII.2.2.

## Chapter VII. Investigation of corrosion protection of alumina by ALD coatings and effect of deposited layer thickness

---

As done on the Cu substrate, porosity calculations were performed in order to estimate the coating sealing performance. Polarization resistance and passive current values were used.  $P_{R_p}$  was calculated using Eq. VII.10 [61,62]:

$$P_{R_p} = \frac{R_p^0}{R_p} \times 100 \quad \text{Eq. VII.10}$$

where  $R_p^0$  and  $R_p$  are polarization resistances of the bare and coated substrates respectively. It should be mentioned that here application of Eq. III.11 is not possible due to the absence of anodic Tafel behaviour and the impossibility of calculating anodic Tafel slope.  $P_{i_{pass}}$  was calculated using Eq. VII.11 [60]:

$$P_{i_{pass}} = \frac{i_{pass}}{i_{pass}^0} \times 100 \quad \text{Eq. VII.11}$$

where  $i_{pass}^0$  and  $i_{pass}$  are the passive current values for the bare and coated substrates respectively. The porosity values are compiled in Table VII.5.

**Table VII.5:** Porosity values obtained from LSV and EIS results

	$P_{R_p}$ (LSV) / %	$P_{i_{pass}}$ (LSV) / %	$P_{R_{ct}}$ (EIS) / %
<b>Bare substrate</b>	100	100	100
<b>Al<sub>2</sub>O<sub>3</sub> 10nm</b>	0.13	0.20	0.23
<b>Al<sub>2</sub>O<sub>3</sub> 20nm</b>	0.03	0.06	0.05
<b>Al<sub>2</sub>O<sub>3</sub> 50nm</b>	0.02	0.03	0.02

The porosity values obtained for the present coatings are comparable with the ones obtained on copper (Chapter III). The same sealing performance is achieved for the 50 nm coating independently of the substrate and its passivation property in the testing corrosive environment. This confirms ALD alumina as an excellent sealant for corrosion protection. One notices that for the 10 and 20 nm coatings, the sealing efficiency is

higher on the aluminium substrate, possibly owing to a better nucleation and less defective growth of the ALD alumina on a surface pre-covered by aluminium oxide.

### VII.3.3. Electrochemical Impedance Spectroscopy of ALD coated aluminium

The EIS Bode and Nyquist plots measured at OCP for coated (and bare) Al substrates are shown in Figure VII.9. The coated samples show considerably higher global impedance and wider frequency range of capacitive response in comparison with the uncoated substrate.

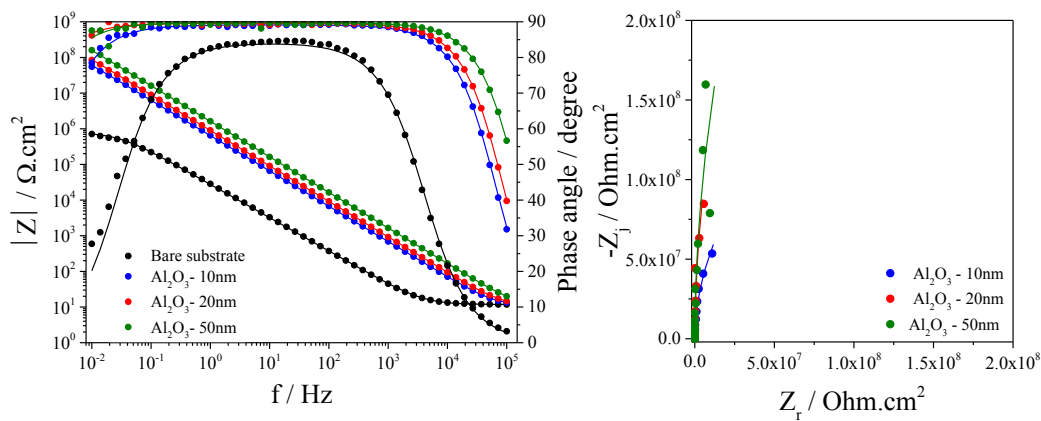


**Figure VII.9:** EIS Bode (left) and Nyquist (right) plots for the bare and ALD alumina coated aluminium substrates in 0.5 M NaCl under argon bubbling (pH = 6) at OCP. Points and lines correspond to measured and fitted data, respectively

The Nyquist plots for coated samples resemble the behaviour of a blocking electrode. This is due to considerably lower current measured in the presence of the coatings leading to higher resistance values increasing the radius of the semicircle in the Nyquist diagram to infinitely large values.

As there is no evidence for the presence of two (or several) time constants for the coated samples and as the coatings are electrochemically inactive, the same equivalent circuit

## Chapter VII. Investigation of corrosion protection of alumina by ALD coatings and effect of deposited layer thickness

used for the bare substrate, E.C.4 (Figure VII.4), was used for fitting the EIS data. The results are compiled in Table VII.6.

**Table VII.6:** EIS data and results related to Figure VII.9 fitted to E.C.4 (Figure VII.4)

	$R_e / \Omega.cm^2$	$R_{ct}^c / \Omega.cm^2$	$Q / F.cm^{-2}.s^{(u-1)}$	$n$	$C_{eff} / F.cm^{-2}$	$C_{th} / F.cm^{-2}$
<b>Bare substrate</b>	11.79	$7.93 \times 10^5$	$6.37 \times 10^{-6}$	0.94	$3.39 \times 10^{-6}$	
<b>10nm ALD Al<sub>2</sub>O<sub>3</sub></b>	11.20	$3.39 \times 10^8$	$2.51 \times 10^{-7}$	0.99	$2.22 \times 10^{-7}$	$5.9 \times 10^{-7}$
<b>20nm ALD Al<sub>2</sub>O<sub>3</sub></b>	11.20	$1.55 \times 10^9$	$1.78 \times 10^{-7}$	0.99	$1.68 \times 10^{-7}$	$3.54 \times 10^{-7}$
<b>50nm ALD Al<sub>2</sub>O<sub>3</sub></b>	10.95	$3.20 \times 10^9$	$9.86 \times 10^{-8}$	0.99	$9.50 \times 10^{-8}$	$1.36 \times 10^{-7}$

Cathodic charge transfer resistance values obtained from the fitting are close to the polarization resistance values obtained from LSV. The slight difference is due to different regimes used in EIS and LSV and non-stationary condition of polarization (1 m.Vs<sup>-1</sup>).

Porosity values were obtained also from the fitting results, using Eq. VII.12:

$$P_{Rp} = \frac{R_{ct}^c}{R_{ct}^0} \times 100 \quad \text{Eq. VII.12}$$

where  $R_{ct}^c$  and  $R_{ct}^0$  are cathodic charge transfer resistances relating to the bare and coated substrates respectively.  $P_{Rp}$  values are listed in Table VII.5. They are in excellent agreement with the values obtained from LSV, as expected.

Effective capacitance values were obtained using the Brug formula (Eq. III.9). As mentioned in Chapter III, for the coated samples,  $C_{eff}$  can also be taken directly as  $Q$  ( $C_{eff} \approx Q$ ) due to the fact that  $n \approx 1$ . The theoretical capacitance values ( $C_{th}$ ) calculated from Eq. III.13 and assuming  $\epsilon = 8$  ( $\epsilon = 7.6-8.4$  for ALD alumina [58,141]) are also provided in Table VII.6. As it can be seen, these values are higher than  $C_{eff}$  values. The reason for this discrepancy is the contribution of capacitance of the native/spurious oxide layer to  $C_{eff}$ . In a simple model, the coating and the native oxide capacitances are in series and related to the total capacitance according to Eq. VII.13:

**Chapter VII. Investigation of corrosion protection of alumina by ALD coatings and effect of deposited layer thickness**

---

$$\frac{1}{C} = \frac{1}{C_{\text{coating}}} + \frac{1}{C_{\text{oxide}}} \quad \text{Eq. VII.13}$$

In this case, if the same dielectric constant is assumed for the ALD and native/spurious aluminium oxide layers, the total thickness can be calculated. Subtracting the coating thickness values of 12, 20 and 52 nm (measured with XRR, Chapter II), from the total thickness, yields the thickness values for the native/spurious oxide as compiled in Table VII.7. These thickness values are around 20 nm, which seems high in comparison with the thickness values obtained for the native oxide layer on the bare substrate. As mentioned in section VII.1, the passive oxide layer on Al substrate grows at higher temperatures [149]. For the present study, the initial waiting time in the ALD reactor (one hour for heating up the reactor to 250°C and 10 minutes at 250°C) leads to growth of a thermal aluminium oxide layer and therefore to the increase of the thickness of the interfacial oxide layer.

**Table VII.7:** Thickness values obtained from  $C_{\text{eff}}$  values for interfacial oxide under the alumina coatings ( $\epsilon = 8$ )

	$C_{\text{eff}} / Q$
<b>native/spurious oxide</b>	
<b>12nm ALD</b>	16.2 nm
<b>20nm ALD</b>	19.8 nm
<b>52nm ALD</b>	19.7 nm

The thickness values obtained from the EIS results could deviate from being precise due to the fact that the dielectric constant for the ALD and the native/spurious aluminium oxides may not be the same. Furthermore, the combination of the capacitances corresponding to the coating and the interfacial oxide could be more complicated than the in-series combination postulated in Eq. VII.13. For instance  $C_{\text{coating}}$  could be in parallel combination with  $C_{\text{oxide}}$  in the pores and channel defects of the oxide, where the ALD coating is deposited due to the high capability of ALD in filling the trenches even for high aspect ratio substrates. Moreover, heating the native oxide layer in the ALD reactor could increase its porosity, which could lead to lower capacitance than that assumed in the calculation of the total thickness, and thus would overestimate the thickness.

#### **VII.4. Conclusions**

Electrochemical and surface analytical methods were applied to investigate the corrosion protection provided to pure aluminium metal by the growth of 10, 20 and 50 nm thick ALD alumina coatings deposited at 250°C.

Characterization of the elemental compositions of the bulk coating, interfacial and substrate regions was possible with ToF-SIMS depth profiling. The presence of significant amounts of native/spurious interfacial aluminium oxide combined to high substrate roughness led to enlarged interfacial regions complicating the characterization of the coating region. The ALD alumina coatings had constant in-depth stoichiometry independent of the film thickness. Their bulk contained residual carbonaceous and hydroxyl fragments from partially unreacted precursors. Increasing deposition time for the thicker coatings led to completion of the reactions and therefore promotion of removal of the contaminating precursor fragments. A higher density was concluded for the thicker coatings from the lower sputtering rate and the lower OH<sup>-</sup> level for them. Interfacial carbon, chloride and hydroxide contamination decreased slightly with increase of deposited thickness.

Substantial enhancement of corrosion properties of the coated Al substrates was confirmed with electrochemical analysis in 0.5 M NaCl aqueous solution. The insulating properties of the alumina coating led to the same shape of polarization curves measured by LSV for the bare and coated specimens, indicating the corrosion of the substrate *via* residual channel defects connecting the substrate to the electrolyte through the coating. The impedance of the bare aluminium at OCP was modeled with a single anodic impedance corresponding to the passive oxide layer. The *in situ* thickness of the passive oxide layer was estimated separately with attribution of CPE to 2D and 3D distributions and application of Brug formula and a power-law model. Higher thickness values were obtained with the latter one. The *ex situ* thickness value obtained from XPS was compatible with the *in situ* thickness value range estimated from the power-law model. The capacitance values obtained for the coated samples were not in agreement with the thickness of the coatings obtained by XRR and therefore the contribution of the interfacial aluminium oxide to the total capacitance could not be ignored. However, the

## **Chapter VII. Investigation of corrosion protection of alumina by ALD coatings and effect of deposited layer thickness**

---

complexity of this contribution prevented a precise calculation of the thickness of the interfacial oxide.

Porosity values were obtained from both LSV and EIS. The decrease of the passive anodic current and increase of the polarization resistance reached 4 orders of magnitude for the 20 and 50 nm coatings, restricting the porosity (uncoated surface fraction) to ~0.02% in the best case. Obtaining lower porosity values for the 10 and 20 nm coatings on aluminium substrate than on copper substrate, is an important achievement considering the high cost of ALD. Apart from significant decrease of the passive current, the pitting potential was shifted to higher values in presence of 20 and 50 nm, which is considered important for corrosion protection of aluminium. For 10 nm coating, although its good sealing properties (low porosity) led to significant decrease of the passive current, its barrier properties (thickness) was not enough for delay of pitting corrosion.

# General conclusions

In this work, nanometre-thick (10 to 50 nm) coatings were grown by atomic layer deposition (ALD) on copper and aluminium substrates for improvement of the corrosion protection. TMA and water were used as precursors for ALD deposition of alumina at 250°C. The corrosion protection properties were studied by combination of electrochemical (LSV and EIS) and surface analysis (ToF-SIMS depth profiling and surface imaging). Microscopy techniques (AFM and SEM) were used as additional methods.

Using ToF-SIMS elemental depth profiling, three regions, the bulk coating region, the interfacial region and the substrate region were identified and characterized. Independent of the film thickness and the substrate material, the alumina coating had constant in-depth stoichiometry. Carbonaceous and hydroxyl fragments were always present in the bulk of the coating, as a result of partially unreacted precursors. Chlorine was also detected in the coating due to the high sensitivity of ToF-SIMS, and its origin was trace (less than 1%) chlorine contamination of the TMA precursor.  $\text{OH}^-$ ,  $\text{C}^-$  and  $\text{Cl}^-$  ions profiles peaks at the extreme surface of the coating and at the coating/substrate interface were attributed to contamination from the ambient after and before the coating deposition. Hydroxyl contamination was always decreasing with increased deposited coating thickness, owing to the fact that increasing deposition time promotes the removal of hydroxyl fragments by completing the reactions of deposition. A lower hydroxyl level of the coating was linked to a higher density and a lower porosity confirmed with electrochemical tests. In the case of copper, phosphorus (from electropolishing and

## General conclusions

---

pre-treatment) and sulphur (segregating from bulk copper) were other contaminants detected at the interface.

For both aluminium and copper substrates, the coating/substrate interface exhibited the presence of an interfacial native/spurious oxide. In the case of copper, only traces of copper oxide were present and the oxide formed most likely a discontinuous layer. For the aluminium on the contrary, the oxide contribution to the interfacial region was noticeable and its composition, similar to the one of the ALD coating, complicated the interpretation of the depth profiles.

The electrochemical analysis done in 0.5 M NaCl aqueous solution evidenced a substantial improvement of the corrosion properties of electropolished copper substrate coated with ALD alumina. This improvement was quantified using porosity calculations based on the comparison of anodic currents, polarization and charge transfer resistances and double layer capacitances obtained from LSV and EIS data, employing four different methods and leading to results with excellent agreement. Application of these methods was established based on the high dielectric properties of ALD alumina leading to the corrosion of the substrate only *via* residual pinholes and/or channel defects through the coating, connecting the substrate to the electrolyte, as evidenced by the same shape of LSV polarization curves for the bare and coated samples. The enhancement of polarization resistance and reduction of anodic current reached four orders of magnitude for the 50 nm coating, limiting the uncoated surface fraction to ~0.01%. The decrease of the measured porosity with increasing coating thickness was in agreement with the trend of hydroxyl contamination observed by ToF-SIMS. The low porosity also obtained for the thinner (10 nm) coating, less than 1%, confirmed ALD alumina as an excellent ultrathin coating for the corrosion protection of copper.

EIS experiments done at OCP and adoption of a proper equivalent circuit model shed more light on the corrosion mechanisms. In spite of observing only one time constant for the coated electropolished copper samples, the results were fitted also with an equivalent circuit model including separate time constants for the coating and the substrate. Using such circuit model, significantly high  $R_{\text{pore}}$  values were obtained, indicating a significantly lower cross section area of the channel defects in the bulk of the coating in

## General conclusions

---

comparison with the interface where the coating is attached to the substrate. This difference was attributed to the fast trenching of the substrate where it is attached to the coating leading to the higher opening of the channel defects at the bottom where they meet the substrate.

The study done in Chapter IV, on the effect of the interfacial copper oxide under the coating, confirmed the appropriate choice of a pre-treatment for the removal of the native oxide before the coating deposition done in Chapter III. Lower corrosion protection for the coating on a substrate without pre-treatment was attributed to the presence of higher amount of Cu(I) sites at the bottom of the channel defects, favouring oxygen reduction. Higher corrosion of the substrate led to higher dissolution of the coating both at the interface and in the bulk coating, confirmed by  $R_{\text{pore}}$  and  $R_{\text{ct}}$  values. However an initial more defective growth of the coating on a substrate without pre-treatment was also supported by the higher  $\text{OH}^-$  level in the bulk of the coating and higher  $\text{C}^-$  level at the interface. More localized corrosion occurred on the coated substrate without pre-treatment as shown by the detection of pits with ToF-SIMS, which was not the case for the pre-treated specimen. Modification of the interfacial oxide by pre-treatment of the copper substrate before ALD deposition was thus shown to have a positive effect on the corrosion resistance of the coated samples.

Topographical alteration of the copper surface by annealing for further reduction of surface asperities for a better performance of the ALD coatings was studied in Chapter V. However, the surface preparation by annealing was shown to lead to poor adhesion properties of the coating. Smoothing of the substrate was implied from the ToF-SIMS profiles and confirmed from AFM images and related roughness calculations. Annealing was also effective in reducing the interfacial  $\text{C}^-$  and  $\text{Cl}^-$  contamination. However, the higher intensity of the  $\text{CuO}_2^-$  and  $\text{OH}^-$  ions on the annealed coated substrates suggested coating detachment for the pristine samples, which was further confirmed with electrochemical measurements as well as ToF-SIMS and SEM imaging on pristine samples. The anodic shift of corrosion potential and increase of cathodic Tafel slopes for annealed coated samples in comparison with the electropolished ones was attributed to the high exposure of interfacial copper oxide to the electrolyte for these samples, in agreement with the ToF-SIMS data. Apart from the initially high porosity values

## General conclusions

---

obtained from EIS, the significant increase of the porosity obtained from LSV denoted coating detachment in the electrolyte, which was further confirmed with SEM imaging and ToF-SIMS chemical mapping on polarized samples. Although on electropolished substrate the best performance was obtained for the thickest coating, it showed the worse performance on the annealed substrate. Apart from mechanical effects, the poor performance for the thickest coating was also attributed to higher local increase of pH for a thicker coating leading to enhancement of dissolution of alumina and delamination of the coating.

In spite of high sealing property of ALD alumina on electropolished copper substrate, the studies presented in Chapter VI revealed its low durability for longer immersion times. Initial resistance and capacitance values measured after 30 min immersion revealed an increase of the coating porosity of one order of magnitude and a decrease of  $9.69 \times 10^{-4} \text{ nm.h}^{-1}$  in thickness as a result of atmospheric corrosion. The decrease in coating thickness accelerated in the electrolyte to  $0.9 \text{ nm.h}^{-1}$  even though its porosity remained unchanged. Coating thickness decrease was confirmed from ToF-SIMS depth profiling and the calculated value was in good agreement with EIS. The absence of marked change in the coating matrix and no notable corrosion of the substrate observed on ToF-SIMS depth profiles were in agreement with unchanged porosity calculated from EIS. Internodular (between two adjacent nodules) preferential dissolution of the coating at nanometric scale was revealed and measured from AFM images.

The study of ALD alumina on aluminium substrate presented in the last chapter showed the successful growth of the coating also on Al substrate. Investigation of its corrosion properties revealed significant improvement of the corrosion protection. Lower porosities were obtained for 10 and 20 nm coatings on Al substrate than on copper, implying a better coating performance on Al substrate. The significant decrease of the passive current for all coating thicknesses demonstrated the good sealing property, however 10 nm did not show sufficient barrier properties to increase the pitting potential. Considering the similar porosity obtained for the 20 and 50 nm coatings, and the increase of the pitting potential in both cases (slightly higher for the latter one), and considering the cathodic shift of the corrosion potential for the 50 nm coating, 20 nm seemed to be the most appropriate choice. Therefore, the best coating performance was obtained with a

## General conclusions

---

lower coating thickness on Al than on copper, which is considered highly beneficial. The long delay between the substrate preparation and the coating deposition in addition to the high roughness of the Al substrate in comparison with the Cu substrate, complicated the interpretation of EIS results coming from the 3D distribution of time constants in the interfacial oxide.

The present thesis work was a fundamental research on the growth of ALD alumina on pure copper and aluminium and the corrosion protection on these two metals. The satisfactory results obtained on electropolished copper and polished aluminium, confirm ALD alumina as a promising candidate for corrosion protection of Al-Cu alloys. Regarding the excellent sealing properties of ALD alumina, it is proposed in combination with more chemically stable ALD coatings in mixture and laminates for corrosion protection of high precision devices where Al and Cu are used.

Future perspective of the present study would be the investigation of corrosion protection of ALD alumina on Al-Cu alloys and in combination with more chemically stable ALD coatings, such as  $\text{TiO}_2$  or  $\text{Ta}_2\text{O}_5$ .



# References

- [1] L. Núñez, E. Reguera, F. Corvo, E. González, C. Vazquez, *Corros. Sci.* 47 (2005) 461.
- [2] S. Chen, Y. Chen, Y. Lei, Y. Yin, *Electrochem. Commun.* 11 (2009) 1675.
- [3] S.M. Milić, M.M. Antonijević, *Corros. Sci.* 51 (2009) 28.
- [4] G. Kear, B.D. Barker, F.C. Walsh, *Corros. Sci.* 46 (2004) 109.
- [5] C. Deslouis, B. Tribollet, G. Mengoli, M.M. Musiani, *J. Appl. Electrochem.* 18 (1988) 374.
- [6] M. Braun, K. Nobe, *J. Electrochem. Soc.* 126 (1979) 1666.
- [7] A.L. Bacarella, J.C. Griess, *J. Electrochem. Soc.* 120 (1973) 459.
- [8] F. King, C.D. Litke, M.J. Quinn, D.M. LeNeveu, *Corros. Sci.* 37 (1995) 833.
- [9] A. Sanjurjo, B.J. Wood, K.H. Lau, G.T. Tong, D.K. Choi, M.C.H. McKubre, H.K. Song, D. Peters, N. Church, *Surf. Coat. Technol.* 49 (1991) 103.
- [10] K.H. Lau, A. Sanjurjo, B.J. Wood, *Surf. Coat. Technol.* 54–55, Part 1 (1992) 234.
- [11] Y. Lin, H. Yasuda, *J. Appl. Polym. Sci.* 60 (1996) 543.
- [12] S. Patil, S.R. Sainkar, P.P. Patil, *Appl. Surf. Sci.* 225 (2004) 204.
- [13] J.B. Matos, E. D'Elia, O.E. Barcia, O.R. Mattos, N. Pébère, B. Tribollet, *Electrochimica Acta* 46 (2001) 1377.
- [14] M. Metikoš-Huković, R. Babić, I. Paić, *J. Appl. Electrochem.* 30 (2000) 617.
- [15] M. Finšgar, I. Milošev, *Mater. Corros.* 62 (2011) 956.
- [16] M. Cubillos, M. Sancy, J. Pavez, E. Vargas, R. Urzua, J. Henríquez-Roman, B. Tribollet, J.H. Zagal, M.A. Páez, *Electrochimica Acta* 55 (2010) 2782.
- [17] Q.Q. Liao, Z.W. Yue, D. Yang, Z.H. Wang, Z.H. Li, H.H. Ge, Y.J. Li, *Corros. Sci.* 53 (2011) 1999.
- [18] W. Chen, S. Hong, H.B. Li, H.Q. Luo, M. Li, N.B. Li, *Corros. Sci.* 61 (2012) 53.

## References

---

- [19] J.B. Bessone, D.R. Salinas, C.E. Mayer, M. Ebert, W.J. Lorenz, *Electrochimica Acta* 37 (1992) 2283.
- [20] Z. Szklarska-Smialowska, *Corros. Sci.* 41 (1999) 1743.
- [21] E. McCafferty, *Corros. Sci.* 45 (2003) 1421.
- [22] C.M.A. Brett, *J. Appl. Electrochem.* 20 (1990) 1000.
- [23] P. Carbonini, T. Monetta, D.B. Mitton, F. Bellucci, P. Mastronardi, B. Scatteia, *J. Appl. Electrochem.* 27 (1997) 1135.
- [24] W.-J. Lee, S.-I. Pyun, *Electrochimica Acta* 44 (1999) 4041.
- [25] S.E. Frers, M.M. Stefenel, C. Mayer, T. Chierchie, *J. Appl. Electrochem.* 20 (1990) 996.
- [26] H.J.W. Lenderink, M.V.D. Linden, J.H.W. De Wit, *Electrochimica Acta* 38 (1993) 1989.
- [27] F.J. Martin, G.T. Cheek, W.E. O'Grady, P.M. Natishan, *Corros. Sci.* 47 (2005) 3187.
- [28] L. Garrigues, N. Pebere, F. Dabosi, *Electrochimica Acta* 41 (1996) 1209.
- [29] A.M. Beccaria, L. Chiaruttini, *Corros. Sci.* 41 (1999) 885.
- [30] J. Halambek, K. Berković, J. Vorkapić-Furač, *Mater. Chem. Phys.* 137 (2013) 788.
- [31] E.-S.M. Sherif, *Int. J. Electrochem. Sci.* 6 (2011) 1479.
- [32] V. Branzoi, F. Golgovici, F. Branzoi, *Mater. Chem. Phys.* 78 (2003) 122.
- [33] F. Mansfeld, *Electrochimica Acta* 38 (1993) 1891.
- [34] S. Lin, H. Shih, F. Mansfeld, *Corros. Sci.* 33 (1992) 1331.
- [35] F. Mansfeld, S. Lin, K. Kim, H. Shih, *Corros. Sci.* 27 (1987) 997.
- [36] X. Nie, E.I. Meletis, J.C. Jiang, A. Leyland, A.L. Yerokhin, A. Matthews, *Surf. Coat. Technol.* 149 (2002) 245.
- [37] K.G. Conroy, C.B. Breslin, *Electrochimica Acta* 48 (2003) 721.
- [38] M. Leskelä, M. Ritala, *Thin Solid Films* 409 (2002) 138.
- [39] S.M. George, *Chem. Rev.* 110 (2010) 111.
- [40] M. Leskelä, M. Ritala, *Angew. Chem. Int. Ed.* 42 (2003) 5548.
- [41] B.S. Lim, A. Rahtu, R.G. Gordon, *Nat. Mater.* 2 (2003) 749.
- [42] R. Matero, M. Ritala, M. Leskela, T. Salo, J. Aromaa, O. Forsen, *J. Phys. Iv* 9 (1999) 493.
- [43] R.L. Puurunen, *J. Appl. Phys.* 97 (2005) 121301.
- [44] T. Suntola, J. Antson, US Patent, 4,058,430, n.d.
- [45] H.S. Nalwa, *Handbook of Thin Film Materials*, Academic Press, 2001.

## References

---

- [46] M. Leskela, M. Ritala, *J. Phys. Iv* 5 (1995) 937.
- [47] V. Miikkulainen, M. Leskel , M. Ritala, R.L. Puurunen, *J. Appl. Phys.* 113 (2013) 021301.
- [48] S.M. George, A.W. Ott, J.W. Klaus, *J. Phys. Chem.* 100 (1996) 13121.
- [49] T. Suntola, *Thin Solid Films* 216 (1992) 84.
- [50] B.T. McDermott, N.A. El-Masry, M.A. Tischler, S.M. Bedair, *Appl. Phys. Lett.* 51 (1987) 1830.
- [51] H. Kumagai, K. Toyoda, K. Kobayashi, M. Obara, Y. Iimura, *Appl. Phys. Lett.* 70 (1997) 2338.
- [52] D. Riihelä, M. Ritala, R. Matero, M. Leskelä, *Thin Solid Films* 289 (1996) 250.
- [53] R. Matero, A. Rahtu, M. Ritala, M. Leskelä, T. Sajavaara, *Thin Solid Films* 368 (2000) 1.
- [54] A.W. Ott, J.W. Klaus, J.M. Johnson, S.M. George, *Thin Solid Films* 292 (1997) 135.
- [55] M. Ritala, M. Leskela, L. Niinisto, P. Haussalo, *Chem. Mater.* 5 (1993) 1174.
- [56] A.C. Dillon, A.W. Ott, J.D. Way, S.M. George, *Surf. Sci.* 322 (1995) 230.
- [57] J.W. Elam, M.D. Groner, S.M. George, *Rev. Sci. Instrum.* 73 (2002) 2981.
- [58] M.D. Groner, J.W. Elam, F.H. Fabreguette, S.M. George, *Thin Solid Films* 413 (2002) 186.
- [59] M.K. Tripp, C. Stampfer, D.C. Miller, T. Helbling, C.F. Herrmann, C. Hierold, K. Gall, S.M. George, V.M. Bright, *Sens. Actuators Phys.* 130-131 (2006) 419.
- [60] B. Díaz, J. Światowska, V. Maurice, A. Seyeux, B. Normand, E. H r könen, M. Ritala, P. Marcus, *Electrochimica Acta* 56 (2011) 10516.
- [61] B. Díaz, E. H r könen, J. Światowska, V. Maurice, A. Seyeux, P. Marcus, M. Ritala, *Corros. Sci.* 53 (2011) 2168.
- [62] E. H r könen, B. Díaz, J. Światowska, V. Maurice, A. Seyeux, M. Vehkamäki, T. Sajavaara, M. Fenker, P. Marcus, M. Ritala, *J. Electrochem. Soc.* 158 (2011) C369.
- [63] E. H r könen, B. Díaz, J. Światowska, V. Maurice, A. Seyeux, M. Fenker, L. Tóth, G. Radnóczy, P. Marcus, M. Ritala, *Chem. Vap. Depos.* 19 (2013) 194.
- [64] E. H r könen, I. Kolev, B. Díaz, J. Światowska, V. Maurice, A. Seyeux, P. Marcus, M. Fenker, L. Toth, G. Radnóczy, M. Vehkamäki, M. Ritala, *ACS Appl. Mater. Interfaces* 6 (2014) 1893.
- [65] E. Marin, A. Lanzutti, L. Guzman, L. Fedrizzi, *J. Coat. Technol. Res.* 8 (2011) 655.
- [66] E. Marin, L. Guzman, A. Lanzutti, W. Ensinger, L. Fedrizzi, *Thin Solid Films* 522 (2012) 283.
- [67] E. Marin, A. Lanzutti, L. Guzman, L. Fedrizzi, *J. Coat. Technol. Res.* 9 (2012) 347.
- [68] L. Paussa, L. Guzman, E. Marin, N. Isomäki, L. Fedrizzi, *Surf. Coat. Technol.* 206 (2011) 976.

## References

---

- [69] M. Fedel, C. Zanella, S. Rossi, F. Deflorian, *Sol. Energy* 101 (2014) 167.
- [70] A.I. Abdulagatov, Y. Yan, J.R. Cooper, Y. Zhang, Z.M. Gibbs, A.S. Cavanagh, R.G. Yang, Y.C. Lee, S.M. George, *ACS Appl. Mater. Interfaces* 3 (2011) 4593.
- [71] M.L. Chang, T.C. Cheng, M.C. Lin, H.C. Lin, M.J. Chen, *Appl. Surf. Sci.* 258 (2012) 10128.
- [72] Z. Chai, Y. Liu, J. Li, X. Lu, D. He, *RSC Adv.* 4 (2014) 50503.
- [73] S.E. Potts, L. Schmalz, M. Fenker, B. Díaz, J. Światowska, V. Maurice, A. Seyeux, P. Marcus, G. Radnóczy, L. Tóth, *J. Electrochem. Soc.* 158 (2011) C132.
- [74] P.A. Jacquet, *Nature* 135 (1935) 1076.
- [75] K. Shimizu, R. Payling, H. Habazaki, P. Skeldon, G.E. Thompson, *J. Anal. At. Spectrom.* 19 (2004) 692.
- [76] John C. Vickerman, I.S. Gilmore, *Surface Analysis - The Principal Techniques*, 2nd ed., Wiley, 2009.
- [77] M.E. Orazem, N. Pébère, B. Tribollet, *J. Electrochem. Soc.* 153 (2006) B129.
- [78] Zaki Ahmad, *Principles of Corrosion Engineering and Corrosion Control*, Butterworth-Heinemann, 2006.
- [79] W.J. Lorenz, F. Mansfeld, *Corros. Sci.* 21 (1981) 647.
- [80] C. Deslouis, B. Tribollet, G. Mengoli, M.M. Musiani, *J. Appl. Electrochem.* 18 (1988) 384.
- [81] O. Barcia, O. Mattos, N. Pebere, B. Tribollet, *J. Electrochem. Soc.* 140 (1993) 2825.
- [82] H.P. Lee, K. Nobe, *J. Electrochem. Soc.* 133 (1986) 2035.
- [83] G. Faita, G. Fiori, D. Salvatore, *Corros. Sci.* 15 (1975) 383.
- [84] K. Rahmouni, M. Keddou, A. Srhiri, H. Takenouti, *Corros. Sci.* 47 (2005) 3249.
- [85] K.F. Khaled, *Mater. Chem. Phys.* 125 (2011) 427.
- [86] A. Moreau, J.P. Frayret, F.D. Rey, R. Pointeau, *Electrochimica Acta* 27 (1982) 1281.
- [87] C.H. Bonfiglio, H.C. Albaya, O.A. Cobo, *Corros. Sci.* 13 (1973) 717.
- [88] C. Deslouis, O.R. Mattos, M.M. Musiani, B. Tribollet, *Electrochimica Acta* 38 (1993) 2781.
- [89] A. Moreau, *Electrochimica Acta* 26 (1981) 1609.
- [90] F.K. Crundwell, *Electrochimica Acta* 37 (1992) 2707.
- [91] A. Moreau, *Electrochimica Acta* 26 (1981) 497.
- [92] R.J.K. Wood, S.P. Hutton, D.J. Schiffrin, *Corros. Sci.* 30 (1990) 1177.
- [93] W. Li, L. Hu, S. Zhang, B. Hou, *Corros. Sci.* 53 (2011) 735.

## References

---

- [94] C.-M. Chu, C. Lee, Y.-Y. Wang, C.-C. Wan, C.-J. Chen, *J. Chin. Inst. Chem. Eng.* 38 (2007) 361.
- [95] C.I. Elsner, R.C. Salvarezza, A.J. Arvia, *Electrochimica Acta* 33 (1988) 1735.
- [96] C. Deslouis, B. Tribollet, G. Mengoli, M.M. Musiani, *J. Appl. Electrochem.* 18 (1988) 384.
- [97] M.V. Vazquez, S.R. de Sanchez, E.J. Calvo, D.J. Schiffrin, *J. Electroanal. Chem.* 374 (1994) 179.
- [98] H. Lal, H.R. Thirsk, *J. Chem. Soc. Resumed* (1953) 2638.
- [99] U. Collisi, H.-H. Strehblow, *J. Electroanal. Chem. Interfacial Electrochem.* 284 (1990) 385.
- [100] H.D. Speckmann, S. Haupt, H.-H. Strehblow, *Surf. Interface Anal.* 11 (1988) 148.
- [101] H.-H. Strehblow, V. Maurice, P. Marcus, *Electrochimica Acta* 46 (2001) 3755.
- [102] H.-H. Strehblow, B. Titze, *Electrochimica Acta* 25 (1980) 839.
- [103] H.-D. Speckmann, M.M. Lohrengel, J.W. Schultze, H.-H. Strehblow, *Berichte Bunsenges. Für Phys. Chem.* 89 (1985) 392.
- [104] M.M. Lohrengel, J.W. Schultze, H.D. Speckmann, H.-H. Strehblow, *Electrochimica Acta* 32 (1987) 733.
- [105] B. Millet, C. Fiaud, C. Hinnen, E. Sutter, *Corros. Sci.* 37 (1995) 1903.
- [106] H.Y.H. Chan, C.G. Takoudis, M.J. Weaver, *J. Phys. Chem. B* 103 (1999) 357.
- [107] J. Kunze, V. Maurice, L.H. Klein, H.H. Strehblow, P. Marcus, *Electrochimica Acta* 48 (2003) 1157.
- [108] F. King, M.J. Quinn, C.D. Litke, *J. Electroanal. Chem.* 385 (1995) 45.
- [109] F. King, C.D. Litke, Y. Tang, *J. Electroanal. Chem.* 384 (1995) 105.
- [110] M.V. Vazquez, S.R. de Sanchez, E.J. Calvo, D.J. Schiffrin, *J. Electroanal. Chem.* 374 (1994) 189.
- [111] G.D. Preston, L.L. Bircumshaw, *Philos. Mag.* 20 (1935) 706.
- [112] J. Kruger, *J. Electrochem. Soc.* 106 (1959) 847.
- [113] A.M.S. El Din, F.M.A. El Wahab, *Electrochimica Acta* 9 (1964) 113.
- [114] F. Mansfeld, G. Liu, H. Xiao, C.H. Tsai, B.J. Little, *Corros. Sci.* 36 (1994) 2063.
- [115] E.M. Sherif, S.-M. Park, *J. Electrochem. Soc.* 152 (2005) B428.
- [116] E. Delia, O.E. Barcia, O.R. Mattos, N. Pebere, B. Tribollet, *J. Electrochem. Soc.* 143 (1996) 961.
- [117] M. Dechialvo, R. Salvarezza, D. Moll, A. Arvia, *Electrochimica Acta* 30 (1985) 1501.
- [118] B. Díaz, E. Hrkönen, V. Maurice, J. Światowska, A. Seyeux, M. Ritala, P. Marcus, *Electrochimica Acta* 56 (2011) 9609.

## References

---

- [119] B. Díaz, J. Światowska, V. Maurice, M. Pisarek, A. Seyeux, S. Zanna, S. Tervakangas, J. Kolehmainen, P. Marcus, *Surf. Coat. Technol.* 206 (2012) 3903.
- [120] B. Díaz, J. Światowska, V. Maurice, A. Seyeux, E. Hrkönen, M. Ritala, S. Tervakangas, J. Kolehmainen, P. Marcus, *Electrochimica Acta* 90 (2013) 232.
- [121] E. Hrkönen, S.E. Potts, W.M.M. Kessels, B. Díaz, A. Seyeux, J. Światowska, V. Maurice, P. Marcus, G. Radnóczy, L. Tóth, M. Kariniemi, J. Niinistö, M. Ritala, *Thin Solid Films* 534 (2013) 384.
- [122] M.E. Orazem, B. Tribollet, *Electrochemical Impedance Spectroscopy*, Wiley, Hoboken, N.J., 2008.
- [123] B.E. Torres Bautista, M.L. Carvalho, A. Seyeux, S. Zanna, P. Cristiani, B. Tribollet, P. Marcus, I. Frateur, *Bioelectrochemistry* 97 (2014) 34.
- [124] J.-B. Jorcin, M.E. Orazem, N. Pébère, B. Tribollet, *Electrochimica Acta* 51 (2006) 1473.
- [125] P. Zoltowski, *J. Electroanal. Chem.* 443 (1998) 149.
- [126] S.H. Ahn, Y.S. Choi, J.G. Kim, J.G. Han, *Surf. Coat. Technol.* 150 (2002) 319.
- [127] R.C. Barik, J.A. Wharton, R.J.K. Wood, K.R. Stokes, R.L. Jones, *Surf. Coat. Technol.* 199 (2005) 158.
- [128] G.J. Brug, A.L.G. Van Den Eeden, M. Sluyters-Rehbach, J.H. Sluyters, *J. Electroanal. Chem. Interfacial Electrochem.* 176 (1984) 275.
- [129] R. Ramesham, M.F. Rose, *Corros. Sci.* 39 (1997) 2019.
- [130] B. Díaz, E. Hrkönen, J. Światowska, A. Seyeux, V. Maurice, M. Ritala, P. Marcus, *Corros. Sci.* 82 (2014) 208.
- [131] V. Maurice, I. Bennour, S. Zanna, L.H. Klein, P. Marcus, *J. Phys. Chem. C* 114 (2010) 7132.
- [132] J. Creus, H. Mazille, H. Idrissi, *Surf. Coat. Technol.* 130 (2000) 224.
- [133] F.C. Walsh, C. Ponce de León, C. Kerr, S. Court, B.D. Barker, *Surf. Coat. Technol.* 202 (2008) 5092.
- [134] R.A. Antunes, M.C.L. de Oliveira, M.F. Pillis, *Int. J. Electrochem. Sci.* 8 (2013) 1487.
- [135] B. Matthes, E. Broszeit, J. Aromaa, H. Ronkainen, S.-P. Hannula, A. Leyland, A. Matthews, *Surf. Coat. Technol.* 49 (1991) 489.
- [136] C. Liu, Q. Bi, A. Leyland, A. Matthews, *Corros. Sci.* 45 (2003) 1257.
- [137] W. Tato, D. Landolt, *J. Electrochem. Soc.* 145 (1998) 4173.
- [138] G.W. Walter, *Corros. Sci.* 26 (1986) 681.
- [139] F. Mansfeld, *Electrochimica Acta* 35 (1990) 1533.
- [140] D.K. Dyer, *Thin Solid Films* 23 (1974) S37.

## References

---

- [141] H. Kattelus, M. Ylilampi, J. Saarilahti, J. Antson, S. Lindfors, *Thin Solid Films* 225 (1993) 296.
- [142] V.M.-W. Huang, V. Vivier, M.E. Orazem, N. Pebere, B. Tribollet, *J. Electrochem. Soc.* 154 (2007) C99.
- [143] D. Weng, P. Jokiel, A. Uebleis, H. Boehni, *Surf. Coat. Technol.* 88 (1997) 147.
- [144] R.D. Armstrong, D. Wright, *Electrochimica Acta* 38 (1993) 1799.
- [145] R.D. Armstrong, J.D. Wright, *Corros. Sci.* 33 (1992) 1529.
- [146] G.W. Walter, *Corros. Sci.* 32 (1991) 1041.
- [147] D.C. Miller, R.R. Foster, Y. Zhang, S.-H. Jen, J.A. Bertrand, Z. Lu, D. Seghete, J.L. O'Patchen, R. Yang, Y.-C. Lee, S.M. George, M.L. Dunn, *J. Appl. Phys.* 105 (2009) 093527.
- [148] M. Pourbaix, *Atlas of Electrochemical Equilibria in Aqueous Solutions*, Pergamon, New York, 1966.
- [149] Christian Vargel, *CORROSION DE L'ALUMINIUM*, Dunod, 1999.
- [150] J.O. Bockris, L.V. Minevski, *J. Electroanal. Chem.* 349 (1993) 375.
- [151] T.H. Nguyen, R.T. Foley, *J. Electrochem. Soc.* 127 (1980) 2563.
- [152] E.-J. Lee, S.-I. Pyun, *Corros. Sci.* 37 (1995) 157.
- [153] J. Galvele, *J. Electrochem. Soc.* 123 (1976) 464.
- [154] S. Pride, J. Scully, J. Hudson, *J. Electrochem. Soc.* 141 (1994) 3028.
- [155] J.R. Galvele, *Corros. Sci.* 47 (2005) 3053.
- [156] J. Bessone, C. Mayer, K. Jüttner, W.J. Lorenz, *Electrochimica Acta* 28 (1983) 171.
- [157] F. Mansfeld, S. Lin, S. Kim, H. Shih, *Electrochimica Acta* 34 (1989) 1123.
- [158] F. Mansfeld, Y. Wang, H. Shih, *Electrochimica Acta* 37 (1992) 2277.
- [159] J. Liang, Y. Hu, Y. Wu, H. Chen, *Surf. Coat. Technol.* 240 (2014) 145.
- [160] M.M. Lohrengel, *Mater. Sci. Eng. R Rep.* 11 (1993) 243.
- [161] T. Hiemstra, H. Yong, W.H. Van Riemsdijk, *Langmuir* 15 (1999) 5942.
- [162] P. Marcus, C. Hinnen, I. Olefjord, *Surf. Interface Anal.* 20 (1993) 923.
- [163] B. Hirschorn, M.E. Orazem, B. Tribollet, V. Vivier, I. Frateur, M. Musiani, *J. Electrochem. Soc.* 157 (2010) C452.
- [164] M.E. Orazem, I. Frateur, B. Tribollet, V. Vivier, S. Marcelin, N. Pebere, A.L. Bunge, E.A. White, D.P. Riemer, M. Musiani, *J. Electrochem. Soc.* 160 (2013) C215.
- [165] B. Hirschorn, M.E. Orazem, B. Tribollet, V. Vivier, I. Frateur, M. Musiani, *J. Electrochem. Soc.* 157 (2010) C458.

## References

---

[166]R. Ambat, E. Dwarakadasa, J. Appl. Electrochem. 24 (1994) 911.

[167]E. McCafferty, Corros. Sci. 37 (1995) 481.

# List of Figures

<i>Figure I.1: Schematic representation of an ALD cycle, from references [43,47] .....</i>	<i>8</i>
<i>Figure I.2: Schematic description of ALD growth rate per growth temperature, from references [39,45].....</i>	<i>16</i>
<i>Figure I.3: Schematic illustration of possible mechanism for the surface chemistry of ALD Al<sub>2</sub>O<sub>3</sub> using TMA and water, from reference [48] .....</i>	<i>18</i>
<i>Figure II.1: Mechanical polishing disks, suspensions and machine for copper disk.....</i>	<i>24</i>
<i>Figure II.2: Electropolishing of copper in H<sub>3</sub>PO<sub>4</sub> .....</i>	<i>25</i>
<i>Figure II.3: Schematic and simplified representation of annealing system.....</i>	<i>26</i>
<i>Figure II.4: SIMS process and “collision cascade” .....</i>	<i>31</i>
<i>Figure II.5: Picture of the ToF-SIMS<sup>s</sup> spectrometer used in the present study.....</i>	<i>34</i>
<i>Figure II.6: Dual beam mode depth profiling, from ToF-SIMS<sup>s</sup> brochure.....</i>	<i>34</i>
<i>Figure II.7: Schematic illustration of AFM tip-sample interaction, from reference [76].....</i>	<i>36</i>
<i>Figure II.8: Sample-tip interaction modes in AFM.....</i>	<i>36</i>
<i>Figure II.9: Three-electrode set up and the electrochemical cell used in the present study.....</i>	<i>40</i>
<i>Figure II.10: Nyquist (left) and Bode (right) representations used for visualisation of EIS data.....</i>	<i>43</i>
<i>Figure II.11: Linear polarization technique: calculation of R<sub>p</sub> (left). Tafel polarization technique: calculation of i<sub>corr</sub> (right).....</i>	<i>45</i>

## List of Figures

---

- Figure III.1:** LSV polarization curves (after 45 min OCP) for bare electropolished Cu substrates in 0.5 M NaCl, (scan rate:  $1 \text{ mV}\cdot\text{s}^{-1}$ ): Pre-treated, under argon bubbling and swept from -0.8 V/SCE (A). Pre-treated, under argon bubbling and swept separately, positive and negative-going from OCP (B). Pre-treated, under lower rate of argon bubbling and swept from -0.8 V/SCE (C). Freshly polished, under ambient conditions and swept from -0.8 V/SCE (D) ..... 49
- Figure III.2:** Representation of measurement of polarization resistance (A) and Tafel slopes (B) on polarization curve presented in Figure III.1.A..... 49
- Figure III.3:** EIS Bode plot for bare copper substrate (after 30 min immersion) in 0.5 M NaCl under argon bubbling (pH = 6) at OCP. Points and lines correspond to measured and fitted data, respectively. .... 55
- Figure III.4:** A: Equivalent electrical circuit of the interfacial impedance of a corroding electrode at open circuit potential. B: Equivalent circuit model adopted for the bare Cu substrate for the present study at open circuit potential (E.C.1). .... 56
- Figure III.5:** ToF-SIMS negative ion depth profiles for 10 nm (A), 20 nm (B) and 50 nm (C) ALD alumina coatings prepared at  $250^\circ\text{C}$  on copper substrate..... 60
- Figure III.6:** ToF-SIMS OH (A) and C<sup>-</sup> (B) ion depth profiles for 10 nm, 20 nm and 50 nm ALD alumina coatings ..... 63
- Figure III.7:** ToF-SIMS Cl<sup>-</sup> and S<sup>-</sup> ion depth profiles for 10 nm, 20 nm and 50 nm ALD alumina coatings ..... 64
- Figure III.8:** Topographical AFM images ( $1 \times 1 \mu\text{m}^2$ ) of ALD alumina coated Cu substrates: (A) pristine 10 nm sample, z range = 50 nm, (B) pristine 20 nm sample, z range = 20 nm, (C) pristine 50 nm sample, z range = 20 nm and (D) 50 nm sample after LSV test, z range = 35 nm..... 66
- Figure III.9:** LSV polarization curves for the bare and ALD alumina coated Cu substrates in 0.5 M NaCl under argon bubbling (pH = 6), swept from -0.8 V/SCE (scan rate:  $1 \text{ mV}\cdot\text{s}^{-1}$ )..... 67
- Figure III.10:** EIS Bode plots for the bare and ALD alumina coated copper substrates in 0.5 M NaCl under argon bubbling (pH = 6) at OCP. Points and lines correspond to measured and fitted data, respectively..... 70
- Figure III.11:** A: Typical equivalent circuit used for coated electrodes. B: Equivalent circuit model adopted for coated Cu substrate for the present study (E.C.3) ..... 71

## List of Figures

---

<b>Figure III.12:</b> Logarithm of the imaginary part of the impedance as a function of logarithm of frequency for coated substrates .....	72
<b>Figure III.13:</b> Adaptation of E.C.1 for coated substrate (E.C.2).....	74
<b>Figure III.14:</b> Channel defects in a coating where: A: channel defect cross section area is equal to the wetted area on the substrate. B: where the wetted area is larger than the channel defect cross section area. C: adaptation of opening at the end of the channel defects in the present study .....	77
<b>Figure III.15:</b> Porosity values calculated from EIS and LSV results for ALD alumina coated Cu substrate.....	79
<b>Figure IV.1:</b> EIS Bode plots for the bare pre-treated and not pre-treated copper substrates in 0.5 M NaCl under argon bubbling (pH = 6) at OCP. Points and lines correspond to measured and fitted data, respectively .....	85
<b>Figure IV.2:</b> LSV polarization curves for the bare pre-treated and not pre-treated copper in 0.5 M NaCl under argon bubbling (pH = 6), scan rate: 1 mV.s <sup>-1</sup> .....	87
<b>Figure IV.3:</b> LSV polarization curves for a freshly polished Cu substrate (Cu-fresh) and B-PT in presence of higher amount of oxygen (argon bubbling done at lower rate) in the electrolyte in 0.5 M NaCl (pH = 6), scan rate: 1 mV.s <sup>-1</sup> .....	90
<b>Figure IV.4:</b> ToF-SIMS negative ion depth profiles for C-PT (A) and C-NPT (B).....	91
<b>Figure IV.5:</b> Comparative representation of ToF-SIMS depth profiles for C-PT and C-NPT for each ion.....	92
<b>Figure IV.6:</b> Comparison of the CuO <sub>2</sub> <sup>-</sup> for C-PT and C-NPT (linear scale).....	93
<b>Figure IV.7:</b> EIS Bode plots for coated (and bare) pre-treated and not pre-treated copper substrates in 0.5 M NaCl under argon bubbling (pH = 6) at OCP. Points and lines correspond to measured and fitted data, respectively.....	95
<b>Figure IV.8:</b> LSV polarization curves for bare and coated substrates in 0.5 M NaCl (pH = 6) under argon bubbling, scan rate: 1 mV.s <sup>-1</sup> .....	99
<b>Figure IV.9:</b> ToF-SIMS negative ion depth profiles for C-PT (A) and C-NPT (B) after immersion and polarization in 0.5 M NaCl (pH = 6), scan rate: 1 mV.s <sup>-1</sup> .....	101

## List of Figures

---

<b>Figure IV.10:</b> Comparative representation of ToF-SIMS depth profiles for C-PT and C-NPT for each ion, after immersion and polarization in 0.5 M NaCl (pH = 6), scan rate: $1 \text{ mV}\cdot\text{s}^{-1}$ .....	102
<b>Figure IV.11:</b> Comparison of the CuO profile for C-PT and C-NPT (linear scale), related to Figure IV.9 .....	103
<b>Figure IV.12:</b> Optical micrograph after immersion and polarization in 0.5 M NaCl (pH = 6), scan rate: $1 \text{ mV}\cdot\text{s}^{-1}$ (A) and comparison of ToF-SIMS CuCl depth profiles of polarized C-NPT in an area without (dark green) and with (light green) an obvious pit (B) .....	104
<b>Figure V.1:</b> ToF-SIMS negative ion depth profiles for 10 nm (A), 20 nm (B) and 50 nm (C) ALD alumina coatings prepared at 250°C on annealed copper substrate .....	110
<b>Figure V.2:</b> Comparative representation of ToF-SIMS depth profiles of selected ions for alumina coatings on annealed (ANLD) and electropolished (ELPL) substrates .....	111
<b>Figure V.3:</b> Comparative representation of ToF-SIMS depth profiles same as Figure V.2 .....	112
<b>Figure V.4:</b> Topographic AFM images ( $5 \times 5 \mu\text{m}$ ) of ALD alumina coated Cu substrates, electropolished and annealed .....	113
<b>Figure V.5:</b> Roughness values (rms) obtained by AFM for ALD as same as Figure V.4 .....	114
<b>Figure V.6:</b> LSV polarization curves for the bare and ALD alumina coated Cu annealed substrates in 0.5 M NaCl under argon bubbling (pH = 6), scan rate: $1 \text{ mV}\cdot\text{s}^{-1}$ .....	115
<b>Figure V.7:</b> EIS Bode plots for the bare and ALD alumina coated annealed copper substrates in 0.5 M NaCl under argon bubbling at OCP (pH = 6). Points and lines correspond to measured and fitted data, respectively .....	118
<b>Figure V.8:</b> EIS Nyquist plots for ALD alumina coated annealed copper substrates in 0.5 M NaCl under argon bubbling at OCP. Points and lines correspond to measured and fitted data, respectively .....	119
<b>Figure V.9:</b> Comparison of porosity values obtained for samples from the same and from different deposition batches on the annealed copper substrate .....	121
<b>Figure V.10:</b> SEM images of a 50 nm ALD alumina coating on the annealed copper substrate .....	123
<b>Figure V.11:</b> SEM images taken from a 20 nm coating on copper annealed substrate after polarization in 0.5 M NaCl .....	124

## List of Figures

---

<b>Figure V.12:</b> ToF-SIMS surface images ( $100\ \mu\text{m} \times 100\ \mu\text{m}$ ) from the 10 nm coating on copper annealed substrate .....	125
<b>Figure V.13:</b> ToF-SIMS chemical images ( $100\ \mu\text{m} \times 100\ \mu\text{m}$ ) from the 50 nm coating on copper annealed substrate .....	126
<b>Figure V.14:</b> ToF-SIMS surface images ( $100\ \mu\text{m} \times 100\ \mu\text{m}$ ) from the 20 nm coating on copper annealed substrate after the polarization test in 0.5 M NaCl .....	126
<b>Figure VI.1:</b> EIS Bode plots versus time for the 50 nm ALD alumina coated electropolished pre-treated copper substrate in 0.5 M NaCl under argon bubbling ( $\text{pH} = 6$ ) at OCP. Points and lines correspond to measured and fitted data, respectively.....	131
<b>Figure VI.2:</b> Coating thickness and porosity versus immersion time in 0.5 M NaCl ( $\text{pH} = 6$ ) and under argon bubbling, obtained from EIS and ToF-SIMS.....	133
<b>Figure VI.3:</b> EIS parameters versus immersion time (Table VI.1) obtained from fitting of EIS results of Figure VI.1 with E.C.3 (Figure III.11.B) .....	134
<b>Figure VI.4:</b> ToF-SIMS depth profiles negative ions for 50 nm ALD alumina coatings on electropolished copper substrate after immersion test .....	136
<b>Figure VI.5:</b> Comparative representation of ToF-SIMS depth profiles for 50 nm aged-immersed coating with a fresh-pristine one.....	137
<b>Figure VI.6:</b> Topographic AFM image ( $1 \times 1\ \mu\text{m}$ ) of 50 nm ALD alumina coated Cu substrate after immersion test, z range = 35 nm .....	139
<b>Figure VII.1:</b> LSV polarization curve for bare aluminium in 0.5 M NaCl, under argon bubbling ( $\text{pH} = 6$ ), scan rate: $1\ \text{mV}\cdot\text{s}^{-1}$ .....	145
<b>Figure VII.2:</b> Illustration of measurement of $R_p$ and $R_{\text{pass}}$ from the linear $i$ - $E$ curves .....	145
<b>Figure VII.3:</b> EIS Bode (left) and Nyquist (right) plots of bare aluminium in 0.5 M NaCl, under argon bubbling ( $\text{pH} = 6$ ) at OCP. Points and lines correspond to measured and fitted data, respectively.....	147
<b>Figure VII.4:</b> Equivalent circuit model adopted for the bare Al substrate for the present study at open circuit potential (E.C.4).....	148

## List of Figures

---

<i>Figure VII.5: Logarithm of the imaginary part of the impedance as a function of logarithm of frequency for bare Al substrate</i> .....	149
<i>Figure VII.6: ToF-SIMS negative ion depth profiles for 10 nm (A), 20 nm (B) and 50 nm (C) ALD alumina coatings prepared at 250°C on aluminium substrate</i> .....	154
<i>Figure VII.7: Comparative representation of selected ToF-SIMS depth profiles for 10, 20 and 50 nm ALD alumina coatings on aluminium substrate</i> .....	157
<i>Figure VII.8: LSV polarization curves for the bare and ALD alumina coated Al substrates in 0.5 M NaCl, under argon bubbling (pH = 6), scan rate: 1 mV.s<sup>-1</sup></i> .....	158
<i>Figure VII.9: EIS Bode (left) and Nyquist (right) plots for the bare and ALD alumina coated aluminium substrates in 0.5 M NaCl under argon bubbling (pH = 6) at OCP. Points and lines correspond to measured and fitted data, respectively</i> .....	162

## List of Tables

<i>Table I.1: Alternative names for ALD, from reference [45] .....</i>	<i>7</i>
<i>Table II.1: Chemical composition of copper disks (wt%) .....</i>	<i>23</i>
<i>Table II.2: Chemical composition of aluminium disks (wt%) .....</i>	<i>27</i>
<i>Table II.3: ALD Deposition conditions for the samples used in this study .....</i>	<i>29</i>
<i>Table III.1: Parameters related to LSV curve presented in Figure III.1 .....</i>	<i>48</i>
<i>Table III.2: Results of fitting EIS data of Figure III.3 with E.C.1 (Figure III.4.B).....</i>	<i>57</i>
<i>Table III.3: LSV parameters related to Figure III.9 .....</i>	<i>67</i>
<i>Table III.4: Average porosity values obtained from LSV and EIS for 2 series of coated samples</i>	<i>69</i>
<i>Table III.5: EIS data and results related to Figure III.10 fitted to E.C.2 (Figure III.13).....</i>	<i>74</i>
<i>Table III.6: Anodic charge transfer (calculated from Eq. III.14), corrosion current and anodic Tafel slopes for coated samples .....</i>	<i>75</i>
<i>Table III.7: EIS data and results related to Figure III.10 fitted to E.C.3 (Figure III.11.B) .....</i>	<i>77</i>
<i>Table IV.1: EIS data and results related to B-PT and B-NPT fitted with E.C.1 (Figure III.4.B). 85</i>	
<i>Table IV.2: LSV data and results related to Figure IV.2 .....</i>	<i>86</i>
<i>Table IV.3: EIS fitting results of EIS data related to coated samples (Figure IV.7) fitted with E.C.3 (Figure III.11.B). Fitting results for bare substrates presented already in Table IV.1 are added again for comparison .....</i>	<i>96</i>

## List of Tables

---

<b>Table IV.4:</b> Porosity values obtained for coated samples from EIS and LSV measurements.....	96
<b>Table IV.5:</b> Parameters related to LSV curves in Figure IV.8 .....	99
<b>Table V.1:</b> LSV data and parameters related to Figure V.6 .....	115
<b>Table V.2:</b> Porosity values obtained from LSV and EIS .....	116
<b>Table V.3:</b> Results of EIS data (Figure V.7) fitted with E.C.2 (Figure III.13).....	119
<b>Table VI.1:</b> EIS results related to Figure VI.1 fitted to E.C.3 (Figure III.11.B).....	132
<b>Table VII.1:</b> Calculated LSV parameters related to Figure VII.1 .....	145
<b>Table VII.2:</b> Results of EIS data in Figure VII.3 fitted with E.C.4 (Figure VII.4) .....	148
<b>Table VII.3:</b> Estimation of thickness of aluminium oxide obtained from assumption of 2D and 3D distributions of time constants in the oxide in addition to application of extreme values of dielectric constant of $Al_2O_3$ .....	152
<b>Table VII.4:</b> Parameters related to the polarization curves in Figure VII.8.....	158
<b>Table VII.5:</b> Porosity values obtained from LSV and EIS results .....	161
<b>Table VII.6:</b> EIS data and results related to Figure VII.9 fitted to E.C.4 (Figure VII.4).....	163
<b>Table VII.7:</b> Thickness values obtained from $C_{eff}$ values for interfacial oxide under the alumina coatings ( $\epsilon = 8$ ) .....	164



**Nanometre-thick alumina coatings deposited by ALD on metals: a comparative electrochemical and surface analysis study of corrosion properties**

Corrosion protection by ultrathin ( $\leq 50$  nm) alumina films deposited by atomic layer deposition (ALD) on copper and aluminium at 250°C was studied in 0.5 M NaCl aqueous solution by combining electrochemical and surface analytical methods in addition to microscopic techniques. The study of ALD Al<sub>2</sub>O<sub>3</sub> on Cu substrate included investigation of the effect of the coating thickness, the effect of an interfacial oxide, the effect of surface preparation and the durability of the coating. For ALD Al<sub>2</sub>O<sub>3</sub> on Al substrate, the work focused on the examination of the effect of the deposited coating thickness. ALD alumina coatings showed excellent corrosion properties on electropolished copper substrates, while they failed to protect the annealed substrate, as a result of poor adhesion to a smoothed surface. Modification of interfacial native copper oxide by its pre-treatment led to better corrosion protection of ALD alumina on copper substrate. Despite its remarkable sealing properties on electropolished Cu substrate, corrosion protection of ALD alumina was not durable. Coating of Al substrate with ALD Al<sub>2</sub>O<sub>3</sub> led to significant decrease of corrosion and passive current and increase of polarization resistance. Better performance was obtained for 10 and 20 nm coatings on Al than on Cu. Apart from significant decrease of current, the pitting potential was increased in presence of 20 and 50 nm coatings, which was not achieved with 10 nm due to its low thickness. This study was a preliminary study for application of ALD alumina coatings for corrosion protection of Al-Cu alloys in combination with other ALD compositions.

**Keywords:**

Corrosion protection; Ultrathin coatings; ALD; Copper; Aluminium, Alumina; Surface analysis; LSV; EIS

**Dépôt par ALD de couches minces d'alumine, étude spectroscopique et électrochimique, propriétés de résistance à la corrosion**

La protection contre la corrosion par des films ultraminces ( $\leq 50$  nm) d'alumine déposées par ALD sur le cuivre et l'aluminium à 250°C a été étudiée dans une solution aqueuse 0,5 M de NaCl en combinant méthodes d'analyse électrochimique et de surface en plus des techniques microscopiques. L'étude de l'alumine ALD sur un substrat Cu comprend l'effet de l'épaisseur du revêtement, l'effet de l'oxyde interfacial, l'effet de la préparation de la surface et la durabilité du revêtement. Pour l'alumine ALD sur le substrat Al, le travail a porté sur l'examen de l'effet de l'épaisseur du revêtement déposé. Les revêtements d'alumine ALD ont montré d'excellentes propriétés de corrosion sur des substrats en cuivre électropoli, tandis qu'ils ont échoué à protéger le substrat recuit, de fait d'une mauvaise adhérence à une surface lissée. L'amélioration de la résistance à la corrosion d'alumine ALD sur le substrat cuivre est obtenue en l'absence de vieillissement de l'oxyde natif interfacial, et sa modification par un prétraitement. En dépit de remarquables propriétés d'étanchéité sur un substrat Cu électropoli, la protection contre la corrosion de l'alumine ALD n'est pas durable. Le revêtement du substrat Al avec l'alumine ALD conduit à la diminution significative du courant de corrosion et à l'augmentation de la résistance à la corrosion. Une meilleure performance a été obtenue pour les revêtements de 10 et 20 nm sur Al que sur Cu. Le potentiel de piqûration est augmenté en présence des revêtements l'épaisseur de 20 et 50 nm, ce qui n'a pas été obtenus avec 10 nm en raison de sa faible épaisseur. Cette étude est une étude préliminaire pour l'application de revêtements d'alumine ALD pour la protection contre la corrosion des alliages Al-Cu en combinaison avec d'autres compositions ALD.

**Mots-clés:**

Protection contre la corrosion; Revêtements ultraminces; ALD; Cuivre; Aluminium; Alumine; L'analyse de surface; LSV; EIS

